

Technische Universität München

Max-Planck-Institut für Physik
(Werner-Heisenberg-Institut)

Detailed study of the binary system LS I +61°303 in VHE gamma-rays with the MAGIC telescope

Tobias Jogler

Vollständiger Abdruck der von der Fakultät für Physik der Technischen Universität München zur Erlangung des akademischen Grades eines
Doktors der Naturwissenschaften
genehmigten Dissertation.

Vorsitzender: Univ.-Prof. Dr. A. J. Buras

Prüfer der Dissertation:

1. Hon.-Prof. Dr. S. Bethke
2. Univ.-Prof. Dr. F. von Feilitzsch

Die Dissertation wurde am 09.09.2009 bei der Technischen Universität München eingereicht und durch die Fakultät für Physik am 19.11.2009 angenommen.

Abstract

In this thesis, the LS I +61°303 X-ray binary system is studied in great detail in Very High Energy (VHE, $E > 50$ GeV) gamma-rays with the Major Atmospheric Gamma-ray Imaging Cherenkov (MAGIC) telescope. X-ray binaries were long suspected to be potential gamma-ray sources. In the 1970's, the *COS B* satellite reported gamma-rays from the vicinity of LS I +61°303. Even after the more accurate measurements of the EGRET detector in the late 1990's, the association of LS I +61°303 as the source of the gamma-rays remained ambiguous until MAGIC (with its higher angular resolution measurements) identified LS I +61°303 as the VHE gamma-ray source.

The total observation time of 225 hours on LS I +61°303 places the binary system among the best studied VHE gamma-ray sources by MAGIC. The data were taken between 2005 and 2008 in three distinct observation campaigns (OC) each with more than 50 hours of observation time.

The huge amount of data taken on LS I +61°303 and the dense sampling of the system's orbital period allowed the detection of a periodicity in the VHE gamma-ray emission. This is the first time that a periodic modulation in a light curve could be proven in observations performed by MAGIC and the second time in the field of VHE gamma-ray astronomy. The obtained period of $P = 26.60 \pm 0.45$ d⁻¹ is compatible with the best measured orbital period of LS I +61°303 obtained by radio measurements.

Further investigations of the system were carried out in orbital phase bins of $\Delta\phi = 0.1$, where the phases (ϕ) reach from 0–1.0 within one orbit. LS I +61°303 is significantly detected in all OC's only in the 0.6–0.7 phase range close to the apastron of the compact object. In this phase range, the light curve shows an outburst of 2–4 days' duration while measurements - for example around the periastron passage of the compact object - yield only upper limits. The spectrum of the gamma-ray excess derived from the outbursts is well described by a simple power law:

$$\frac{dF}{dE} = (2.6 \pm 0.3_{\text{stat}} \pm 0.8_{\text{syst}}) \times 10^{-12} \left(\frac{E}{1.0} \right)^{-(2.6 \pm 0.2_{\text{stat}} \pm 0.2_{\text{syst}})} \text{TeV}^{-1} \text{cm}^{-2} \text{s}^{-1} \quad (1)$$

In the most recent measurements conducted in 2007 and 2008, additional significant fluxes were measured in the 0.8–1.0 phase range, not seen in previous observations. The derived spectrum in this phase range is poorly described by a simple power law. The spectrum is fitted better by a power law with an energy-dependent spectral index of the following form:

$$\frac{dF}{dE} = (39.9 \pm 6.7_{\text{stat}} \pm 12.0_{\text{syst}}) \times 10^{-12} \left(\frac{E}{0.3} \right)^{(-3.94 \pm 0.33_{\text{stat}}) + ((1.31 \pm 0.65_{\text{stat}}) \log(E))} \text{TeV}^{-1} \text{cm}^{-2} \text{s}^{-1} \quad (2)$$

This hint for spectral variability might be caused by a different production mechanism of the VHE gamma-rays dominating the emission at these phase ranges compared to the periodic outburst.

The diurnal light curves were investigated for flux variability on short timescales (less than a few hours). Several nights present hints for short-time variability. The most promising of those nights indicates a flux increase by a factor of three on a timescale as short as 30 minutes. Similar behavior is observed in the X-rays by several measurements performed in the last few years.

In addition to the VHE gamma-ray measurements, multiwavelength studies have been carried out at radio frequencies and X-ray energies in several observation campaigns. The LS I +61°303 X-ray spectra obtained in this thesis are all compatible with absorbed power laws. The spectral index of these power laws lies between 1.34–1.87 in agreement with previously published results by other observations. No prominent accretion disc feature such as iron-line emission or black-body radiation - as expected in the case of a microquasar - is detected in X-rays.

Evidence for a correlation between the flux levels in simultaneously taken X-ray and VHE gamma-ray data is found on a level of 3.4σ significance. A correlation study on the phase bin averaged light curve in X-ray and VHE gamma-rays was performed in a distinct observation campaign. A hint for correlation on the 2σ significance level is obtained by this study.

The correlated fluxes in the two energy bands can be explained by assuming that X-ray and VHE gamma-ray emission originate from the same particle population. In this case, the higher flux at X-ray energies favors a leptonic origin of the emission. In this scenario, the X-rays are attributed to synchrotron radiation of relativistic electrons. These electrons produce the VHE gamma-ray emission due to inverse Compton upscattering of UV photons provided by the companion star.

Theoretical models try to explain the emission of LS I +61°303 either in terms of a microquasar scenario or by proposing that a compact pulsar wind is responsible for the VHE gamma-ray emission. In terms of the observational results presented here, several microquasar models can be excluded by the measured VHE gamma-ray light curve and spectra. Nevertheless, two other leptonic microquasar models are compatible with the VHE gamma-ray emission.

In the case of the pulsar wind models, the scenario - attributing the emission to a mono-energetic free pulsar wind - can be rejected. On the other hand, the free pulsar wind, consisting of a power law distribution of electrons, can at least explain the VHE gamma-ray part of the presented results very well.

Two models attribute the VHE gamma-ray emission to the shocked (by the stellar wind) pulsar wind. One of the models suggests a hadronic origin of the VHE gamma-rays, which is improbable due to the X-ray/VHE gamma-ray flux correlation described above but cannot be fully excluded.

The spectral energy density derived in this work provides important information for the further development of the models.

The technical part of this thesis describes the development and implementation of the

MAGIC II camera control software.

In addition, the stability of the telescope's performance was studied between 2005–2008 in terms of investigating the effects on the Crab Nebula light curve and on its spectrum which are generated by the various hardware setups, the observation modes, the background light conditions and the zenith angle ranges used over a time span of four years. The stability study exhibits only a slight systematic increase both of the integral flux (by 12%) and the spectral index of $\Delta\Gamma = 0.2$, after the change to the 2 GHz read-out system of MAGIC. This systematic uncertainty is small compared to statistical uncertainties of measurements of weak sources like LS I +61°303. Generally, the MAGIC telescope displayed a very stable performance between 2005 and 2008.

Zusammenfassung

Gegenstand dieser Dissertation ist die detaillierte Studie des Röntgenstrahlen emittierenden Binärsystems LS I +61°303 in sehr hochenergetischen Gammastrahlenbereichen ($E > 50$ GeV) mithilfe des Major Atmospheric Gamma-ray Imaging Cherenkov (MAGIC) Teleskops. Schon früh wurde die These aufgestellt, Röntgenstrahlen emittierende Binärsysteme seien potentielle Quellen von Gammastrahlung: In den 1970er Jahren konnte erstmals Gammastrahlung in der unmittelbaren Nähe von LS I +61°303 durch den Satelliten *COS B* gemessen werden. Nachdem selbst präzisere Messungen des EGRET detectors in den 1990er Jahren LS I +61°303 nicht eindeutig als Gammastrahlenquelle identifizieren konnten, gelang es schließlich mithilfe der hohen Winkelauflösung des MAGIC Teleskops, LS I +61°303 in sehr hochenergetischen Gammastrahlenbereichen zu beobachten.

Aufgrund der immensen Beobachtungsdauer von insgesamt 225 Stunden gehört das Binärsystem LS I +61°303 zu den den am besten untersuchten sehr hochenergetischen Gammastrahlenquellen des MAGIC-Projekts. Die Daten wurden in drei verschiedenen Observationszyklen aufgenommen, die jeweils über 50 Stunden Beobachtungszeit umfassen und zwischen 2005 und 2008 stattfanden.

Die große Menge an Daten, die an LS I +61°303 genommen wurden und die dicht aufeinander folgenden, stichprobenartigen Messungen der Umlaufbahnperiode des Systems ermöglichten die Entdeckung einer Periodizität innerhalb der sehr hochenergetischen Gammastrahlenemission. Erstmals im Rahmen des MAGIC-Projekts und zum zweiten Mal innerhalb der sehr hochenergetischen Gammastrahlenastronomie konnte auf diese Weise die periodische Modulation einer Lichtkurve bewiesen werden. Deren gemessene Periode von $P = 26.60 \pm 0.45 \text{ d}^{-1}$ stimmt mit der am präzisesten gemessenen Umlaufbahnperiode von LS I +61°303, abgeleitet von Messungen im Radiobereich, überein.

Weitergehende Untersuchungen des Systems fanden in den Intervallen der orbitalen Phasen mit einer Spanne von $\Delta\phi = 0.1$ statt, dabei reichen die orbitalen Phasen (ϕ) von 0–1.0 innerhalb einer Umlaufbahn. In allen drei Observationszyklen kann LS I +61°303 nur im Phasenbereich 0.6–0.7, nahe des Apastron des kompakten Objekts, mit hoher Signifikanz beobachtet werden.

In diesem Phasenbereich zeigt die Lichtkurve einen deutlichen Ausschlag im Laufe einer Zeitspanne von zwei bis vier Tagen, während Messungen in anderen Phasen - z.B. während der höchstmöglichen Annäherung des kompakten Objektes an den Stern - nur obere Grenzen für mögliche Emissionen liefern. Das Spektrum des von den Ausschlägen erzeugten Gammastrahlenüberschusses kann sehr gut durch ein einfaches Potenzgesetz beschrieben werden:

$$\frac{dF}{dE} = (2.6 \pm 0.3_{\text{stat}} \pm 0.8_{\text{syst}}) \times 10^{-12} \left(\frac{E}{1.0} \right)^{-(2.6 \pm 0.2_{\text{stat}} \pm 0.2_{\text{syst}})} \text{ TeV}^{-1} \text{ cm}^{-2} \text{ s}^{-1} \quad (3)$$

In den jüngsten, zwischen 2007 und 2008 vorgenommenen Messungen konnten weitere signifikante Flüsse im Phasenbereich 0.8–1.0 beobachtet werden, die in früheren Observationen nicht sichtbar waren. Das Spektrum dieses Phasenbereichs lässt sich jedoch nur unzureichend durch ein einfaches Potenzgesetz beschreiben. Eine bessere Anpassung ermöglicht ein Potenzgesetz mit energieabhängigem Exponenten in der folgenden Form:

$$\frac{dF}{dE} = (39.9 \pm 6.7_{\text{stat}} \pm 12.0_{\text{syst}}) \times 10^{-12} \left(\frac{E}{0.3} \right)^{(-3.94 \pm 0.33_{\text{stat}}) + ((1.31 \pm 0.65_{\text{stat}}) \log(E))} \text{TeV}^{-1} \text{cm}^{-2} \text{s}^{-1} \quad (4)$$

Dieser Hinweis auf spektrale Variabilität könnte durch einen vom Produktionsmechanismus des periodischen Ausbruchs abweichenden Prozess, der innerhalb dieser Phasenbereiche die sehr hochenergetische Gammastrahlen Emission dominiert, verursacht werden.

Lichtkurven einzelner Tage wurden auf Variabilität der Flüsse innerhalb kurzer Zeitskalen (wenige Stunden) untersucht. In einigen Nächten lassen sich Hinweise auf Kurzzeit-Variabilität finden. Die meistversprechende dieser Nächte bezeugt eine Steigerung des Flusses um das Dreifache innerhalb einer Zeitdauer von nur 30 Minuten. Ein ähnliches Verhalten kann bei Röntgenstrahlung beobachtet werden, wie zahlreiche Messungen der letzten Jahre belegen.

Neben den Messungen der sehr hochenergetischen Gammastrahlung wurden zusätzliche Multi-Wellenlängen Studien in mehreren Observationszyklen in Radiofrequenzen und Röntgenenergien unternommen. Alle im Rahmen dieser Arbeit erstellten LS I +61°303 Röntgenstrahlenspektren sind kompatibel mit absorbierten Potenzgesetzen. Der Exponent dieser Gesetze liegt, in Übereinstimmung mit bereits publizierten Ergebnissen anderer Messungen, zwischen 1.34–1.87. Keines der bekannten Merkmale von Akkretionsscheiben, wie Emission einer Eisenlinie oder Schwarzkörperstrahlung, die man im Falle eines Mikroquasars erwartet würde, kann im Röntgenbereich nachgewiesen werden.

Hinweise auf eine Korrelation zwischen den Flussebenen der parallel gemessenen Röntgen- und sehr hochenergetischen Gammastrahlen lassen sich mit einer Signifikanz von 3.4σ feststellen. Die durchschnittlichen Lichtkurven der Phasenintervalle sowohl von Röntgen- als auch sehr hochenergetischer Gammastrahlen wurden in einer Korrelationsstudie miteinander verglichen. In dieser Studie können die Hinweise auf Korrelation mit einer Signifikanz von 2σ angegeben werden.

Die Korrelation der Flüsse in den beiden Energiebereichen könnte aufgrund der Annahme erklärt werden, dass die Emissionen von Röntgenstrahlen und sehr hochenergetischen Gammastrahlen von der gleichen Teilchenpopulation verursacht werden. In diesem Fall spricht der höhere Fluss im Röntgenstrahlenbereich für einen leptonen Ursprung der Emission. Somit entsprechen diese Röntgenstrahlen den Synchrotronstrahlen relativistischer Elektronen. Diese Elektronen erzeugen durch inverse Comptonstreuung von UV-Photonen des Begleitsterns die sehr hochenergetische Gammastrahlenemission.

Theoretische Modelle versuchen die Emissionen von LS I +61°303 zu erklären, indem das Binärsystem entweder durch Mikroquasarmodelle beschrieben, oder ein kompakter Pulsarwind als Quelle der sehr hochenergetischen Gammastrahlung angenommen wird. Aufgrund der hier dargelegten Lichtkurven und -spektren können mehrere Mikroquasarmodelle ausgeschlossen werden. Nur zwei der leptonen Modelle bieten eine Erklärung für die sehr

hochenergetische Gammastrahlenemission, die nicht mit den gemessenen Daten im Widerspruch steht.

In Falle der Pulsarwindmodelle können monoenergetische freie Pulsarwinde als Ursache der Emissionen ausgeschlossen werden. Dagegen bietet der freie Pulsarwind, bestehend aus Elektronen, deren Energieverteilung einem Potenzgesetz folgt, zumindest ein gutes Erklärungsmodell für die sehr hochenergetischen Gammastrahlen und stimmt in diesem Sinne mit den hier ermittelten Daten überein.

Zwei Modelle schreiben den durch Sternwinde geschockten Pulsarwinden die sehr hochenergetische Gammastrahlenemission zu. Eines dieser Modelle nimmt einen hadronischen Ursprung der sehr hochenergetischen Gammastrahlung an. Im Hinblick auf die oben beschriebene Korrelation der Flüsse zwischen Röntgen- und sehr hochenergetischen Gammastrahlen ist ein hadronischer Ursprung sehr unwahrscheinlich, kann aber nicht vollends ausgeschlossen werden.

Die spektrale Energiedichte, die in dieser Arbeit gemessen wurde, stellt wichtige Informationen für die weitere Entwicklung von Modellen bereit.

Im technischen Teil dieser Arbeit werden die Entwicklung und Inbetriebnahme der Kontrollsoftware der Kamera für MAGIC II beschrieben.

Auch die Prüfung der Stabilität der Leistungsfähigkeit des Teleskops zwischen 2005 und 2008 bildete einen Teil dieser Arbeit. Für diese Zeitspanne wurden die Lichtkurve und das Spektrum des Krebsnebels auf mögliche Auswirkungen von Aktualisierungen der Teleskopkomponenten und der Observationsmethoden, Stärke des Untergrundlichts und unterschiedlichen Zenithwinkelbereichen überprüft. Die Untersuchungsergebnisse der Stabilität der Leistungsfähigkeit des Teleskops zeigen nur einen kleinen systematischen Anstieg sowohl des integrierten Flusses (von 12%) als auch des spektralen Indexes um $\Delta\Gamma = 0.2$ nach dem Wechsel zum 2 GHz Auslesesystem von MAGIC. Diese systematische Unsicherheit erweist sich als klein im Vergleich zu statistischen Unsicherheiten, die sich bei der Messung schwacher Quellen wie LS I +61°303 ergeben. Im Allgemeinen lässt sich sagen, dass das MAGIC Teleskop in der Zeit von 2005 bis 2008 eine sehr stabile Leistungsfähigkeit aufwies.

Contents

Abstract	i
Zusammenfassung	v
List of abbreviations and acronyms	1
Preface	5
1 VHE gamma-ray astrophysics	7
1.1 Cosmic rays	7
1.2 Particle acceleration mechanism	10
1.2.1 Acceleration mechanisms	10
1.2.2 Maximum energy achieved by cosmic accelerators	11
1.3 VHE gamma-rays	12
1.3.1 Leptonic production	12
1.3.2 Hadronic production	15
1.3.3 VHE gamma-ray absorption	16
1.4 VHE gamma-ray sources	16
1.4.1 Pulsars	17
1.4.2 Pulsar wind nebulae	19
1.4.3 Supernova remnants	20
1.4.4 Unidentified sources	21
1.4.5 Star clusters	21
1.4.6 Blazars	22
1.4.7 Radio galaxies	22
1.4.8 Gamma-ray bursts	23
1.5 Fundamental physics	23
2 Gamma-ray binaries	25
2.1 A classification of X-ray binaries	25
2.2 Microquasars	26
2.2.1 Accretion	27
2.2.2 Jets	29
2.2.3 The different emission states	33
2.2.4 VHE gamma-ray emission	34
2.3 Pulsar wind binaries	40

2.3.1	VHE gamma-ray emission	41
2.4	Absorption in binary systems	42
2.5	Detected binary systems in gamma-rays	43
3	Imaging Atmospheric Cherenkov Telescopes	45
3.1	Extensive air showers	45
3.2	Cherenkov light production	49
3.3	The imaging technique	53
3.4	The uncertainties in IACT measurements	54
4	The MAGIC telescopes	57
4.1	MAGIC I	58
4.1.1	The camera of MAGIC I	59
4.1.2	The read out system of MAGIC I	59
4.1.3	The trigger system of MAGIC I	60
4.1.4	The calibration system of MAGIC I	61
4.2	MAGIC II	63
4.2.1	The camera of MAGIC II	64
4.2.2	The camera control program of MAGIC II	67
4.2.3	The read out system of MAGIC II	70
4.2.4	The trigger system of MAGIC II	70
4.2.5	The calibration system of MAGIC II	71
5	The data analysis	73
5.1	The MAGIC data analysis	73
5.1.1	From FADC counts to shower image parameters	74
5.1.2	The shower image parameters and their correlation	80
5.1.3	Gamma/hadron separation	81
5.1.4	The energy estimation	88
5.1.5	Arrival direction estimation	90
5.1.6	The observation modes	92
5.1.7	The signal event selection	93
5.1.8	Angular resolution and source extension	96
5.1.9	Monte Carlo simulations	97
5.1.10	Flux calculation and spectral energy distribution	99
5.1.11	Upper Limit calculation	102
5.1.12	Summary of the cut values used in the analysis	102
5.2	Systematic uncertainties	103
5.3	X-ray analysis	104
5.4	Periodicity searches	107
5.4.1	Periodic, quasiperiodic or not at all?	108
5.4.2	Tests for periodicity	109

6	Performance of the MAGIC telescope from 2005-2008	115
6.1	Data selection	115
6.2	The Crab Nebula data sample	116
6.3	The temporal behavior of the integral flux	116
6.4	The stability of the spectrum	119
6.5	The influence of moonlight on the measurements	120
6.6	Performance summary of MAGIC I	123
7	Observation of LS I +61°303	125
7.1	The orbital parameters of LS I +61°303	125
7.2	The multiwavelength behavior of LS I +61°303	128
7.2.1	The radio behavior of LS I +61°303	128
7.2.2	The X-ray behavior of LS I +61°303	129
7.2.3	The high energy emission from the vicinity of LS I +61°303	133
7.3	VHE gamma-ray observations with MAGIC	134
7.4	LS I +61°303 a VHE gamma-ray emitting binary	136
7.5	The temporal behavior of the flux	137
7.6	Periodicity searches	147
7.6.1	The search at the orbital period	149
7.6.2	Scan of a larger frequency domain	151
7.6.3	Conclusions from the periodicity search	154
7.7	Spectral properties	156
7.8	Summary of the LS I +61°303 measurements by MAGIC	161
7.9	Observations of LS I +61°303 by VERITAS	162
7.10	The multiwavelength data	163
7.10.1	X-ray and TeV data	164
7.10.2	Simultaneous X-ray and TeV observations	165
7.10.3	Simultaneous radio and TeV observations	170
7.11	The spectral energy density of LS I +61°303	171
7.12	Interpretation of the LS I +61°303 observations	173
7.12.1	The microquasar scenario	174
7.12.2	The pulsar wind scenario	178
7.13	Conclusions resulting from the LS I +61°303 observations	185
7.14	Future observations with MAGIC I and MAGIC II	185
8	Conclusion and Outlook	187
A	LS I +61°303 observational details	191
A.1	LS I +61°303 light curve for MAGIC OC III	191
A.2	LS I +61°303 intranight light curves	194
A.3	LS I +61°303 spectra	201
A.4	Correlation significance estimation	203
	List of figures	210
	List of table	211

List of abbreviations and acronyms

1E	First <i>EINSTEIN</i> catalogue
2EG	Second EGRET catalogue
4U	Fourth Uhuru satellite catalogue
ADC	Analog to digital converter
AGN	Active galactic nucleus
AMC	Active mirror control
AMP	Amplifier
ARF	Ancillary response file
<i>ASCA</i>	Advanced satellite for cosmology and astrophysics
ASM	All sky monitor (instrument of <i>RXTE</i>)
AU	Astronomical unit
AUI	Associated Universities, Inc.
BAT	Burst alert telescope (instrument on board <i>Swift</i>)
<i>BeppoSAX</i>	Satellite per astronomia X
caco	Camera control
CCD	Charge coupling device
CG	<i>COS B</i> gamma (catalogue)
<i>CGRO</i>	Compton gamma-ray observatory
<i>Chandra</i>	Chandra X-ray observatory
CMB	Cosmic microwave background
COG	Center of gravity
COMPTEL	Compton telescope (instrument on board <i>CGRO</i>)
<i>COS B</i>	Cosmic ray satellite (option B)
cCPF	Complementary cumulative probability density function
CPF	Cumulative probability density function
CU	Crab Nebula unit
Cyg	Cygnus (constellation)
DAC	Digital to analog converter
DAQ	Data acquisition
DEC	Declination
DC	Direct current
DT	Discriminator threshold
EAS	Extensive air shower
EC	External Compton
EGRET	Energetic gamma-ray experiment telescope
<i>EINSTEIN</i>	<i>EINSTEIN</i> X-ray satellite

EM	Electro magnetic
EPIC	European photon imaging camera (main instrument of <i>XMM-Newton</i>)
EVN	European very long baseline interferometry network
FADC	Flash analogue to digital converter
<i>FERMI</i>	<i>FERMI</i> gamma-ray telescope
FoV	Field of view
FWHM	Full width half maximum
GBI	Green Banks interferometer
GC	Globular cluster
GeV	Giga electron volt
GRB	Gamma-ray burst
GT	Gregory & Taylor (catalogue)
GUI	Graphical user interface
GZK-cutoff	Greisen Zatesepin Kuz'min cutoff
HBL	High frequency peaked BL Lac
HE	High energy
HEGRA	High energy gamma-ray astronomy
HESS	High energy stereoscopic system
HMXB	High mass X-ray binary
HPD	Hybrid photo diode
<i>HR</i>	Hardness ratio
HSS	High soft state
HV	high voltage
IACT	Imaging atmospheric Cherenkov telescope
IC	Inverse Compton
IC	Index catalogue
IFS	Independent fourier spacing
<i>INTEGRAL</i>	International gamma-ray astrophysics laboratory
IR	Infrared
IPRC	Individual pixel rate control
ISM	Inter stellar medium
JD	Julian date
keV	Kilo electron volt
kpc	Kilo parsec
L1	level one
LAT	Large area telescope (instrument on board <i>FERMI</i>)
LC	Light curve
LBL	Low frequency peaked BL Lac
LED	Light emitting diode
LHS	Low hard state
LMXB	Low mass X-ray binary
M	Messier (catalogue)
MAGIC	Major atmospheric gamma-ray imaging Cherenkov (telescope)
mas	milliarcsecond
MC	Monte carlo (simulation)

MERLIN	Multi-element radio linked interferometer
MeV	Mega electron volt
MHD	Magneto hydro-dynamic
MJD	Modified Julian date
MOS	Metal oxide semiconductor
Mrk	Makarian
MW	Multi wavelength
MUX	Multiplexing 2GHz FADC read out
NDF	Number of degrees of freedom
NN	Next neighbor
NRAO	National radio astronomy observatory
NS	Neutron star
OC	Observational campaign
PC	Photo counting
PCI	Peripheral component interconnect
PDF	Probability density function
PIN	Positive intrinsic negative (diode)
PKS	Parkes catalogue of radio sources
PMT	Photo multiplier tube
PP	Partly periodic
PSF	Point spread function
PSR	Pulsar (normal radio pulsar)
PW	Pulsar wind
PWN	Pulsar wind nebula
QE	Quantum efficiency
QP	Quasi-periodic
QPO	Quasi-periodic oscillations
Quasar	Quasi stellar object
RA	Right ascension
RATAN	Academy of science radio telescope
RF	Random forest
RMS	Root mean square
<i>ROSAT</i>	Röntgen satellite
RX	<i>ROSAT</i> X-ray catalogue
<i>RXTE</i>	Rossi X-ray timing explorer
SCCP	Slow control cluster processor
SED	Spectral energy density
SNR	Supernova remnant
SS	Stephenson and Sanduleak catalogue
SSC	Self-absorbed synchrotron Compton
STI	Sampling time interval
TeV	Tera electron volt
Tuc	Tucana (constellation)
UHE	Ultra high energy
UL	Upper limit

ULX	Ultra luminous X-ray source
UV	Ultra violet
VCSEL	Vertical-cavity surface-emitting laser
VERITAS	Very energetic radiation imaging telescope array system
VHE	Very high energy
VLA	Very large array (radio telescopes)
VLBA	Very long baseline array
VLBI	Very long baseline interferometer
VME	Versa module eurocard
WC	Winston cone
WR	Wolf-Rayet (star)
<i>XMM-Newton</i>	X-ray Multi-Mirror Newton (X-ray satellite)
XRБ	X-ray binary
XRT	X-ray telescope (on board <i>Swift</i>)

Preface

Very high energy (VHE, $E > 50\text{GeV}$) gamma-ray astronomy is a recent and very rapidly developing field of science. In 1989, the Whipple collaboration discovered the first VHE gamma-ray signal on a 9-standard deviation level: The Crab Nebula. Since then, 1989 is considered as the birth year of contemporary VHE gamma-ray astronomy. A lot of new sources were discovered in the following years, most of them by the new third generation of imaging atmospheric Cherenkov telescopes. The MAGIC, HESS and VERITAS telescopes belong to this new generation of instruments. My work in this very interesting field is focused on the study of VHE gamma-ray binaries with MAGIC. Due to the work reported in this thesis, LS I +61°303 is identified as a VHE gamma-ray binary, increasing the number of known gamma-ray binaries to three and thus establishing a new class of VHE gamma-ray sources. Prior to the discovery of the PSR B1259-63 and LS 5039 binary systems by the HESS collaboration and LS I +61°303 by the MAGIC collaboration, no binary system had been established as a VHE gamma-ray emitter.

The topic of this thesis is the detailed study of LS I +61°303 with the MAGIC telescope. The detailed analysis of the 225 hours observation time leads to the first ever detection of a periodic VHE gamma-ray signal by MAGIC. This is the second time periodicity could be proven in VHE gamma-ray astronomy. Analysis of the spectral and temporal behavior of the VHE gamma-ray emission from LS I +61°303 strongly constrains several theory models and even excludes several of them. With the multiwavelength data at radio frequencies and X-ray energies that were taken simultaneously, the first solid spectral energy densities (SED) could be presented. In addition to the VHE gamma-ray data, I analyzed the *Swift* X-ray data. This simultaneous SED provides a benchmark for all models for testing if they can describe not only the VHE gamma-ray emission of LS I +61°303 but also the full emission processes taking place in this system.

My further contributions to the MAGIC experiment are the development of analysis tools and the improvement of the existing ones. In addition, I have developed the software for the MAGIC II camera control and designed a test for its control components. I also contributed to the commissioning of the 2 GHz read-out upgrade of MAGIC I (the so-called “MUX”) .

The thesis is organized as follows: The first chapter briefly explains both my interest in VHE gamma-ray astronomy and the basic production mechanisms of this radiation in the cosmic accelerators. Afterwards, the source types currently detected in VHE gamma-rays, as well as the processes leading to the emission, are summarized. In the second chapter, the X-ray binaries and their potential as VHE gamma-ray emitters are discussed. The different possible scenarios are outlined and the expected emission features discussed. The third chapter introduces the imaging atmospheric Cherenkov technique for detecting VHE gamma-rays from the ground. The MAGIC telescopes are described in the fourth chapter, with emphasis on the components such as the 2 GHz read out upgrade of MAGIC I and the camera of MAGIC II on which I worked. In the fifth chapter, the analysis of the MAGIC data is described in great detail. In addition, the X-ray analysis which I performed for the LS I +61°303 data is explained briefly. Finally, the method to test for periodicity in light curves is explained. The sixth chapter deals with the first long-term performance study of MAGIC I and the investigation of the effects of observation modes, the hardware setups, the performance parameters of the telescope and moonlight observations both on the spectrum and on the light curve measurements. Within the seventh chapter, the LS I +61°303 observations in VHE gamma-rays and the multiwavelength campaigns undertaken both in the X-rays and in the radio band are discussed in detail. After this, the flux correlation of these lower energetic emissions with the VHE gamma-ray measurements are presented. Finally, the impact of the VHE gamma-ray and multiwavelength observation results on the models of the emission from LS I +61°303 are discussed. The conclusions of the results presented here are drawn in chapter eight. Finally, a short outlook is given for the (already planned) future observations of LS I +61°303.

Chapter 1

VHE gamma-ray astrophysics

Very high energy (VHE) gamma-ray astronomy, explores the radiation above $E > 50$ GeV in the universe . It is the most recently opened window onto electro magnetic (EM) radiation for the purpose of exploring our universe. This chapter will give a brief overview of how these very high energetic messengers are created and how their observation can help us to understand the violent processes in our universe. First, I shall explain about cosmic rays - the first very high energetic cosmic radiation to be discovered. From the observation of cosmic rays, the questions of how are these particles created and accelerated in the universe arise. What type of cosmic accelerators generate them? Where are the sources located and how can we detect them? To try to answer these questions, the theoretically possible acceleration mechanism of charged particles in magnetic and electrical fields will be discussed briefly. In this context, the production of cosmic rays will inevitably lead to VHE gamma-ray production. Then, the interaction of the VHE gamma-rays with the environment (at their origin) and the resultant inferences will be considered. After outlining these basic production processes, I shall give an overview of the various cosmic accelerators which are good candidates for VHE gamma-ray production and summarize the current detection successes. Here, I shall also comment on other very interesting topics which can be studied by VHE gamma-ray astronomy.

1.1 Cosmic rays

The first evidence for charged particles hitting the Earth's atmosphere was found in the famous balloon experiment by Victor Hess (Hess, 1912). Hess found that the higher the balloon's altitude, the faster an electrometer discharges. He concluded that the discharge must come from charged particles which are more abundant in the higher atmosphere and hence come from outer space. Since the discovery of cosmic rays, a very large effort has been made to measure their energy spectrum and composition. One of the main questions

still open is: What are the sources of these cosmic rays? To understand the difficulties in answering this question, the cosmic ray spectrum must be considered. The spectrum of cosmic rays (see Fig. 1.1) extends over 13 orders of magnitude in energy and reaches as high as 10^{20} eV. Several distinct features are visible in the cosmic ray spectrum. The lower

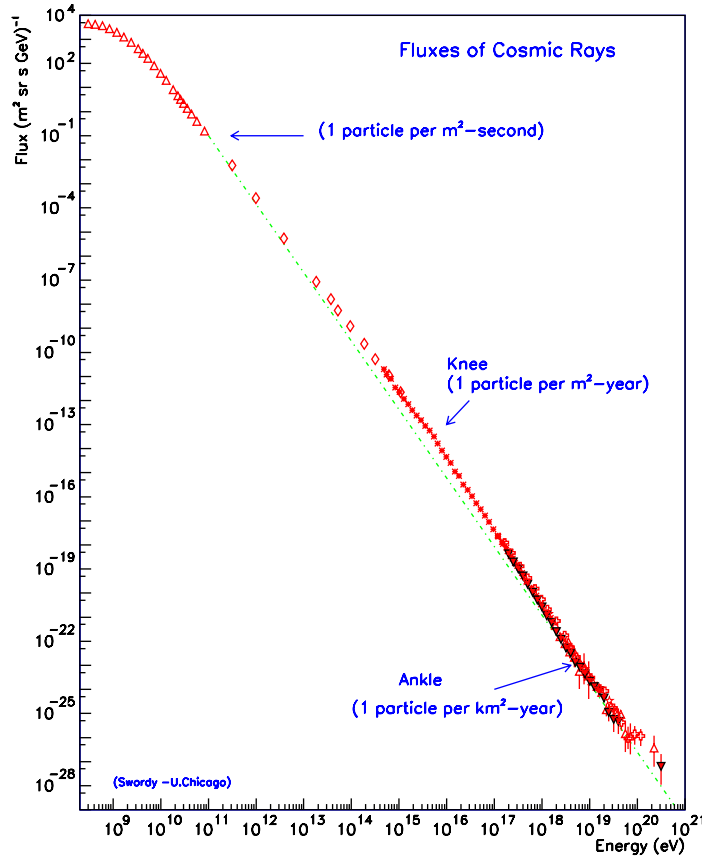


Figure 1.1: The cosmic ray spectrum as measured over 13 orders of magnitude. The most significant features are indicated as well as some more intuitive particle fluxes. Figure taken from Swordy (1997).

energetic part ($E < 1$ GeV) is dominated by the solar wind and particles accelerated in the interplanetary shock in our solar system. Above this energy, the spectrum follows a power law with spectral index $\Gamma = -2.7$ up to energies of about 3×10^{15} eV. The cosmic rays responsible for this part of the spectrum are thought to be of galactic origin. For even higher energies, the spectrum shows a softening and the point at which this occurs is called the “knee”. Particles with energy above the knee are probably of extra galactic origin, since they could not be confined within our galaxy’s magnetic field. For a recent review about this energy range, see Bluemer et al. (2009). At the highest energies, a cutoff in the spectrum is predicted due to the interaction of the cosmic rays with cosmic microwave background (CMB)

radiation - the famous GZK-cutoff (Greisen, 1966; Zatsepin and Kuz'min, 1966). Despite many theoretical suggestions where to look for the sources of cosmic rays, no definite answer about their sources has been given up to now. One complication is that the tracing of the sources is not possible in terms of the cosmic rays themselves. Since the cosmic rays consist of charged particles, they are deflected by the galactic magnetic field and thus do not give information about the direction of their source. Nevertheless, wherever they are produced, the mechanism will not only produce them but also, due to their interaction with matter, will always generate byproducts like leptons from charged pion decay and gamma-rays from neutral pion decay. From these particle decays, the resulting neutrinos and gamma-rays are not deflected by the magnetic fields and point directly back to the source. In consequence these particles are perfect messengers of the cosmic ray sources.

In Fig. 1.2 the possible sources which can accelerate particles to ultra high energies (UHE, $E > 10^{15}$ eV) are shown. This plot was first compiled by A.M. Hillas (Hillas, 1984) and shows the maximum energy which can be reached in various sources, depending on their magnetic field and its extension. In addition, these sources are potential places for VHE gamma-ray production and thus natural targets for VHE gamma-ray astronomy to study in detail the high energy processes taking place in them. Recently, a correlation of cosmic

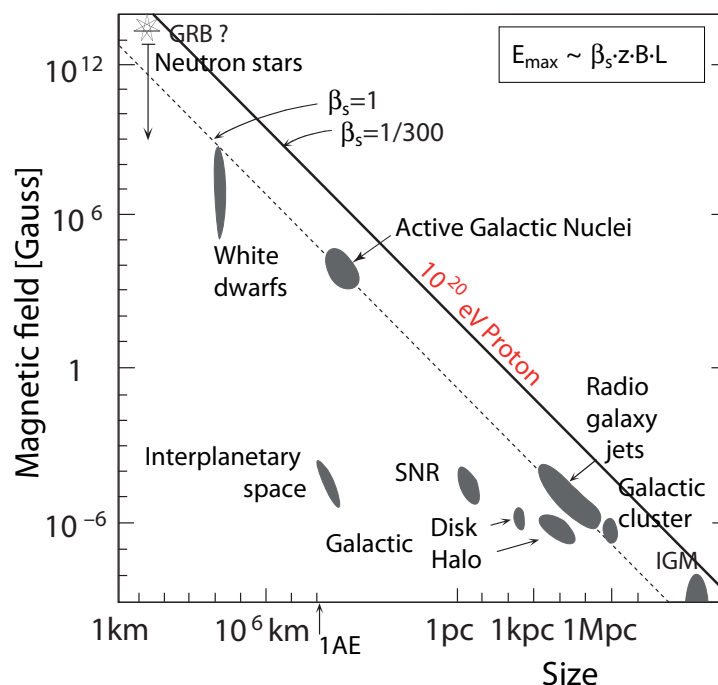


Figure 1.2: The so-called Hillas plot (Hillas, 1984) shows the potential sources of the ultra high energy cosmic rays ($E \sim 10^{20}$ eV). The maximum energy is determined by the magnetic field in the source and the extension of the magnetic field. The figure is adapted from Blümer and Kampert (2000).

ray event arrival directions (with energies above 5.7×10^{19} eV) with the position of nearby (75 Mpc) Active Galactic Nuclei (AGN's) has been claimed by the Auger experiment (The Pierre Auger Collaboration et al., 2007). If this claim is true, one source of UHE cosmic rays would have been found - but the correlation is not very significant and better statistics to be recorded in future years will show if this correlation does in fact hold true.

1.2 Particle acceleration mechanism

A very interesting question is how particles are accelerated in the cosmic objects. On Earth, we can accelerate particles but we need huge energies to do so and the efficiency is in general rather low. However, nature must have some efficient mechanism to accelerate particles to VHE or even UHE, considering the maximum achieved energy of the measured cosmic ray spectrum.

1.2.1 Acceleration mechanisms

There are several processes which can lead to efficient particle acceleration. One-shot acceleration in huge electric fields will accelerate all charged particles to the same energy, where the energy gain is equal to the difference in the electrical potential. Other acceleration mechanisms use magnetic fields to accelerate the particles. Proposed processes involving magnetic fields are First- and Second-order Fermi acceleration (Fermi, 1949) and shear acceleration (Ostrowski, 2000). Here, only the basic principle of Fermi shock acceleration will be described and, for a detailed treatment, the reader is referred to the literature (Gaisser, 1990; Longair, 1994).

In Fermi Second-order acceleration, the magnetic field scatters the particle (without a collision) into a molecular cloud. The cloud moves with random speed V and scatters the particle, which gains in average energy per collision. If the mean free path between clouds is L , the energy gain over time can be written as:

$$\frac{dE}{dt} = \frac{4}{3} \left(\frac{V^2}{cL} \right) E = \alpha E \quad (1.1)$$

From eq. (1.1) it is clear that the energy gain is Second order in V and, taking into account the diffusion energy losses, the following particle spectrum is obtained.

$$N(E) = \text{const} \times E^{-\Gamma} \quad (1.2)$$

Here $\Gamma = 1 + (\alpha t_{\text{esc}})^{-1}$ where t_{esc} is the characteristic time the particle remains in the acceleration region. So the Second-order Fermi acceleration mechanism leads to a non-universal power law index and the energy gain is rather slow.

Another more efficient possibility is the First-order Fermi acceleration. In this scenario, a strong plain supersonic shock is assumed and high energy particles pass through the shock. Due to scattering, the particles' velocity distribution in front of the shock is isotropic. The particles gain some energy by passing through the shock and then their velocity distribution becomes isotropic (with respect to the flow behind the shock front), again by scattering on the turbulence behind the shock. If the particles move again across the shock front, they encounter gas moving towards them with the same speed as the shock front and, again, increase their energy by the same amount. Thus, the particles gain every time they cross the shock front energy. The important point is that their velocity distribution becomes isotropic as soon as they cross the shock. It can be shown that the energy gain per particle is $\sim \frac{V}{c}$ and thus proportional in first order to the speed of the shockwave. The energy gain of the particle is taken from the kinetic energy of the shock. In the case of non-relativistic shocks, the energy distribution of the particles is again a power law but this time with the universal exponent $\Gamma = 2$. This is a remarkable process since strong shocks occur in many astrophysical sources, as will be discussed in subsequent sections. The spectral index is modified if the shock is relativistic or weak. In the case of weak shocks, steeper spectra are expected and the same is true for electron spectra which suffer synchrotron radiation (e.g. Heavens and Meisenheimer 1987). In addition, relativistic particles will modify the magnetic field of the shock by their movement and this can lead to enhancement in the maximum energy achievable in fixed acceleration dimension (see Berezhko 1996; Berezhko and Völk 1997).

1.2.2 Maximum energy achieved by cosmic accelerators

A vital parameter for identifying sources of VHEs and UHEs is the maximum energy achievable for individual particles in any cosmic accelerator. In general, interactions with the ambient medium around or in the accelerator can alter the maximum achievable energy by several orders of magnitude. These circumstances will be discussed in more detail in the next section.

Every accelerator can only increase the energy of any charged particle as long as it remains in it. This leads to the so-called Hillas criterium (Hillas, 1984) which states that the maximum energy is reached when the Lamor radius ($r_L = E/qB$ with E particle energy, q particle charge and B magnetic field in the accelerator) of the particle exceeds the extension of the accelerator (d_a). Hence, the maximum achievable energy until the inevitable escape of the particle from whatever accelerator is:

$$E_{\max} = qBd_a \tag{1.3}$$

To study further the maximum energy reachable in a given source, details about the acceleration timescales must be known. In general, the maximum energy is reached after a time $t_{\text{acc}} = t_{\text{esc/cool}}$ where $t_{\text{esc/cool}}$ is the escape or cooling time. Normally, the acceleration time in the absence of cooling processes can be defined (source-independent) as

$$t_{\text{acc}} = \eta \frac{r_L}{c} = \eta \frac{E}{qBd_a} \quad (1.4)$$

The parameter η represents the accelerator efficiency and depends on the details of the acceleration mechanism (see the previous section). Often η is left as a free parameter in models of VHE gamma-ray emission to be determined by fitting the model to the measurements.

The different cooling processes decrease the maximum possible acceleration time for $t_{\text{cool}} < t_{\text{esc}}$. In addition, they may lead to the production of VHE gamma-rays and lower energetic photons. These very important cooling processes are explained in the next sections.

1.3 VHE gamma-rays

Just as the acceleration of charged particles in shock waves was described in the previous section, this section will explain how these particles generate VHE gamma-rays and which types of processes will modify the observed spectrum on Earth. It is important to know the different cooling times to determine the dominant emission channel of the source. For each possible VHE gamma-ray, source different ambient parameters have to be taken into account which makes a case to case evaluation necessary. Nonetheless it is mandatory to know the basic processes and the dependency on the various parameters present in the accelerator or production site¹. It is clear that each radiative production of VHE gamma-rays will modify the energy distribution of the radiating particle population. In almost all models, an equilibrium by newly injected particles and cooling losses is assumed. The time of dynamical emission to reach this equilibrium is often not considered. This is different in the dynamical emission expected from binaries which is described in chapter 2.

1.3.1 Leptonic production

If the accelerated particles are leptons (electrons), then there are three major processes through which photons can be generated.

- synchrotron radiation in magnetic fields

¹The production site of VHE gamma-rays can be different to the site of particle acceleration. See section 1.4.4 for one possible scenario.

- Bremsstrahlung
- inverse Compton scattering of seed photons

The production of VHE gamma-rays by leptons is only possible via inverse Compton (IC) scattering and Bremsstrahlung. Nevertheless, the synchrotron emission process is very important for VHE gamma-ray emission since it is often the dominant cooling process and thus can prevent the particle acceleration to VHE if the magnetic field is too high. In addition, the seed photon population which is upscattered by the IC effect can be dominantly produced by synchrotron radiation. Here, I shall summarize in brief the most important aspects for gamma-ray astronomy of all three processes. Special attention is given to the spectral energy distribution of the photons produced by these processes and the cooling timescales.

Synchrotron radiation

Synchrotron radiation will always occur if electrons are accelerated in magnetic fields. The produced synchrotron photon energy spectra will peak at

$$E_{\text{peak}} = \gamma_e^2 \frac{eB}{2\pi m_e} \quad (1.5)$$

Where γ_e is the electron Lorentz factor, m_e the electron mass, e the electron charge and B the magnetic field. Since a power law distribution of electron energies is expected, it is useful to note that such a distribution would lead to a power law distribution in the synchrotron photon energy. Another important effect is the synchrotron self-absorption which leads to a spectral change in the lower energies. The self-absorbed part of the spectrum will be $dN/dE \propto E^{5/2}$ and thus the spectral index will be independent of the particle spectrum which emits the synchrotron radiation. It is evident that the synchrotron emission will not extend to TeV energies, at least for electrons. For a detailed description of the synchrotron emission and derivation of the most interesting relations, see e.g. Longair (1994).

In general, not only electrons but all charged particles will produce synchrotron radiation. As stated in the last section, for the maximum energy achieved by the accelerator the cooling time is an important quantity. For any type of charged particle, the synchrotron cooling time in a disordered magnetic field can be described as

$$t_{\text{syn}} \approx 4 \times 10^2 \left(\frac{em}{qm_e} \right)^4 B^{-2} E^{-1} [\text{s}] \quad (1.6)$$

Here q is the particle charge and m its mass, m_e is the electron mass, B is the magnetic field in Gauss and E the particle energy in TeV. Due to the strong dependency on the particle mass, the cooling time only plays a role for electrons.

Bremsstrahlung

Bremsstrahlung is emitted essentially by electrons and the derivation of the energy loss in the case of ultra relativistic electrons was first calculated by Bethe and Heitler (1934). The most important property in the context of VHE gamma-ray production is that the energy loss is proportional to the energy of the electron. Furthermore, a power law distribution of electrons will generate a power law spectrum of bremsstrahlung photons with exactly the same spectral index as the electrons. The maximum energy of the bremsstrahlung photons is equal to the electron energy and is, on average, one third of it. This emphasizes that bremsstrahlung might produce VHE gamma-rays and has to be taken into account whenever the ambient medium consists out of atoms or molecules. Bremsstrahlung plays a major role in the development of cascades, for example when a cosmic ray hits the atmosphere of the Earth, as will be explained in chapter 3 or the VHE gamma-rays penetrate a dense stellar wind of a massive star like in a binary system (see chapter 2).

Inverse Compton scattering

The most important process for the production of VHE gamma-rays is undoubtedly inverse Compton scattering (IC). In this process, low energetic photons are upscattered by relativistic electrons and can reach the same energy as the electrons.

The cross-section of IC can be calculated in the classical limit for $E_\gamma E_e \ll m_e^2 c^4$ and is simply the Thomson cross-section.

$$\sigma_{\text{th}} = \frac{8}{3} \pi r_e^2 \quad (1.7)$$

Here $r_e = e^2/4\pi\epsilon_0 m_e c^2$ is the classical electron radius. In the ultra relativistic case ($E_\gamma E_e \gg m_e^2 c^4$), the cross-section can be approximated as a special case of the Klein-Nishina cross-section.

$$\sigma_{\text{kn}} \approx \pi r_e^2 \frac{1}{\epsilon} \left(\ln 2\epsilon + \frac{1}{2} \right) \quad (1.8)$$

Where $\epsilon = E_\gamma/m_e c^2$ is the photon energy in units of the electron rest frame energy. In this energy regime, the electrons suffer high energy losses and the maximum achievable energy is approximately

$$E_{\text{ic,max}} \approx 4\gamma^2 E_\gamma \quad (1.9)$$

This energy can be well in the VHE gamma-ray domain if the electrons are energetic enough.

The important cooling time in the Klein-Nishina regime, for a black-body distribution of seed photons, is:

$$t_{\text{cool,ic}} \approx 10^2 \left(\frac{R}{R_*} \right)^2 T^{-2.3} E^{0.7} \text{ [s]} \quad (1.10)$$

where R and R_* are the distance to the origin and the radius of the seed photon region. The unit of the black-body temperature T is 10^4 K and, for the electron energy, E TeV.

For detailed modelling of individual source spectra, the full angular dependent Klein-Nishina cross-section must be calculated to obtain a realistic value for the flux expected at the observer location.

1.3.2 Hadronic production

Hadronic particles can produce VHE gamma-rays via proton-proton (pp) interactions

$$p + p \rightarrow \pi_0 + \pi_+ + \pi_- \quad (1.11)$$

$$\pi_0 \rightarrow \gamma\gamma \quad (1.12)$$

$$\pi_- \rightarrow \mu_- + \bar{\nu}_\mu \quad (1.13)$$

$$\pi_+ \rightarrow \mu_+ + \nu_\mu \quad (1.14)$$

The cooling timescale for pp collisions is (Kelner et al., 2006):

$$t_{\text{cool,pp}} \approx \frac{10^{15}}{n_t} \text{ [s]} \quad (1.15)$$

Here n_t is the target density per cm^3 . An energy threshold of $E_{th} \sim 140$ MeV exists for the inelastic pp collisions which corresponds to the rest mass of the pions. For typical target densities in the cosmic accelerators, the maximum energy is most likely limited by the escape time and not the cooling time.

In pp interactions not only gamma-rays are produced. While the π_0 decay into gamma-rays, the charged pions will produce neutrinos and electron/positrons. The positrons can produce again gamma-rays via pair annihilation with ambient electrons (if present). The luminosity of all end products of the various decay channels is expected to be within a narrow range allowing a maximum flux deviation of a factor of 2 (Kelner et al., 2006). Thus, cosmic hadron accelerators should be detectable in neutrino telescopes like IceCube or ANTARES and yield about the same flux as in gamma-rays.

Another hadronic production mechanism of VHE gamma-rays is the photon-meson production. The process is described in detail in Kelner and Aharonian (2008). The energy threshold for this interaction is

$$E_{\text{th,p}\gamma} = m_p c^2 \epsilon_{\text{th,p}\gamma} / 2\epsilon = 5 \times 10^8 T^{-1} \text{ TeV} \quad (1.16)$$

where m_p is the proton rest mass and ϵ , $\epsilon_{\text{th,p}\gamma}$ is the energy of the target photon in the laboratory and the proton rest frame, respectively. The cooling time can be approximated

as:

$$t_{p,\gamma} \sim \frac{10^{18}}{N_X} [\text{s}] \quad (1.17)$$

with $N_X \approx L/4\pi\epsilon R^2 c$ where L is the luminosity of the photon field and R the distance to the source of the photons. As in the case of pp collisions, the cooling time is very long if the photon source is, for example, a massive star and thus the maximum energy is again limited by the accelerator dimension.

1.3.3 VHE gamma-ray absorption

The produced VHE gamma-ray radiation is not necessarily the one observed on Earth. The very important absorption processes have to be taken into account, especially in the study of VHE gamma-ray emission of compact binary systems which are investigated in this thesis. Another example where absorption plays a vital role is the VHE emission from distant AGN's. The absorption in the VHE regime is mainly photon-photon absorption and requires either high target photon densities, as in the case of compact high mass X-ray binaries (HMXB), or large distances with low target photon densities, as in the case of distant AGN's. The absorption process modifies not only the photon distribution but can lead to electro magnetic pair cascading. These processes can significantly alter the emission spectrum of the source. For cascading in a strong magnetic field, a sharp super exponential cutoff in the gamma-ray spectrum is expected. A prime example of cascading yielding dominant gamma-ray emission is the magnetosphere of pulsars. What is more, cascading might also play a vital role in the vicinity of AGN accretion discs or compact binary systems. The detailed processes which are possible in binaries will be described in more detail in the chapter 2.

1.4 VHE gamma-ray sources

The previous sections described how charged particles are accelerated and produce not only cosmic rays but can yield a significant flux in gamma-rays and neutrinos as well. So one fundamental question which can be answered by VHE gamma-ray astronomy is: What are the sources of cosmic rays and where are these sources? However, this is not the only very interesting question. As can be seen from the previous sections, the acceleration mechanism and their properties can be tested and studied by the investigation of VHE gamma-ray sources. Together with the study of radio to soft gamma-ray multiwavelength behavior of any accelerator, a deep insight can be gained on the processes taking place in them and their surrounding medium. This understanding of the various processes taking place in the cosmic accelerators will enhance our understanding of astronomy, plasma physics, electrodynamics

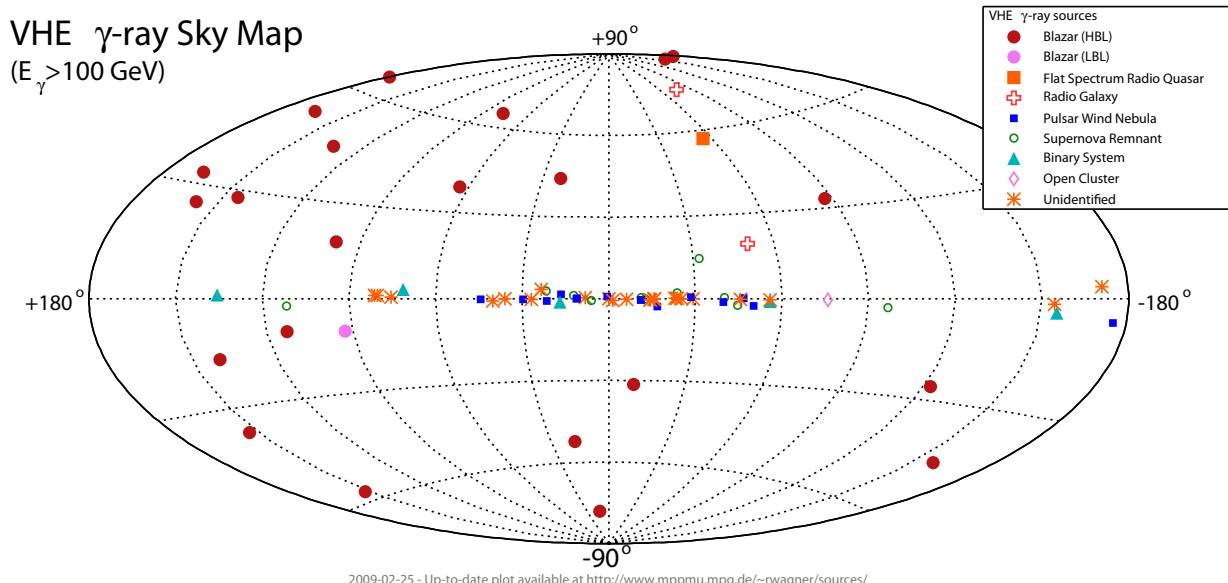


Figure 1.3: All sources detected in VHE gamma-rays up to February 2009 are shown in this skymap in galactic coordinates. The legend shows the individual source types. Most of these sources have been discovered by the current generation of Cherenkov telescopes.

and general relativity. In particular, compact binary systems (see the next chapter) provide excellent laboratories for these kinds of studies. Here a brief description of the up-to-now detected source classes, together with the resultant physics studies is presented. In total more than 80 sources have been discovered in VHE gamma-rays up to February 2009 and MAGIC² contributed eleven discoveries to the total amount. All currently known sources are displayed in the skymap shown in Fig. 1.3.

1.4.1 Pulsars

Pulsars are believed to be fast rotating neutron stars (NS) which have the strongest magnetic fields known in the universe ($B \sim 10^{12}$ G). Pulsars are observed as periodic emitters of EM radiation from radio frequencies up to gamma-ray energies.

The first pulsar was discovered in radio and as of today most known pulsars are radio pulsars. This discovery triggered the question what mechanism causes the emission. Here I will only comment on the emission of gamma-rays. The pulsar forms, due to its fast rotating magnetic field, a so called “light cylinder”. The light cylinder is defined as the surface parallel to the rotation axis at the distance of the last closed magnetic field line.³

²Major Atmospheric Gamma-ray Imaging Cherenkov (telescope)

³At this distance the speed of light is equal to the speed of the moving magnetic field and since it cannot move faster than this all magnetic field lines extending beyond this distance are not closed anymore.

A co-rotating plasma is thought to fill the light cylinder because the particles are confined to the magnetic field lines. This plasma prevents due to its conductivity the induction of electrical fields (Goldreich and Julian, 1969). There are three exceptional regions proposed which are called gaps (see Fig.1.4 for an illustration).

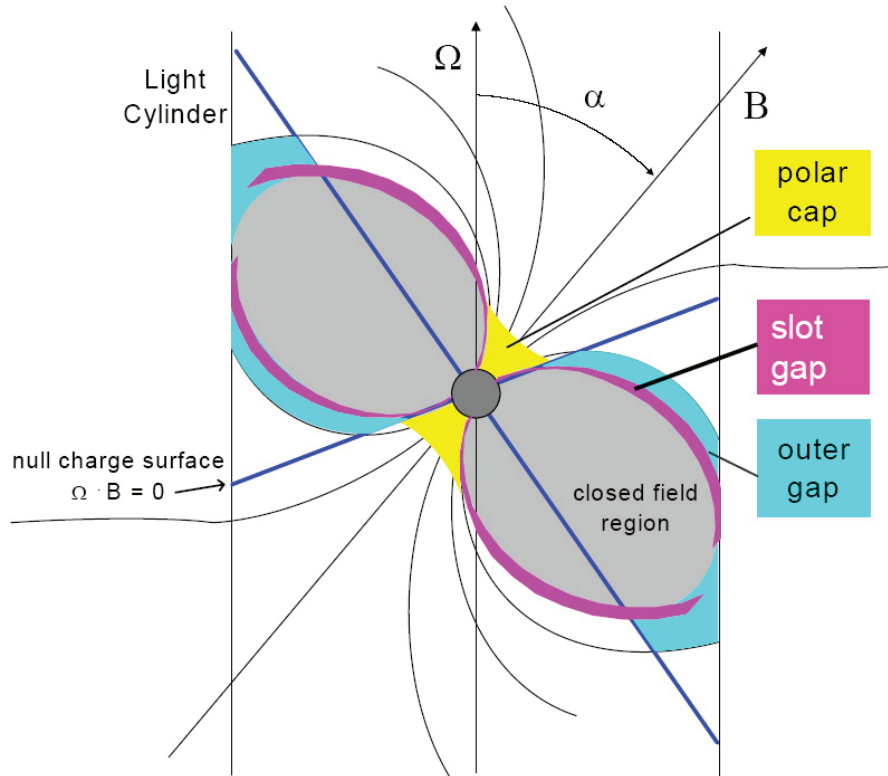


Figure 1.4: Schematic view of the cross-section of the poloidal plane of the pulsar. The possible sites of particle acceleration are marked as well as the light cylinder the rotation axis (Ω), the magnetic field axis (B) and the inclination angle between them α . Popular sketch by A. Harding

In the polar cap model the electrical field region is above the polar cap and charged particles are thought to be accelerated in it and producing gamma-rays due to synchrotron radiation and IC upscattering of lower energetic photons. The gamma-rays will interact with the extremely strong magnetic field and undergo pair production leading to a sharp super-exponential cutoff in the gamma-ray spectrum at a few GeV. For example models and details see Sturrock (1971); Ruderman and Sutherland (1975); Daugherty and Harding (1982); Harding et al. (2002) and references therein.

Another type of models are the outer gap models, originally proposed by Cheng et al. (1986a,b). They assume that between the open field lines and the last closed field line a gap in the plasma is formed because of the escape of the particles following the open field lines. In this gap particles can be accelerated. Since the magnetic field is less in this region

compared to the polar cap (which is close to the NS surface) the produced gamma-rays do not suffer from the strong magnetic pair cascading but only from $\gamma\gamma$ absorption. Thus the predicted spectral cutoff is only exponential in case of the outer gap models and the predicted gamma-ray spectrum extends to higher energies. For more recent outer gap modelling see e.g. Hirovani (2007).

Finally there is an intermediate case between the previously mentioned scenarios called slot gap model (see Muslimov and Harding (2003) and references therein). The main advantage of this model is that it can describe the wider pulse profiles observed by experiments, compared to the polar cap model yielding always very narrow pulse shapes. The predicted energy cutoff in the gamma-ray spectrum is intermediate between the outer gap and polar cap predictions.

Despite the intense search for pulsed VHE gamma-ray emission from various pulsars, the first detection was not achieved until 2008 when the MAGIC collaboration discovered, 19 years after the steady emission, the Crab Nebula pulsed emission above energies of 25 GeV (Aliu et al., 2008b). From this measurement the polar cap model is disfavored but not yet ruled out.

The periodic pulses detected from the pulsar are not caused by the emitting process but due to the fast rotation of the pulsar. Whenever the emission region in the pulsar vicinity is not aligned with the rotational axis of the pulsar then the emission region describes a circle on the celestial sphere and thus is only visible for a very short time for an observer at any location on the circle. This results in an observed pulsed light curve at the observer. Due to this fact, commonly the term “pulsed emission” is used even so the pulse shape of the light curve is only caused by the rotation, while the emitter is thought to be constant.

The pulsars are the power supply of the pulsar wind which consists of the out-streaming particles from the open field lines. The pulsar wind propagates for some time freely and forms then by interaction with the ambient medium a pulsar wind nebula.

1.4.2 Pulsar wind nebulae

The first detected VHE gamma-ray source, the Crab nebula, is a so-called pulsar wind nebula (PWN). The pulsar accelerates charged particles in its magnetosphere (see Pulsars in the previous section) and these particles build a free particle wind when they leave the light cylinder of the pulsar. This wind propagates freely until it has swept up ambient medium with mass equal to its own energy. Then a termination shock forms and in this shock the particles can be accelerated to even higher energies. The different regions of the pulsar wind nebula are shown in Fig. 1.5 and more details about possible emission from PWN’s will be

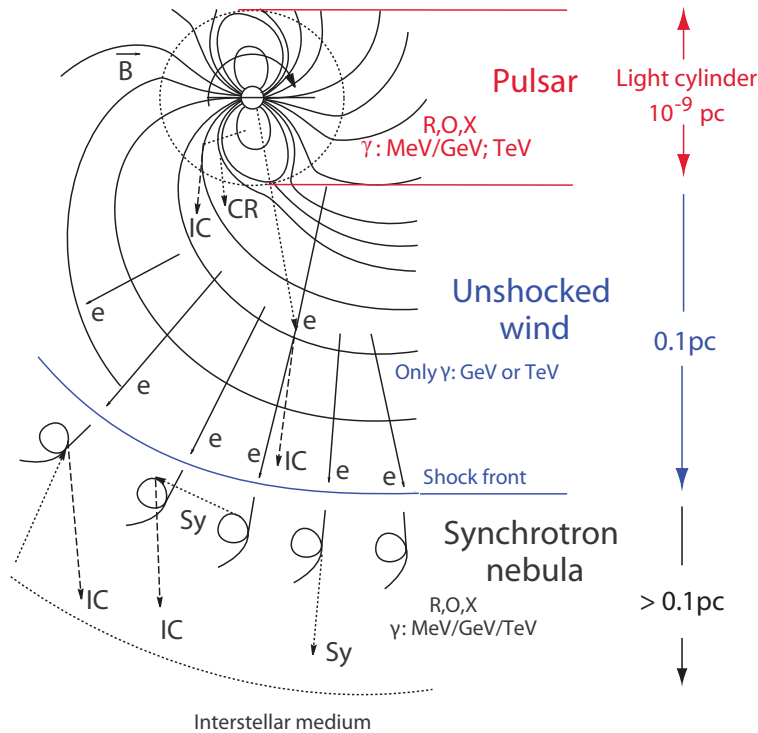


Figure 1.5: The different regions expected in the surrounding of a magnetized high frequency spinning neutron star. For a description, see section 1.4.2. The figure is adapted from Aharonian and Bogovalov (2003).

given in the section about gamma-ray binaries. For a recent review on PWN see Kirk et al. (2007).

1.4.3 Supernova remnants

Stars with more than $5 M_{\odot}$ will most likely end their lives in a super nova explosion, expelling most of their mass into the ambient medium. The thus-expanding supernova shock will form a shell type supernova remnant (SNR). The shell will expand and shock the ambient medium producing a termination shock and accelerate particles in this shock front. Depending on the evolutionary model of the supernova remnant, the time when the SNR shell emits gamma-rays may be different. It takes rather longer to accelerate particles to VHE energies. These particles can produce gamma-rays either by leptonic or hadronic processes. Due to energy considerations, shell type supernova remnants could contribute the majority of the galactic cosmic rays. Prominent shell type super nova remnants emitting VHE gamma-rays are RX J1713.7-3946 (Aharonian et al., 2004b) or Cassiopeia A (Aharonian et al., 2001; Albert et al., 2007c). Both of these SNR's are possible cosmic ray accelerators but the exclusion of leptonic models is not straight-forward and thus the question whether SNR's are the sources

of galactic cosmic rays remains open for the time being.

1.4.4 Unidentified sources

A large class of new detected VHE gamma-ray sources, with no clear identified counterpart in any other waveband, are called unidentified sources Aharonian et al. (2008). The first source discovered of this type is TeV J2032 +4130 (Aharonian et al., 2002; Albert et al., 2008c) and, up to now, the origin of the VHE gamma-rays detected from it has not been solved. One possible scenario to explain the emission is that VHE protons escape from an old SNR shock⁴ and travel through space until they hit a molecular cloud and produce VHE gamma-rays inside it (see Aharonian et al. 1994; Gabici et al. 2007 and references therein). This could lead to no counterpart in other wavelengths at the position of the VHE gamma-ray emission. Such a scenario of an interacting SNR with a molecular cloud might be at work in the newly discovered VHE gamma-ray source MAGIC J0616+225 inside the SNR IC443 (Albert et al., 2007a).

1.4.5 Star clusters

There are two types of star clusters - open clusters and so-called globular clusters (GC). Star clusters are places where stars are formed at the same time. Young open clusters can contain a large amount of heavy, short-lived O and B stars which have high mass loss rates and fast stellar winds with termination velocities of several thousand kilometers per second. In the shocks between the stellar winds, particles could be accelerated to VHE and produce gamma-rays. Until now HESS J1023-575 is the only VHE gamma-ray source found inside an open cluster (Aharonian et al., 2007b) and it is not clear if the emission is due to the open cluster or originates from a Wolf-Rayet⁵ (WR) binary system. Up to now no isolated WR binary was discovered in VHE gamma-rays (Aliu et al., 2008a) but no other open cluster has been discovered either.

The other type of star clusters, the GC, are among the oldest known objects in the universe. GC contain only evolved stages of the stellar sequence and are likely to contain a large amount of millisecond pulsars (Tavani, 1993). These millisecond pulsars produce strong winds which will collide inside the GC with each other and might accelerate particles in these shocks, which produce VHE gamma-rays (Bednarek and Sitarek, 2007; Venter et al.,

⁴The expanding SNR shock will lead to lower magnetic fields the longer it expands and at the same time the particle energy increases due to the acceleration. So, after some 10^4 years, the protons cannot be confined in the shock anymore.

⁵For a detailed review of Wolf-Rayet stars see Crowther (2007).

2009). Indeed, the FERMI gamma-ray telescope (FERMI) has discovered high energy (HE) gamma-ray radiation from the southern GC Tuc47 (Abdo, 2009). Up to now only upper limits in VHE exist, for example on Tuc47 (Aharonian et al., 2009b) and on M13 (Jogler et al., 2009).

1.4.6 Blazars

Blazars are a subclass of the AGN's to which all of the extragalactic VHE gamma-ray sources belong. It is widely believed that galaxies where the galactic nucleus is many times brighter than the host galaxy have a super massive black hole in their center. This super massive black hole accretes matter and might eject relativistic collimated plasma outflows (jets). In these jets, shocks can form and accelerate particles. The gamma-rays produced by the accelerated relativistic particles will be boosted towards an observer who looks down the jet. AGN's which have the jet directed to Earth are called blazars. Blazars are the strongest variable gamma-ray sources detected so far (GRB's - Gamma Ray Bursts - might be brighter) and can reach flux levels several times higher compared to the strongest steady source, the Crab Nebula - as observed, for example, in Mrk 501 (Aharonian et al., 1999; Albert et al., 2007e) and PKS 2155-304 (Aharonian et al., 2007a).

Blazars should display a similar behavior as the microquasar subclass of binary systems. The microquasars are described in more detail along with the similarities to blazars in chapter 2.

1.4.7 Radio galaxies

Besides the blazars, there are some other types of galaxies which display or might display VHE gamma radiation. The most famous example is the giant elliptical radio galaxy M87 (Aharonian et al., 2006b) which is the central galaxy in the Virgo galaxy cluster. M87 displays a jet visible from radio to hard X-rays but the inclination of the jet towards the Earth is very large compared to blazars. Several models try to describe the VHE gamma-ray emission from M87 (e.g. Neronov and Aharonian (2007)) and recent measurements suggest that the origin of the emission is very close (a few Schwarzschild radii) to the black hole (Albert et al., 2008b).

Another radio galaxy very recently discovered in VHE gamma-rays is Centaurus A (Aharonian et al., 2009a) which is amongst the brightest extragalactic radio sources. Both currently discovered radio galaxies are very close to our galaxy and, in the case of Centaurus A, a very dim VHE gamma-ray source (0.8% of the Crab Nebula flux above 250 GeV). Nevertheless, the detection of two radio galaxies in VHE gamma-rays makes this type of galaxy a

new class of object in the extreme Universe.

1.4.8 Gamma-ray bursts

Gamma-ray bursts (GRB) are the most energetic events known in the universe. They last only up to tens of seconds during which they release power to the order of $P \sim 10^{51} - 10^{54} \text{ erg s}^{-1}$. This is the so-called prompt emission and it is sometimes followed by an afterglow (van Paradijs et al., 2000).

Most of the GRB's take place at large cosmological distances and the most distant one (GRB 090423) was detected at a red-shift of $z \sim 8$. For VHE gamma-ray detection, a relatively close-by GRB ($z < 1$) would be needed, otherwise the universe would be opaque for VHE gamma-rays due to the extra galactic background light absorption (Albert et al., 2008c). To observe VHE gamma-rays from a GRB, a low energy threshold and fast reaction time (or large field of view) is required. These conditions are very well fulfilled by the MAGIC telescope and the FERMI satellite. Until now, no GRB has been detected at VHE and only upper limits are reported (Albert et al., 2007b). A recent review about the theory of GRB's can be found in Mészáros (2002).

1.5 Fundamental physics

The search for the sources of cosmic rays is an important topic for VHE gamma-ray astronomy but not the only one. The multiple types of VHE gamma-ray sources discovered so far, have resulted in the study of various high energy phenomena such as jet physics, particle acceleration mechanisms and absorption processes and have thus extended the fundamental understanding of physics. VHE gamma-ray astronomy might even give insight to more fundamental open questions like the search for dark matter or the test of Lorentz invariance (Albert et al., 2008). These are more exotic topics but they are of great interest to the scientific community and thus will naturally be addressed by VHE gamma-ray observatories like MAGIC. So far, no evidence for dark matter annihilation into VHE gamma-rays has been found and upper limits are derived for some candidate sources (Albert et al., 2008a; Aliu et al., 2009b).

Chapter 2

Gamma-ray binaries

Most stars in our galaxy belong to a multi-star system. Most of these are binary systems and the majority of them are not interesting for the VHE gamma-ray astronomer. A special subclass of binary systems, the X-ray binaries (XRB), were long suspected to be emitters of VHE particles. Despite some claims of discovery of VHE gamma-rays from XRB's (all of which could not be verified by other experiments), it was not until 2005 that the first binary system - PSR B1259-63 - was discovered to be a VHE gamma-ray emitter (Aharonian et al., 2005a). Soon afterwards, two more systems were discovered: LS 5039 (Aharonian et al., 2005b) and LS I +61°303 (Albert et al., 2006). The last two were classified as microquasar at the time of their discovery and there has been a large effort to understand the processes taking place in these systems. In this thesis, the LS I +61°303 system is studied in the greatest detail from its discovery until the latest data taken by MAGIC. In this chapter, the basic concept of VHE gamma-ray emission from binary systems will be explained. In addition, the scientific interest in these systems will be explained as well as the methods used to help in answering the many open questions about these systems.

The chapter is organized in the following way: First, the two possible scenarios of VHE gamma-ray emitting binaries are introduced. Then, the various processes affecting the emission from the binary and its consequences for the observations will be discussed. In the final section of this chapter, the current status of the gamma-ray emitting binaries not observable from the MAGIC site will be reviewed.

2.1 A classification of X-ray binaries

X-ray binaries are divided into two subclasses: the High Mass X-ray Binaries (HMXB) and the Low Mass X-ray Binaries (LMXB). Each of these systems consists of a compact object,

which is either a neutron star or a black hole and an optical companion star¹. Depending on the mass of the companion star the system is referred to as an HMXB in the case of a massive O or B star and as an LMXB in the case of a less massive (typically $M_{\star} < M_{\odot}$) star. The main difference between both classes is the photon field of the optical star. In the case of the HMXB, a fast stellar wind is present and the system is most likely powered by wind accretion where the X-ray luminosity is $L \approx 10^{35} - 10^{36} \text{ erg s}^{-1}$ while, in the case of accretion via Roche lobe overflow, the luminosity is $L \approx 10^{38} \text{ erg s}^{-1}$. In LMXB's, the accretion is always due to Roche lobe overflow. A detailed description of the various properties of these systems is out of the scope of this thesis and the interested reader is referred to the review book written by Lewin and van der Klis (2006). In total 114 HMXB have so far been identified in our galaxy and they are listed with their properties in Liu et al. (2006) and the 128 of the Magellanic clouds are listed in Liu et al. (2005). The same type of catalogue exists for LMXB (Liu et al., 2007) and useful information, as well as further references for each object, are provided therein.

To reference the potential to emit VHE gamma-rays, another classification scheme of XRB's is preferable and two other subclasses are introduced. One class is formed by the microquasars in which the non-thermal emission is powered by accretion and the other class is the pulsar wind binaries, in which the non-thermal radiation is powered by the rotational energy of the pulsar. Both types will be described in the following sections.

2.2 Microquasars

Microquasars are XRB's which are accretion-powered and display collimated plasma ejections which emit synchrotron radiation in the radio frequency. The term microquasar was introduced after the discovery of the two-sided collimated radio jets around the compact X-ray source 1E1740.7-2942 by Mirabel et al. (1992).

The name already suggests that microquasars are downscaled versions of the extra galactic quasi-stellar objects (quasars) displaying similar behavior. Since most properties of these systems are directly related to the mass of the compact object, the study of microquasar can reveal vital information about processes which would take million of years to observe in the extragalactic quasars. Fig. 2.1 shows the dimensional differences of the microquasar and quasar. Since their discovery, microquasars have been studied in detail at all wavelengths, especially to understand the jet-accretion-disc coupling and the jet formation processes. In the following paragraphs, the different processes in microquasars will be introduced and their

¹Optical companion star means that the companion star is emitting in the optical wavelength.

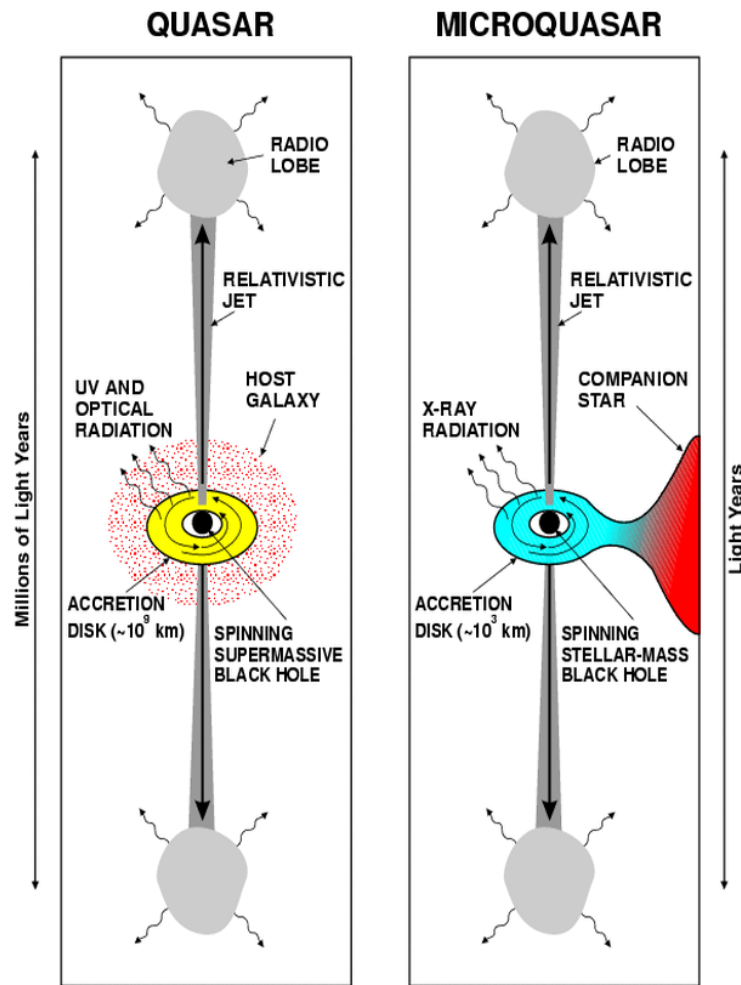


Figure 2.1: Comparison of a quasar (left) and a microquasar (right). The main difference is thought to be the dimensions due to the difference in the black hole mass by a factor of one million. Figure taken from Mirabel and Rodríguez (1998).

relevance for VHE gamma-ray production discussed.

2.2.1 Accretion

Accretion is the process by which a compact object captures matter from its surroundings - from its companion star in the case of a binary system. Accretion can take place via disc-accretion or wind-accretion. An accretion disc is formed around the compact object and maintained by the matter flow from the optical companion via the inner Lagrange point if the optical companion fills its Roche lobe²(see e.g. Shapiro and Teukolsky 1986). In the case of wind-accretion, there might be no accretion disc but simply spherical accretion. Plasma

²The Roche lobe is the equipotential surface around two stars in a binary system which connects the two stars. A star can be larger than its Roche lobe and this is called Roche lobe overflow.

in the accretion disc loses its angular momentum due to friction, thus heating the plasma to such high temperatures that it emits a black body spectrum peaking in the X-rays. The inner part of the accretion disc is hotter than the outer plasma.

In general, accretion is a very difficult topic and has to be studied for each binary individually. The following aspects have to be taken into account:

- The three-dimensional geometry of the accretion flow: can it be described hydrodynamically (short mean-free path of the particles in the plasma)?
- The dominant heating and cooling mechanisms: is the medium optical thin or thick in relation to the radiation it emits?
- The magnetic field and its role (stress induction in the plasma) in the cooling and heating processes
- The radiation pressure and its effect on the accretion plasma
- The flow boundary conditions when the material hits the NS and the boundary to the ambient medium of the accretion disc³

Thus the time dependent, multidimensional, relativistic, magneto-hydrodynamic (MHD) equations, including radiative transfer, must be solved. This is only possible with numerical simulations or in very simplified models. Idealized accretion models with analytic solutions can be found in Shapiro and Teukolsky (1986). A more recent review including MHD simulations is given by Done et al. (2007).

While the detailed description is out of the scope of this thesis, the basic properties will be given, assuming a simplified model, to show dependencies on the mass of the compact object.

The most important quantity is the accretion rate which determines the maximal amount of energy ready to be radiated. The accretion rate depends on the type of accretion described in the beginning of this section and on the geometry of the orbit of the compact object. In the simple case of spherical symmetric accretion (as present in many HMXB's), the accretion can cause a maximum luminosity called the Eddington-luminosity. The reason for the upper luminosity boundary is that the in-falling material radiates away its angular momentum and the resulting radiation induces radiation pressure onto the electrons in the plasma of the accretion disc. The electrons transfer the pressure via the electrostatic force to the protons

³In case of a black hole as the compact object, the boundary problem is only present between the accretion disc and the ambient medium, since the event horizon prevents any violation of boundary conditions.

in the plasma and, hence, the accretion onto the compact object can be stopped by its own radiation. The condition for this is that the gravitational force is equal to the radiation pressure.

$$\frac{\sigma_{\text{th}}L}{4\pi r^2 c} = \frac{GMm}{r^2} \quad (2.1)$$

$$L_{\text{edd}} = \frac{4\pi GMmc}{\sigma_{\text{th}}} \quad (2.2)$$

Here σ_{th} is the Thomson cross-section, M the mass of the compact object and m the combined mass of the proton and the electron. It is important to notice that L_{edd} depends only on the mass of the compact object. Higher luminosity than L_{edd} can be achieved in different accretion geometries but they will not exceed much L_{edd} . In almost all accretion prescriptions, the luminosity is given in units of L_{edd} .

In addition to the accretion energy, the emission spectrum of the accretion disc in binaries is of great interest. The main emission feature of the disc is caused by its temperature and can be described as a multiple black-body radiation spectrum. The reason for more than one black-body component is that the temperature in the accretion disc is radius-dependent. In addition to the black body component, a corona around the accretion disc can be present which might considerably alter the observed spectrum in relation to the black body spectrum. The accretion disc can be truncated towards the compact object and a hot corona-like flow formed around the compact object. Such a truncation of the disc can be formed by instabilities in the plasma which will control the heating and cooling processes in the disc. A detailed description of these complex processes is given in Done et al. (2007) and references therein.

Another common feature in accretion disc spectra is the iron $K\alpha$ -line emission. The energy range of the emission is for stellar mass black holes, like those present in binaries, in the soft ($E > 0.1$ keV) to hard X-rays ($E > 10$ MeV). The detailed spectral shape depends on the emission state of the binary which is explained in section 2.2.3.

2.2.2 Jets

Jets are collimated plasma outflows which are, by definition, present in all microquasars. It is thought that the jets are collimated and driven by the poloidal component of the magnetic field (Blandford and Znajek, 1977; Blandford and Payne, 1982; Ferreira, 1997). The complex jet-launching process and the jet accretion connection is not fully understood and many models simply assume an injected luminosity into the jet which is a fraction of the accretion rate ($L_{\text{inj}} = L\dot{M}_{\text{acc}}$), where L is the electron kinetic luminosity and thus a free parameter to be determined by model fits to the measured spectral energy density (SED).

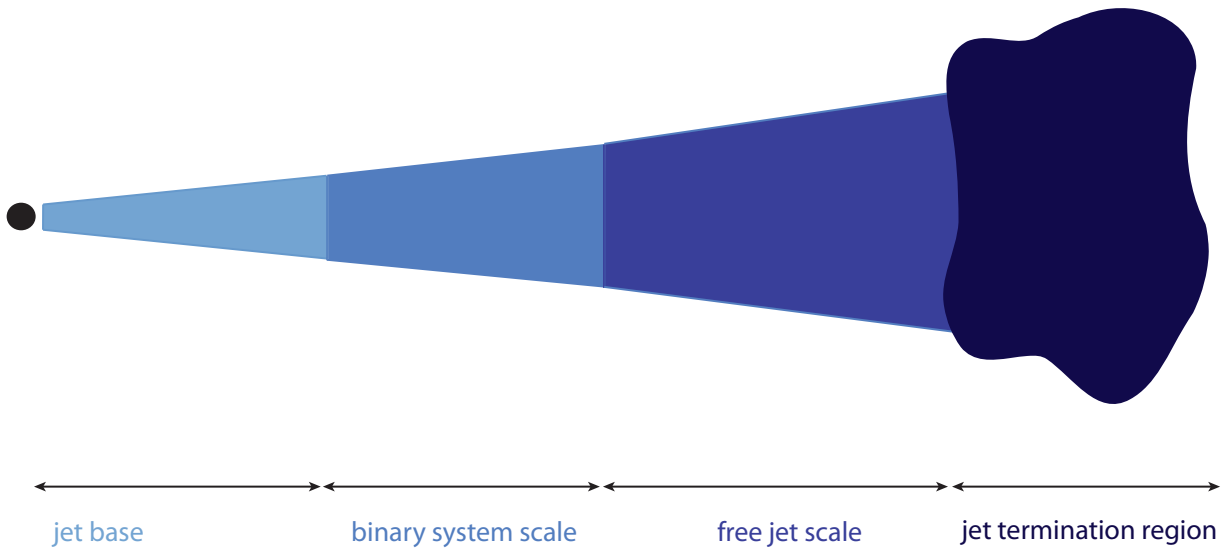


Figure 2.2: The individual jet regions and scales in which the various particle acceleration processes take place. For more information see section 2.2.2.

This assumption is reasonable, as observations suggests a correlation between accretion rate and jet power (Fender et al., 2004).

Jet physics are very interesting but the focus here is on the particle acceleration, interaction of the jet with the ambient medium and VHE gamma-ray emission in the case of binary systems.

In most cases, the model of the jet assumes a homogenous jet and such models are called one-zone models. The more complicated models that distinguish between a faster spine in the jet and slower moving outer sheets are denoted as two- or multi-zone models. In addition, there might exist distinct regions along the jet at certain distance scales from the compact object. Thus the jet can be divided into subregions which are defined by their distance from the compact object. This is illustrated in Fig. 2.2 and the division in these zones is useful to account for the different ambient medium conditions present, as well as for the internal parameters of the jet.

At the jet base, particles might be accelerated by magnetic energy dissipation through MHD instabilities (see for example Zenitani and Hoshino (2001)). A magneto-centrifugal mechanism taking place very close to the Kerr black hole could accelerate particles as well and such processes are proposed to explain the VHE gamma-ray emission for non-blazar AGN's, as found in M87 (Neronov and Aharonian, 2007; Rieger and Aharonian, 2008).

At scales of the binary system dimensions, first and second order Fermi acceleration as well as shear acceleration can work efficiently to produce multi TeV particles. In the case of shear acceleration, a multi-zone model of the jet would be required. Fermi-acceleration can

take place in internal shocks (first order) or in magnetic turbulence (second order) in the jet. The strong wind in HMXB's can lead to a jet bending due to the anisotropic pressure on the jet and this can lead to recollimation shocks, in which particles can be accelerated as well. Such behavior is predicted by MHD simulations performed by Perucho and Bosch-Ramon (2008). The dense stellar wind can even lead to jet disruption and prevent observable large-scale jet-like features.

On the free jet scale ($10^{15} - 10^{16}$ cm), no interaction between the jet and the ambient medium is expected due to the very high ram pressure of the jet compared to the interstellar medium (ISM). The only possibility of particle acceleration would be plasma blobs moving with different velocities in the jet. Upon encounter, these could create shock fronts. Therefore, the jet could be invisible at these scales or display distinct emission knots, as observed in extragalactic AGN's - for example in M87 (see Harris 2001 for a review).

The farthest region from the compact object is the so-called termination region, in which the swept-up ISM inertia starts to affect the jet propagation. This may cause two shocks - the reverse shock, moving backwards in the jet, and a forward bow shock. There is also the possibility that the jet is distorted and mixes with the ISM without producing shocks (Heinz and Sunyaev, 2002).

In the individual parts of the jet, particle acceleration might have different appearances and this can lead to distinct observational expectations - for example, in relation to the detection of extended emission regions, or SED features, which are caused by the contribution of the distinct emission processes in the individual jet regions. Detailed observation in a wide energy range (multiwavelength observations) can reveal the various processes at work. For example the VHE gamma-ray emission can provide vital information about the relativistic particle population and about absorption effects on the binary scale if the injection power into the jet can be estimated by X-ray observations of the accretion flux.

To be able to interpret the multi wavelength (MW) SED, it is necessary to study the dominant cooling mechanism in the individual jet regions. The possible mechanisms taking place for photon production are already described in chapter 1.3 and the detailed balance of the processes depends on the binary system components such as stellar wind density and speed, stellar surface temperature, orbital eccentricity, orbital inclination and jet inclination with respect to the orbital plane (only to name the most important ones). Thus a detailed, general description cannot be derived but an individual modelling of each microquasar must be performed.

Finally, the jet does not have to be a continuous plasma flow but can be composed of distinct ejecta called bubbles. The famous example of the giant outburst of GRS 1915+105



Figure 2.3: Jet ejecta evolution vs time of the microquasar GRS 1915+105 as measured at 8.4 GHz by the VLA radio interferometer in 1994 by Mirabel and Rodriguez (1994). Image courtesy of NRAO/AUI.

is shown in Fig. 2.3. In this figure, another feature of the microquasar jets is shown - the superluminal motion. Superluminal motion means that the apparent jet velocity measured is higher than the speed of light⁴ and this is caused by dopplerboosting of the relativistic jet and commonly found in extragalactic AGN's. This is another indication of the similarity of the microquasar to their extragalactic counterparts. These similarities found between the extragalactic and galactic jet sources suggests that, by studying one type, additional information about the other can be obtained.

⁴Of course, this is only true for the measured apparent velocity.

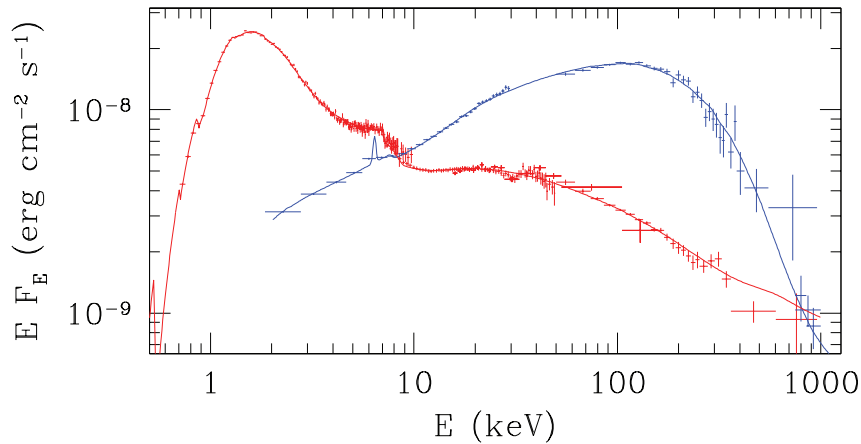


Figure 2.4: The low-hard state (blue) and high-soft state (red) of Cyg X-1. The system also displays intermediate states (not shown) which mark the transition from one of the two main states to the other. The figure is adapted from Gierliński et al. (1999).

2.2.3 The different emission states

Distinct emission states of the microquasar systems are very interesting phenomena. These states are believed to be caused by instabilities in the accretion disc which can trigger each other and thus lead to quasi-periodic oscillations (QPO) between different accretion components. A detailed description of the various states can be found in Done et al. (2007). The main states are the so-called low-hard state, LHS (or only hard state) and the high-soft state, HSS (or soft state). The naming convention is a bit confusing since the terms were created when only X-ray observations in the soft X-rays were available. Thus, the low in LHS (high in HSS) means that the flux is low (high) at the low energetic ($E \lesssim 2$ keV) X-rays. When the higher energetic X-rays could be measured the state name was defined, in addition to the flux level at soft X-rays, by the spectral index of the power law at higher X-ray energies. Thus, the hard in LHS (soft in HSS) stands for a hard (soft) power law at higher ($E \gtrsim 2$ keV) X-ray energies. The X-ray spectra of the microquasar Cyg X-1 in the LHS and HSS are shown in Fig. 2.4.

In the LHS, the accretion disc is truncated far from the last stable orbit and the inner part between the disc and the last stable orbit is filled by a hot plasma (corona). In this state, the jet should be present and the X-ray spectra could be partially emitted by the accelerated particles (synchrotron radiation and bremsstrahlung) in the jet. There exist theories which predict that the jet could even dominate over the emission from the accretion disc and corona.

The current understanding of the different states is that the balance of the disc and corona is a function of time, due to the influence of the instabilities in the accretion disc

to each other. One description for the LHS is that the corona yield a hard X-ray spectrum peaking around 100 keV. The corona scatters soft photons from the cool disc to hard X-rays and hard photons from the corona are reflected by the cool disc. The reflection component can produce the line features in the LHS state. The jet which is expected to be present in the LHS is thought to emit infrared (IR), radio and maybe X-ray photons. The jet should also be responsible for the HE and VHE radiation, as described in the next section.

In the HSS, the accretion disc should extend close to the last stable orbit and no corona and no jet should be present, only small hot plasma (active regions) above and below the disc might be left over from the corona. In this state, the cold accretion disc dominates the X-ray spectrum by its black body radiation. The extending soft power law feature present in the HSS can be caused by the active regions due to the upscattering of soft X-rays from the disc. The hard X-rays will be reflected from the accretion disc and cause a reflection feature as in the LHS. An illustration of the two states, together with a model of the contributions from the different components for Cyg X-1 is shown in Fig. 2.5. While the detailed investigation of the X-ray spectrum is important to understand the jet-launching mechanism and the disc-corona-jet coupling, a simultaneous observation in VHE gamma-rays might give crucial insights into the particle population dominating the emission in the jet. For this reason MW campaigns are vital to draw a comprehensive picture of the processes in microquasars.

2.2.4 VHE gamma-ray emission

The only likely source of VHE gamma-ray emission in a microquasar is the jet. So far, all of the measured fluxes at MeV energies from accretion processes (disc + corona) are much too low (if they extend at all to higher energies) to expect detectable fluxes at VHE gamma-rays with the current generation of gamma-ray detectors.

Nevertheless, the accretion process and especially its injection of energy into the jet are vital parameters to model the VHE emission from microquasars. As explained in the previous section, the jets might not be present in all states and thus a variability, not necessarily connected to the orbital period, is expected from such systems. Furthermore, the injected energy into the jet must not be constant, nor is there a clear dependence between the accretion rate \dot{M}_{acc} and the emission state. This increases the expectation of non-periodic, variable emissions. On the other hand, a quasi-periodic (QP) emission depending on the state can be expected if the jet injection energy is constant during the state. Therefore, a detailed investigation of periodicities and variability timescales in VHE gamma-rays and their correlation (both in flux level and spectral index) with the X-ray and radio emission could provide vital information about the jet/accretion connection and the position of the

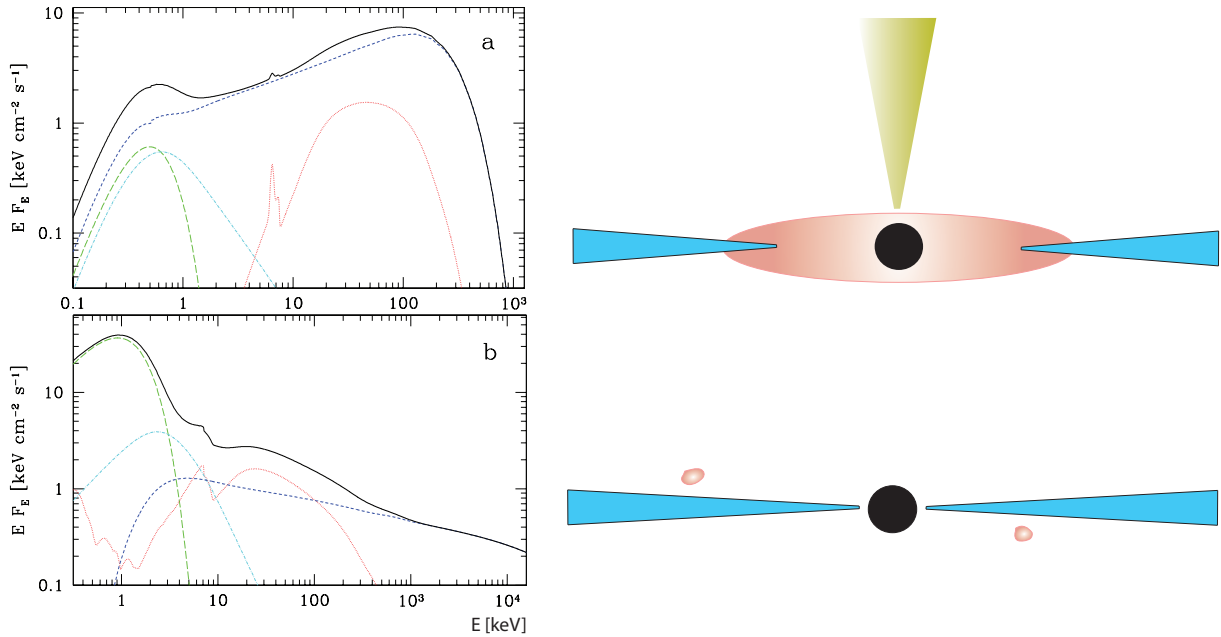


Figure 2.5: In the left panel, the X-ray spectra of the two different states LHS (upper panel) and HSS (lower panel) as measured in Cyg X-1 are shown. The black solid line shows the complete spectrum, the blue (dashed) line give the comptonization component due to a) hot thermal electrons, b) nonthermal electrons. The green (long dashed) and red (dotted) lines correspond to the black-body and reflection component. Finally, the cyan (dashed dotted) shows a Compton scattering component with different spatial origin than the corona in a) and in b) by thermal electrons. The spectra are taken from Zdziarski and Gierliński (2004). The right panel shows schematically the components present in the states, the jet (yellow) is only present in the LHS and the hot corona (red) dominates the inner part of the accretion zone, while the cold accretion disc (blue) is truncated already far away from the last stable orbit. In the HSS, the accretion disc reaches up to the last stable orbit and only very small patches of the corona still exist above and below the disc.

emitter along the jet.

The link between the observed and emitted VHE gamma-rays is confused by gamma-ray propagation and absorption in the binary system. The photon-photon absorption or cascading effects can alter the observed spectrum considerably or even prevent the detection of VHE gamma-rays. On the other hand, if absorption effects are observed in a VHE spectrum, then the emission region must be within the binary, thus providing valuable information. Another source of variability can be the clumpy wind structure in HMXB's (see Dessart and Owocki 2003, 2005; Puls et al. 2006 and references therein). The effect on VHE gamma-ray emission level was estimated to be a variability of a few percent (Owocki et al., 2009).

Besides the location of the emitter, the particle population responsible for the emission can also provide information on the jet composition and interaction. The jet can be dominantly composed of hadrons (protons and ions) or electrons. A split into hadronic and leptonic dominated models for the explanation of VHE gamma-ray emission is convenient.

Hadronic VHE gamma-ray emission models for microquasars are suggested by several authors (Romero et al., 2003, 2005; Bednarek, 2005; Aharonian et al., 2006a). In the hadronic scenario, secondary leptons will also be produced and thus a synchrotron component is expected (as in the leptonic models) as well as a contribution to the VHE gamma-ray component. One model where hadronic production dominates the VHE emission is shown in Fig. 2.6. The model is used here as an illustrative example, the details are provided in Romero (2008). It is obvious that a considerable amount of synchrotron radiation is produced by secondary pairs which might be detectable in X-rays if the luminosity of the accretion disc is not too high. In some cases, the primary hadronic emission spectrum can be considerably changed by the secondary emission - especially if the magnetic field is low enough to allow for cascades (Orellana et al., 2007; Bosch-Ramon et al., 2008). The dependency of the cascading on the magnetic field is illustrated in Fig. 2.7. Several other models for cascading exist (Bednarek, 1997; Aharonian et al., 2006a) and the effect of the cascade on the emission depends not only on the magnetic field but also on the stellar radiation, on the geometry of the system and on the inclination of the orbital plane to the line of sight of the observer. Consequently, a detailed discussion of these effects must be applied individually to each binary system.

The aforementioned spectra are produced by a VHE emitter within the binary system. Outside of the system, the cascade could dominate the radio emission and might even prevent the radio jet from identification.

The free section of the jet would be dark in VHE gamma-rays in case of hadronic domination but, in the termination region, VHE gamma-ray emission might again be produced

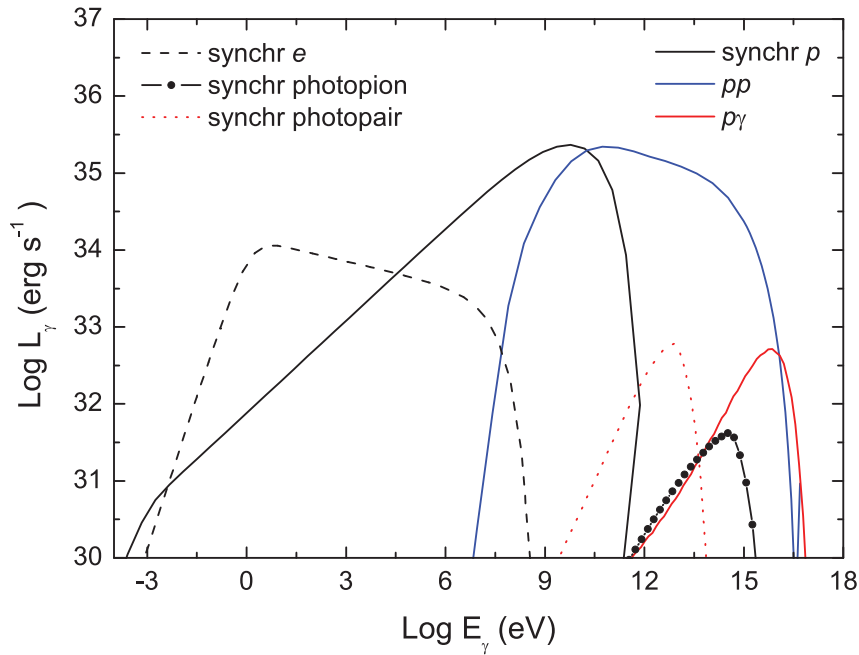


Figure 2.6: The SED for a hadronic microquasar scenario taken from (Romero, 2008). The synchrotron emission of secondary pairs and protons dominate the SED at energies below 1 keV and above it, respectively. The VHE emission is essentially produced by the inelastic proton-proton interactions, while proton-photon production plays a minor role below 100 TeV.

by hadronic interaction.

Two major possibilities for leptonic VHE gamma-ray emission processes exist. Either the synchrotron emission generated by the electrons is upscattered by IC to VHE gamma-rays (self-absorbed synchrotron Compton, SSC) or photons from the stellar companion are up-scattered (external Compton, EC). In HMXB, due to the high target density of UV photons, the external Compton effect is most likely at work. In LMXB systems, the target photon field provided by the stellar wind does not yield a high efficiency for EC, so the SSC model is more likely. The SSC model is the preferred model to explain the VHE gamma-ray emission in extragalactic AGN's (see e.g. Ghisellini et al. 1998). For microquasar emission, this model was suggested by several authors (Atoyan and Aharonian, 1999; Gupta et al., 2006). In the case of the SCC mechanism, the jet might be detected even in the free region (Atoyan and Aharonian, 1999) if the jet is powerful enough to produce internal shocks at this range.

The EC process is most likely taking place at the binary scale as long as the emitting region is close to the luminous star. On larger scales, the SSC component might become dominant. The detailed measurement of the VHE gamma-ray part of the SED might reveal

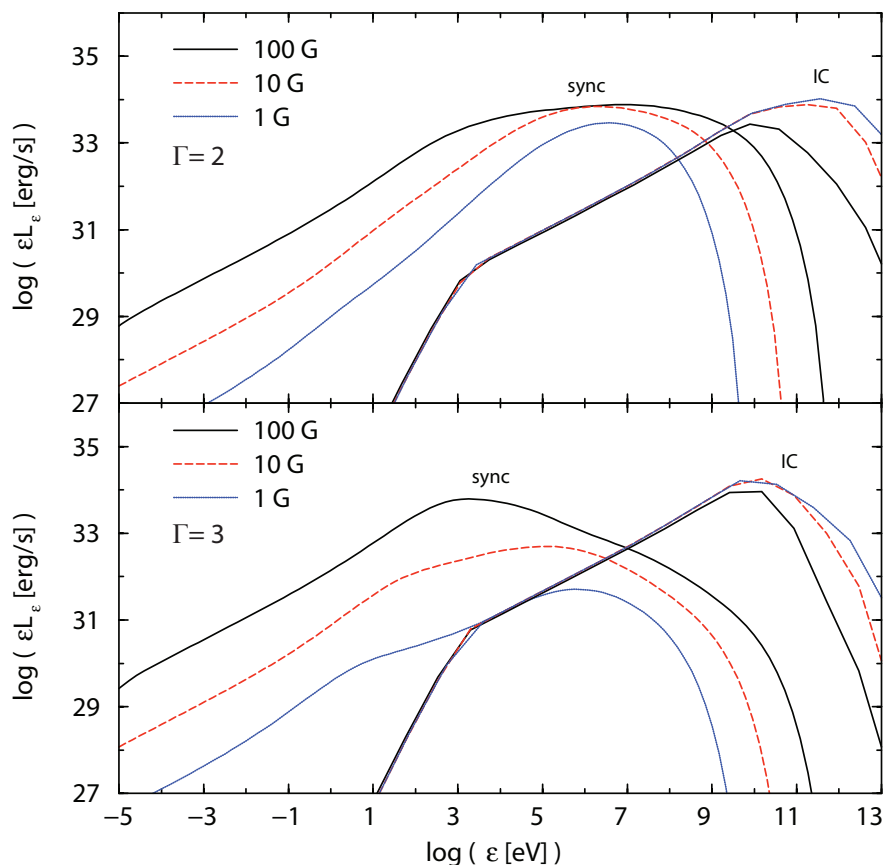


Figure 2.7: The SED dependence on the magnetic field for secondary pair created photons. The upper panel shows the SED for a power law distribution of injected primary gamma-rays with spectral index $\Gamma = 2$ and the lower panel for $\Gamma = 3$. It is evident that strong magnetic fields suppress the IC component significantly while increasing the synchrotron emission. A very high magnetic field can even suppress the development of the cascade. The figure is taken from Bosch-Ramon et al. (2008).

the processes at work. If the orbit is highly eccentric, as it is the case for several microquasars, the anisotropy of the photon density along the orbit should be visible in the light curve. The detailed spectral shape is, in general, difficult to predict because gamma-ray absorption might play a vital role and should cause a time variability in the flux.

Several assumed processes in microquasars are the same as in their extragalactic counterparts. Thus, knots in the jet and jet disc coupling can be effectively studied in the microquasars as well as dependencies of the accretion rate which is, in principle, more easy to estimate because the mass loss of the donor star can be directly measured. Nevertheless, some differences are expected and, especially in the VHE gamma-ray domain, one difference is vital.

The inclination of the jet to the observer's line of sight is a crucial parameter for the observed spectra of VHE gamma-rays. In the case of blazars, the gamma-rays in the jet are doppler boosted to VHE's. Consequently, only AGN's with a jet pointing directly at the observer are detected in VHE gamma-rays. The flux observed at Earth is related to the doppler boosting factor given by

$$F_{\text{obs}} \propto L \frac{\delta_{\text{jet}}^4}{d^2} \quad (2.3)$$

$$\delta_{r,a} = [\Gamma_{\text{jet}} (1 \pm \beta_{\text{jet}} \cos \theta)]^{-1} \quad (2.4)$$

Here F_{obs} is the observed flux at Earth and L is the luminosity of the source, $\delta_{\text{jet}} = \delta_a + \delta_r$ is the doppler boosting factor composed from the approaching and receding jet and Γ is the relativistic gamma factor of the jet and $\beta = v_{\text{jet}}/c$. This strong flux dependency on δ makes possible the detection of blazars up to at least $z = 0.536$ (Albert et al., 2008c). Only two very close-by AGN's which do not belong to the class of blazars have so far been detected. So blazars are detected because their jet points at us, leading to a strong relativistic boosting. This is not the case for the microquasars, at least if they are not too distant. For example, in GRS 1915+105 the inclination of the jet towards us is $\theta \geq 70^\circ$ (Mirabel and Rodríguez, 1999) and thus both jets - and not only the approaching one as for blazars - are seen with almost the same contribution to the total flux. It is even more dramatic because of the superluminal motion of the jets in GRS 1915+105 ($\Gamma \sim 2.5$) which leads to both jets being deboosted, meaning $\delta < 1$ and hence the movement reduces the observed flux at Earth. This is quite the contrary to what is observed in blazars. Extragalactic blazars can be observed at Earth, even if their luminosity is much below the Eddington luminosity, if their doppler boosting factor is high enough (commonly values of 10–100 are assumed for current detected blazars). A much higher accretion luminosity is needed for microquasars so that the jets can be powerful enough to be detected in VHE gamma-rays.

In analogy to blazars, there could be microblazars which have their jets pointed directly at Earth. Good candidates of such systems would be jet sources where only one jet is detected. An example of such a case might be Cyg X-3 (Mioduszewski et al., 2001). The relativistic boosting makes microblazars interesting targets for VHE gamma-ray observations even if they are as distant as Cyg X-3 ($d \sim 7$ kpc). It was suggested that the ultraluminous X-ray sources (ULX) detected in other galaxies might be microblazars with their jet directed towards Earth (Georganopoulos et al., 2002). But, there exists evidence that the ULX's might be powered by thermal emission of intermediate mass black holes (Winter et al., 2006).

2.3 Pulsar wind binaries

A pulsar wind binary denotes a binary system which consists of an optical companion star and a rotational powered pulsar which produces a compact pulsar wind within the binary system. The basic definition of pulsar and pulsar wind are already given in section 1.4.1 and 1.4.2. Here, some more details about the expected emission features and the influence of the companion star wind on the VHE gamma-ray emission will be discussed. The pulsar wind will certainly interact with the stellar wind and create a termination shock between them. The main question is which wind is more powerful and will confine the other wind. In a HMXB, the stellar wind is rather powerful and might create a bow shock in the pulsar wind and it was suggested that this might lead to a *cometary tail* radio feature as proposed for LS I +61°303 by Dhawan et al. (2006). If this geometry should prove to be valid, the maximum power of the pulsar wind can be estimated by balancing it with the stellar wind power. The detailed shape of the termination shock is challenging to determine and might vary with orbital phase, depending on the orbital parameters and the class of the optical companion star in the system.

There will be always two components of the pulsar wind present, the free wind and the shocked wind. The shocked wind is known to be a potential accelerator to TeV energies and thus VHE gamma-ray emission from this region is expected. The lower energetic emission from both wind regions are essentially synchrotron radiation and IC emission which can be both identified as power law distributions in radio (only synchrotron) and X-rays. A thermal component in the X-ray, as in the accretion scenario, is not expected. The radio morphology should not show jet-like features but can give changing appearances along the orbit of the compact object, since the distance between the star and neutron star (especially in orbits of high eccentricity) will vary and so will the position of the shock front between their winds. This might lead to a moving peak position of the radio flux with respect to the orbital phase.

A clear identification of the pulsar wind scenario would be the detection of radio pulses from the binary. Nonetheless, the pulsar light beam might not be directed at Earth or the pulsed emission might be absorbed if the binary is very compact. The later is observed in PSR B1259-63 when the pulsar is close (around periastron) to its companion (Johnston et al., 2005).

If the pulsar would be accreting, it should show the typical bursts⁵ detected from such systems.

⁵The hydrogen accreted by the NS can pile up on its surface. When enough hydrogen is gathered that the critical density for thermonuclear fusion to helium is reached a sudden flare visible in X-rays can be observed. This process is similar to the novae observed from white dwarf stars.

So there exist several possibilities to distinguish the accretion from the rotation powered scenario from the radio to X-ray emission. The VHE gamma-ray production inside the pulsar wind binary and its emission features are described in the next section.

2.3.1 VHE gamma-ray emission

That pulsar wind nebulae can be strong VHE gamma-ray emitters is undoubted, for example the strongest steady source (the Crab Nebula) is a PWN. Most of the identified galactic VHE gamma-ray sources are thought to be PWN's, making these objects prime candidates for the search for VHE gamma-ray emission. It is natural to assume that a pulsar in a binary can produce a powerful PWN which is shocked by the companion wind, with particles being accelerated in this shock. One of the first suggestions of such a model for the non-thermal emission in binaries was made by Maraschi and Treves (1981). After the discovery of the first binaries in VHE gamma-rays, an increased interest revived this emission mechanism for binaries and several more models appeared (Dubus, 2006b; Chernyakova et al., 2006; Cerutti et al., 2008; Sierpowska-Bartosik and Torres, 2008). The models vary in suggesting the origin of the VHE gamma-ray emission. While Dubus (2006b) and Chernyakova et al. (2006) see the termination shock as the emitter region, the free pulsar wind is suggested as the emitter by Cerutti et al. (2008) and Sierpowska-Bartosik and Torres (2008). The free pulsar wind could consist out of TeV electrons which produce VHE photons by IC upscattering of the photons from the companion star⁶. Up to now, no model includes both wind regions as emitters and so the task to find a complete description for PWN binaries remains open.

In addition to the emitting region, there are more individual assumptions in the models. Leptonic emission models producing VHE gamma-rays only due to IC are proposed by Cerutti et al. (2008) and Sierpowska-Bartosik and Torres (2008). There exists as well a model which suggests an additional hadronic component to explain the VHE gamma-ray emission while attributing the X-ray to soft gamma-ray emission to IC of electrons (Chernyakova et al., 2006). In the hadronic model, some ions or protons must be present in the pulsar wind and, indeed, some theories assume that the neutron star is covered by an iron crust which can be heated and thus emit iron nuclei which might be accelerated in the magnetosphere and ionized by the large electric fields of the pulsar. They could contribute some small fraction to the particles in the pulsar wind (PW). These ions might then interact with the matter of the stellar wind, creating VHE gamma-rays via π_0 decay or from IC by secondary leptons from the charged pion decays.

⁶Note that the UV photons of the star can propagate into the pulsar wind without being hindered by the termination shock. The shock is created by the matter in the stellar wind.

The VHE gamma-ray emission due to the pulsar wind might be modulated by propagation and absorption effects in the binary. The geometry of the orbit and the direction towards the observer will determine which parts of the wind (free and/or shocked) are dominating the observed emission (see i.e. Sierpowska-Bartosik and Torres (2009)). Another possible source of variability is the development of cascades which might be time-dependent due to different magnetic fields present at the emitter depending on the orbital geometry and the shock position. The effect of cascading would be the same, as described in the microquasar case. The wind clumps in HMXB could cause variability on short timescales and this was first suggested by Zdziarski et al. (2008). In case of a strongly clumped wind, the calculation of the termination shock is very difficult and, up to now, no detailed description has been possible. In case of a clumped wind, there might even be beamed emission in the direction of the observer while, in general, only non-beamed emission is expected for the pulsar wind scenario. This implies that only near-by ($d \lesssim 4$ kpc) PWN binaries should be visible in VHE gamma-rays.

The emission from the system can be periodically modulated if strong anisotropic absorption effects (eccentric orbit of compact object) occur in the system.

2.4 Absorption in binary systems

Photon absorption effects are very important in HMXB, since the massive stars have a high luminosity ($L \gtrsim 10^{38}$ erg s⁻¹). Since these OB type stars have, in general, high surface temperatures ($T \sim 3 \times 10^4$ K), the target photons have energies peaking in the UV range. The absorption effects in binaries are calculated by several scientist but differ, for example, in accounting for the finite size of the star (Protheroe and Stanev, 1987; Moskalenko and Karakula, 1994; Bednarek, 1997; Böttcher and Dermer, 2005; Dubus, 2006a; Khangulyan et al., 2008; Reynoso et al., 2008; Sierpowska-Bartosik and Torres, 2008). From all these calculations, it is evident that the absorption processes in binaries play a vital role and will often dominate the shape of the emission spectrum. Absorption effects could cause an orbital periodicity in the emission or might even suppress the VHE emission if the photon field of the star is too dense. Such a case might be true for the microquasar Cyg X-3 which is among the most compact systems known, with an orbital period of only 0.4 days and a hot WR star as the optical companion.

The detailed influence on the observed spectrum and light curve of every source must be calculated individually. More information about these effects on LS I +61°303 are given in chapter 7.

2.5 Detected binary systems in gamma-rays

With the advent of the new generation of very sensitive VHE gamma-ray detectors like MAGIC, H.E.S.S. and VERITAS, the first binary systems could be identified as VHE gamma-ray emitters. This thesis presents the up-to-now most detailed analysis of LS I +61°303 and all available information on it can be found in chapter 7. The other detected binaries are PSR B1259-63 (Aharonian et al., 2005a) and LS 5039 (Aharonian et al., 2005b). Another VHE source possibly associated with a binary is HESS J0632+057 (Aharonian et al., 2007c; Hinton et al., 2009; Acciari et al., 2009). The VHE gamma-ray source HESS J0632+057 is pointlike and emits variable radiation in the radio and X-rays band and thus makes it a good candidate for a binary system. An extragalactic source shining through the Milky Way is rather disfavored since a Be star is detected at the same position and Be stars are very often members in HMXB. Whether this Be star is accompanied by a compact object can be tested by measuring its radial velocities to obtain the orbital parameters of the system.

A hint for VHE gamma-ray emission in a short transient event ($T_{obs} \sim 80$ min) is found in Cyg X-1 by MAGIC (Albert et al., 2007f). The significance of this signal is unfortunately marginal with 3.2σ in the whole observation night ($T_{obs} \sim 160$ min). Despite a huge amount of additional data taken in 2007–2008 on this source, no further emission is detected (Saito et al., 2009).

Most of the theories discussed here and the suggestions about how the emission mechanism might work were published after the detection of the three solid detected sources (LS I +61°303, LS 5039, PSR B1259-63). This emphasizes the fact that the VHE gamma-ray emission of binary systems is still an unsolved puzzle but, as more data becomes available, the better understood are the emitter mechanisms. The importance of high quality data in the VHE gamma-ray domain for the development and tuning of the various models can be well traced by the publication avalanche triggered each time new VHE gamma-ray data becomes available (see, for example, chapter 7 about LS I +61°303 in this thesis). One of the main questions is which emission scenario (microquasar or PWN binary) is valid in the detected binaries. While the detection of radio pulses in PSR B1259-63 makes this case clear, it is not so obvious in the other binaries. Up to now, no definite microquasar has been detected in VHE gamma-rays - a solid detection of Cyg X-1, GRS 1915+105 or SS 433 would solve this question and give vital information to confirm or reject what is at present merely the hypothesis about the microquasar scenario. This is the reason why so much observation time is invested in the VHE gamma-ray study of clearly identified microquasar systems. Up to now, these observations have yielded no detection. Nevertheless, even non-detection can

constrain severely the emission models by conflicting with their predictions.

The question which scenario is true for LS I +61°303 is one of the main topics of this thesis and the interpretation of the VHE gamma-ray emission from the system is discussed in great detail in section 7.12. This question cannot be solved by VHE gamma-ray studies alone but must also include the other emission bands of non-thermal emission (radio, X-rays). In the study of LS I +61°303 extensive multiwavelength campaigns are undertaken to understand the complete SED and each model which describes the SED correctly can be accepted as a description of the system. More and more data taken over long timescales are needed in order to understand better the energy processes taking place in binaries. The large amount (hundreds of hours) of highly competitive observation time granted in ground-based VHE gamma-ray detectors such as MAGIC and X-ray satellites like *Chandra* and *XMM-Newton* indicates how important these studies are and how high their scientific impact.

Chapter 3

Imaging Atmospheric Cherenkov Telescopes

In this chapter, the most successful detection method to observe gamma-rays of energy above 25 GeV from the Earth's surface is explained. Since our atmosphere is opaque to EM waves of that energy, only indirect detection is possible. To be able to detect them, the Earth's atmosphere is used as a calorimeter and the Cherenkov light emitted by the charged particles is detected by an imaging telescope on the surface of the Earth. To understand the dependencies between the shower development and the Cherenkov light transmission on the atmosphere, several characteristics of the shower development and Cherenkov light production are described. In section 3.4, the systematic uncertainties in the measured fluxes and spectra obtained by ground-based VHE gamma-ray astronomy (and how to take them into account) are discussed.

3.1 Extensive air showers

Whenever a particle hits the atmosphere and its energy is high ($E \gtrsim 5$ GeV), a particle cascade is initiated. The primary particle interacts with the molecules in the air and produces secondary particles which interact again with the air molecules and thus iteratively more and more particles are generated and each particle generation carries less energy than their parent generation. After some time the individual particles do not carry enough energy to split up further and the energy loss due to ionization and absorption dominates, thus the particle number decreases and the cascade dies out. Such a cascade is called an extensive air shower (EAS).

The shape of the cascade is different for the different particle types. The main difference is given by the dominant interaction of the particle with the atmosphere. While all charged particles can interact electromagnetically, the hadrons will dominantly interact hadronically

because the cross-section is much larger than the EM cross-section. This is important since gamma-ray astronomy is interested only in gamma-rays whereas most particles hitting the atmosphere are cosmic rays (mainly protons) - and these are background events to be rejected. The difference in cascade development depends on the dominant interaction, leading to a wider lateral spread in hadronic-induced showers, since the transverse momentum transfer is higher in these interactions compared to the EM interactions. In addition, the interaction length of the hadrons is much larger compared to the EM interaction length of leptons (and gamma-rays), leading to a deeper penetration into the atmosphere for the hadronic particles compared to the gamma-rays. Furthermore the larger hadronic interaction length leads to larger fluctuations between showers initiated by primary particles with the same energy.

In Fig. 3.1 a typical hadronic- and gamma-ray- induced air shower are shown to illustrate the differences in appearance.

Hadronic showers develop EM subshowers due to neutral pion production in the hadronic interaction. The π_0 decays almost always via the channel $\pi_0 \rightarrow \gamma\gamma$ and thus initiates two EM subshowers. These EM showers carry roughly one third of the energy of the primary particle since the neutral pions make one third of all produced pions and should carry on average, due to momentum conservation, one third of the primary particle energy. Thus, the EM part of a hadronic shower is roughly comparable to a gamma-ray- induced cascade with only one third of the energy of the hadron. The details of EAS development can be studied only by Monte Carlo (MC) simulations. In the case of the EM cascades, a description with simplifying formulas is possible and helpful to understand the basic properties.

A description of the development of an EAS can be obtained by coupled transport equations (Gaisser, 1990), which describes the propagation of the particles transversing the atmosphere.

$$\frac{dN_i(E, X)}{dX} = -\left(\frac{1}{\lambda_i} + \frac{1}{d_i}\right)N_i(E, X) + \sum_j \int \frac{F_{ij}(E_i, E_j)}{E_i} \frac{N_j(E_j)}{\lambda_j} dE_j \quad (3.1)$$

In equation (3.1) $dN_i(E, X)/dX$ is the change of the particle number of type i per slant depth (X). On the right side, the first term gives the decrease of the number of type i particles due to decay and interaction while the sum over the integral describes the probability that a particle of type i decays to a particle of type j ¹. The integral is needed because of the different energies which the daughter particles may have. This equation can be solved for EM cascades and the solution found by Greisen (1956) for the longitudinal development is given in equation 3.2.

¹resulting in an increase in the number of type j particles

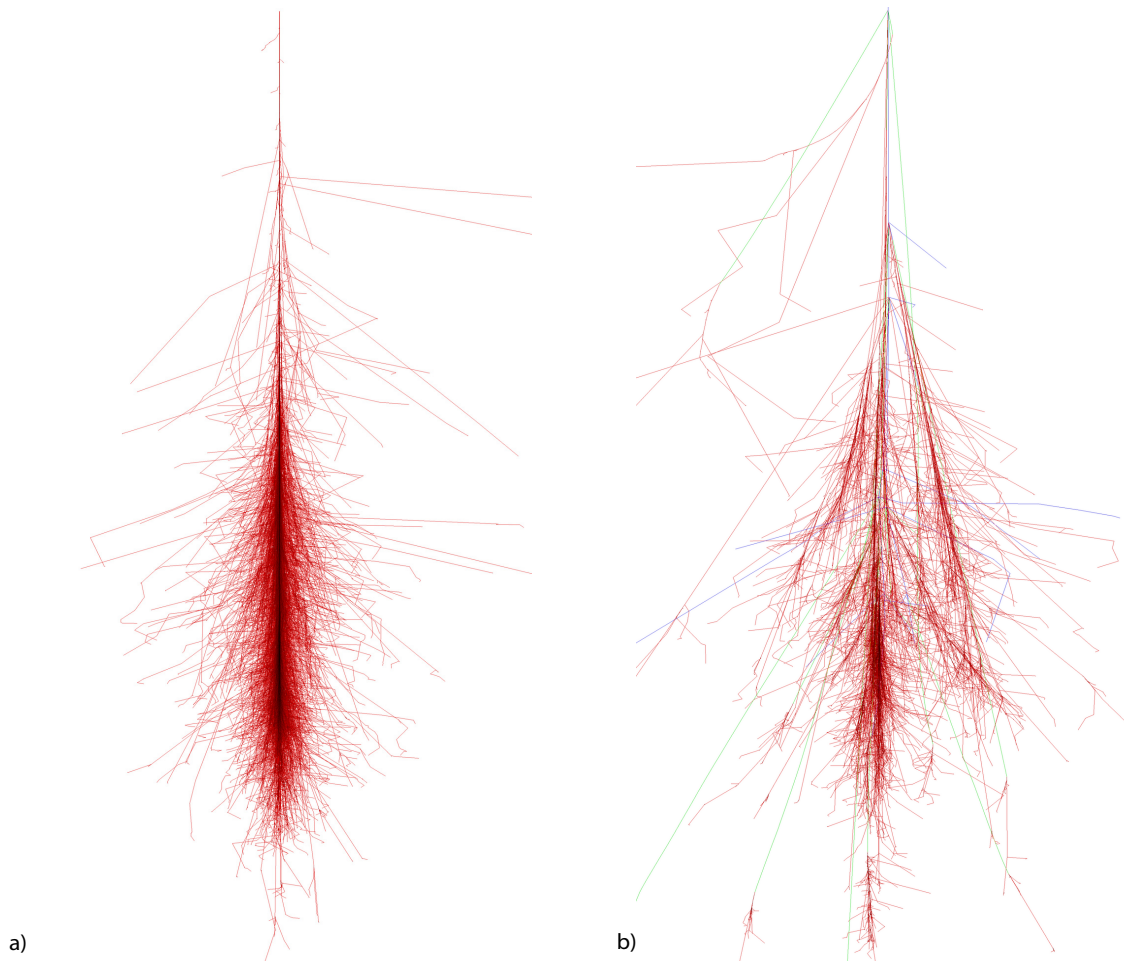


Figure 3.1: a) shows a simulated gamma-ray- and b) a simulated proton-induced air shower. In both plots, the red particles are electrons and positrons while the green lines indicate gammas and the blue trajectories are muons. The showers were simulated with the Corsika extensive air shower package and both primary particles had an energy of $E = 200\text{GeV}$. Courtesy of F. Schmidt, Leeds, now Chicago.

$$N_e = \frac{0.31}{\sqrt{\log[E_0/E_c]}} e^{T(1-1.5(\log[S]))} \quad (3.2)$$

In this equation, E_0 is the energy of the primary particle, E_c the critical energy (need to from a cascade), T is the shower depth and S is the shower age.

The shower depth is the distance the particles have transversed in the atmosphere measured in radiation length. The shower age is a relative parameter that reaches from 0 (start of the cascade) to 2 (died-out cascade) and describes the development of the shower in a way that the shower maximum is at $S=1$. The shower age is related to the shower depth with equation (3.3).

$$S = 3/(1 + 2(\log[E_0/E_c])/T) \quad (3.3)$$

To be able to describe the shower development in the atmosphere, an atmospheric model must be assumed. If a simple isothermal atmosphere with an exponential density profile is assumed, a relation between T and the height measured from ground h is given by equation (3.4).

$$T = \frac{X}{\lambda} e^{-h/H} \quad (3.4)$$

Here, X is the slant depth at ground ($X = 1023 \text{ g/cm}^2$), λ is the interaction length in air and H is the height at which the pressure is decreased to $1/e$ of the pressure at sea level. In Fig. 3.2 N_e is shown for three different energies.

The following conclusions can be drawn from eq. 3.2 and Fig. 3.2:

- The higher the primary particles energy, the higher the number of secondary particles
- Higher energetic primary particle cascades develop their maximum of secondary particles deeper in the atmosphere
- The showers of primary particles with energy less than 500 GeV will have no considerable amount of particles reaching the ground.

From these facts, one can already see that the amount of particles in the shower gives a good indication of the energy and this can even be refined using the height of the maximum number of particles in the cascade. In addition, it is clear that any observatory which wants to measure lower energetic primary particles cannot do so at low altitudes. Furthermore, a dense coverage on the ground is needed so as not to miss some of the view particles in the cascade. This renders direct detection of cascade particles for low energies ($E < 500 \text{ GeV}$)

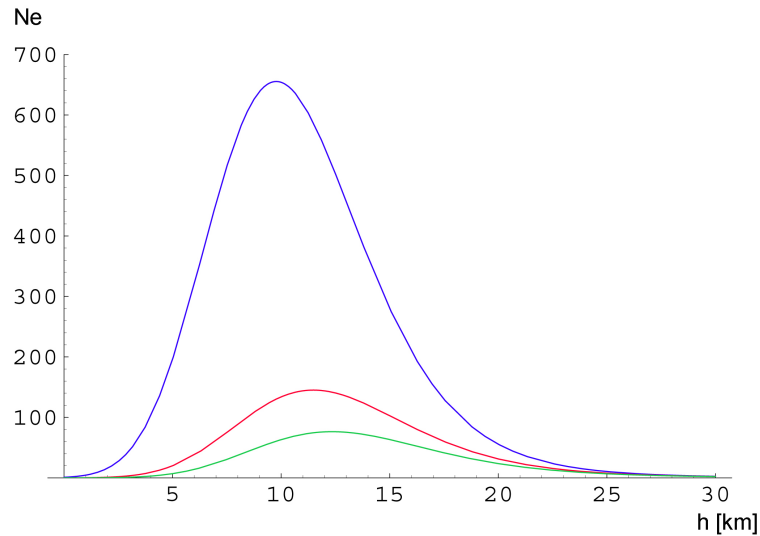


Figure 3.2: The number of e (N_e) versus the height measured from the ground for 500 GeV (blue), 100 GeV (red) and 50 GeV (green) gamma-ray- initiated cascades. NOTE: the height of the maximum is shifted to higher values for lower energies.

expensive if the low fluxes from the astronomical sources are to be measured. A better method to obtain a large effective detector area is to measure the particles in the cascade indirectly with the help of their Cherenkov light emission. This technique is described in the next section.

3.2 Cherenkov light production

Cherenkov light is emitted by all charged particles which move in a polarizable medium above the speed of light in this medium. The amount of light emitted by any cascade is in first order proportional to the energy of the cascade and thus to the primary particles' energy. In our atmosphere, the speed of light is not constant but changes with altitude, this variation of speed being caused by the density changes of the atmosphere. Since the speed of any particle is determined by its mass and its momentum, the threshold energy for Cherenkov light production depends on the mass, as follows:

$$E_{\text{th}} = \frac{m_0 c^2}{\sqrt{1 - n^{-2}}} \quad (3.5)$$

Here m_0 is the rest frame mass of the particle and n is the refraction index of the medium. Assuming an exponential behavior, of the refraction index as a function of altitude in the atmosphere gives the minimum energy needed to emit Cherenkov light for the different particles present in an air shower. As can be seen from Fig. 3.3, the threshold energy of the electrons (and positrons) is at the lowest level. Thus, mainly electrons and positrons emit

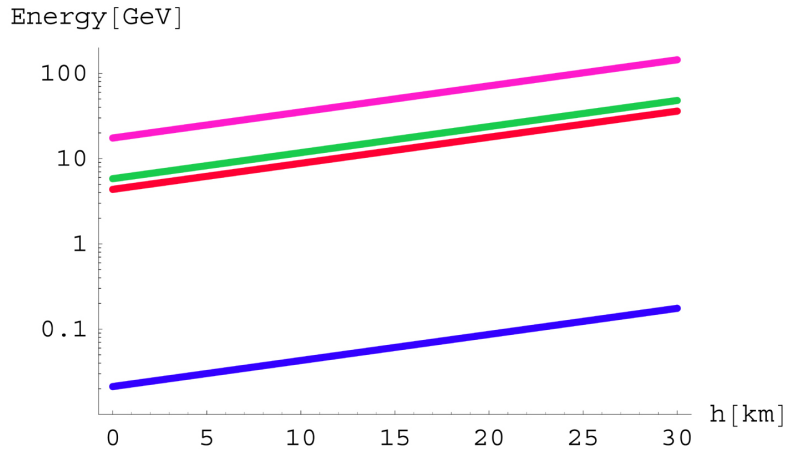


Figure 3.3: The minimum energy needed for Cherenkov light production versus the height of the particle emitting the light. The magenta line is for kaons, the green line for pions, the red line for muons and the blue line for electrons. An exponential dependency is assumed for the density of the atmosphere as a function of the height.

Cherenkov light since they form in EM cascades rapidly and, even at energies below 30 MeV, they emit Cherenkov light at sea level. The other particle types must have considerably higher energies to emit Cherenkov light and given that they are much less abundant, even in hadronic events, they contribute little to the total light intensity emitted by the cascade.

Cherenkov light is emitted under a certain angle which is given by:

$$\theta = \arccos\left(\frac{1}{\beta n}\right) \quad (3.6)$$

The so-called Cherenkov angle depends on the refractive index n and thus changes with altitude. Since the secondary particle tracks have different inclination angles to the trajectory of the primary particle, the Cherenkov light of the cascade is not simply a circle on the ground but a superposition of many hollow circles and ellipses, one for each shower particle above the threshold energy. The 2D intensity profile (at the observation level) of the cumulative Cherenkov light of all EAS particles is called the Cherenkov lightpool. There is no analytical formula to obtain the Cherenkov lightpool emitted from any cascade on the ground and Monte Carlo simulations are needed to get this information. The Cherenkov lightpool created by a gamma-ray- and a hadronic-induced cascade are shown in Fig. 3.4. The high intensity of the Cherenkov light up to impact parameters of 120 m is caused by direct Cherenkov light from the shower, while the light recorded further away is scattered by the atmosphere with a rare large scattering angle. Another relevant parameter is the Cherenkov light spectrum. This spectrum is important to optimize the response of the detector and to understand the

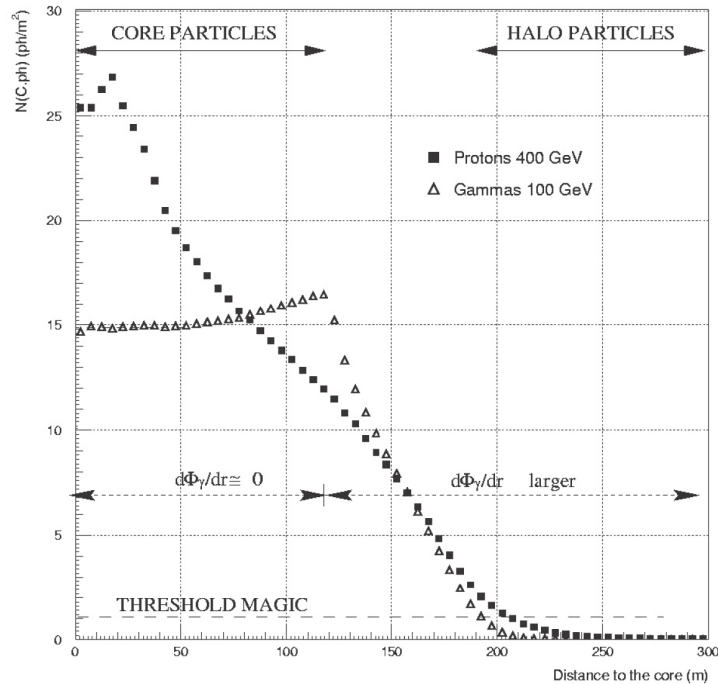


Figure 3.4: Cherenkov light intensity as a function of the distance of the telescope to the shower’s main axis. The triangles represent a MC simulation for 100 GeV gamma-induced showers while the squares represent a 400 GeV-induced proton shower. The zenith angle of the simulation is 0° and the observation level at 2200 m altitude.

importance of the refraction and absorption effects in the atmosphere.

Assuming that the refraction index is constant with wavelength (λ) the basic intensity dependency on the emitted wavelength is:

$$I(\lambda) \propto \lambda^{-2} \quad (3.7)$$

This dependency leads to the highest emission at UV and blue optical wavelengths. The total intensity of Cherenkov light emitted by the cascade is, of course, proportional to the number of electrons above the Cherenkov light production threshold in the cascade and thus, in first order, proportional to the energy E of the primary particle.

Not all Cherenkov photons reach the ground and attenuation effects, which are in general wavelength dependent, have to be taken into account to obtain the intensity at the observation level. Unfortunately, the highest intensity part of the Cherenkov emission suffers from almost total absorption. Cherenkov photons with $\lambda < 280$ nm do not reach the observation level due to the very strong absorption of ozone (O_3) and oxygen. A comparison between the emitted and the observed (with observation 2200 m above sea level) Cherenkov light spectra from EAS of different energies is shown in Fig 3.5, together with the transmission of light from space to the observation level and the major absorption mechanism at work.

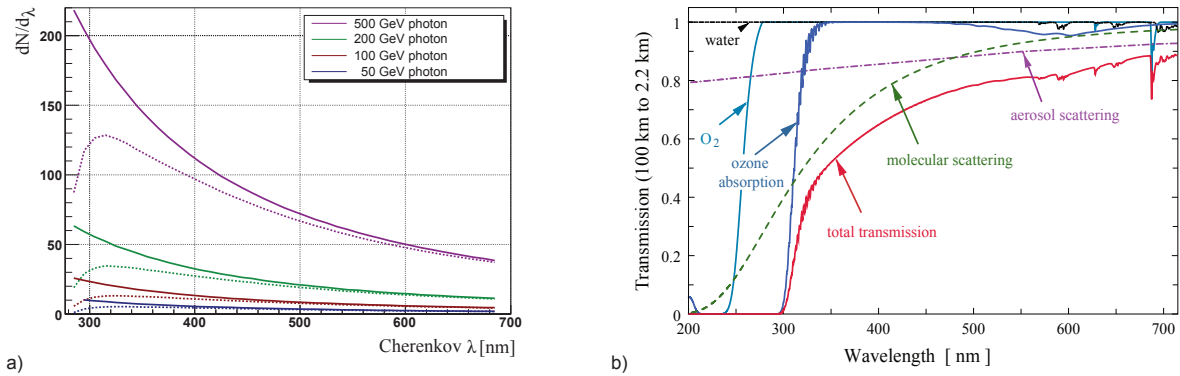


Figure 3.5: a) shows the wavelength dependent Cherenkov light intensity as emitted (solid) by EAS of different energies and as observed at the observation level (dashed). b) displays the different absorption effects and their wavelength dependence for the transmission of light from space. Figure a) is taken from Wagner (2006) and b) adapted from Bernlöhner (2000).

There are two main components of the interaction of Cherenkov light and the particles in the atmosphere: The Rayleigh and the Mie scattering. Rayleigh scattering is inevitable even in a perfect atmosphere but it is theoretically and experimentally well-described and can be taken into account in the MC simulation, at least as an ideal. Ideal meaning that the atmosphere can of course change with seasons, pressure, humidity and so on. So the description will be only valid within a range of these parameters. A detailed study about the different atmospheric models and atmospheric composition on the Cherenkov light spectrum is given in Bernlöhner (2000).

The Mie scattering is mainly caused by particles in the air which are large compared to the wavelength of the Cherenkov light and no good theoretical description of the cross-sections exists. The dominant materials causing Mie scattering are aerosols and dust in the air.

Another important fact is the short spread in the arrival times of the Cherenkov light at the observation level. The time span in which the whole emitted light of the cascade reaches the detector is only a few nanoseconds. Thus, a detector must have a very fast response and a short integration time, otherwise the night sky background light (see Roach and Gordon (1973) for a review on night sky background light) would be much more intense compared to the Cherenkov light. The exact arrival time spread of a Cherenkov shower, which is recorded by a detector, can be used for the identification of the primary particle as well as the geometrical shape of the shower (Aliu et al., 2009a). The arrival time distribution is again obtained by MC simulations. The use of arrival times in the analysis of the shower images

successfully improved the sensitivity of the MAGIC telescope, compared to the analysis without exploiting the time information. A detailed description of the usage of the arrival times of the Cherenkov photons will be given in chapter 5.1.1 which describes the analysis of the MAGIC data.

3.3 The imaging technique

The Imaging Atmospheric Cherenkov Telescope (IACT) records a picture of the Cherenkov light emitted by a cascade and characterizes it by evaluating the properties of the image. As described in the previous sections, the properties of the shower depend on the particle initiating the cascade but this information is exclusively needed to reject non gamma-ray-induced background events. If the gamma-rays are identified then several parameters, such as the direction from which it was emitted and the energy of the particle, are of interest.

To obtain the Cherenkov light image, the telescope must be inside the lightpool of the shower. The projection of a shower in the imaging plane of the telescope is shown in Fig. 3.6. Since the camera has a limited size, the shower image can be truncated if the shower has a large impact parameter and high energy. From Fig. 3.6 it is evident that the later developing cascade (lower in the atmosphere) is imaged by the farther outlying pixels and these are the parts of the cascade most likely to be truncated. Modern IACTs like MAGIC have camera diameters of 3.5–5 degrees and are able to image showers completely only in a certain range of impact parameters and energies. Truncated images suffer from worse energy and direction reconstruction compared to fully contained images. The details of the reconstruction mechanism and the effects of the limited camera size are given in the analysis description, see chapter 5. It is clear that the limited size of the camera² of any IACT limits the effective collection area in which it can record shower images useful for analysis. Nevertheless, the collection area of IACT's is in the order of several 10^4 m², thus enabling them to detect the faint fluxes of the gamma-ray sources. The strongest steady gamma-ray source, the Crab Nebula, has an integral flux above $E > 300$ GeV of $(1.31 \pm 0.03) \times 10^{-10}$ cm⁻² s⁻¹, meaning that several gamma-rays are recorded per minute by an IACT like MAGIC.

This makes a significant detection of a gamma-ray source, like the Crab Nebula, possible in few minutes. The advantage of recording shower images from cascades in a much larger area compared to the size of the telescope and the large accessible energy range, from 70 GeV up to 20 TeV, makes IACT's excellent instruments for VHE gamma-ray astronomy.

²In fact the size of the trigger region of the camera is the most limiting factor if it is not identical to the camera size, as in the case of MAGIC

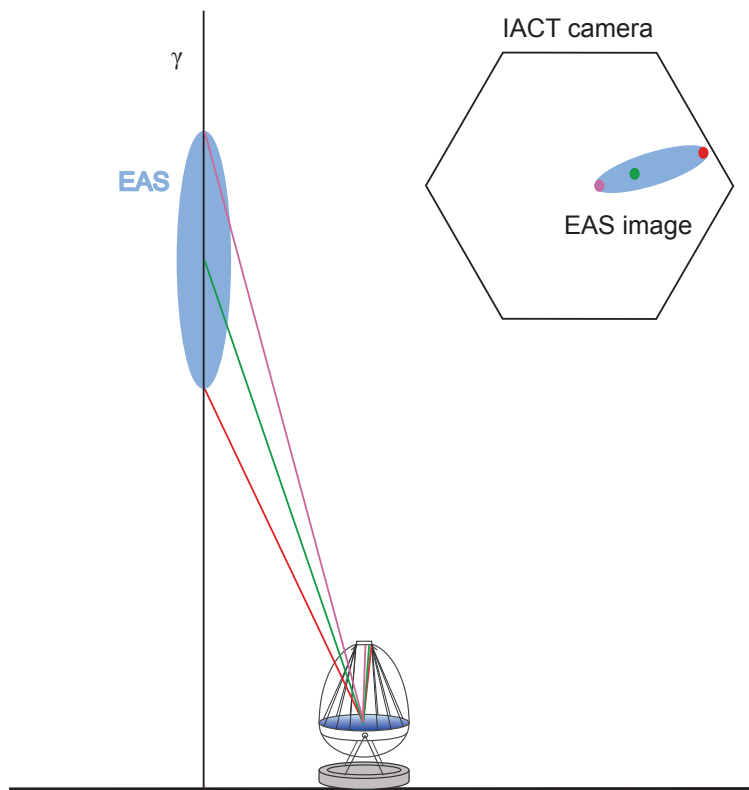


Figure 3.6: Schematic view of the mapping of the shower onto the focal plane and the image obtained in the IACT camera. The asymmetric deformation of the shower due to the non linear mapping function is indicated.

3.4 The uncertainties in IACT measurements

A very important topic is the understanding of the systematic uncertainties of any experiment. In the case of gamma-ray astronomy with IACT's it is very important to think of observations instead of experiments. With an IACT, a gamma-ray source can only be observed with no guarantee that the source will be observed again in the same emission state as it was in the previous observation. A prominent example for such unique events are GRB's and to some extent AGN outbursts and transient phenomena in binaries.

Since the observer cannot influence the source behavior it is important to know the detector performance and uncertainties in the measured quantities. Only if the uncertainties are known is the interpretation of transient phenomena possible. Here, two different types of systematic uncertainties must be distinguished. The first type of uncertainty is related to the telescope and the description of the ideal atmosphere, along with the Cherenkov light production by cascades. In all parts (detector, shower simulation, atmospheric model), systematic uncertainties are present but they can be evaluated and are constant in time.

The other type of uncertainty is time dependent and these uncertainties are more important for the interpretation of the measurements. Their major source is the change in atmospheric conditions. The atmosphere is not a stable medium and several important parameters such as aerosol abundance, humidity, temperature, air pressure and dust grain content can change, even on short timescales. All these parameters cannot be easily monitored from the observation level but they might have an effect on the measurement. For example, higher humidity or aerosol abundance will increase the amount of Cherenkov light which is scattered away from the camera and at the same moment increases the background light of the night sky. This will lead to worse signal to noise ratio in the camera and reduce the reconstructed Cherenkov light intensity of the shower. Thus, the detected shower image will not lead to the primary particle parameters since the image deviates from the MC estimated expectation which is used in the analysis.

These time-dependent uncertainties are very difficult to compensate for and until now only good quality data is analyzed and the remaining data is discarded. Good quality data must fall within a predefined range of atmospheric parameter values. In that way, the uncertainties of the measurements can be evaluated and the gamma-ray parameters can be reconstructed with the use of the ideal atmospheric MC simulations. The data quality can be most efficiently judged by the trigger rate of the telescope. The trigger rate is caused mainly by protons since they are much more abundant compared to gamma-rays but the effect on both shower types due to atmospheric conditions is similar. The method of the data quality evaluation proceed in the following steps. The standard candle, the Crab Nebula, is observed on a very transparent night. The trigger rate of this observation is noted and the data is analyzed to obtain a reference VHE gamma-ray spectrum from the Crab Nebula. Then the Crab Nebula is observed under various atmospheric conditions (different trigger rates) and the individually obtained spectra are compared to the reference spectrum. All observations which yield spectra within the statistical errors of the reference measurement are defined as good quality data. The trigger rates of the good quality observations define an interval of conditions in which reliable measurements are possible. From the good quality data, a minimum trigger rate is defined which corresponds to the worst condition in which data can still be analyzed.

This data quality check uses the following assumption. The standard candle source must display constant behavior in time. This is the case for the Crab Nebula, since all spectra from all different IACT taken over more than two decades agree well within their estimated systematic uncertainties. Another point which should be taken into account is that worse atmospheric conditions affect the lower energetic showers more dramatically and thus a

source with a very soft spectrum might be more affected when compared to the Crab Nebula observations.

A detailed description of the estimation of the performance parameters of MAGIC and their stability is given in chapter 6.

Chapter 4

The MAGIC telescopes



Figure 4.1: The MAGIC telescopes just after sunset in December 2008

The Major Atmospheric Gamma-ray Imaging Cherenkov (MAGIC) telescopes are located at the Observatorio de Roque de los Muchachos on the Canary Island La Palma (28.75°N , 17.86°W , 2225 m above sea level). The telescopes are spaced 85 m away from each other. The first MAGIC telescope began operation in 2004 and was commissioned until 2005. In 2006, it was decided to construct a second MAGIC telescope on the same site to enable stereoscopic observations. The commissioning of the second telescope began in December 2008 and will take until autumn 2009. Since the second telescope incorporates many design improvements compared to the first it is often called an improved clone. Here, I will describe both MAGIC telescopes and focus on the MAGIC II camera and the camera control program

because I contributed a major part into its development and programming.

Both telescopes have the light weight structure of the reflector and the light weight camera in common in order to reduce the moment of inertia of the telescope, thus enabling it to reposition as fast as possible to react on short transient phenomena like GRB's. The total weight of each of the telescopes is around 60 tons. A maximum time of 100 s is needed to point it to any position in the sky. The average positioning time is about 40 s making MAGIC the fastest moving Cherenkov telescope in the world.

Furthermore, both telescopes possess 17 m diameter parabolic reflectors with a focal length of 17 m. This gives them a fast optical system with a $f/1$ ratio. These fast systems require good mirror properties to achieve reasonable point spread functions (PSF) at the border of the camera. Due to coma (an optical aberration present in all parabolic mirrors) a point-like image gets distorted to a triangle shape pointing to the camera's center. The optical quality of the telescopes guarantee that the PSF is completely enclosed in the area of one pixel, at least in the trigger area. In addition, the focusing of the mirror elements is done for each pointing direction and corrects slight bending of the light weighted frame. This active mirror control (AMC) is described in detail in Biland et al. (2008).

Another consequence of the slight bending is the need for a pointing accuracy check. This is done by means of a system called *star guider* which consists of a charge coupling device (CCD) camera in the center of the reflector with the reference light emitting diodes (LED) arranged in a circle on the photo multiplier tube (PMT) camera frame. The star guider CCD is simultaneously imaging the night sky, along with the MAGIC PMT camera and half of the LED circle on the PMT camera frame. From the LED position, the camera center position can be readily determined and the comparison between the recognized stars and their catalog position provides the celestial coordinates of the camera center. This position can be monitored continuously, providing corrections for the telescope pointing deviations. The current pointing accuracy of MAGIC is 1 arcmin and can be improved to ~ 30 arcsec with a calibrated star guider system. The whole star guider system, its calibration and the pointing model applied in MAGIC, is described in Wagner (2006).

4.1 MAGIC I

MAGIC I has a tessellated reflector of 17 m diameter built by 964 single mirrors with dimensions 49.5×49.5 cm². The single mirrors are mounted in groups of four and at the rim of the reflector in groups of three on panels which can be moved by the active mirror control. Each

panel is adjusted for the current pointing direction in such a way that the reflector shape is a parabola. This reflector shape is chosen to minimize the arrival time spread of the photons on the camera plane. The total mirror area of *MAGIC I* is 239 m². The structure supporting the reflector is made of carbon fibre tubes to reduce the total weight of the telescope to about 60 tons.

4.1.1 The camera of *MAGIC I*

The camera of *MAGIC I* has a hexagonal shape and covers a field of view (FoV) of 3.5 – 3.8°. The camera consists of 576 PMT's where two sizes of PMT's are used. The inner camera with a diameter of about one degree is formed by 396 0.1° diameter PMT's surrounded by four rings of 0.2° diameter PMT's. On top of each hemispherical PMT, a hexagonal hollow winstone cone (WC) is attached. The WC is used to guide the light to the sensitive area of the PMT entrance window and minimizes the dead space between the PMT's. Each PMT is coated by a lacquer which includes a wavelength shifter (Paneque et al., 2003). This additional coating improves the light collection efficiency of the telescope by $\sim 5\%$ (Paneque, 2004).

The PMT's are designed to be able to operate under moderate moonlight without damage. For this reason, the PMT's possess only six acceleration dynodes instead of the ten stages in common PMT's. Thus the gain of the *MAGIC* PMT's is only about 10^4 and the signal is further amplified by a low noise amplifier before it is converted by multimode vertical-cavity surface-emitting lasers (VCSEL) to an analog optical signal and then transmitted by optical fibres to the *MAGIC* counting house. The readout electronics are not included in the camera but placed in the control building 100 m away from *MAGIC I*. This reduces the weight of the camera, its power consumption and the necessary cooling capacity and enabling the use of flash analogue to digital converters (FADC) for the readout system. Detailed information about the *MAGIC I* camera and its performance can be found in Paneque (2004) and Gaug (2006).

4.1.2 The read out system of *MAGIC I*

MAGIC I used 300 MHz FADC's to make a dense sampling of the time structure of the signal. To obtain a larger dynamic range the signal is split up into two identical signals. One of these signals is amplified by a factor of 10 (high gain signal) while the other is non amplified (low gain signal). The reason for this is to increase the dynamic range of the system which works with only 8 bits. The FADC samples both gain levels after each other and each is sampled by 16 time slices. Each time slice is an integration of 3.3 ns. The time

slice information is stored temporarily for $t = 100 \mu\text{s}$ in a ring buffer and saved to disc when a trigger signal arrives. More information about the 300 MHz FADC system can be found in Albert et al. (2008a).

Since the arrival time information can be exploited only if the time resolution is high enough, an upgrade of the read out system to multiplexed 10 bit 2 GHz FADC's (abbreviation MUX) was performed in April 2006. For commissioning and testing, only the trigger region was connected to the new MUX and, in addition, the old FADC readout was used in parallel. To do this the signal was split up before going to the trigger and one signal went to the old FADC, the other to the MUX. Each of the MUX channels samples the signals of 16 pixels by delaying the signal between the pixels by multiples of 40 ns. This leaves the MUX 40 ns to sample the signal of each pixel before switching to the next pixel. Each time slice has a width of only 0.5 ns giving a far superior time resolution compared to the previously used FADC's. Due to the larger dynamic range, when compared with the 300 MHz FADC's the splitting into high and low gain signals is not needed anymore, making the calibration easier. The advantage in the analysis of the MUX FADC's will be described in chapter 5 in detail. I contributed to the commissioning of the MUX, which took until April 2007. At this time, all pixels were changed to the MUX read out. More information about the MUX can be found in Goebel et al. (2007).

4.1.3 The trigger system of MAGIC I

The trigger area of the MAGIC I telescope is limited to the inner camera and has a diameter of about 0.9° . The trigger system of MAGIC I consists of two stages. The first stage, denoted level 0, is a discriminator which checks if the individual pixel signal amplitude is above a certain threshold. These discriminator thresholds (DT) are adjusted individually for each pixel by the individual pixel rate control (IPRC). The IPRC uses one DT set for each source depending on the background light level in the FoV of the source. Accidental triggers due to stars in the camera FoV can be evaded by this procedure. The IPRC is always active during the observation and thus the DT values for any given pixel vary with time and are not constant. For all signals above the DT, a square pulse of 6 ns width is produced and further evaluated by the level one trigger (L1). All pixels belonging to the trigger are grouped into 19 regions consisting of 36 pixels each (see Fig. 4.2). These regions are called macrocells and all pixel signals within one macrocell can be combined by a trigger logic. To generate a L1 trigger a number of n next neighbor (NN) pixels must be fired in coincidence in any macrocell. Currently, the 4 NN condition is used as a trigger. The L1 triggers the start of the readout process described in the previous section. The trigger energy threshold of MAGIC

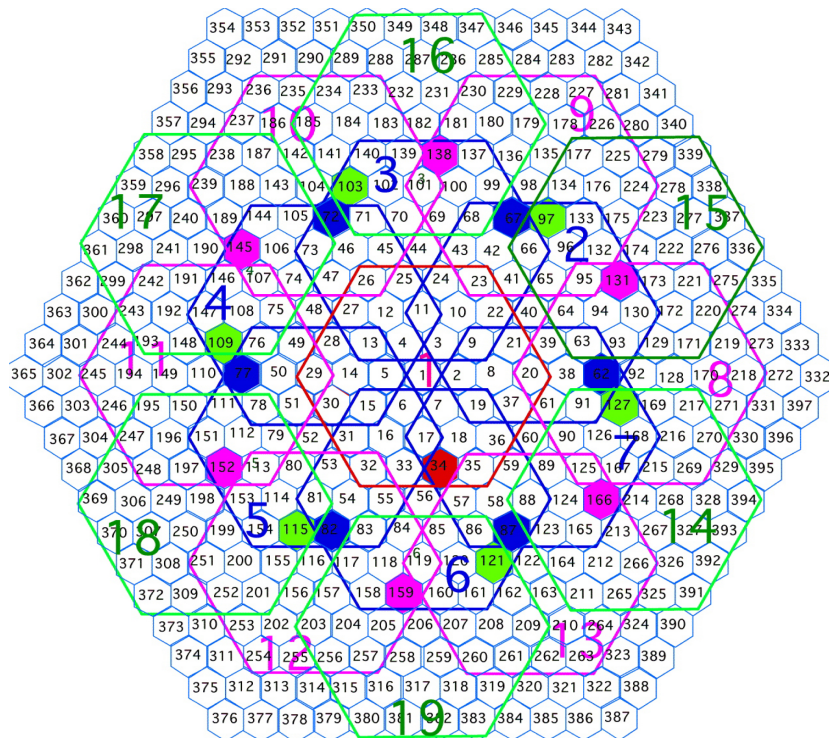


Figure 4.2: The 19 macrocells are forming the trigger region of the MAGIC I telescope. Not all small pixels in the inner camera are included in the trigger. The macrocells overlap to give a high trigger efficiency.

is about 55 GeV using the L1 trigger.

To further reduce the energy threshold by keeping the trigger rate below 1.3 kHz ¹, a new trigger scheme was implemented in late 2007, the so-called sum trigger. In this trigger, all signals of a closely packed number of 19 pixels (called a patch) is summed up and compared to an adjustable DT. To evade triggers caused by afterpulsing of PMT's, broken individual pixels or bright stars in the FoV, all signals are clipped at a level of six phe charge. This allows to keep the DT of the sum trigger low without generating huge trigger rates caused by accidental triggers. With the sum trigger, a lower energy trigger threshold of 25GeV can be achieved. The system is described in more detail in (Aliu et al., 2008b).

4.1.4 The calibration system of MAGIC I

The calibration system of MAGIC is schematically shown in Fig.4.3. There exist three distinct methods to calibrate the measured Analog to Digital Converter (ADC) counts to photons. The calibration light pulse is produced by 16 pulser boards equipped with identical LED's. 13 modules carry five LED's each while one board carries only one LED and two

¹This is the maximum rate the data acquisition (DAQ) can handle

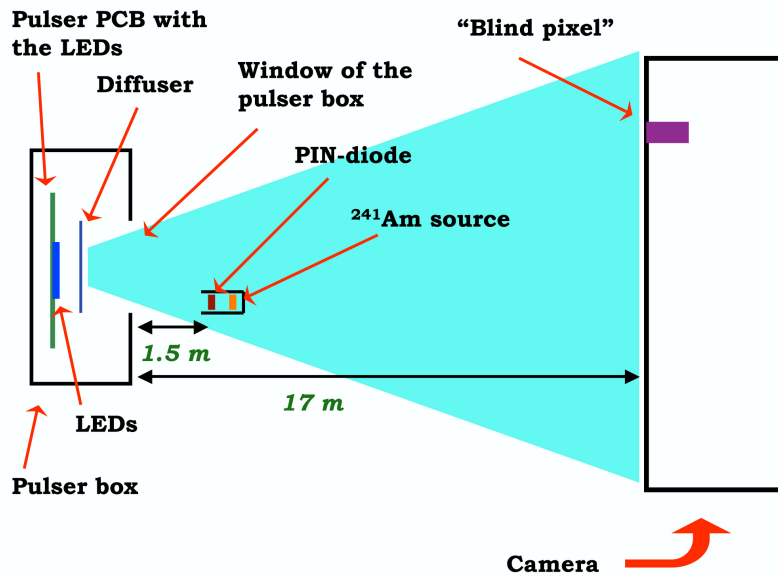


Figure 4.3: The schematic view of the MAGIC I calibration system setup.

other boards carry three LED's each. The LED's can emit light at three different wavelengths (370 nm, 460 nm, 520 nm). This enables the user to check wavelength depended calibration of each individual PMT. The calibration pulse duration is about 2–3 ns full width half maximum (FWHM).

Three different methods can be used to find the exact amount of light emitted by the calibration pulser box. The first is the positive intrinsic negative (PIN) diode method, where a calibrated PIN diode is used to measure the exact amount of photons which fall onto its entrance window. By counting the amount of photons one can easily calculate the photons per area at the camera. The PIN diode is cross calibrated with an ^{241}Am source, radiating 59.95 keV photons.

The second calibration method measures the light arriving at the camera plane directly by using a so-called blind pixel. The blind pixel is operated at a higher gain and has an entrance window (sensitive area) of exactly 1 cm^2 . Additionally, there is a calibrated attenuator which reduces the light amplitude by a factor of 1000. The attenuation makes it possible to measure single phe in the blind pixel, while the rest of the PMT's can be operated at nominal data taking parameters and still get enough light to produce large individual signals. Knowing the quantum efficiency (QE) of the blind pixel and the measured number of phe, one can easily calculate the photons per cm^2 at the camera plane and thus calibrate the signals in all pixels.

The last calibration method does not use any additional photon detector but instead uses the deviation from the poissonian statistics in the camera pixel signals. It is called the excess

noise factor method. The mean number of phe at the first dynode is given by:

$$\overline{m_{phe}} = F^2 \cdot \frac{(\overline{Q}) - \overline{P}}{\sigma_Q^2 - \sigma_P^2} \quad (4.1)$$

Here \overline{Q} denotes the mean charge and σ_Q the standard deviation of the distribution. While \overline{P} is the pedestal and σ_P the electronic noise. F is defined as:

$$F = \sqrt{1 + \left(\frac{\sigma_G}{\overline{G}}\right)^2} \quad (4.2)$$

\overline{G} is the gain of the PMT and σ_G its standard deviation. The F factor is measured by evaluating single photon electron spectra from each individual PMT. Knowing the F factor and measuring $\overline{m_{phe}}$, eq. 4.1 can be used to evaluate the mean charge.

4.2 MAGIC II

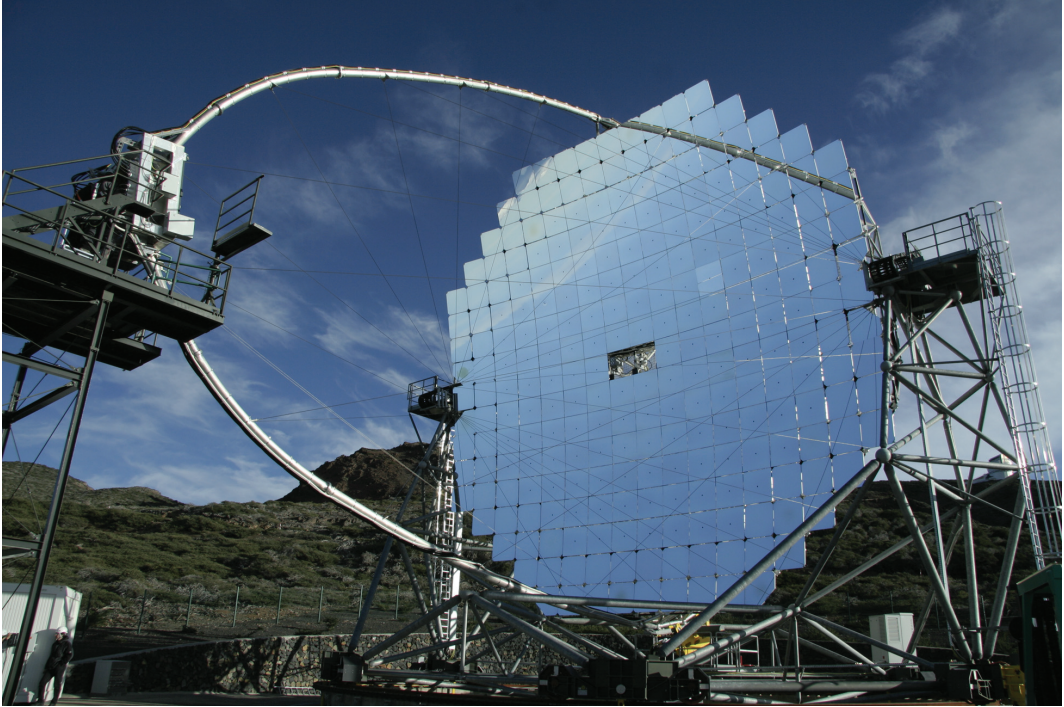


Figure 4.4: The MAGIC II telescope during installation of the optical fibres for the PMT signal transmission in December 2008. The two different mirror types used in the reflector can be identified by the black laser hole containing the AMC laser in the middle of the inner aluminium mirrors.

Many hardware improvements have been implemented in the MAGIC II telescope as compared to MAGIC I. Most of these changes were done to improve the sensitivity of the

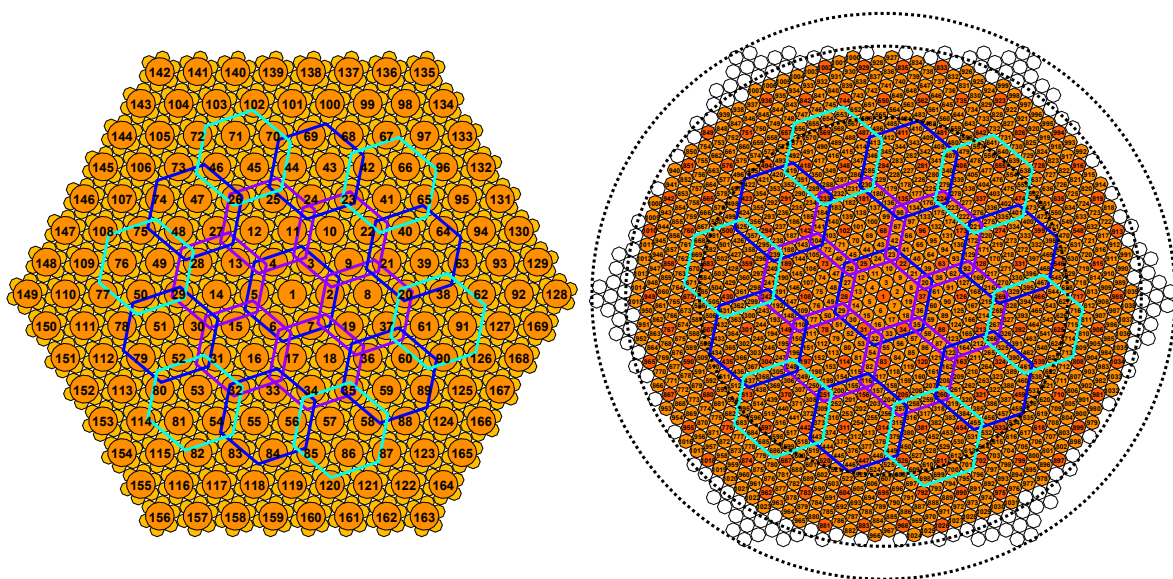


Figure 4.5: The left sketch shows the cluster arrangement in the MAGIC II camera and the right shows the single pixel configuration. If all clusters are completely equipped with pixels, the shape would be hexagonal. The current configuration leads to a more symmetric round shape.

telescope and make operation, upgrades and maintenance easier. Here, I will summarize the systems of MAGIC II, emphasizing the new camera design to which I contributed the control program and several tests of hardware components.

The basic structure was slightly modified to make the frame supporting the reflector stiffer. The first test showed a better tracking compared to the first telescope. In addition, the reflector (Bastieri et al., 2007) consists out of 240 1 m^2 quadratic mirrors each mounted on one moveable panel steered by the AMC. Two types of mirrors are used; while the inner reflector is composed out of aluminium milled mirrors with a honeycomb support structure like in MAGIC I, the outer mirrors are made of glass. The aluminium mirrors have a hole drilled in the middle to support the AMC laser needed to track the panel position. In the case of the glass mirrors, the lasers are mounted at the corner of the mirror. The optical performance of the mirrors should give a total PSF similar to the one of MAGIC I ($\sim 10\text{--}13 \text{ mm}$).

4.2.1 The camera of MAGIC II

A new camera has been designed for MAGIC II which is very different from the one in MAGIC I (see Fig 4.5). The only similar parameter is the FoV of 3.5° . The camera has a round shape and consists of 1039 PMT pixels of 25.4 mm diameter (the same as the small pixels in MAGIC I). The PMT's are Hamamatsu R1408 which provide a high peak QE of

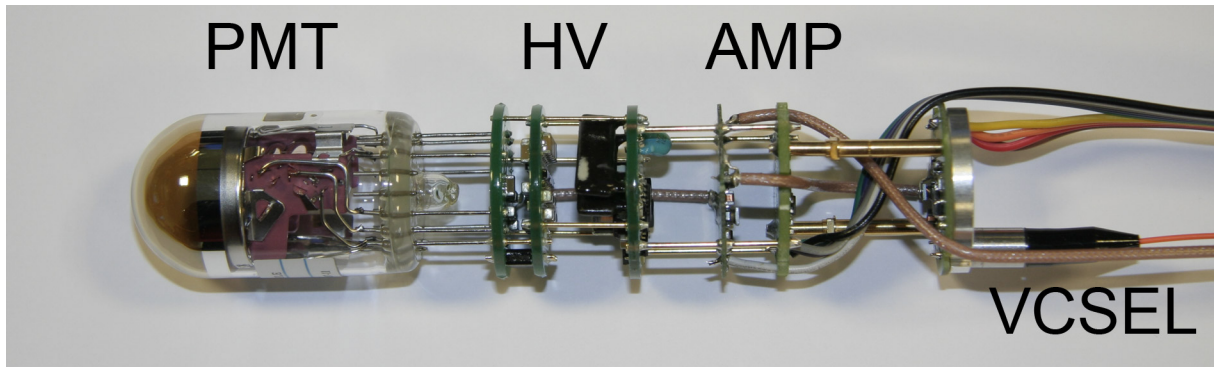


Figure 4.6: The Pixel design for MAGIC II. The PMT and the HV generator are manufactured at Hamamatsu and the Amplifier (AMP) and VCSEL are produced at the Max Planck Institute in Munich.

$\sim 32\%$. This should lead to an enhancement of the sensitivity over MAGIC I. Each pixel in MAGIC II consists of a hexagonal WC on top of the PMT, followed by the HV converter, the amplifier and the VCSEL. The assembly of a pixel is shown in Fig. 4.6. The camera was modular designed in the sense that seven pixels form together a so-called cluster. Clusters at the border of the camera may have less than seven pixels. In total 169 clusters are installed in the camera while six clusters are currently not equipped with any pixels.

Each cluster provides the slow control of all seven pixels and, in case of a failure, the complete cluster can be replaced by a spare one. This provides the advantage that normal operators can exchange the large and easy to handle clusters. Due to this simple exchange principle, the lost observation time during the repair should be minimal. Another advantage of this modular design is that clusters with other light sensors like the hybrid photo diodes (HPD) can be easily mounted in the camera without the need to change geometry or cables.

The steering and monitoring of the parameters of each of the seven pixels is done in one cluster. Each cluster possesses a Slow Control Cluster Processor (SCCP) which controls the readout and setting of all parameters of the seven pixels. Parameters which can be controlled are: HV setting, HV reading, VCSEL bias current setting, photo diode current reading, VCSEL temperature reading and the attenuation setting of the pixel pulse injector. In addition, each cluster can give information about the two chip temperatures of the ADC's and Digital to Analog Converters (DAC) on the SCCP. Each pixel possesses its own HV converter, VCSEL and pulse injector. The pulse injector is a new feature in the MAGIC II pixels. It can be used to inject charge pulses in the VCSEL without having HV present. This is an advantage since it makes tests of the read out chain during daylight possible without the waste of precious observation time.

Another feature of the camera is an improved cooling system. Since more pixels are



Figure 4.7: The front cooling plate with two out of 169 clusters installed. The second cooling plate can be seen through the holes of the front plate. The clusters have direct contact with the cooling plate through the rear plate behind the pixels and the SCCP and cable housing.

inside the MAGIC II camera a powerful cooling system had to be installed. To avoid space problems in the camera housing, the two cooling plates used to reduce the heat serve, in addition, as a support structure for the clusters. In Fig. 4.7 the front plate can be seen with some installed clusters. The cooling system keeps the camera at a stable temperature of 27°C during operation². The total power consumption of the camera is $\sim 1\text{ kW}$.

The camera is controlled via two versa module eurocards (VME) crates placed at the bottom and the top of the cooling plates inside the camera. Each VME crate has one interface card and four mainboards. Every mainboard has 22 connectors to which the clusters are connected and each VME crate is controlled by one peripheral component interconnect (PCI) card placed in a computer in the electronics room of the counting house (see Fig. 4.8). The VME interface cards in the camera and the PCI cards used are the SIS3100/1100 systems manufactured by the company *Struk Innovative Systeme*.

In addition, there are three SCCP's installed in the camera to control the power of the low voltage power supplies, for steering the lids and the star guider target of the camera, reading the humidity at four and the temperature at six different positions in the camera. They also control the intensity of the AMC LED's and the Starguider LED's. These SCCP's do not control any pixels and are connected to one of the mainboards of the VME crates.

²measured during commissioning in December 2008

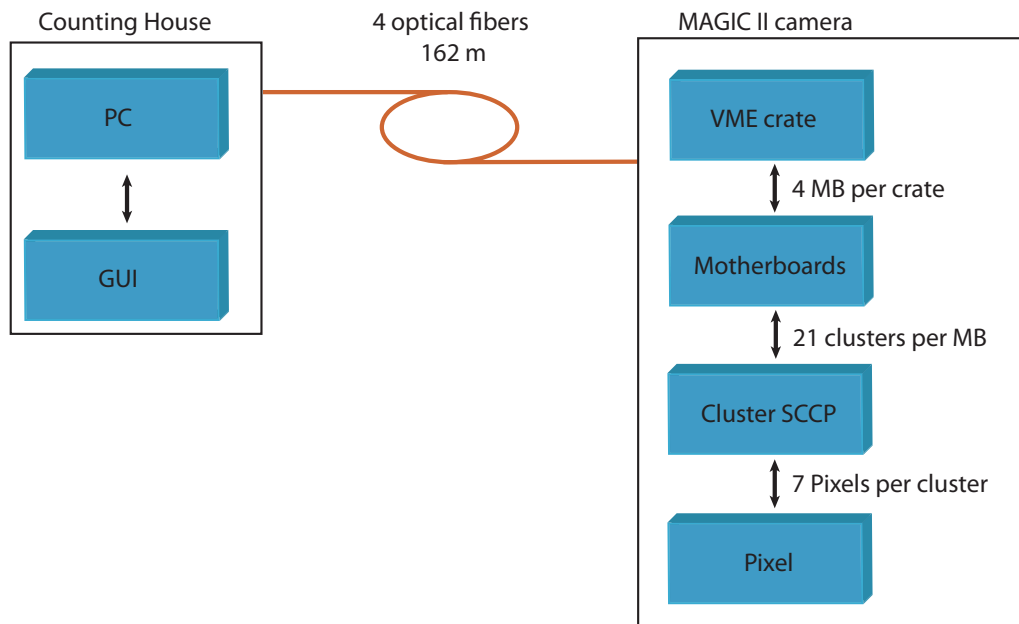


Figure 4.8: The communication schema of the camera. There are two PCI cards in the photo counting (PC), one for each VME crate in the camera. The Interface cards in the VME crate are SIS3100 and the PCI cards are SIS1100 manufactured by *Struk Innovative Systeme*.

They are steered by the same program as the cluster SCCP's.

4.2.2 The camera control program of MAGIC II

The control program of the camera (*caco*) is written in LabView and gives the user full control over all parameters of the camera. The main features are lid control, temperature and humidity monitoring, monitoring and controlling of the pixel and cluster settings, reading of environmental conditions and error handling. Since the communication and the hardware of MAGIC II are different from those used in MAGIC I, I wrote a completely new camera control program. One of the challenges was to make the control fast enough to be able to read out all parameters, especially the direct currents (DC), with a high enough rate to react fast enough to dangerous conditions, thereby preventing damage to the pixels or the clusters. The other challenge was to make the program flexible enough to react to special needs during the commissioning of the telescope. The program has a lot of different processes which run in parallel. These processes are:

- The graphical user interface (GUI)
- Menu control (user control)
- Graphical display of all parameters

- Reading routine for all pixel and cluster parameters
- Report generation for central control
- Communication with the central control program
- Control routine of processes communicating with the camera
- Control routine for pixel and cluster parameters
- Control routine for camera operation parameters
- Control of weather conditions
- Subsystem status check routine
- Hot pixel control routine
- Internal logbook of all parameters and errors
- Error handling

Many of these tasks interact with each other and a schematic overview of the program is given in Fig. 4.9. The **central variables** in Fig. 4.9 are the information storage of the camera control program. They store all vital information about the camera status, like the individual pixel HV, VCSEL temperature, VCSEL bias current, DC, attenuator setting, SCCP chip temperature, AMC Led intensity, star guider LED intensity, temperatures and humidities for the camera and low voltage power supply boxes. As can be seen from Fig. 4.9, almost all tasks either collect information and write it to the central variables or they take information from the central variables and use it, i.e. for displaying a camera parameter to the user or in order to check if the parameter is within the operation limits.

The general communication between the camera SCCP's and the caco program works as follows. A command is sent to the SCCP and the SCCP executes it, then an answer is sent to the caco program by the SCCP. The SCCP can only execute one command at a time therefore the caco program has to wait for the answer until it can send a new command to the SCCP. To avoid command and answer confusion when communicating with the SCCP, the caco **comm control routine** (see Fig. 4.9) stops all read processes which would access the same SCCP(s) until the answer of the SCCP has arrived. To illustrate this the setting of the HV of all pixels is described. First the **read loop cluster parameters** is stopped by the **comm control routine**, not to interfere with the HV setting process. Then, in parallel, all first pixels in each SCCP are set to their HV values. As soon as the answer

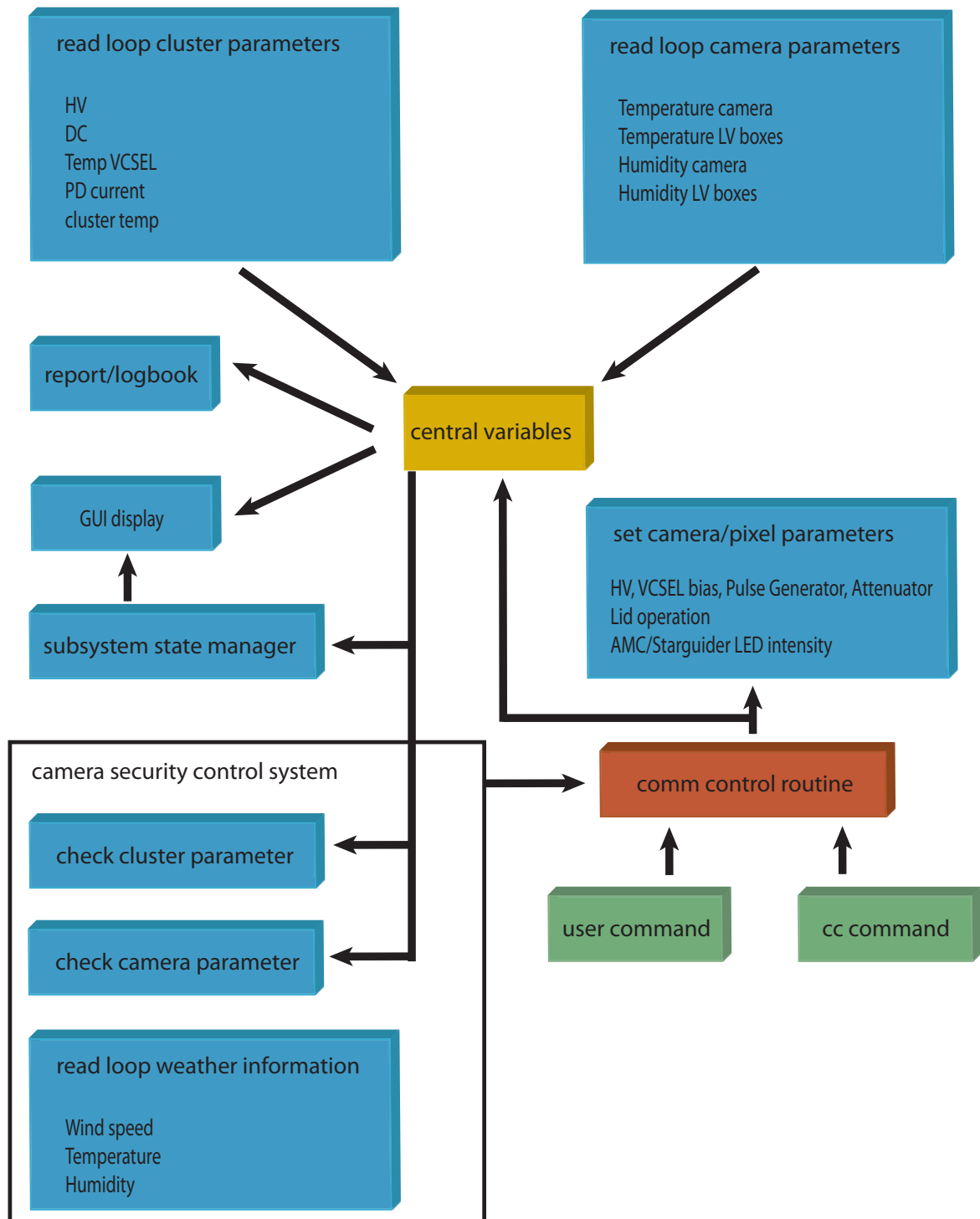


Figure 4.9: The basic working principle of the caco of MAGIC II. The arrows indicate the transfer direction of information between the individual routines. The comm control routine is the only routine which executes the setting of any parameter in the camera and thus assures that there is no conflict between the different processes.

that the command is executed by all SCCP's has arrived, the next pixel HV value is set in all SCCP's. This process is iterated until all pixels in all clusters are set. Afterwards the `comm control` routine starts the `read loop cluster parameters`. All interactions with the camera's SCCP are only possible via the `comm control` routine in order to guarantee that no conflict between processes accessing the camera parameters can occur.

Another very important part of the `caco` program are the security routines. These routines check the various camera and pixel parameters such as the DC, the VCSEL temperatures, the camera temperature and humidity, and the weather conditions. The parameters are then compared to the user provided security limits and appropriate actions taken, which are then communicated via the `comm control` routine to the camera and reported by an alert in the GUI to the user. Often more than one security interval of individual parameters are defined to be able to react according to the severity of the problem.

The `caco` program can either be used manually by a user or can be controlled by the central control program (Zanin et al., 2009) which runs in normal operation mode on both MAGIC telescopes.

4.2.3 The read out system of MAGIC II

The read out system is a 2 GHz ring sampler called Domino II. While the principle is different from the MUX, the system should provide the same time resolution at a lower cost per channel compared to the MUX system of MAGIC I. This is important since MAGIC II has 473 channels more than MAGIC I. An additional advantage is the lower power consumption which results in less heat. The system is currently in the commissioning stage and the first shower events were sampled and read out by the data acquisition (DAQ) in December 2008. The full system was installed in January 2009 and will be commissioned until autumn 2009. More information about the read out of MAGIC II can be found in Tescaro et al. (2009).

4.2.4 The trigger system of MAGIC II

The trigger system of MAGIC II is a slightly modified version of the MAGIC I trigger. Again, a 4 NN coincidence in any macrocell will yield a trigger by the L1 system. One change is the distribution of the macrocells which was necessary to increase the trigger area in the camera of MAGIC II (see Fig. 4.5). The increase of the trigger area by a factor of ~ 2 will increase the effective area in which showers can trigger the telescope and thus should yield a higher sensitivity compared to MAGIC I. An improvement in sensitivity compared to MAGIC I is possible, especially in the case of wobble mode observations where the source is tracked off axis from the camera center and for extended sources.

4.2.5 The calibration system of MAGIC II

In MAGIC II the calibration will be performed by the F-factor method and thus there is neither a PIN diode nor a blind pixel. The calibration light will be emitted by a phase locked Nd-YAG laser operated at the third harmonic ($\lambda = 355$ nm) and producing pulses of 700 ps FWHM duration. The intensity can be regulated by two consecutively mounted filter wheels which have four identical filters each. Due to the 16 combination of the filters, a wide range of intensities from 1–1000 phe in each pixel can be covered: This enables the precise monitoring of the linearity of the complete signal chain. To guarantee a homogenous illumination of the camera, an integrating sphere (Ulbricht sphere) is used to diffuse the laser light before sending it to the camera of the telescope. In the future there is a plan to upgrade the MAGIC I calibration system to that of MAGIC II.

Chapter 5

The data analysis

In this chapter, I shall describe the methods and procedures I used for the analysis of the MAGIC telescope data in detail. This will provide the reader with a solid knowledge about the analysis steps performed for this thesis. The chapter is organized as follows: First the MAGIC analysis is described, then the systematic uncertainties of the measured quantities are discussed followed by the explanation of the X-ray analysis carried out in this thesis and finally a description is given of the test for periodic structures in unevenly sampled data sets, as applied to the data investigated in this thesis.

5.1 The MAGIC data analysis

The analysis of IACT data relies mostly on MC simulations which describe the shower development, together with its Cherenkov light production and the detector response. Since it is not possible to calibrate the atmosphere (used by the IACT as the calorimeter), we have larger systematic uncertainties than the high energy physics experiments in accelerators. Nevertheless, we are able to monitor the performance of our telescope and can determine the effect of these uncertainties. Thus IACT measurements can provide meaningful input to the theoretical predictions - and even test for time structures like periodicity from long term data monitoring, as shown in this thesis.

Since a lot of technical terms related to the IACT analysis will be used in this chapter, some definitions are given here. In general, each trigger of the telescope generates an event, this event consisting first of a camera image which is then processed by various tasks to obtain the primary particle parameters which are then further analyzed to obtain, at the end, the high level products. By “high level products” I understand physical quantities of the gamma-ray source, such as the temporal sampled integral gamma-ray fluxes (light curve or LC), the differential energy spectrum (spectrum) of the gamma-ray emission and the

reconstructed positions of the source in the sky (skymaps). These high level products are the results of the analysis that are interesting for the physics interpretation. The scheme in Fig. 5.1 will help to understand the various names and steps used to obtain these high level products. In this scheme, the various steps of the low level data analysis are shown and the corresponding names of the products obtained by following the steps.

5.1.1 From FADC counts to shower image parameters

After recording the raw data by the DAQ system, the data has to be calibrated. To extract the signal pulses from the recorded FADC time slices, three different extraction methods can be used: Namely the digital filter, the sliding window, and the spline method. These methods show slightly different performances depending on the data and the requirements such as speed and precision of timing information of the analysis. Every extraction method is useful and the preferred method was changed more than once in the time the data presented in this thesis was taken. A comparison of the different extraction method performances is given in Albert et al. (2008a) showing that the major difference among them is the robustness of the methods depending on the stability of the telescope operating parameters - for example, if the time delays of the signals from the individual pixels are precisely adjusted so that the whole signal pulses are in the FADC time slices for all pixels.

After the signal extraction, the calibration is performed by evaluating the conversion factor between the FADC counts and photoelectrons (phe) using the calibration constants for each individual pixel. To obtain the calibration constants, a calibration run is carried out before each source observation and interleaf calibration events are taken with a rate of 25 Hz to monitor any changes during data-taking. The details of the calibration routine can be found in Gaug (2006).

The calibrated data still consists of the full information (all pixels) which is present in the camera. To obtain an image of only the shower, a procedure called “image cleaning” is performed. The name can be taken literally because all pixels which do not belong to the shower image are set to zero. The pixels belonging to the shower are identified by two different procedures depending whether the data was sampled by the 300 MHz FADC’s or by the MUX (for the definition see section 4.1.2). In the former case, the arrival time of the pixel signal is ignored and only its charge in phe is taken into account. Each pixel containing more than 10 phe is called a core pixel and thought to belong to the shower image. In addition, each pixel which has at least 5 phe and a border to at least one core pixel is called a boundary pixel and taken to be a shower pixel as well. This image cleaning is called a 10/5 image cleaning because of the values chosen for the core/boundary pixel thresholds.

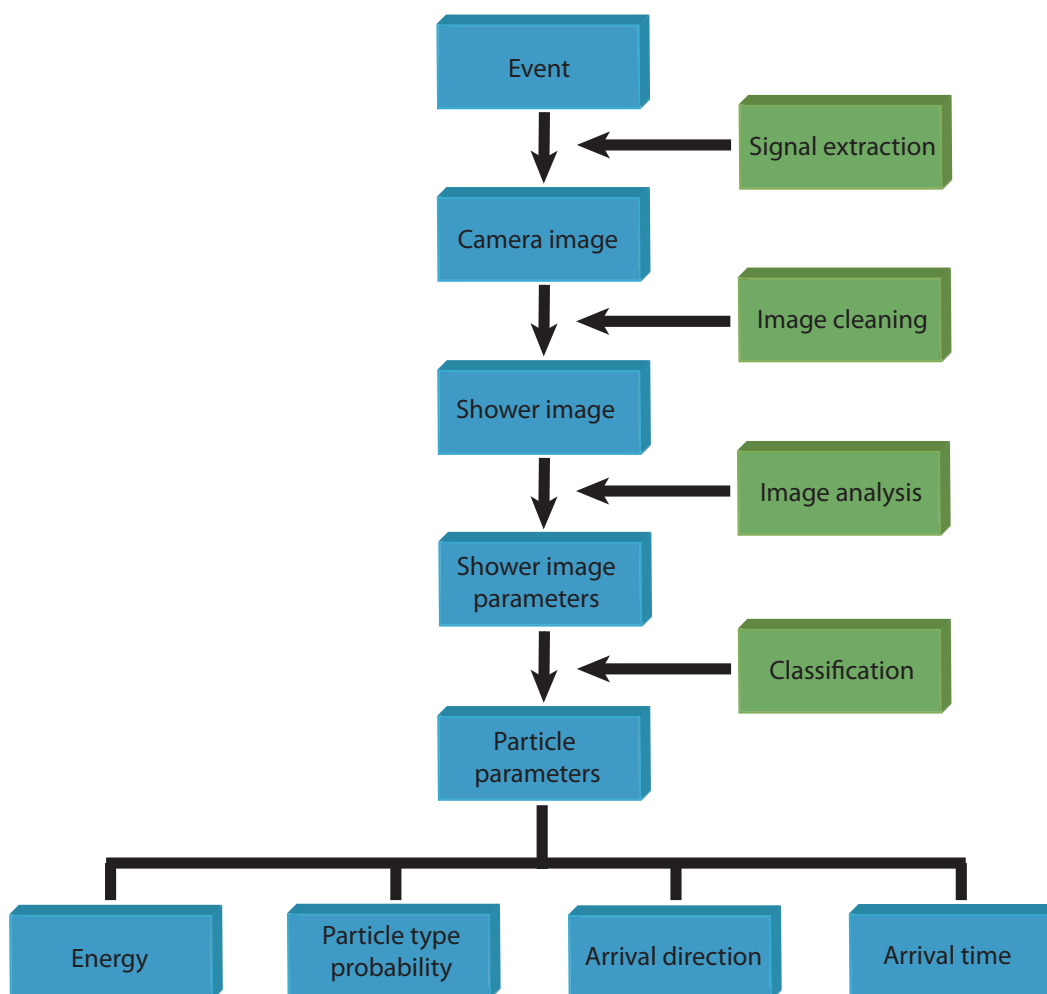


Figure 5.1: The numerous steps from the raw data to the primary particle parameters are shown. The blue boxes represent the names of the products obtained by the processes represented by the green boxes. The processes are explained in the next sections and the names of the products will be used frequently. The primary particle parameters are used for the signal selection and to generate the high level products.

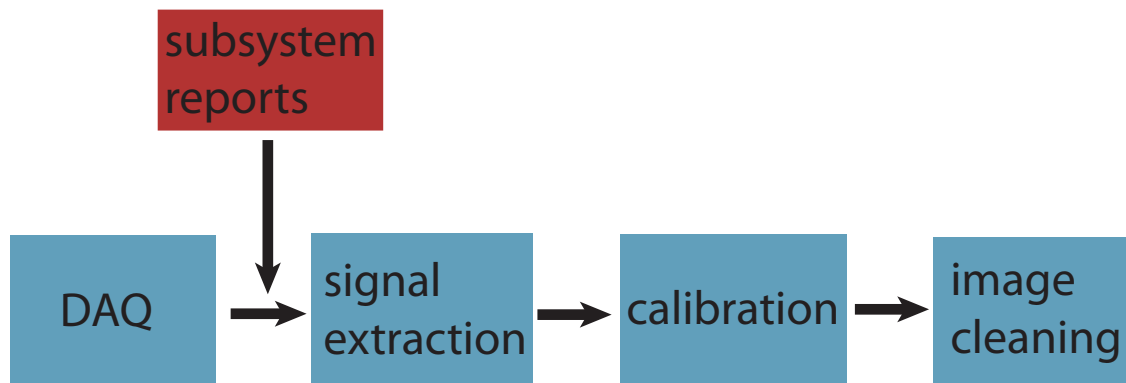


Figure 5.2: The principle data processing pipeline in a schematic view. After data acquisition, the sub-system information like the pyrometer, starguider and weatherstation data is merged into the raw data. Afterwards, the signal is extracted from the FADC time slices and then calibrated. Finally, the image is cleaned and image parameters are calculated.

The advantage of the 10/5 image cleaning is that it is more robust during slightly different background light conditions compared to the 7/5 which had been used for some time. In this thesis, all data analyzed from the era of the 300 MHz FADC's was processed with the 10/5 image cleaning.

For data recorded by the MUX, the arrival time of the individual pixels and their location in the camera is used to find an additional criteria for discriminating between pixels belonging to the shower image and pixels containing only high fluctuations of background light from the night sky. The high time resolution of the MUX read-out enables the exploitation of the fact that the shower information arrives in a short time interval, while the background light is uniformly distributed in time. This type of cleaning is called “time image cleaning” and works as follows: First, the same image cleaning technique used on the 300 MHz FADC's is performed with lower thresholds of 6/3 which lead to more pixels surviving the cleaning compared to the 10/5 non-time cleaning; then the mean of all arrival times of the core pixels (called the “shower core arrival time”) is calculated; the arrival time of each individual pixel is defined as the time of the rising edge of the pulse at 50% of the maximum intensity; each pixel signal's arrival time should only deviate by a maximum of 4.5 ns from the shower core arrival time; furthermore, the time difference in the arrival times between adjacent pixels should not exceed 1.5 ns. Consequently, the pixels not displaying the expected time characteristic of the shower information are removed and, thus, less pixels survive the time image cleaning compared to the simple 6/3 non-time image cleaning. But more information about the shower can be saved with the 6/3 time image cleaning as compared to the 10/5 non-time cleaning. This leads to a more precise shower parameter reconstruction, especially

for lower energetic air shower images - as can be seen in Fig. 5.3. A detailed comparison between the different image cleaning techniques can be found in Aliu et al. (2009a).

After the image cleaning, the shower parameters (known as Hillas parameters (Hillas, 1985)) width (W), length (L), distance (D), alpha (α) and size (S) are calculated, along with some additional parameters characterizing the charge distribution in the image. These additional parameters are denoted as density (ρ), third moment (M_3), concentration (p_{conc}) and the additional timing parameters - time gradient (t_{grad}) and time RMS (t_{rms}) which characterize the time evolution of the shower¹.

The Hillas parameters are a special representation of the second moments. The matrix of the second moments is simply diagonalized by rotating the image by an angle θ which is then chosen to result in zero entries for off-diagonal elements.

The moments of the image are given by:

$$\bar{x} = \frac{\sum_i q_i \cdot x_i}{\sum_i q_i} \quad (5.1)$$

$$\bar{y} = \frac{\sum_i q_i \cdot y_i}{\sum_i q_i} \quad (5.2)$$

$$\overline{x^2} = \frac{\sum_i q_i \cdot x_i^2}{\sum_i q_i} \quad (5.3)$$

$$\overline{y^2} = \frac{\sum_i q_i \cdot y_i^2}{\sum_i q_i} \quad (5.4)$$

$$\overline{xy} = \frac{\sum_i q_i \cdot x_i \cdot y_i}{\sum_i q_i} \quad (5.5)$$

In these equations, the sum runs over all the individual pixels and q_i , x_i , y_i denote the charge and the center position of pixel i . The first moments are simply the center of gravity (COG) of the image. The second moments are correlated and the correlation is given by the following equations:

$$\sigma_x^2 = \overline{(x - \bar{x})^2} = \overline{x^2} - \bar{x}^2 \quad (5.6)$$

$$\sigma_y^2 = \overline{(y - \bar{y})^2} = \overline{y^2} - \bar{y}^2 \quad (5.7)$$

$$\sigma_{xy} = \overline{(x - \bar{x})(y - \bar{y})} = \overline{xy} - \bar{x} \cdot \bar{y} \quad (5.8)$$

With these equations, the 2-dimensional correlation matrix² can be written as:

$$C_{\text{cor}} = \begin{pmatrix} \sigma_x^2 & \sigma_{xy} \\ \sigma_{xy} & \sigma_y^2 \end{pmatrix} \quad (5.9)$$

¹The time parameters are only used with the MUX read-out and not with the 300 MHz FADC's data

²This matrix is called covariance matrix too

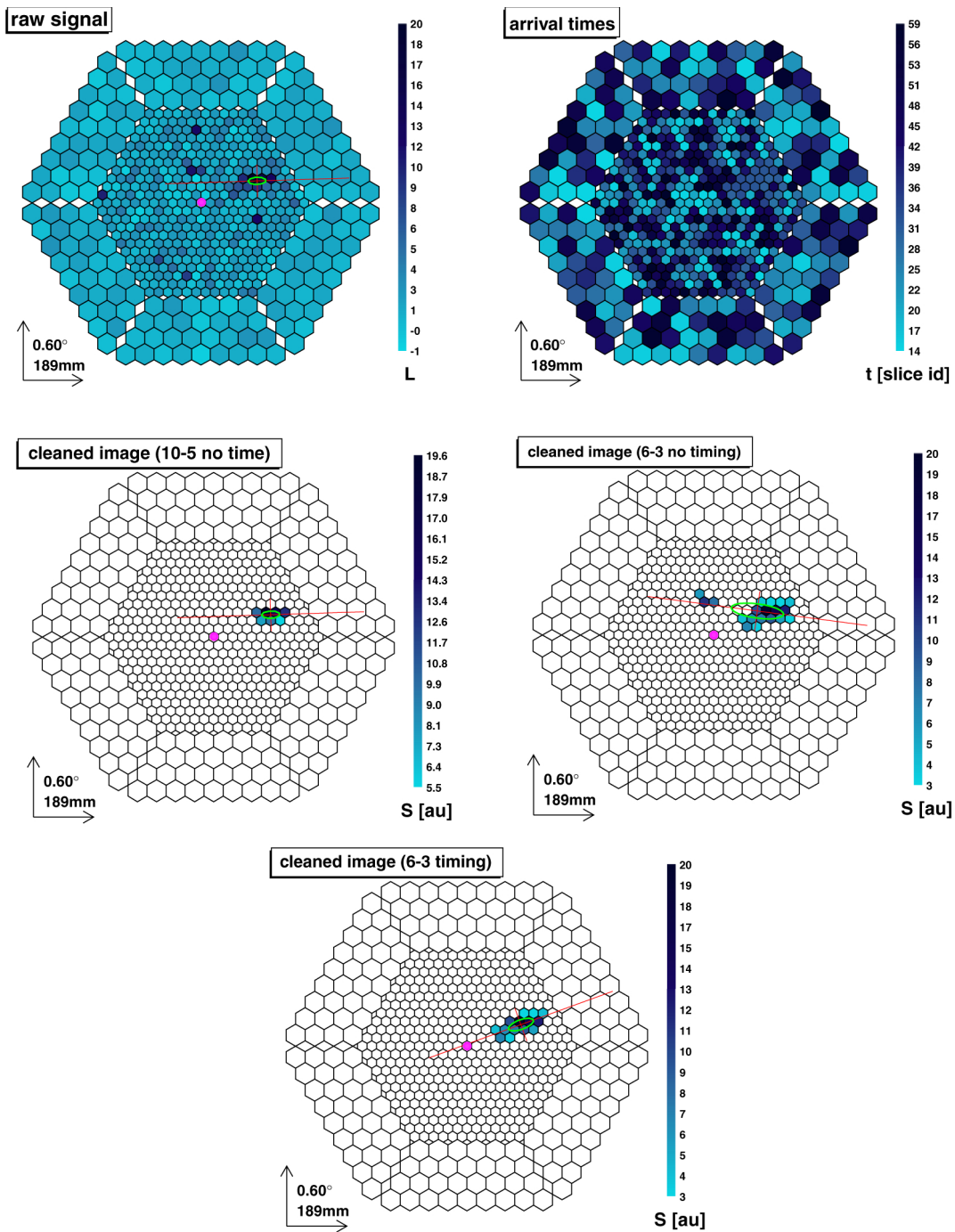


Figure 5.3: Illustration of the improvement of the shower parameter reconstruction using the time image cleaning compared to standard non-time image cleaning and a lower threshold non-time image cleaning. The shower image is taken from a MC simulation of a gamma-ray of $E = 71$ GeV and an impact parameter of 111 m. The magenta point marks the source of the gamma-rays, the ellipse shows the Hillas parameters and the red line shows the reconstructed shower arrival direction. The time cleaning shown in the lowermost panel reconstructs the arrival direction correctly because of the use of all the shower information. The 10/5 non time cleaning loses information and thus the reconstruction is much less accurate. Lowering the non-time image cleaning thresholds can lead to pollution by background noise to the shower image which can result in completely wrong image parameters. The figure is taken from Aliu et al. (2009a).

The correlation matrix describes the shower in the camera frame. By demanding $\sigma_{xy} = 0$, it is diagonalized and this leads to a relation between the rotating angle θ and the correlation parameters in the following way:

$$\tan(2\theta) = 2 \frac{\sigma_{xy}}{\sqrt{\sigma_x^2 - \sigma_y^2}} \quad (5.10)$$

To give a short formula, the following shortcuts are used:

$$d = \sigma_y^2 - \sigma_x^2 \quad (5.11)$$

$$z = \sqrt{d^2 + 4 \cdot \sigma_{xy}} \quad (5.12)$$

$$u = 1 + \frac{d}{z} \quad (5.13)$$

$$v = 2 - u \quad (5.14)$$

The following formulas are used to calculate the Hillas parameters from the variances.

$$L = \sqrt{\frac{\sigma_x^2 + \sigma_y^2 + z}{2}} \quad (5.15)$$

$$W = \sqrt{\frac{\sigma_x^2 + \sigma_y^2 - z}{2}} \quad (5.16)$$

$$D = \sqrt{\bar{x}^2 + \bar{y}^2} \quad (5.17)$$

$$a = \sqrt{\frac{1}{2} (u \cdot \bar{x}^2 + v \cdot \bar{y}^2) - \frac{2\sigma_{xy} \cdot \bar{x} \cdot \bar{y}}{z}} \quad (5.18)$$

$$\alpha = \arcsin\left(\frac{a}{D}\right) \quad (5.19)$$

$$\rho = \frac{\sum_i q_i}{\pi W \times L} \quad (5.20)$$

The concentration p_{conc} is the charge in the two highest charged pixels divided by the total charge of the shower image and the third moment (M_3) is the deviation of the COG of the shower charge distribution on its main axis compared to the geometrical mean. The geometrical interpretation for the most important parameters is schematically shown in Fig. 5.4.

The t_{grad} measures how fast the arrival times change on the major axis of the shower image. The parameter is obtained as follows: all shower image pixel coordinates are projected onto the major axis and then the arrival times of these points are fitted by a straight line $t = m \times x + b$ and $t_{\text{grad}} = m$. The t_{rms} is the root mean square of the arrival times of all shower image pixels left after the image cleaning.

The shower image is well characterized by all these parameters and all the other information is no longer used in the analysis. The next steps in the analysis are the identification of

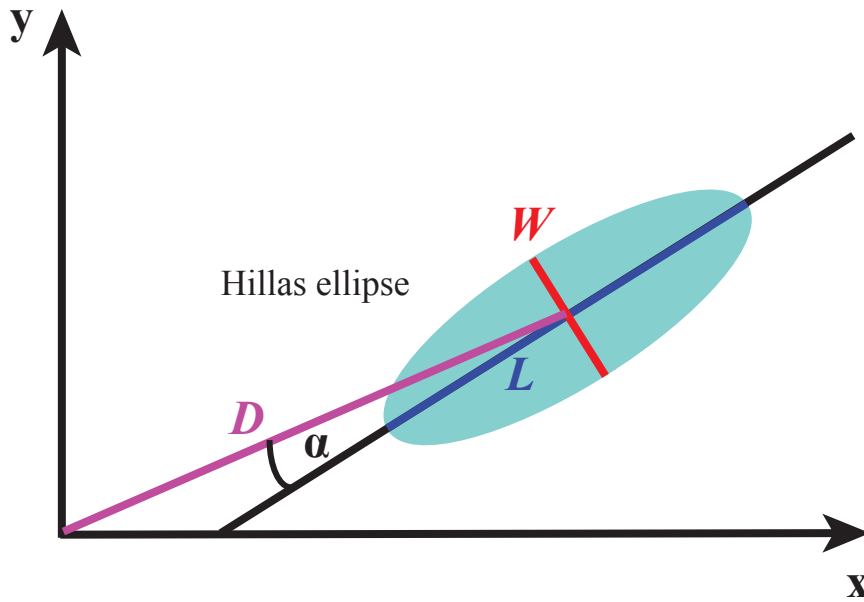


Figure 5.4: Here, the Hillas parameters are shown schematically. The cyan ellipse illustrates the Hillas ellipse with the major axis as the parameter L and the minor axis as W . The angular distance from the showers COG to the center of the camera is the parameter D and α is the angle between the L -axis and the D -axis.

the gamma-ray induced shower images, the reconstruction of their energy and their arrival direction. These particle parameters are the basis to produce high level products like spectra, skymaps, light curves and to obtain the detection significance.

5.1.2 The shower image parameters and their correlation

The shower image parameters defined in the previous section are the basis for the evaluation of the shower parameters. For example, the shower image parameters are used to identify gamma-ray induced shower images and for the energy reconstruction of these showers. The prime energy estimator is the parameter S but using only S would not result in the best energy resolution because S is correlated with the D parameter and, since D is so strongly correlated with the impact parameter of the shower (if it is a gamma-ray event), it has an influence on the amount of light hitting the camera from the Cherenkov light pool. Another vital parameter is the zenith angle of the observations. The zenith angle is the angle between zenith-axis and the pointing direction axis of the telescope. The higher the zenith angle of any observation is, the closer to the horizon points the telescope. This causes the Cherenkov light to transverse more atmosphere compared to lower zenith angle observations. This implies that the Cherenkov light suffers stronger absorption and scattering compared to small zenith

angle observations. In addition the Cherenkov light pool spreads out over a larger area at the reflector plane of the telescope. All this leads to zenith angle dependent shower image parameter distributions. In the analysis only shower images in a zenith angle range where the deviation in the image parameters is small are analyzed with the same process. Later the individual data sets are combined to obtain the high level product.

The most important correlations of the image parameters are shown in Fig. 5.5 and Fig. 5.6.

These correlations are very important since they play a major role during gamma/hadron separation and energy estimation. Since the shower image parameters will be used to classify gamma-ray induced events, it is interesting to investigate the image parameter distribution for gamma-ray and hadron induced events. This is done in Fig. 5.5, which shows that there is not a small range in each image parameter which defines a gamma-ray induced event but rather a broad region. This region in each parameter can be reduced if the parameter is analyzed in a bin of the other parameters, thus yielding a better separation between the shower types. This leads to complicated cuts in the individual shower image parameters to perform the gamma/hadron separation but this can be effectively achieved using multidimensional classification tools like the Random Forest method, as described in the following section.

5.1.3 Gamma/hadron separation

Gamma/hadron separation is very important since the rate of cosmic rays is much higher in the VHE domain than in the gamma-ray flux of the strongest steady source. The first discrimination between both particle events is performed at the hardware level, the trigger is optimized for accepting gamma-rays and, due to the difference of the hadronic induced cascades, the trigger is less efficient for this type of shower. The average rate after image cleaning at zenith angles below 30° is around 110 Hz, while the average gamma-ray rate of the Crab Nebula is about 0.1 Hz. This means that a further suppression by a factor of 1000 is needed to make significant detections.

To achieve such a good background suppression, the image parameters and time parameters of the shower image are exploited with a Random Forest (RF) method (see Albert et al. 2008b and references therein). The RF method is a multidimensional classification tool which uses the image parameters to define a parameter called “hadronness”, denoting the probability that an event is produced by a hadronic induced cascade.

The procedure works as follows. First, the RF must be created and this process is called the “training”. In the training, a decision map is generated which is later used to calculate the hadronness for each individual event. The decision map is called a “tree” because it is

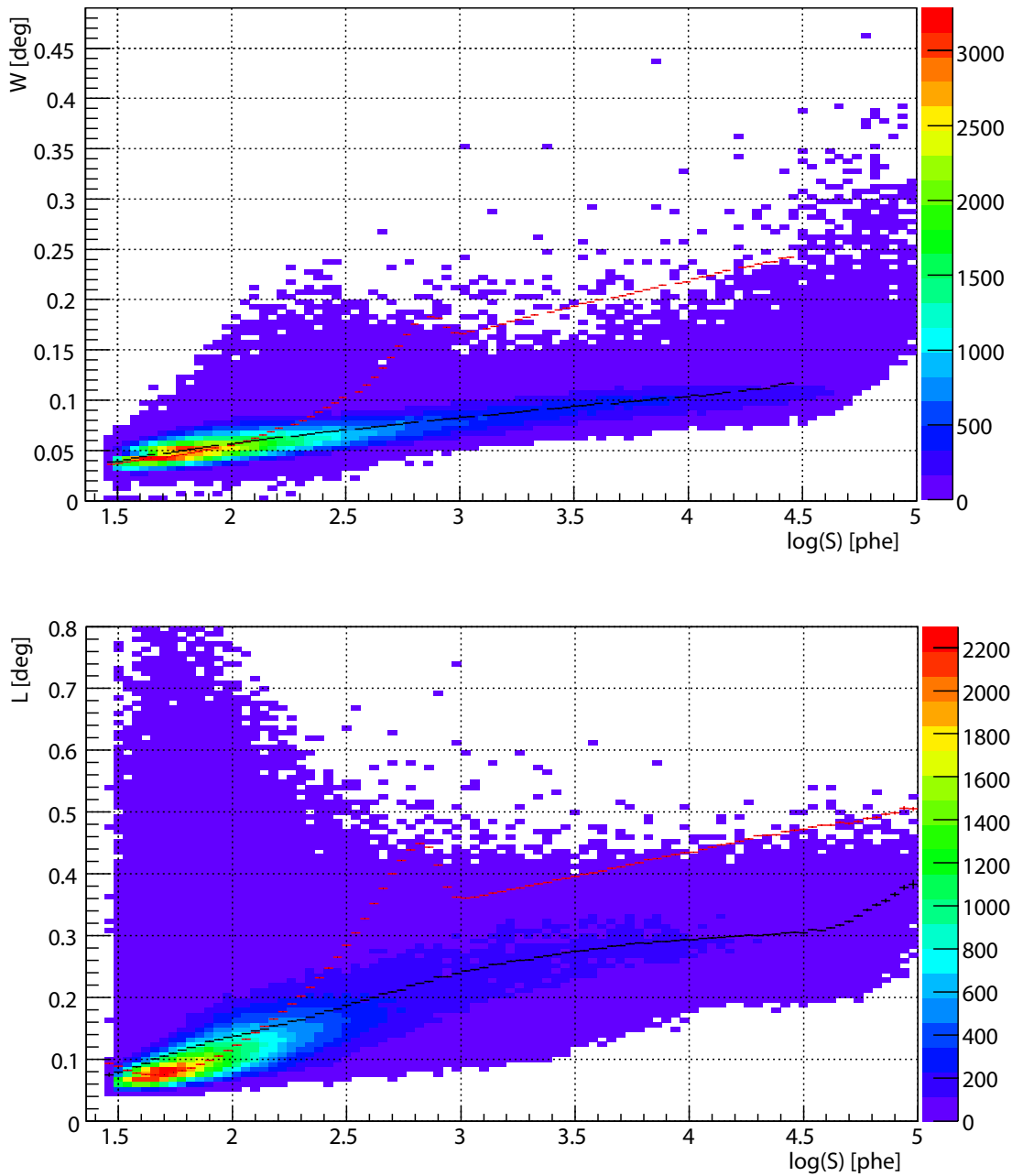


Figure 5.5: The upper panel displays the parameter W vs $\log(S)$ for simulated MC gamma-ray events. The black points show the mean W of the MC gamma-ray events while the red points show the mean W for real data (mainly protons) taken under the same zenith angle range as the gamma-rays. The distance between the means of the two distributions indicates the separation power. The complete overlap below $S = 100$ phe shows that there is no separation possible with this parameter. The lower panel shows the same distributions for the parameter L vs. $\log(S)$.

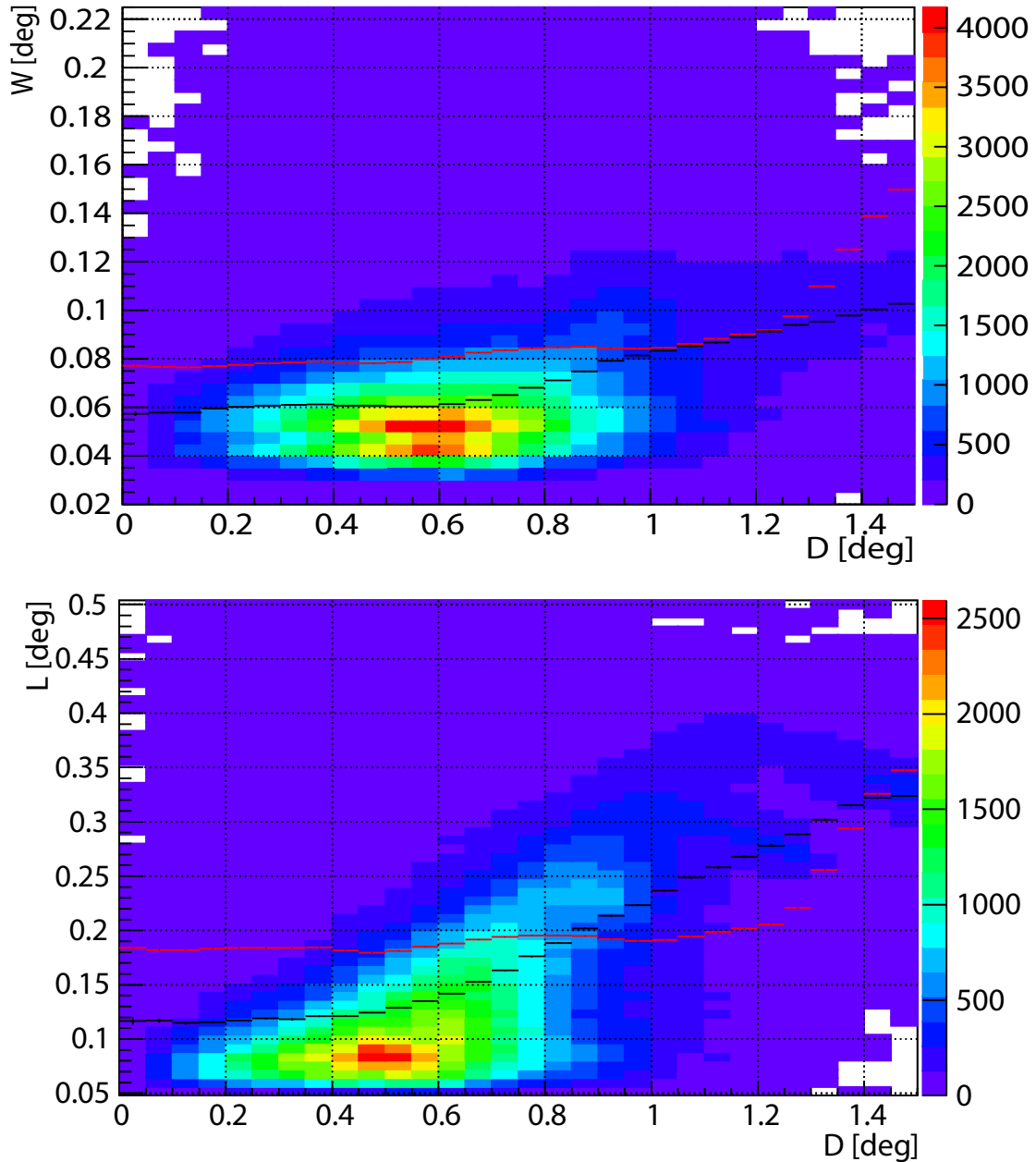


Figure 5.6: The upper panel displays the parameter W vs D for simulated MC gamma-ray events. The black points show the mean W of the MC gamma-ray events while the red points show the mean W , together with the spread of the distribution for real data (mainly protons) taken under the same zenith angle range. The lower plot shows the same for L . The distance between the means of the two distributions indicates the separation power. The hadron events do not show a correlation between W or L and D in contrast to the gamma-ray events. The rise of W and L for $D > 1.2^\circ$ is due to the finite camera size and the trigger area which fills only the inner camera ($\varnothing \sim 1^\circ$). Only very high energetic showers can trigger the system and have a COG at the border of the camera.

based on a tree's structure. For the training procedure, a set of gamma-ray shower images and hadronic background events is needed. The set of gamma-ray events is obtained from an MC simulation (for details, see section 5.1.9 about MC) and, for the hadron event, real data (from the sample to be analyzed) are taken. The real data contain almost only proton events and possibly a small contamination of gamma-ray events which do not affect the training procedure, as shown in Albert et al. (2008b). To guarantee an artifact-free training, the hadron sample for training is selected as a subsample from the real data, so that the same total charge (S) distribution and zenith angle range of the shower images are given for the MC gamma-ray and the hadron event samples. This is required to avoid S being used as a cut parameter which would result in comparing shower image parameters of events with different energies. If the S distribution is the same for hadron and gamma-ray induced events, then S is effectively used as a binning parameter. The same procedure is applied for the zenith angle in the recent analysis software. The final sample of gamma-ray and proton events are called "training samples".

In the training procedure, a set of image and timing parameters is given by the analyzer, together with the training samples. All events of both training samples start in the same starting node. Then, three of the event parameters are drawn randomly and among them the best parameter for separation of both particle types is chosen. This selection of the parameter and its split-up value is determined by the minimization of the Gini-index (Gini, 1921). The Gini-index Q_{Gini} can be expressed in terms of the node class population N_γ and N_H , as well as the total node population N .

$$Q_{Gini} = 4 \cdot \frac{N_\gamma}{N} \cdot \frac{N_H}{N} = 4 \cdot \frac{N_\gamma \cdot (N - N_\gamma)}{N^2} \in [0, 1] \quad (5.21)$$

By minimizing equation (5.21), the variance of the population of gamma and hadron induced events in the node is minimized, yielding a purification of the type of events in the node. This is called the "split-up procedure" because it calculates the split-up value and all events of the training samples will either go to the left node or right node, depending on whether their split-up parameter value is higher or smaller compared to the previously determined split-up value. In each node, the split-up procedure takes place again and this process is iterated until one of the following criteria is fulfilled: If the maximum number of allowed split-ups by the user has occurred; or if the minimum number of events in one node has been reached. The split-up procedure then stops in this node which becomes a termination node. A schematic view of the procedure of the RF is shown in Fig. 5.7. Typically 100 trees are grown in each RF and each event is classified by each tree. Consequently, the event ends in 100 different termination nodes (in each tree in one node) and has 100 different hadronness

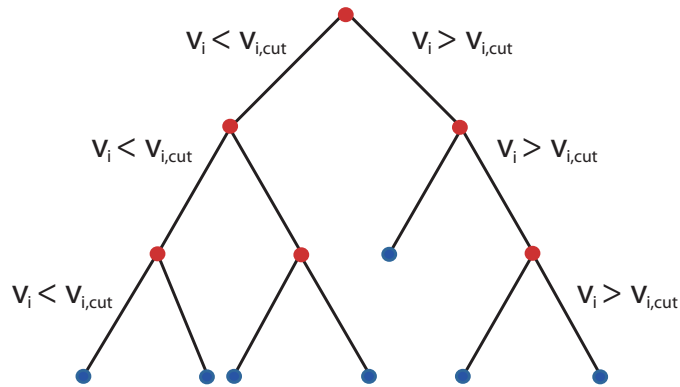


Figure 5.7: The working principle of the random forest is illustrated. The shower image parameters are given as a vector (\mathbf{v}) to the RF which select one parameter (v_i) and compares its value to the cut value in this image parameter. Depending on this comparison the event descends to the next left or right node. The blue nodes are termination nodes where the split-up has stopped due to the abortion criteria.

values assigned to it from which the average is calculated. This average is called hadronness (the prefix “averaged” is usually omitted) and is the main parameter used for separation.

To check that the RF produces a good separation between hadron and gamma-ray induced events, a test sample of background and MC gamma-ray events is processed by the RF and the mean hadronness, along with the spread of the hadronness distribution, is plotted for both event types versus the S parameter. This plot directly shows in which S regime the separation is powerful. An example for low zenith angle observation is shown in Fig. 5.8.

The separation power between gamma-ray and hadron induced events of MAGIC is clearly a function of energy of the event and determines the analysis energy threshold which is, except for pulsar observations,³ much higher compared to the trigger threshold.

To perform a good gamma/hadron separation, some working procedures are followed in the analysis presented in this thesis. First, the image parameters fed into the RF should show some potential for the gamma hadron separation and should be well defined during the observation period in which they are used. This means that, during all nights analyzed, the parameter distributions must be the same for the recorded data. Only then is it guaranteed to make a correct classification of the event type. Second, the number of trees should be sufficiently large, which is achieved if the spread of the hadronness between different trees is no longer changed by adding additional trees. Third, the node size at which any node becomes a termination node should be chosen to get a good separation and simultaneously

³In pulsar analysis, the folding with the period of the pulsar provides a very powerful separation method and no hadronness cut is needed

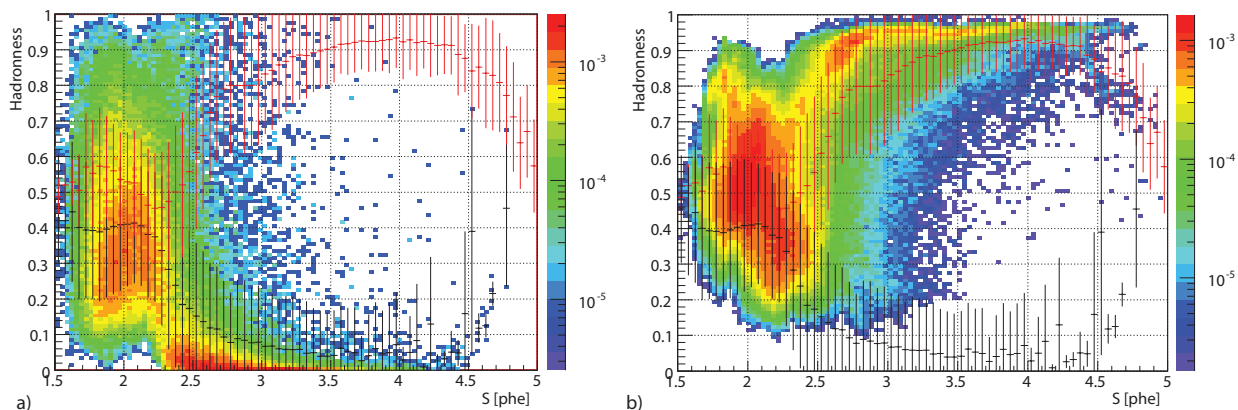


Figure 5.8: The hadronness mean value and spread of the distribution for hadrons (red, and colored distribution in b)) and simulated gamma-ray (black, and colored distribution in a)) induced events is plotted against the parameter S which is strongly correlated with the energy of the event. Powerful separation is possible wherever the spreads of both event types do not overlap.

avoiding further split-ups which will not improve the gamma/hadron separation. Fourth, the zenith angle range of the events should not be too large, since the image parameters start to vary rapidly with increasing zenith angle (ϑ) i.e. if $\vartheta > 40^\circ$. If the observation data stretches over large zenith angle ranges, then different RF's are trained in smaller sub-zenith angle ranges to make the classification scheme more efficient. In this thesis, for four different zenith angle ranges ($[0^\circ, 32^\circ]$, $[32^\circ, 44^\circ]$, $[44^\circ, 50^\circ]$ and $[50^\circ, 55^\circ]$), individual RF's are trained.

Most of the image parameter distributions are different for gamma-ray induced events compared to the hadronic ones. The difference is shown in Fig. 5.9 and partly in Fig. 5.5 to show in which energy regime the parameter is useful to separate between both particle shower images. Furthermore, the image parameters depend on the telescope operation parameters like the PSF of the reflector or the stability of the calibration and time adjustment in the trigger delays. While all these parameters are monitored and checked, the PSF can vary and there exists for each PSF value a dedicated MC sample which is used for the corresponding time period. The change in PSF is caused by the light weight and thus less rigid frame of MAGIC.

The sensitivity of the analysis can, of course, change if the PSF changes. The main reason for this is the dependency of the energy estimation on the various image parameters. The image parameters get more diluted if the PSF is too large, making the image parameters insensitive to the details of the shower and thus worsening the energy estimation and

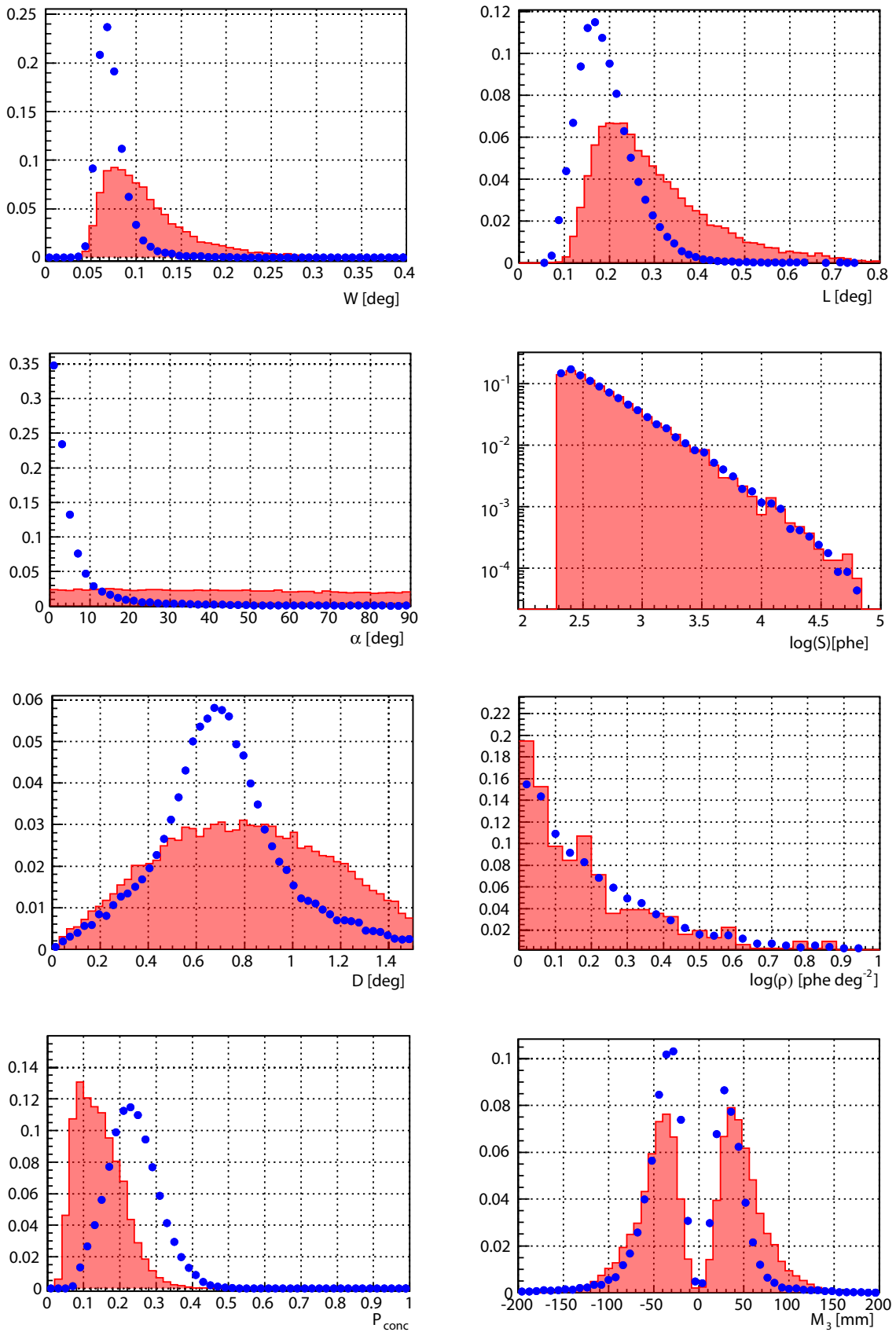


Figure 5.9: The individual Hillas parameters used as input to the RF. The blue points represent the MC simulated gamma-ray event distributions and the red solid area shows the real data (almost only protons) distribution. The full separation potential is only used if the parameters are exploited by multidimensional classification processes like the RF.

the background rejection power. For this reason, the key performance parameters of the telescope, such as the energy resolution, are given for each analysis in this thesis.

5.1.4 The energy estimation

The energy estimation is also carried out by applying the RF method. In this thesis, the regression method was used in the RF to estimate the energy (Albert et al., 2008b). The image parameters of a training sample of MC generated gamma-ray- induced events are used to train the RF. The image parameters selected are: S , W , L , D , ρ , p_{conc} , t_{rms} , t_{grad} , ϑ and N_{L1} . Here N_{L1} is the ratio of the charge in the outermost pixel ring of the camera to S and called leakage1. The source dependent parameters are only used if the analysis is done with respect to a source position.

Depending on the telescope performance parameters, the energy resolution and any possible bias are the vital parameters for the high level products. The energy resolution and the energy bias as a function of the true energy is shown in Fig. 5.10.

The zenith angles of the different analyses range from 6° – 32° and 32° – 44° . The energy resolution is very good ($\Delta E \sim 20\%$) for a single telescope. Another important parameter is the bias of the energy estimation. As can be seen from Fig. 5.10, the bias changes with energy and can even shift from overestimation at lower energies to underestimation at higher energies. The bias is larger for lower energy and positive, which reflects that lower energetic showers are more likely to be overestimated in their energy. The reason for this is that only showers can trigger the telescope if they have an upward fluctuation in the recorded shower image charge S . Such showers are then taken as higher energetic showers. Since the sensitivity of the telescope is smaller at lower energies, most of these showers cannot be separated from the background events and so do not contribute to the signal. On the other hand, high energetic showers ($E > 6$ TeV) do not have shower images fully contained in the camera which leads to a worsening of the energy resolution at higher energies and can cause an increased negative bias due to the lack of a fully reconstructed charge of the shower image. A great improvement is seen if the timing information is used for the shower parameter reconstruction (compare black triangles with the other curves in Fig. 5.10).

The energy bias and the resolution is corrected in the spectrum by the unfolding procedure. The unfolding procedure works like this: A sample of MC gamma-ray events (denoted test sample and independent from the training sample) is processed by the RF and the same signal selection cuts as for the analyzed data are performed on the test sample. Then, the test sample is plotted in a binned $E_{\text{true}}-E_{\text{est}}$ plane, where the binning is not necessarily the same in E_{true} and in E_{est} . This migration matrix can be used to evaluate how many events

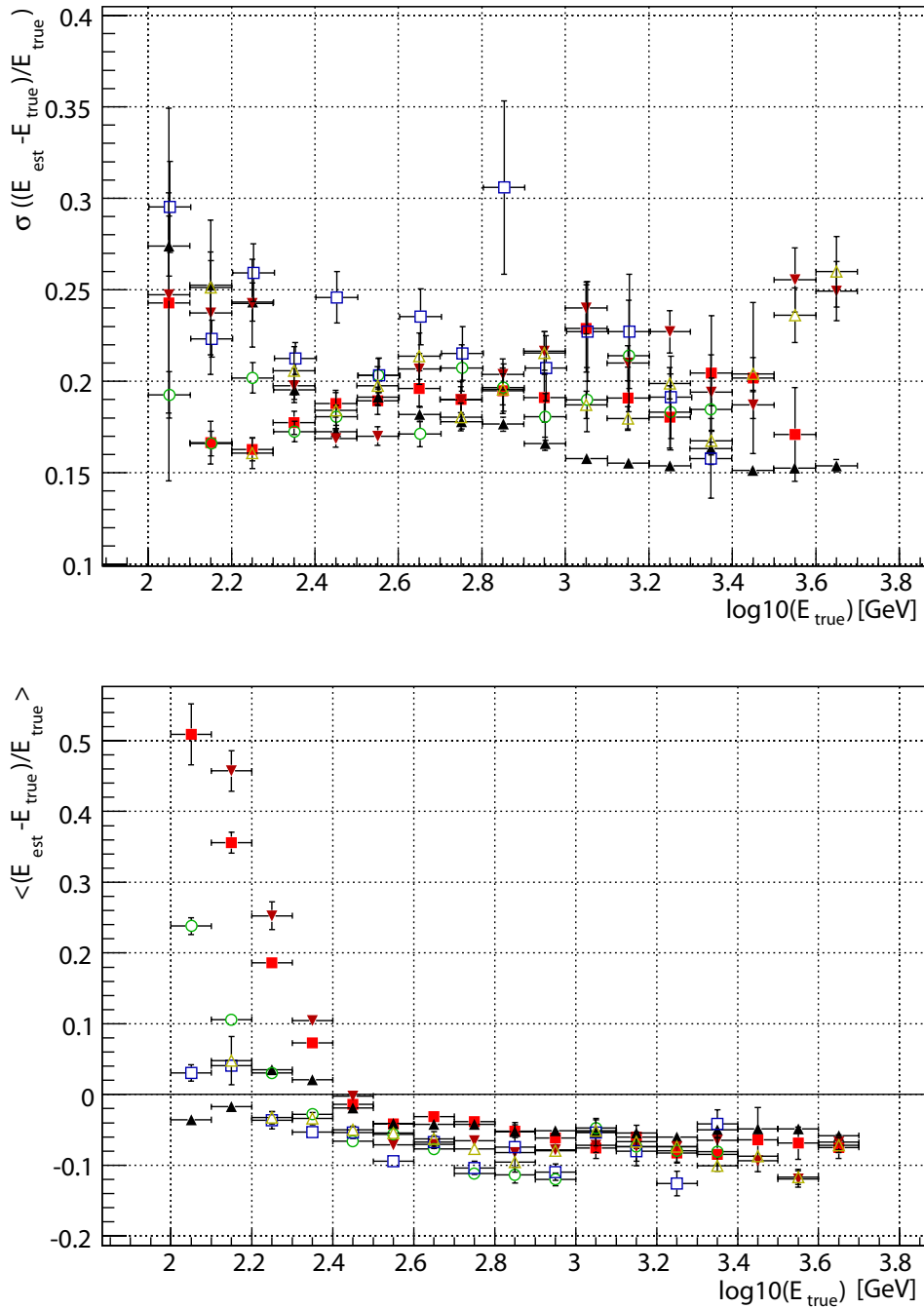


Figure 5.10: The upper panel shows the energy resolution as obtained from a gaussian fit as a function of energy. The different symbols represent the different MC simulations of gamma-ray events used for analyzing the data in this thesis. The red squares are the 2005 to early 2006 MC in ON/OFF mode. The dark red upside down triangles are the late 2006 MC with improved PSF and the splitters installed for the MUX but recorded with the 300 MHz FADC. The black upright triangles are the MC with time parameters used from September 2007 to January 2008. All these are produced for zenith angles of 32° – 44° . The hollow points and squares are for $\vartheta < 30^\circ$ where the hollow squares are the MC used for 2007 with MUX but without source position dependent parameters and the hollow points are used for the 2008 data with source dependent parameters and time information.

in bin i of $E_{\text{true}}(S_i)$ will end up in bin j of $E_{\text{est}}(Y_j)$. The unfolding can be written in matrix notation as:

$$Y = M \cdot S \quad (5.22)$$

where S is the real distribution and Y the measured one. The aim of the unfolding method is to obtain S by inverting equation (5.22). Since M is in general not of type $n \times n$, the solution for S can be found in general by minimizing the least square expression

$$\chi_0^2 = (Y - M \cdot S)^T \cdot K^{-1} \cdot (Y - M \cdot S) \quad (5.23)$$

The general solution to equation (5.23) can have large errors which are caused by the method (see Albert et al. 2007d and references therein). Another option is to use an unfolding with regularization.

$$\chi^2 = \frac{w}{2} \cdot \chi_0^2 + \text{Reg}(S) \quad (5.24)$$

Here, w is the regularization parameter, steering the strength of the regularization and $\text{Reg}(S)$ is the regularization term. There are different methods, using different $\text{Reg}(S)$ terms and three of them are applied in this thesis to all unfolded spectra and the results are compared. The methods are denoted **Schmelling** (Schmelling, 1994), **Tikhonov** (Tikhonov and Arsenin, 1979) and **Bertero** (Bertero, 1989) methods. More information about the details of the unfolding methods and the implementation in the MAGIC analysis software can be found in Albert et al. (2007d).

5.1.5 Arrival direction estimation

The arrival direction of the shower is also deduced from the shower image parameters. This method is called the ‘‘disp-method’’. The parameter $\text{disp}(\psi)$ is defined as:

$$\psi = a(S) + b(S) \cdot \frac{W}{L + \eta(S) \cdot N_{L2}} \quad (5.25)$$

Here, a and b are second order polynomial functions of $\log(S)$ and N_{L2} is a measure of the leakage of the shower image, defined as the ratio of the charge in the two outermost pixel rings of the shower image to S . The disp method uses the elongation information of the shower image to determine the source position which is assumed to lie on the major shower axis (L -axis) at a certain distance from the COG of the shower. The eccentricity of the image parameter ellipse is correlated to the distance of the COG (of the shower image) from the source position. This method was developed by the Whipple collaboration (Fomin et al., 1994) and used in the HEGRA experiment. The parametrization given above leads to improved results for the MAGIC analysis compared to the original one (Domingo Santamaria,

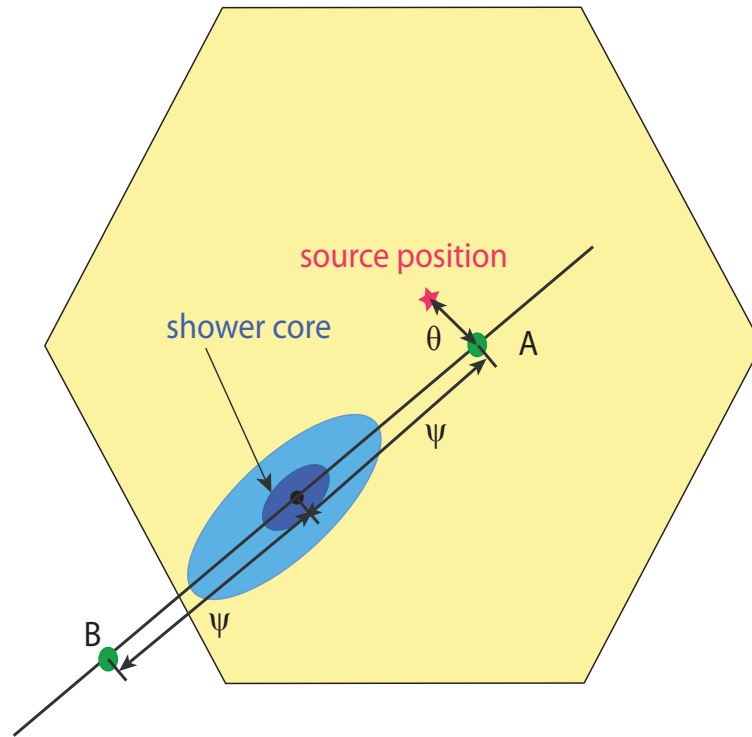


Figure 5.11: Schematic view of the MAGIC I camera. The shower image is shown as the blue ellipse and the shower core is shown as a darker blue ellipse inside the shower image. The disp method leads to the possible pointing positions A and B. A is the correct pointing position since the shower core lies within the shower image in the direction of A. The true source position is indicated as well and the angular separation θ which is used as a signal selector (see section 5.1.7).

2006). As can be seen from Fig. 5.11, the reconstructed pointing position should be in the direction to which the COG of the shower core is displaced compared to the geometrical mean. With the disp method, an origin of each primary particle is calculated and related to a position in the sky. From this information, a so-called “skymap” can be derived. A skymap is a map around a potential source position in the sky. This map is a 2D-graph where x and y coordinates are the celestial coordinates (either right ascension (RA) and declination (DEC) or galactic longitude and latitude) and the value at this point ($P(x, y)$) is the number of excess events which point to a direction with a predefined squared angular distance (θ^2) to $P(x, y)$. The skymap can also be given with the significance or integral flux value at each point. To avoid any possible bias, no image parameters which are related to the source position in the camera can be used in the analysis chain from which the skymap is generated. This is the reason why two RF’s are always trained: one with an assumed source position using all image parameters and one without the source position dependent parameters.

5.1.6 The observation modes

In gamma-ray astronomy by IACT's, two observation modes are commonly used. One is the so-called ON/OFF mode and the other is the wobble-mode (Fomin et al., 1994).

In the ON/OFF mode, the potential source is tracked at the center of the camera and the shower image parameters of each event are calculated with respect to the camera center. This data set is called the ON-sample or ON-data. In an additional data run, a close-by region without any known gamma-ray source is tracked with similar observation conditions such as zenith angle range, moon phase, star field and hardware conditions. This data set is called the OFF-sample or OFF-data and is used as a background estimation sample for the signal selection as described in the next section. One important requirement is that the image parameters of the OFF-sample (without hadronness-cut) match the ON-sample image parameter distributions. If there are strong deviations, this is most likely an indication of different observation conditions.

The other observation mode is the wobble-mode which tracks a point offset by 0.4° from the source position. To avoid systematic effects due to sensitivity differences in the camera, this position is changed each 20 min by 0.8° so that the source is again 0.4° away from the tracking position but 180° rotated with respect to the previous position. These two positions are called W1 and W2. It is worthwhile to mention that different starfields are present in the camera for W1 and W2 and, therefore the trigger efficiency may not necessarily be the same for W1 and W2.

The background is estimated by calculating the shower image parameters with respect to an OFF-source position. These positions lie on a circle with a 0.4° radius around the camera center and are rotated by 90° , 180° and 270° with respect to the source position. Since the MAGIC telescopes are azimuthal mounted telescopes, the camera field rotates with the Earth's rotational speed. This leads to a rotation (along the circle) of the source and the OFF-source positions with observation time. An illustration of the geometry and the movement of the positions is given in Fig. 5.12.

Both data-taking modes are used in the data presented in this thesis. While the wobble-mode has the advantage of the same observation conditions for the background data and the source data, it exhibits slightly less sensitivity compared to the ON/OFF mode. This is because of the limited trigger region of MAGIC I and the offset of the source position with respect to the center of the trigger region. The lower energetic showers must have smaller D values to trigger the telescope, so the asymmetry of the trigger area gives them a smaller trigger probability. On the other hand, background data is taken at the same time as the source data and thus the effective observation time of the source is higher for wobble mode

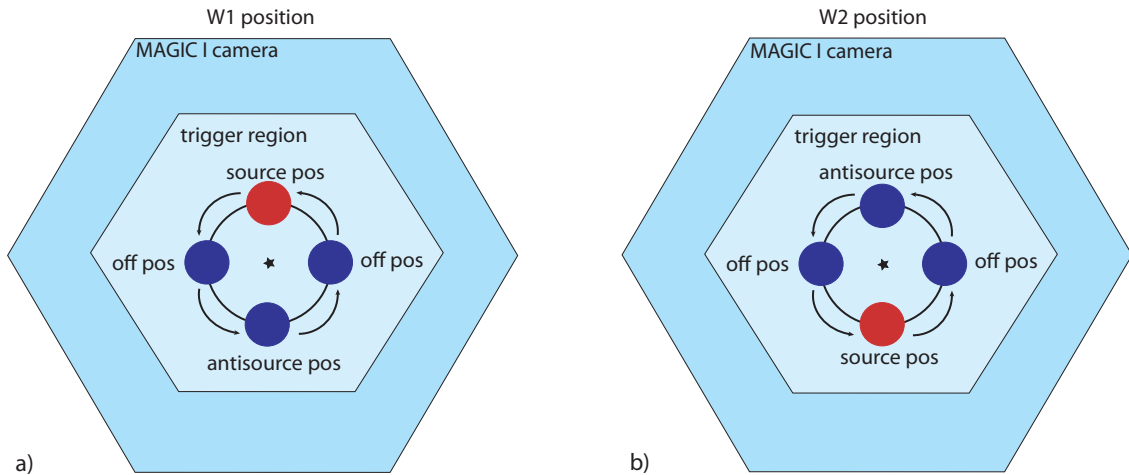


Figure 5.12: Illustration of the wobble observation mode; the source is at the center of the red circle and the blue circles indicate the regions of the background sample. All regions rotate with the Earth's rotational speed, so after 6 hours the source will be in the position of one of the adjacent off-positions. The star marks the center of the camera which is tracked by the telescope and this position is called a wobble position. When the wobble position is changed, the source and antisource position swaps places.

when compared to ON/OFF mode.

5.1.7 The signal event selection

After the shower image parameters are calculated, the event is processed by the RF software to calculate the hadronness, the energy and the disp of the event.

To get an optimized gamma/hadron separation, the hadronness cut value (to select the gamma-rays) is chosen for bins in estimated energy. The requirement is to keep at least 80% of the MC gamma-ray test sample events after the hadronness cut. The efficiency value is chosen to give an optimal significance of a test Crab Nebula data sample. To avoid systematic uncertainties due to low statistics, the efficiency is chosen to be as high as possible.

To get a good separation, a cut in S is applied so that only images with $S > 300$ phe are used for the signal selection in the search for a new VHE gamma-ray source or to obtain a light curve of the source flux. The cut is relaxed for the determination of the spectral energy distribution because there the significance is calculated for each energy bin and the systematic effect of the A_{eff} does not effect all energy bins. In addition, a cut in $D < 1.2^\circ$ is applied in the case of ON/OFF observations and this leads to a better background suppression because images extensively truncated⁴ are not analyzed.

⁴Such shower images will not lead to correct reconstructed shower parameters and particle type identification

In addition to the hadronness, another cut on the arrival direction of the event is made. This cut depends on the observation mode and the possible source extension. For a point-like source, which is expected for all observed sources in this thesis, two parameters can be used: Either α which should be around 0° for gamma-ray events since it is the angle between the source direction and the major shower axis (compare Fig. 5.9); or θ^2 which is the squared angular distance from the pointing direction of the shower to the source location in the camera (see Fig. 5.11). The shower direction parameter is plotted for the events from the source region and for a background sample after the hadronness cut is applied. The cut in the direction parameter is chosen so that 70% of the MC test sample events survive the cut. Each cut is optimized in an energy bin to take into account the dependency of the shower image parameters on the primary particles' energy. This yields much improved results compared to cut values for the integral energy range.

The arrival direction parameter (α or θ^2) is compared for the ON and OFF events which leads to a typical plot as shown in Fig. 5.13: Such plots are used to evaluate the remaining background and to calculate the significance of the possible signal.

The θ^2 method (see Fig. 5.11) can also be applied for extended sources but no source position dependent parameters can be used in the RF and no cut is allowed in D . This can reduce the significance of the signal since less information is available to the RF for classifying the particle types. On the other hand, skymaps for the complete camera FoV can be derived from an analysis that is independent of source position since all showers are kept independent of the position to which they are pointing. Thus one can search for sources with unknown coordinates in the camera FoV.

The background sample is either taken from dedicated OFF-data or from shower images which point to one of the OFF regions for wobble data (see Fig. 5.12). The OFF regions are chosen to be less than 0.2° in diameter, for point-like sources they are commonly as small as 0.17° .

To claim a discovery of a new VHE gamma-ray source, an excess with a significance of at least 5σ is required. The significance of a signal is calculated by the equation derived by Li and Ma (1983) (their equation 17).

$$S = \sqrt{2} \left(N_{\text{on}} \ln \left[\frac{1 + \kappa}{\kappa} \left(\frac{N_{\text{on}}}{N_{\text{on}} + N_{\text{off}}} \right) \right] + N_{\text{off}} \ln \left[(1 + \kappa) \left(\frac{N_{\text{off}}}{N_{\text{on}} + N_{\text{off}}} \right) \right] \right)^{1/2} \quad (5.26)$$

Here, N_{on} and N_{off} are the number of events in the signal region of the source sample and the background sample. The parameter $\kappa = t_{\text{on}}/t_{\text{off}}$ is the ratio between the effective observation time of the source region compared to the background region: This implies that $N_{\text{background}} = \kappa \cdot N_{\text{off}}$ and the number of gamma-ray candidates from the source becomes

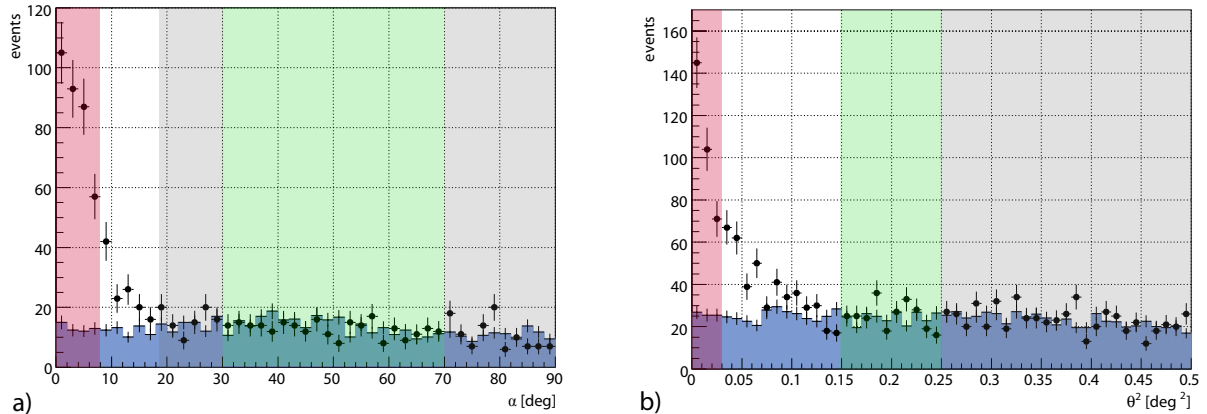


Figure 5.13: The ON events are shown in black points and the background sample in blue bars for the α parameter in a) and the θ^2 parameter in b). In both cases, the same Crab Nebula data set is used and the signal region is shown by the red area and the background normalization region by the green area. The grey areas are used to check if the background normalization worked as expected. The number of excess events N_{ex} is determined by subtracting the number of background events from the ON events in the signal region. It is worthwhile noticing that the significance in the case of the source-dependent α approach is 18.8σ while, in the case of the θ^2 method, it is only 14.5σ .

$N_{\text{ex}} = N_{\text{on}} - \kappa \cdot N_{\text{off}}$. The meaning of κ is a normalization factor of the background events to get the correct background estimation for the observation time of the source. In the analysis presented in this thesis, κ is not simply the ratio of the observation times but it is corrected by a comparison of the integral events in a signal-free region of the θ^2 or in an α -plot between the ON and OFF events: This region is called the background normalization region (see Fig. 5.13). This approach is more reliable for estimating the background since slight fluctuations in the event rate can happen between different observation nights and, in the case of wobble mode observations, the camera can have different acceptances in the individual regions because of the different starfields, PMT characteristics, broken pixels and trigger inefficiencies present. These differences are very small for $S > 200$ but not negligible.

In the case of wobble data, an even amount of observation time spent in both wobble positions averages out most of these inhomogeneities. The small remaining discrepancies are cancelled by the normalization of the integrated event number between the OFF and ON control region.

To compare the sensitivity of different experiments or the performance of the telescope in different time periods, the sensitivity level is defined as the minimum flux level needed to achieve a 5σ detection within an observation time of 50 h. To evaluate the significance, a

simplified gaussian approach is preferred to using equation (5.26).

$$\Omega(t) = \frac{N_{\text{ex}}}{\sqrt{N_{\text{bg}}}} \cdot \sqrt{\frac{t}{t_{\text{obs}}}} \quad (5.27)$$

Here, N_{ex} is the number of excess events, N_{bg} the number of background events and t_{obs} the observation time. Ω gives the significance observed from this source in the time t . Often the significance for the Crab Nebula with $t = 50$ h is calculated. To get the sensitivity in units of Crab Nebula flux (often called crab units, CU), the minimum flux needed to achieve a 5 sigma detection within $t = 50$ h is calculate by

$$F_{\text{min}} = \frac{5}{\Omega_{\text{crab}}(50 \text{ h})} \text{CU} \quad (5.28)$$

The F_{min} in CU is an adequate measure to compare the sensitivity between different observational periods of the same instrument with the same energy threshold and this has been the procedure adopted in this thesis.

To compare F_{min} with other experiments, a source-independent determination would be better since the spectral energy distribution shape can have a major influence on the sensitivity, especially if the energy range in which $\Omega(t)$ is obtained is not exactly the same for both experiments. To compare the sensitivity of two experiments, the spectral energy distribution of the source must be taken into account. This can lead to very different results compared to the comparisons usually made assuming a power law with the spectral index close to that of the Crab Nebula ($\Gamma = 2.6$).

5.1.8 Angular resolution and source extension

To obtain an idea of a possible source extension a θ^2 plot is produced from the data and compared to the angular resolution determined from a MC test sample simulated for a point-like source and processed by the same analysis chain as the data. The extension of the source should be visible by any deviation from the expected shape obtained from the MC test sample. The angular resolution is first determined by the MC test sample for different energy bins by calculating the $r_{50,\text{psf}}$ radius. This is the θ -radius in degrees in which 50% of the signal events of a point-like source are contained. This method is a bit different from the standard method which takes the σ of a 2D-gaussian as the angular resolution but the $r_{50,\text{psf}}$ method is more realistic because of the shape of the PSF of the MAGIC telescope.

The PSF is a composition of two different shapes which can be well described by two 2D-gaussian functions. One describes the tail of the PSF and the other the more narrow part at the center (called the peak). The tail of the distribution originates either from the

optical aberrations of the reflector or from the shower image reconstruction mechanism or any combination of both.

It is very challenging to fit the θ^2 -distribution in such a way that the result does not rely on the starting parameters of the fit and gives reproducible and good fit results. To achieve this, the first 2D-gaussian is fitted for $0.15 < \theta^2 < 0.25$ and describes the tail of the PSF, the fit parameters of this 2D-gaussian are then fixed and a second 2D-gaussian is added to the fit function⁵ and fitted to the whole $\theta^2 < 0.25$ distribution. The standard deviation of the second 2D-gaussian is the σ_{psf} . This procedure leads to very small angular resolution because the second 2D-gaussian describes only the very peak of the θ^2 -distribution and depends strongly on the fit parameters of the tail of the PSF. As long as the same fit properties such as the θ^2 -ranges of the two fits and reasonable χ^2 are obtained, the results can be used to check for deviations between the MC test sample and the source data to find a possible source extension. If the amount of excess events from a source is not high enough to get a solid estimate for the tail of the PSF (no excess events at higher θ^2), the source extension can be only calculated if it is much larger than the σ_{psf} . An example of the test for extended emission for the Crab Nebula (a very strong source) is shown in Fig. 5.14.

The angular resolution as defined in optical astronomy is the minimum separation of two independent point sources that can be completely separated. For this definition, the $r_{50,\text{psf}}$ is a much better measure than the σ_{psf} as defined above. If significant deviations are found, a further analysis of the emission shape can be carried out by testing more complicated shapes compared to the two 2D-gaussian fit of the θ^2 -distribution.

5.1.9 Monte Carlo simulations

The main reason why MC simulations are the vital element to analyze IACT data is that a test beam cannot be injected into the atmosphere to get a calibration of the full system. While most elements are extensively studied, the atmosphere and the shower development together with the telescope performance parameters enter into the MC simulation, as well as all their related uncertainties.

The basic code for the shower development is the CORSIKA 6.019 code (Heck et al., 1998) for extensive air showers. With this code, the shower particles together with all their interactions and the Cherenkov light emissions of the air shower are simulated. All photons hitting the ground in the vicinity of the telescope are stored along with all relevant parameters (such as wavelength, incoming direction and arrival time). The next step is the so-called

⁵The fit function consists of two 2D-gaussians where the parameters of the tail describing 2D-gaussian are fixed.

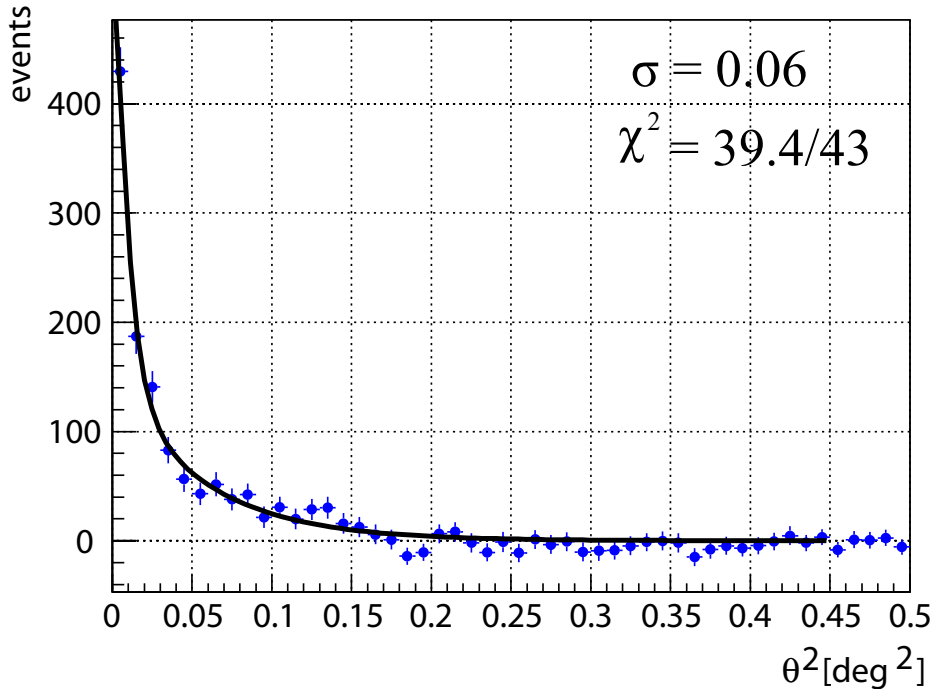


Figure 5.14: The θ^2 plot of the Crab Nebula and the fitted source extension shape (two 2D-gaussian functions). The extension shape is determined from simulated MC gamma-ray events. The Crab Nebula is a point-like VHE gamma-ray source for MAGIC since the shape describes the obtained plot very well and the σ_{psf} is compatible with the one obtained from a point-like MC simulated gamma-ray source. The true angular resolution of the MAGIC telescope is larger (see section 5.1.8 for more information).

reflector which takes into account the absorption and scattering of the Cherenkov photons in the atmosphere. The assumed atmospheric model is the US standard atmosphere (National, 1992), and the Mie-scattering is calculated using the Elterman model (Elterman, 1964). In addition, **reflector** is used to calculate the mapping of the Cherenkov light onto the camera plane and contains all optical aberrations and performances of the MAGIC reflector. The next part is called **camera** and contains the simulation of the PMT camera and the complete read-out chain including the PMT signal response, the VCSEL's, amplifiers, optical cables, the trigger simulation and the FADC read-out. After processing the full chain from CORSIKA to **camera**, the MC raw data is ready to be analyzed by the MAGIC analysis chain as done with real raw data. All parameters of the telescope, such as gain fluctuation distributions, noise levels of the above listed components and signal shapes, are obtained from measurements of real data taken with MAGIC and implemented in the simulation programs.

The simulated showers are gamma-ray- induced air showers between energies of 30 GeV and 30 TeV where the impact parameter of the showers reaches up to 400 m. The simulation used in this thesis spans zenith angle ranges from 0° – 60° and was simulated with a flat distribution in $\cos(\vartheta)$. The ϑ -distribution is chosen to match that of the real data to be analyzed. The processing of the data is done in different zenith angle bins if the range is too large (i.e. $32^\circ < \vartheta < 55^\circ$ is split in three analysis bins 32° – 44° , 44° – 50° , 50° – 55°).

The hadronic simulated events (mainly protons) take much longer simulation time since they can trigger the telescope from much larger impact parameters (up to 800 m) due to their larger lateral spread. In addition, the trigger probability of a hadronic induced shower is only $\sim 0.2\%$. This leads to low statistics in the MC proton events. To achieve a solid training of the RF for all event energies, a high statistic is needed. Thus real data is taken instead of simulated proton events. Since the ratio of hadron to gamma-ray events is almost one to one thousand in the case of real data, even for the Crab Nebula real data is an excellent proton sample for the training. For more information on the MC simulation for MAGIC I, see Majumdar et al. (2005).

5.1.10 Flux calculation and spectral energy distribution

The most important results of the analysis are the high level products which are directly linked to the physical processes of the source of the VHE gamma-rays. These high level products are the differential flux (spectrum, for short), the temporal resolved integral flux values (denoted light curve, LC) and the previously described skymaps. The skymaps help in identifying the source location and possible extension of the source, thus enabling the identification of the physical object of the emission. The other two products give direct information about the possible acceleration mechanism in the source.

The differential spectrum is defined as:

$$\frac{dF}{dE}(E) = \frac{dN_\gamma}{dE dA_{\text{eff}} dt_{\text{obs}}} \quad (5.29)$$

Here, N_γ is the number of measured excess events, A_{eff} the effective area and t_{obs} the effective observation time. All quantities are calculated in small energy bins. The effective area of the detector characterizes the detection efficiency for gamma-ray- induced showers and is calculated from an MC simulated gamma-ray event test sample (independent from the sample used for the training of the RF). The effective area depends on the trigger efficiency, the FoV of the trigger and the camera, the reflectivity of the mirrors, the zenith angle of the

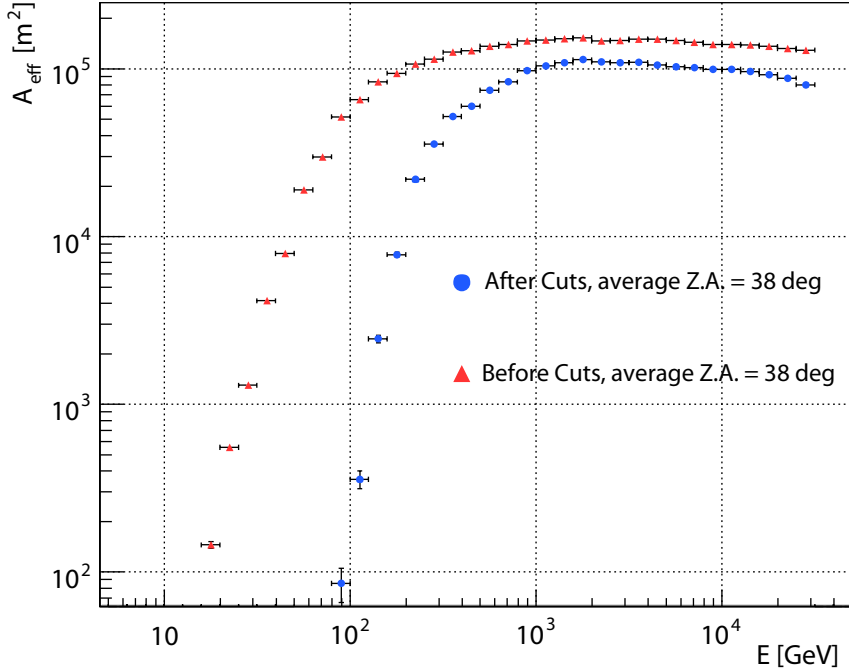


Figure 5.15: The A_{eff} before separation cuts (light red triangles) and after separation cuts (blue points) as a function of estimated energy. The A_{eff} errors are one sigma statistical errors only. For the spectral energy distribution, the A_{eff} is further computed for each zenith angle bin (not shown here). The step rise in the lower energy section indicates that, due to the finite energy resolution, a significant systematic uncertainty enters the flux calculations at these energies. Integral fluxes as computed for light curves should have energy thresholds where ΔA_{eff} varies little between adjacent energy bins.

observation and the other performance parameters of the telescope and, of course, on the cuts applied in the analysis chain. A typical A_{eff} is shown in Fig. 5.15. The A_{eff} has a steep rise at lower energies, because the trigger probability of the gamma-ray induced showers is rapidly increasing at these energies. The lower the energy of the primary gamma-ray, the less light is emitted by the cascade and the lower the trigger probability. Small fluctuations in the Cherenkov light yield can prevent the low energy showers from triggering the telescope. As soon as the shower fluctuations are small compared to the total amount of light, the trigger probability becomes more stable and the effective area remains almost constant. The gamma/hadron separation cuts make this step rise even more dramatic, since most showers of low energy do not differ in the shower image parameters between gamma and hadronic induced events. This leads to a selection of events with upward fluctuations in S because of the S -cut in the signal event selection. Thus, the systematic uncertainties dominate for low energy bins in the spectral energy distribution.

The number of energy bins used for the spectrum calculation cannot be chosen arbitrarily high. For the energy bin, the minimum bin size must be larger than the energy resolution but, for realistic gamma-ray sources and observation times, the bin size is much larger since the number of excess events and the spectral shape limit the amount of events inside any energy bin. To be able to fit the spectrum, the significance in each point should be at least above 1.5σ . Since background and signal fluctuations will never provide equal significance in all energy bins, it is difficult to give an optimal energy binning a priori. If a gamma-ray signal is obtained with a 5σ significance, then experience has shown that, with four energy bins per decade in energy, a spectrum with four significant points can be obtained. At least this is true if the spectrum can be described by (up to now) observed spectral shapes.⁶

The energy bins in this thesis are determined by demanding a certain number of bins per energy decade. The number is selected so that there is a reasonable significant signal (1.5σ) in at least four bins before the unfolding procedure.

The light curve is the integral flux over a specific energy range versus the time. The integral flux is defined as:

$$F(E > E_0) = \int_{E_0}^{\infty} \frac{dN_{\gamma}}{dE dA_{\text{eff}} dt_{\text{obs}}} dE \quad (5.30)$$

Here again, the quantities are calculated in the energy range and the A_{eff} is computed for a power law ($dF/dE = a_0 E^{-\Gamma}$) with spectral index of $\Gamma = 2.6$. The LC is determined for bins in time, where t_{obs} is the bin width and the A_{eff} is calculated for the zenith angle distribution of the data in each time bin. This leads in general to a slightly time-dependent A_{eff} . The most important quantity to be chosen is the lower energy for the integral flux. The systematic uncertainty of the LC is dominated by the uncertainties of the A_{eff} at the lowest energies. Since the gamma-ray spectra are always power laws, the exponentially growing number of gamma-rays when lowering E_0 , makes the lower energy events dominate the excess events. At the same time, the A_{eff} has higher systematic uncertainties the lower E_0 becomes and this leads to a very fast rise in the systematic uncertainties of the integral flux. As previously explained, the A_{eff} should only slightly deviate between adjacent energy bins for the chosen E_0 to avoid large systematic uncertainties in the LC. Adequately chosen E_0 are always guaranteed in the data presented in this thesis. In general: to make significant light curves, the integral flux is determined above energies of 300–400 GeV for $\vartheta \in [32^\circ; 44^\circ]$ (see Fig. 5.15).

⁶Spectra with four points are compatible with pure power laws and the spectral photon index is measured between 2–4. Of course, future measurements with improved low-energy sensitivity might reveal sources with steeper spectra.

Period	S -cut [phe]			
	spectrum	LC	α or θ^2 -plot	skymap
zenith angle $> 32^\circ$				
2005	250	400	400	400
2006	250	400	400	400
2007	250	250	300	400
2008	250	250	300	400
zenith angle $< 32^\circ$				
2005	100	300	300	400
2006	100	300	300	400
2007	100	300	300	400
2008	100	300	300	400

Table 5.1: Used S - cut values

5.1.11 Upper Limit calculation

Whenever no significant signal is found, an upper limit on the differential and/or the integral flux is derived. To determine the upper limit, the method developed by Rolke is used (Rolke et al., 2005) to derive an upper limit on the number of excess events. A 30% systematic uncertainty is assumed (see chapter 5.2) and a confidence interval width of 95% chosen. Deviations from these parameters are mentioned explicitly in this thesis.

From the upper limit on the number of excess events, the upper limit on the flux is calculated simply by dividing by the A_{eff} and the t_{obs} in each energy bin or in the energy range. The assumed spectrum for the source is a power law with a spectral index similar to the one of the Crab Nebula ($\Gamma = 2.6$). Since the spectrum of the source is not known, no unfolding is taken into account. The dependence on the spectral shape for the upper limit is very small assuming reasonable spectra as investigated in detail by Galante (2006).

5.1.12 Summary of the cut values used in the analysis

Throughout this thesis the cut values were determined by checking them once on a Crab Nebula sample and are not changed unless special circumstances require it. So, unless explicitly stated otherwise, the S -cut values are always the ones shown in Table 5.1. The main cut that changes is the lower S cut. As seen in Fig. 5.8 for lower S values which correspond to lower energetic events, the separation between gamma-rays and hadronic induced events is very small. To get a good signal to noise ratio, and thus small errors on the integral flux values, the lower energy showers are left out. This also leads to more stable LC's because the lower energetic showers are more effected by systematic uncertainties, especially the atmospheric transmission, which can shift the threshold considerably. In addition, the direction infor-

mation for higher energetic showers is much better, so the S and hadronness cut ($h < 0.1$, $S > 400$ phe) is more strictly chosen for skymaps to obtain a better angular resolution. For the differential energy spectra, the S -cut is more relaxed to obtain the lowest energetic point possible. Here, the systematic uncertainties affect only the low energy points and can be estimated by the A_{eff} slope and the systematic flux shift visible due to the different unfolding procedures.

Beside the skymaps, the hadronness and direction parameter cut are always chosen from gamma acceptance efficiencies (80% and 70%, respectively) and never changed in the analysis of this thesis.

5.2 Systematic uncertainties

In this section, the systematic uncertainties of the integral flux and the spectral index are investigated for MAGIC I. The time dependence of the systematic uncertainties is in detail investigated in chapter 6. The most important uncertainties are:

- **Photon detection efficiency:**

The mirror reflectivity is assumed to be 85% and is monitored by reflectivity measurements. In addition, the size of the PSF is important to know the amount of light reflected in individual pixels. The accuracy of the PSF and the mirror reflectivity determination are estimated to be about 5%. Furthermore, the protective plexiglass in front of the PMT's might yield less transmission due to dust pollution as well as light losses at the PMT winston cones. The effect is estimated to contribute 3% and 5% to the overall uncertainties.

Another source of uncertainty is the photon to photoelectron conversion efficiency. The main contribution to this uncertainty originates from the uncertainty of the light collection efficiency of the first photon diode and is estimated to be 5% – 10%. Further contribution of about 2% comes from the equalization of the PMT gains. The absolute light calibration system adds another 8% and the trigger inefficiencies and malfunctioning PMT's yield additional 10% to the systematic uncertainties. The trigger inefficiencies are most pronounced for primary gamma-rays below 150 GeV while the effect is much smaller at high ($E > 500$ GeV) energies (around 3–5%). All these systematic uncertainties affect the energy estimation or act on the A_{eff} and are energy dependent.

- **Atmospheric model:**

In the MC simulation the US standard atmosphere is taken as the atmospheric model.

This model represents an ideal atmosphere but was not developed for the Canary Island La Palma. The effect of the difference between the model and the real atmosphere at the observatory is estimated to be 10%. The effect of different weather conditions or changing atmospheric conditions is investigated in more detail in chapter 6.

- **Analysis chain:**

Possible dead times in the system, not taken into account in the analysis, will affect the effective observation time and thus, the flux at all energies in the same way. The uncertainty is estimated to be of the order of 2%.

Differences in the analysis methods (signal extraction, image cleaning, RF training, unfolding method) might cause additional systematic uncertainties and were estimated to be about 3%.

- **MC simulation:**

The assumed cross sections in the forward direction at TeV energies are not measured and rely on extrapolation. This uncertainty affects the shower development. Additional uncertainties result from the Cherenkov light production and spectral dependent scattering in the atmosphere. In addition, the simulation of the detector and especially the measured signal shapes and responses (e.g. DT, optical splitters, VCSEL, trigger) on slight variations in the signal shapes might lead to systematic uncertainties which could be but may not be energy dependent. The effect of these uncertainties is estimated to be about 10%.

With regard to the above given energy and flux uncertainties, the overall systematic uncertainty on the integral flux is estimated to be about 30%, assuming a spectral index of $\Gamma = 2.6$. The systematic uncertainties will be higher for softer spectra ($\Gamma > 2.6$). The systematic uncertainty on the spectral index is estimated to be $\Delta\Gamma_{\text{sys}} = \pm 0.2$. A detailed investigation of the systematic uncertainties and their temporal behavior is investigated in chapter 6.

All errors given in this thesis are one sigma statistical errors only unless explicitly stated otherwise.

5.3 X-ray analysis

The X-ray analysis was carried out using the `heasoft 6.6.3` software package (available from <http://heasarc.nasa.gov/docs/software/lheasoft/>) together with the remote calibration database setup. This guarantees that the most recent calibration files are always chosen

automatically by all analysis tasks which require them.

The X-ray data analysis is described only briefly since excellent documentation for the programs is provided which explains every step in detail. Here, only the steps necessary for the analysis shall be explained and some important points emphasized which are not that prominent in the documentation.

For the analysis of X-Ray Telescope (XRT) data, the following programs are used: `heasoft` 6.6.3 with the XRT software package, especially the `xrtpipeline` script and the `xrtmkarf` task. For source event selection, background estimation as well as for extraction of uncorrected LC's, spectra and skymaps the task `xselect` and the fits viewer `ds9` are used. The rebinning and weighting of the spectra files is carried out using `GRPPHA`. For fast checks without the need of absolute flux values, LC's are generated using `Xronos`. All manuals necessary for the various tasks are available on the `heasoft` webpage, except for the XRT specific tasks which are described in the *Swift* XRT data reduction Guide available from <http://heasarc.nasa.gov/docs/swift/analysis/>.

The following steps are carried out to obtain a LC with absolute flux units:

1. The data for the XRT instrument and auxiliary files are downloaded.
2. The data are processed with the `xrtpipeline` to produce cleaned events with the most recent calibration files.
3. The observations are splitted up into pointings⁷ using the time filter of `xselect`. This step is only performed if the individual pointings within an observation are separated by a big gap of more than half a day.
4. For each pointing
 - (a) the source position in the detector is determined
 - (b) a background region is selected
 - (c) the `exposuremap` is generated for the source region in case it covers the bad columns in the XRT camera⁸
5. The ancillary response file (ARF) for the source spectrum is generated which takes into account the `exposuremap`, the vignetting and the PSF corrections to the `responds` matrix.

⁷An observation spans usually one day but is splitted up into several pointings where each pointing lasts about 1–2 ks and might be separated by gaps with no data taking on the source.

⁸*Swift* was hit by a micro-meteorite in 2005. This event resulted in two noisy columns in the XRT CCD, which have been excluded from the analysis.

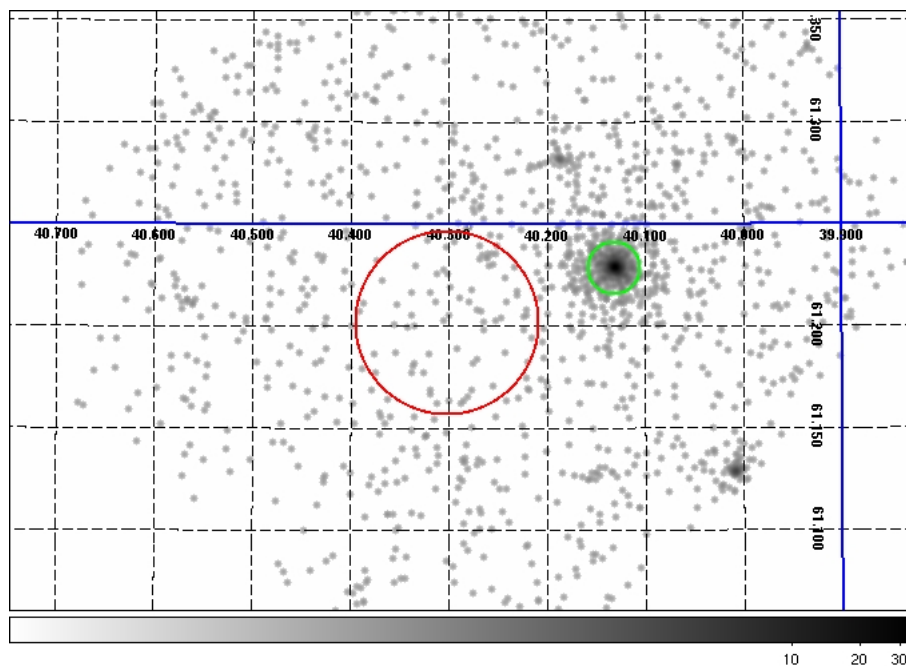


Figure 5.16: The XRT camera image of the region around LS I +61°303. The vertical axis shows the DEC and the horizontal axis the RA. The green circle is centered on LS I +61°303 and shows the region from which the source spectrum and the LC are extracted. The red circle corresponds to the region from which the background events are obtained. The background region does not contain any known X-ray source and is considerable larger compared to the source extraction region in order to yield smaller statistical errors on the small number of background events present. The map is smoothed with a gaussian ($\sigma = 3$ arcs) in order to make the events more visible.

6. The source data is rebinned by GRPPHA so that at least 20 events are contained in each bin.
7. The final spectrum is fitted using XSPEC 12.5ac (Arnaud, 1996) whereas one common model is fitted to all pointing within one observation.
8. The most simple spectrum yielding a reasonable χ^2 is selected and the unabsorbed integral flux in the energy range 0.3–10 keV calculated.

An example of the source and background region selection in the LS I +61°303 data set of September 2007 is shown in Fig. 5.16. The source region is circular and 47 arcsec in diameter. This guarantees that 90% of all events of a point like source are contained within this region. The background extraction region is much larger in order to yield smaller errors, since the number of background events is very low at X-ray energies.⁹

⁹Compared to VHE gamma-rays, the X-ray data is almost background-free.

Some circumstances must be considered when analyzing X-ray data. First, the so called “pile-up” will occur, when more than one X-ray photon hits the camera before the frame has been read out. When two X-ray photons are recorded in the same frame it is not possible to discriminate them and thus no energy estimation is possible. This happens mainly in the longer exposed ($t_{\text{exp}} = 2.5$ s) photo counting (PC) mode which is used when observing weaker X-ray sources. Pile-up corrections must be applied if the source’s count rate is above 0.6 counts/s. LS I +61°303 is a rather weak X-ray source taken in PC mode, yielding usually less than 0.3 counts/s and thus, no pile-up correction is needed for the XRT camera.

The spectra are fitted using XSPEC with an absorbed power law. In case of the LS I +61°303 XRT spectra, the weighting used in the fitting routine is set to a method suitable for few counts per energy bin developed by Gehrels (1986). From the fitted spectra, the unabsorbed flux is calculated by integrating the spectrum over the sensitive energy range of XRT (0.3–10 keV). All calculated errors of the X-ray analysis stated in this thesis are 1σ statistical uncertainties, unless explicitly mentioned otherwise.

5.4 Periodicity searches

In the analysis of binary systems, the search for possible variability and periodicity is a primary goal. While the test for variability is rather simple (by making a χ^2 test of a constant flux and evaluating the probability from the derived χ^2 and the number of degrees of freedom NDF), the search for periodicity is a much more challenging task.

The reason for periodic emission in binary systems are manifold and I distinguish two major possibilities.

1. The emission of the system is periodic. This means that the emitted flux of the system is a periodic function of time with a fixed period.
2. The measured flux on Earth is a periodic function of time but, in the binary system, the emitted flux is constant or variable and only due to geometric effects (jet precessing or a moving beam of emission), as in pulsars, the emission seems to be periodic for the observer on Earth.

The distinction between the two scenarios can be very difficult but is of great interest since it has a very high impact on the understanding of the source.

For the method used to proof a periodic flux measured on Earth, the two distinctions are of no interest. So I will discuss this topic in chapter 7 about LS I +61°303 and not in this section.

Another distinction can be made if a system shows strictly periodic fluxes. This question is directly related to the question of how to prove periodic emission and this will be discussed in the next subsection.

5.4.1 Periodic, quasiperiodic or not at all?

Many definitions of periodic and quasi-periodic (QP) exist and it is often unclear which definition the author is using in a publication. To avoid confusion, I will define the different terms in this section.

- **Periodic:** A periodic flux measurement means that the LC shows a reproducible time structure with a fixed period P . It must be possible to describe the LC with a periodic function. The only exception to this behavior is that an average of several LC's has to be periodic, while a single LC can deviate from the average shape. This exception is done so that pulsars can be counted among the periodic sources.
- **Quasi-periodic:** This means that the sources show a periodic behavior of the LC from time to time, with an interval in between where no periodic behavior is observed. This is very common in microquasars where a periodic behavior is only noticed in certain emission states and is absent in other states.
- **Partly periodic:** This means that there is a periodic component in the LC's which is overlaid by non- periodic emission. This partly periodic (PP) emission is a new definition introduced in this thesis. It can be used to describe deviation from the periodic case without using the QP case, which is connected to state transitions and the requirement of periodic emission in at least one state of the source.

The influence of the type of emission (periodic, QP, PP) is important when considering the method used to search for periodicity in the emission. When no distinction is made between the three cases, or it does not matter which case is investigated, I will simply write about periodicity. Almost all methods for testing periodic behavior test if the recorded signal is uniform, so they will give some result if the signal is not constant but shows some regular behavior. This means that the methods will indicate in all three cases that there is some periodicity in the signal. The significance of this periodicity will, of course, depend on the case (periodic, QP, PP) and on the method used. If the emission is QP, then the selection of certain states due to the evaluation of spectral properties of the data might yield higher significance for certain states than for others and can thus reveal the QP nature of the signal. The behavior of the test used in this thesis in relation to the different possible flux types will be shown in the next sections.

5.4.2 Tests for periodicity

To test for periodicity, the data must be given in a time series.

$$\{f(t_0), f(t_1), \dots, f(t_n)\} \quad (5.31)$$

Here $f(t_i) \equiv f_i$ is the measured flux at the time t_i . One common problem in the search for periodicity is, that the data is not evenly spaced in time. In astronomy, the sampling of the source cannot be freely chosen, there are the natural gaps due to the night-day change and, in addition, standard IACT's can only observe during moonless nights. Even MAGIC, which is specially designed to be able to cope with higher background light, cannot observe during moon phases of more than 50%. More reasons for the uneven sampling are weather conditions and, of course, the source is only visible for a limited time from the observatory location.

The gaps in the LC give rise to rather big problems in the search for periodicity in the signal and especially in the estimation of the significance determination of a peak value found in the periodogram. The challenge is the testing of unevenly sampled data and the method most suitable for this is the one developed by Lomb (Lomb, 1976) and elaborated by Scargle (Scargle, 1982). Their method modifies the definition of the periodogram as used in the Fourier transformation. While in Fourier transformation, the data are weighted by time interval, the modified periodogram weights the data by point and is equal to an estimation of the harmonic content by a least square fit of $A \sin(\omega t) + B \cos(\omega t)$ to the data.

The periodogram is defined as:

$$P_N(\omega) = \frac{1}{2\sigma^2} \left\{ \frac{[\sum_i (f_i - \bar{f}) \cos(\omega(t_i - \tau))]^2}{\sum_i \cos^2(\omega(t_i - \tau))} + \frac{[\sum_i (f_i - \bar{f}) \sin(\omega(t_i - \tau))]^2}{\sum_i \sin^2(\omega(t_i - \tau))} \right\} \quad (5.32)$$

Here τ is defined by

$$\tan(2\omega\tau) = \frac{\sum_i \sin(2\omega t_i)}{\sum_i \cos(2\omega t_i)} \quad (5.33)$$

This particular choice of τ makes equation (5.32) completely independent of shifting the t_i by any constant. $P_N(\omega)$ is called the normalized periodogram, since σ is in the denominator of equation (5.32) and, with this normalization, $P_N(\omega)$ has an exponential probability distribution (Scargle, 1982) in the case of the null hypothesis.

This means that, if M independent frequencies are tested, the probability to get a value for $P_N(\omega)$ (from now on $P_N \equiv P$) larger than z is

$$p(> z) \equiv 1 - (1 - e^{-z})^M \quad (5.34)$$

In general, the number of frequencies tested will be the number of independent frequencies in the case of equally spaced data (independent fourier spacing, IFS) which is given by

$$N_{\text{IFS}} = \frac{\Delta f}{T_{\text{min}} - T_{\text{max}}} \quad (5.35)$$

Here, $T_{\text{min}} - T_{\text{max}}$ is the total timespan of the LC and Δf is the investigated frequency range. To assure a good sampling of the frequency range, an integer multiplication of N_{IFS} frequencies are tested. The multiplicand is called the oversampling factor and should be chosen high enough so that each peak in the periodogram is sampled by several test frequencies.

The remaining question is how many of the tested frequencies are independent. This depends on the spacing of the data, the gaps between them and if the data are “clumped”. In the case of the sources analyzed in this thesis, the data are always “clumped” - meaning that there are several data points per observation night and then a gap until the next observation night. Since the amount of data points per night is not always the same, M cannot be easily estimated analytically. For this reason, I programmed an MC simulation to estimate the probability for any given $P(\omega)$.

My simulation works as follows: The actual observation time stamps of the data are taken and, for each of these data points, a gaussian noise value is generated. This yields one simulated noise series and $P(\omega)$ is calculated from this noise series for all test frequencies. To obtain the probability distribution, 10^7 such series are generated and the $P(\omega)$ are filled in separate histograms for each frequency. This yields as many histograms as test frequencies. Then, the probability distribution for each frequency is fitted by the exponential probability density function (PDF, e^{-z}) and the fit parameters compared with each other as shown in Fig. 5.17. This is done to assure the PDF does only depend mildly on the tested frequencies.

In the same simulation, the cumulative PDF (CPF) is generated by selecting the highest power $P(\omega)$ from each simulated periodogram. The CPF gives the post-trial probability to obtain a $P(\omega) = z_0$. The question of interest for the periodicity search is the probability to obtain any $P(\omega) > z_0$ which is given by means of the complementary CPF (cCPF). The cCPF is constructed by subtracting the integral of the CPF above the value z_0 from 1. The cCPF should possess the shape of equation (5.34) and the fit of the cCPF with this equation yields the true value of M for the independent frequencies.

If the shape of the cCPF is not well described by equation (5.34) with any M , the number of simulated noise periodograms can be increased and the post trial probability can be calculated as the ratio $N(z > z_0)/N_{\text{tot}}$ directly from the histogram. If $P(\omega)$ is so large that there are too many simulations to carry out, an upper limit of the probability can be given which is good enough to show that any $P(\omega)$ which cannot be calculated anymore is definitely

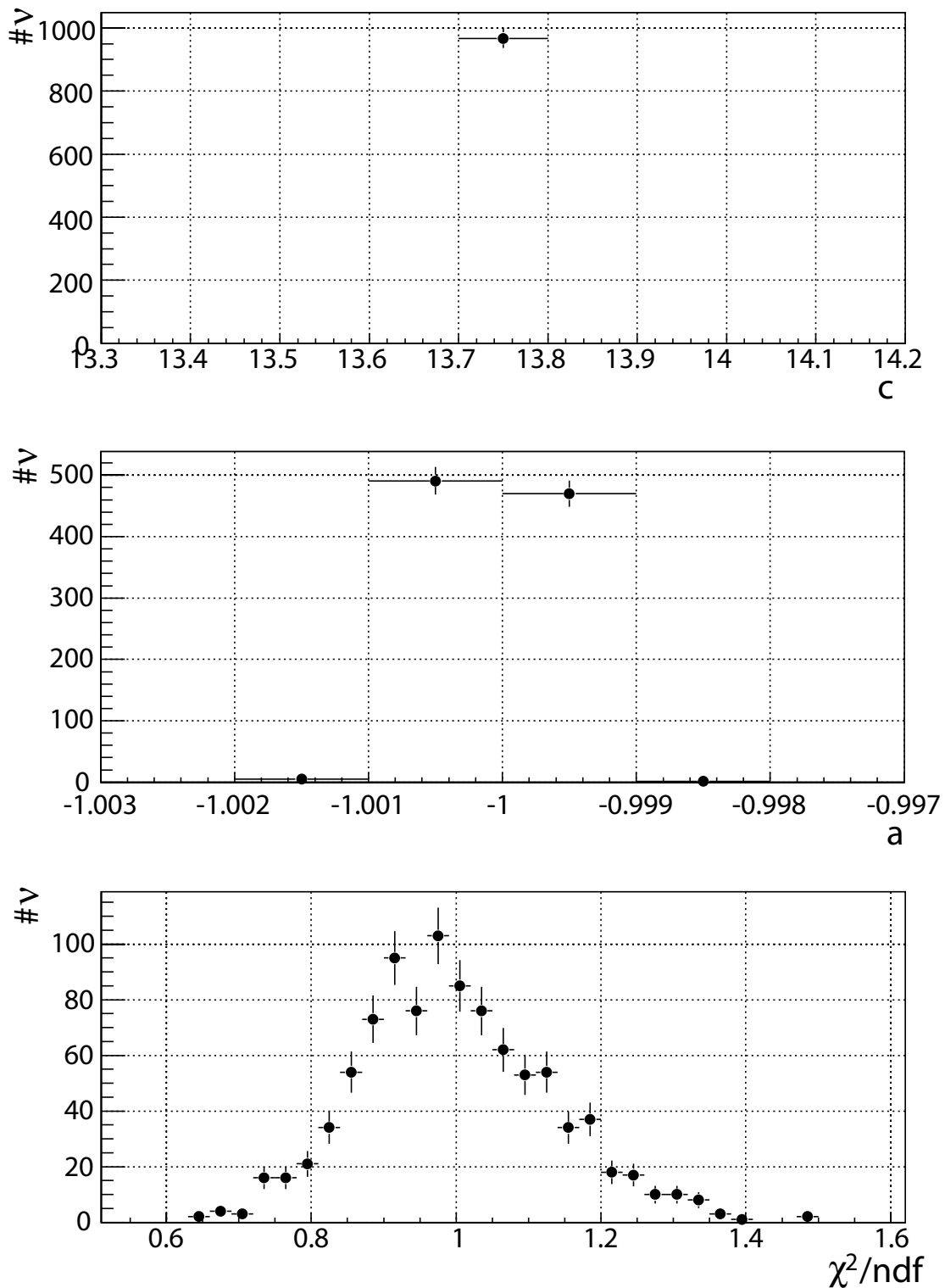


Figure 5.17: The fit parameters of the function $c \cdot \exp(-a \cdot z)$ to the PDF of all test frequencies for simulated gaussian (white) noise with the sample time intervals of LS I +61°303. The fit parameters have only a very tiny spread around the pronounced mean and can be assumed as constant for all test frequencies. The χ^2 distribution indicates that for all frequencies the PDF is well described by the theoretically predicted shape.

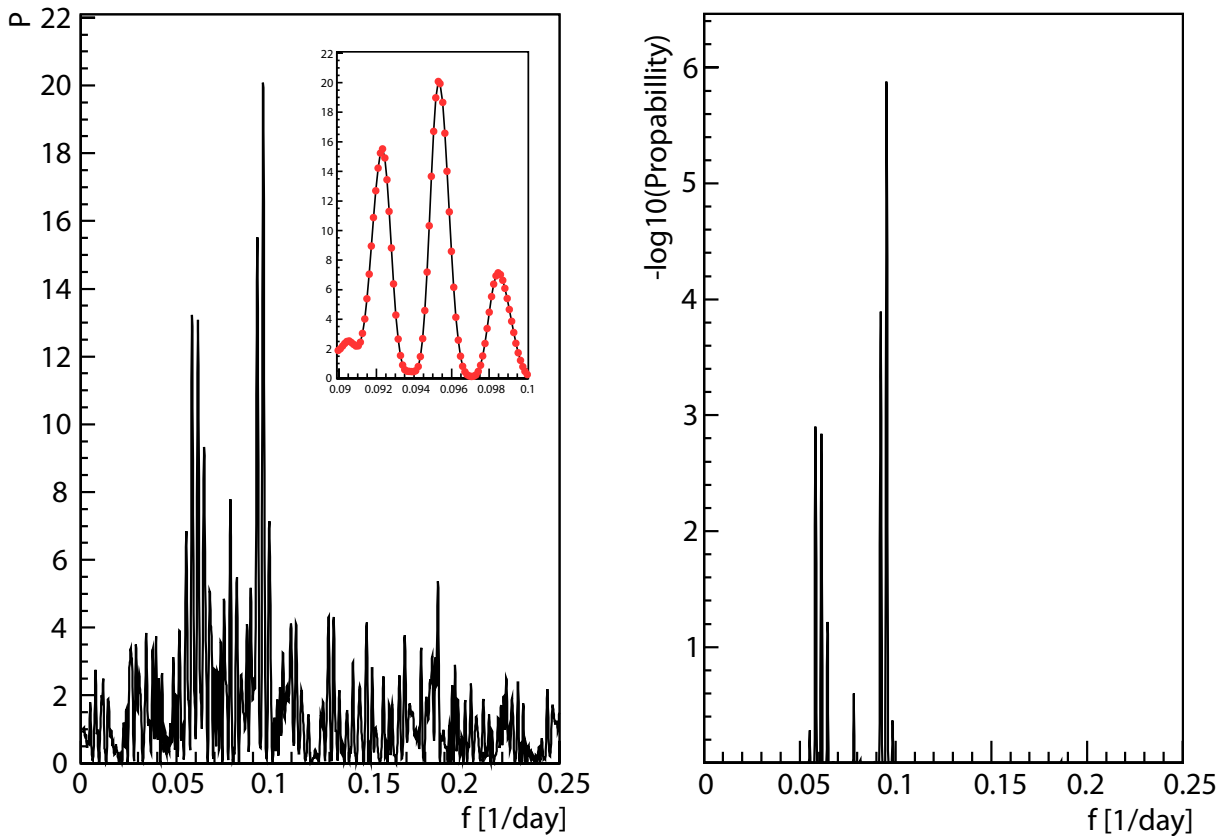


Figure 5.18: On the left the $P(\omega)$ for a simulated sinus function with frequency $\nu = 1/10.5 \text{ d}^{-1}$ and an overlaid gaussian white noise is shown. In the inset, the individual test frequencies are displayed by red points showing that each peak is oversampled. On the right, the post-trial chance probability for each $P(\omega)$, as computed from the cCPF, is shown. It is evident that additional peaks with less significance beside the real signal peak are present. These peaks are caused by the uneven spacing and are removed if the signal is subtracted.

significant. This method can be applied to other statistical tests as well. However, the PDF should not change (or only very smoothly) with frequency, which is the case for the Lomb Scargle method as can be seen in Fig. 5.17. An example periodogram of a simulated sinus function with frequency $\nu = 1/10.5 \text{ d}^{-1}$ and an overlaid gaussian white noise is shown in Fig. 5.18, together with the post-trial probability of each obtained $P(\omega)$.

In the method described here, the cCPF is computed from white noise and this means that possible periodic variations in the data are not taken into account. Even so, the flux values should show a gaussian distribution and there can be some slight modulation over time due to different time - dependent systematic effects in the determination of the fluxes.

1. Zenith angle range of the sampling points can differ and thus will have different systematic uncertainties, especially since the atmospheric conditions have more effect, the

higher the zenith angle of the data.

2. Background light due to moonlight or changing night sky background light. The telescope could have different efficiencies if operated under moonlight. The effect is currently not corrected in the data since there are no dependencies of the fluxes on the moonlight observed.¹⁰
3. Changing weather conditions can cause different systematic shifts which might be of the order of 20% as shown in the section about the stability estimation of the MAGIC I performance.

These changes could (even if very unlikely) yield a high P value and thus reduce the significance of $P(\omega)$ obtained under the assumption of gaussian-distributed noise. To counteract these effects, the simultaneously taken background data are used to produce a periodogram as well. If any of the above-mentioned effects cause a significant peak in the periodogram of the signal, it should be visible in the background periodogram as well, since it would not come from the true signal in the data.

The background data sample is generated by dividing the background rate by the A_{eff} for the gamma-ray- like events. This is not the true proton flux, of course but this does not matter. Any change in the above systematics should affect all gamma-ray- like events in the same way since they survive the same separation cuts.

In the case of ON/OFF observations, the background flux is determined by taking the gamma-ray candidates from the ON sample in a region of $30^\circ < \alpha < 80^\circ$ where almost no gamma-rays from the source are expected. If no significant peak shows up in the background sample at the frequency of the significant peak in the excess sample, then the peak is not caused by the systematic dependent effects mentioned above. With this method, a reliable test for periodicity is at hand.

Finally, it is investigated if the significance of the peaks in the periodogram dependent on the chosen sampling bin width of the LC. The LC is binned with a certain binwidth which I call the sampling time interval (STI), this time interval selected so that the errors of the measured fluxes are of the same order of magnitude. Only if the individual point errors have the same order of magnitude can each point be treated equally. This leads to a clumping of points at each individual observation night and thus M is significantly lower than the number of data points. To check the change of the false alarm probability of a peak, a simulated sinus function with frequency $\nu = 1/10.5 \text{ d}^{-1}$ is sampled with different STI's and the results

¹⁰For further explanation, see chapter 6.5

compared. The periodogram for the STI = 45 min is the one shown in Fig. 5.18. The test of different STI's is carried out with the observation time coordinates of LS I +61°303 since this is where the “clumping” of sampling points is the most pronounced. The results are given in Table 5.2. It is evident that the smaller the STI, the more points are available and the smaller the false alarm probability becomes. This shows that the method is more powerful in finding weak periodic signals if more sampling points are available. This is not at all surprising since more points mean more information and thus reveals the periodicity. Of course, this effect is limited since the signal to noise ratio reduces as the STI gets smaller and smaller. The frequency of the most significant peak is not affected by any changes of the STI and no additional peaks appear in the periodogram.

STI [min]	Period [d ⁻¹]	Power	P($z > z_0$)
1440	9.5	7.5	0.24
60	10.52	14.5	$3.1 \cdot 10^{-4}$
45	10.49	20.2	$1.2 \cdot 10^{-6}$
30	10.51	17.32	$2.4 \cdot 10^{-5}$
15	10.48	42.8	$1.7 \cdot 10^{-16}$

Table 5.2: The dependency of the false alarm probability and the derived frequency on the STI, as shown for a simulated sinus signal.

Chapter 6

Performance of the MAGIC telescope from 2005-2008

In this chapter, the performance and the stability of the performance of MAGIC I is investigated. As described in the previous chapter, several telescope parameters influence the shower images and thus the particle parameter reconstruction. In addition, the atmospheric changes on various timescales can have a large impact on the obtained results. To check the stability of the high level products, the Crab Nebula - the strongest known point-like steady source - has been investigated on a timescale of four years.

This is the first time such a detailed investigation of the long term stability of the performance of MAGIC I has been carried out. The investigation is vital to show the systematic uncertainties as a function of time over the large timescale of four years (when data studied in this thesis was taken). The Crab Nebula is visible from the observatory at La Palma at the same time as LS I +61°303 is observed and thus the uncertainties obtained from the Crab Nebula results can be readily applied to the LS I +61°303 sample.

6.1 Data selection

The data is screened for technical problems and adverse weather conditions. This is done by first checking the trigger rate and rejecting runs which are outside of the predefined range 250 ± 100 Hz. This required trigger rate range imposes loose constraints on the data quality but removes most of the unusable data, even before processing it with the analysis chain, and thus saves time. In addition, the event rate after image cleaning and a mild S -cut ($S < 60$ phe) is checked as a function of zenith angle and all observation runs with a rate of less than 50 Hz are removed. This is an additional rejection of technical problematic data which has a high accidental trigger rate caused by e.g. too low trigger threshold settings. The remaining data is used in the analysis to obtain the high level products. This data

period	obs. time [h]	zenith angle	condition	mode	read out
2005	3.6	6.5°–30°	dark	ON/OFF	300 MHz
2006	8.0	6.5°–30°	dark	wobble	300 MHz
2007	8.0	6.5°–30°	dark	wobble	2 GHz MUX
2007	6.6	6.5°–30°	moon	wobble	2 GHz MUX
2007	2.5	32°–44°	dark	wobble	2 GHz MUX
2008	3.8	6.5°–28°	dark	wobble	2 GHz MUX

Table 6.1: Observation log of the Crab Nebula data used for the performance study of MAGIC I.

selection procedure is applied to all data analyzed in this thesis, assuring approximately the same data quality in each analysis.

6.2 The Crab Nebula data sample

The Crab Nebula data was selected to be taken in the same periods as the LS I +61°303 data to guarantee the same telescope performance parameters in the two data sets. The Crab Nebula data sample is analyzed for zenith angles below 30° since only in this zenith angle range is enough data available to make systematic studies possible. A cross-check is done for medium zenith angles (32°–44°) with a sample of 2007 Crab Nebula data. This is the same zenith angle range as for the LS I +61°303 data sample and shows possible effects of the higher zenith angles to measured physical quantities.

The observation mode was ON/OFF mode for 2005 and wobble mode for all other periods. This corresponds to the same observation modes as used for the LS I +61°303 observations.

The observation parameters (data period, observation time, light conditions, observation mode and read out system) are summarized in Table 6.1.

6.3 The temporal behavior of the integral flux

The light curve (LC) is derived for integral fluxes above $E = 300$ GeV and the time interval is chosen to be 60 min to give small statistical errors. For some observation nights, the time bin width is smaller because the total observation time was not an integer multiple of 60 min¹. This is not at all a problem since the real observation time per bin is taken into account in the flux calculation and shorter observation times only increase the error on the flux value.

The derived LC is shown in Fig. 6.1 and indicates the systematic differences between

¹In fact the average observation time per light curve point is ~ 45 min

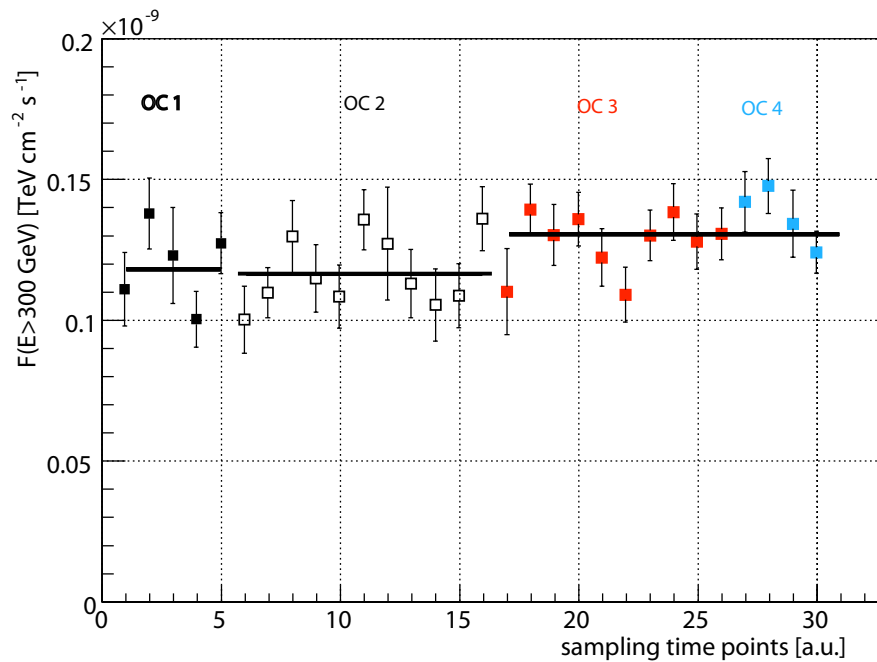


Figure 6.1: The integral flux $F(E > 300 \text{ GeV})$ for different measurements of the Crab Nebula. The data are fitted to constant lines within each OC except for OC3 and OC4 which are fitted with the same constant flux level since they do not show any deviation from each other. Further details are given in the text.

the different observational campaigns (OC) of the MAGIC telescope as given in Table 6.2.

OC	Date	$F(E > 300 \text{ GeV})$ [$10^{-10} \text{ cm}^2 \text{ s}^{-1}$]	χ^2/ndf	$p(\chi^2/\text{ndf})$
1	2006-06	1.18 ± 0.05	6.74/4	0.15
2	2007-02	1.16 ± 0.04	11.86/10	0.29
3	2007-12	1.31 ± 0.03	14.36/13	0.34
4	2008-12	1.31 ± 0.03	14.36/13	0.34

Table 6.2: The Crab Nebula data and the fit parameters of a constant flux to the different observation cycles. The χ^2 and its corresponding probability to obtain an even higher χ^2 value are given as well.

Data taken during OC1 is sampled with the 300 MHz FADC as well as in OC2, but for the latter the optical splitters (see chapter 4.1.2) were installed for the test of the MUX read-out. In OC3 and OC4, the data were taken with the MUX read-out and the flux level can be accurately described as being constant in time.

The deviations between individual nights in each OC can have several explanations as described in section 3.4. The major influence is thought to be the atmospheric conditions, as well as changes in the background light conditions and slight changes in the telescope

operating parameters such as camera temperature, PMT gain, trigger thresholds and focusing accuracy. From Fig 6.1, it is evident that the short-term variations are almost absent for the OC3 and OC4 where the LC can be described very well as a constant flux without any significant deviation from the expected behavior. This is slightly different for the OC1 and OC2 where the spread of the individual LC points is a bit more pronounced but still small. The lower variability in the later OC's (3/4) is most likely the result of improved monitoring of the observational parameters.

The averaged flux in OC1 and OC2 is compatible within the errors indicating that any systematic differences introduced by the splitters or other minor hardware changes are smaller than the statistical errors. The difference in the flux level between OC1/OC2 and OC3/OC4 has its origin in the change of the read-out to the MUX FADC's. This major hardware change causes a systematic increase of 12% of the integral flux for OC3/OC4 compared to the OC1/OC2 data. This effect should be taken into account, especially in the data analysis of long-term monitoring of sources and the detailed study of sources over long time intervals, as it is the case for LS I +61°303, studied in this thesis.

A systematic uncertainty in the flux level due to the read-out can be caused by the signal extraction process. In the case of the 300 MHz FADC the calibration of low and high gain channels (see chapter 4.1.2 and 5.1.1 for details) very much complicated the correct signal extraction and calibration. Furthermore, the stretching of the signal to 6 ns width needed by the 300 MHz FADC is an additional source of systematic uncertainties. With the introduction of the MUX read-out, the signal extraction was simplified, since only one gain level exists and the faster sampling (2 GHz) omits the stretching of the signal. Since the 300 MHz FADC system is no longer operational, no further test measurements can be made to find the source of the systematic differences but the systematic shift is small compared to the statistical errors of the source investigated in this thesis. Taking all these effects into account, the upscaling by 12% of the OC1 and OC2 integral fluxes is preferred since the sensitivity of the later taken data is higher, the system better understood and more stable. This can be verified when the *FERMI* Crab Nebula spectrum will be released and compared to the MAGIC measurements in the same energy range.² Since *FERMI* has a calibrated calorimeter, it has a very low level of systematic uncertainties in its flux measurements when compared to IACT's.

For this thesis, an additional 12% systematic uncertainty in the integral flux level is assumed for the data recorded by the 300 MHz FADC system. The calculated integral fluxes

²*FERMI* has a small effective detector area of less than one m² at energies above 100 GeV. So it will take a long time until the statistical fluctuations of the *FERMI* Crab Nebula spectrum are small enough to enable reasonable comparison to the IACT data.

OC	$f_0 [10^{-12} \text{ cm}^{-2}\text{s}^{-1}]$	Γ	$a_0 [\text{TeV}]$	χ^2/ndf
1	1.0 ± 0.1	2.59 ± 0.09	0.5	7.3/4
2	1.31 ± 0.04	2.64 ± 0.03	0.5	29.8/6
3	1.31 ± 0.03	2.43 ± 0.03	0.5	8.1/6
4	1.47 ± 0.05	2.47 ± 0.04	0.5	4.8/6

Table 6.3: The spectral fit parameters of the individual OC Crab Nebula spectra.

are not scaled by this factor but left as provided after the analysis chain. Nevertheless, a 12% uncertainty is very small when compared to the much larger statistical errors usually present in measurements of sources like LS I +61°303.

6.4 The stability of the spectrum

The spectra are derived with a very low cut in $S > 100$ phe to obtain a low energy threshold. This, of course, leads to large systematic uncertainties in the lowest energy bins of the spectra due to the uncertainties of the A_{eff} (see chapter 5.1.10) but these points can be neglected in the comparison if a higher analysis threshold is chosen. Still, the systematic uncertainties at the threshold are interesting to study where the analysis threshold should be meaningful for the physical interpretation.

To obtain the spectrum, the energy range is divided into six bins per decade in energy. Such fine binning is only possible in the case of a strong gamma-ray flux but allows the analyzer to look for fine features (like absorption) in the spectra.

The spectra are derived for all four OC's and all data in each individual OC is combined for the spectrum calculation. The derived and unfolded spectra are shown in Fig. 6.2 and are all fitted by simple power laws of the form:

$$\frac{dF}{dE} = f_0 \left(\frac{E}{a_0} \right)^{-\Gamma} \quad (6.1)$$

The corresponding fit parameters are given in Table 6.3 and indicate that the systematic differences between the individual OC's is of the order of 0.2 for the spectral photon index. This value is estimated from the differences observed between individual spectra obtained with the two different read-out systems. The obtained spectral shape and parameters are compatible with the measurements of other IACT's within the assumed systematic uncertainties (Hillas et al., 1998; Aharonian et al., 2004a, 2006c).

For the 2007 OC3 data, a comparison between spectra for the low zenith angles ($\vartheta < 30^\circ$) and the medium zenith angles ($32^\circ < \vartheta < 44^\circ$) is performed. Beside the slightly increased energy threshold for the medium compared to the lower zenith angles, no difference

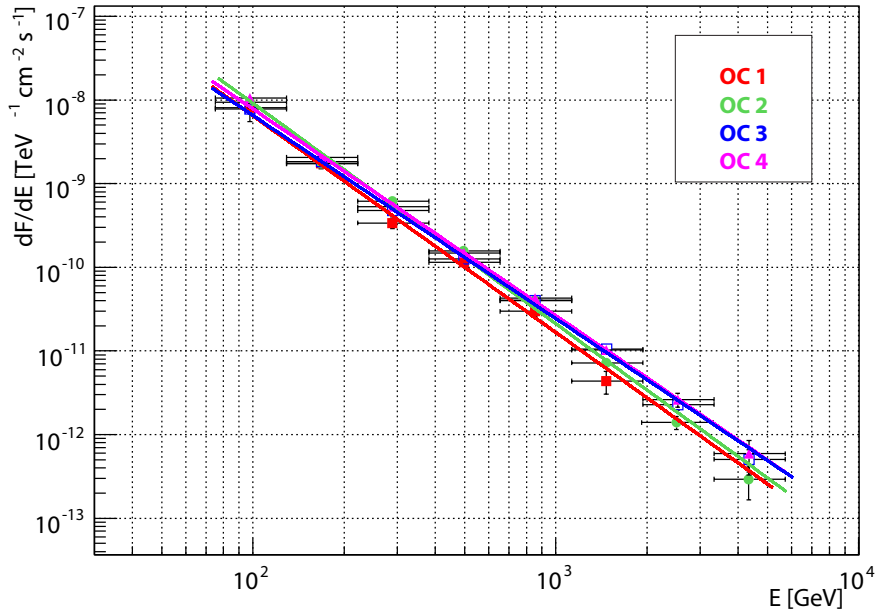


Figure 6.2: The four derived spectra for OC1 (red squares), OC2 (green points), OC3 (blue hollow squares) and OC4 (magenta triangles). The spectra are well described by simple power laws. A difference in the spectra as well as in the flux level is observed between the data taken with the 300 Mhz read-out (OC1 & OC2) and the one recorded by the 2 GHz MUX system (OC3 & OC4). The difference is due to the change of systematic effects of the read-out system and yield a systematic uncertainty on the spectral photon index of 0.2.

is observed as expected of a stable system. The corresponding spectra are shown in Fig. 6.3.

6.5 The influence of moonlight on the measurements

In the sampling of variable sources and the search for transient phenomena, the duty cycle should be as high as possible. Due to this fact, the data selection criteria in this thesis are much more relaxed compared to the analysis of e.g. pulsars. This results in slightly increased systematic uncertainty which can be reduced by increasing the analysis threshold. Another important factor is the observation under moonlight conditions which increases the duty cycle by up to 30% for the observations presented in this thesis. The effect of moonlight is currently being investigated in detail by several scientists in the MAGIC collaboration (Britzger et al., 2009).

For this thesis moon time data was taken only on some observation nights. Moon time data is defined as having the moon above the horizon during the data-taking. Many of the observations labelled moon were carried out on an almost dark night (moon less than 18°

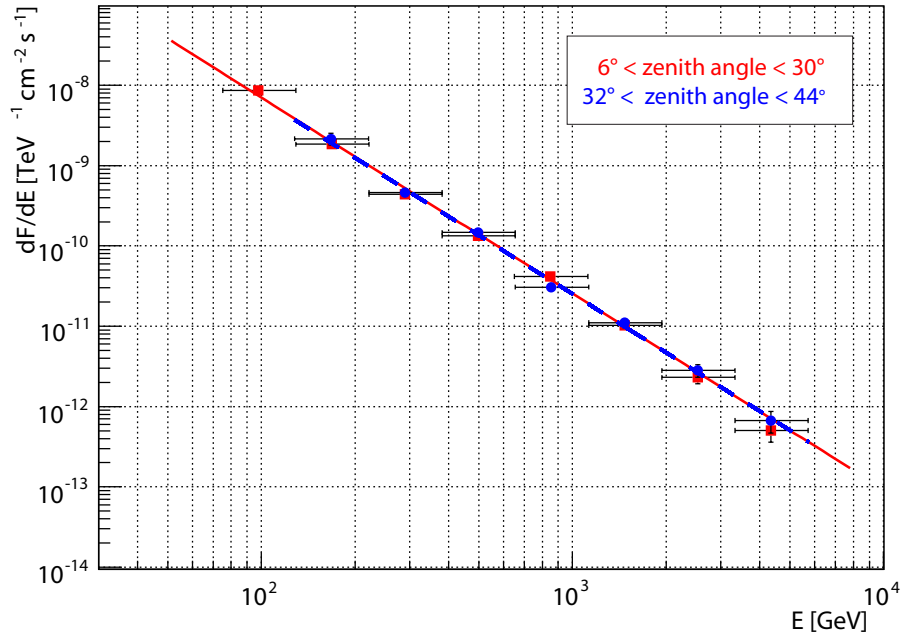


Figure 6.3: The Crab Nebula energy spectrum is shown for low ($\vartheta < 30^\circ$) zenith angle in red (solid) line and for medium zenith angle ($32^\circ < \vartheta < 44^\circ$) in blue (dashed) line. No systematic differences are seen apart from the slightly higher energy threshold for the medium zenith angle analysis.

below the horizon but not yet above it) and only several minutes at the end of the observation night were taken in the presence of the moon.

To describe the intensity of the moonlight, many different methods are possible and in this thesis a simple but effective one is chosen. The DT's as described in section 4.1.3 are responsible for the trigger threshold of the telescope. In the presence of the moon, the background light intensity increases and the DT values are increased to avoid accidental triggers. The higher the intensity of the background light caused by the moon (which hits the camera), the higher is the averaged³ DT setting when compared to dark night observations.

A lot of factors play a role in the effect of the moonlight on the DT but they are not investigated in this thesis. The effect on the high level products is tested by studying the changes of the Crab Nebula data taken under various different DT settings in 2007. The deviation of the integral flux values of moon and dark night Crab Nebula data is then taken to evaluate the systematic uncertainty caused by the moon. In principle, one could try to get correction factors from this comparison of moon and dark night data but unfortunately a huge assembly of data with different observation conditions would be needed for all different hardware setups, especially since the background light in the camera caused by moonlight

³over all pixels

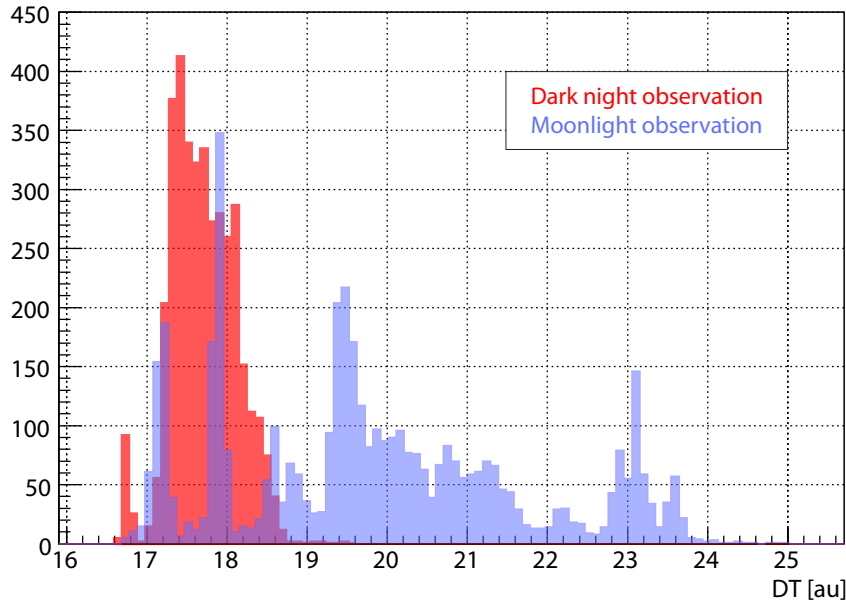


Figure 6.4: Average (over all pixels) DT value of the dark night (red) and moonlight (blue) Crab Nebula data samples. The moonlight was only moderate and distinct peaks in the DT curve indicate the individual observation nights taken under different moon phases.

is increased by the scattering of moonlight in the atmosphere. An even larger set of data compared to the dark night studies presented in the previous sections would be needed for each DT set to investigate the details of the effect of various atmospheric conditions. Since such a data set is not available, an averaged moon condition is chosen and from the comparison only an increased systematic uncertainty estimated.

The comparison is carried out by means of the spectrum which is compared between a dark night Crab Nebula data sample and a moonlight Crab Nebula data sample. The moonlight sample consists of four different nights taken in autumn 2007 and the data is processed by exactly the same analysis chain as the dark night data (as if there would be no moon present in the moon data). The DT values for both data sets are shown in Fig 6.4. The obtained spectral energy distributions do not show any significant difference in the spectral slope. Indeed, the moon data is taken under excellent atmospheric conditions and shows even a slightly higher flux compared to the spectrum obtained from the dark nights. The only disadvantage of the moonlight data is that the analysis threshold is increased compared to the dark night data, since the main influence of the DT level is to change the trigger threshold. The spectral energy distribution of both data sets are shown in Fig. 6.5. From this comparison, as long as the analysis threshold is not close to the trigger threshold, no strong effect of the moonlight onto the high level data products can be seen. This is always true in

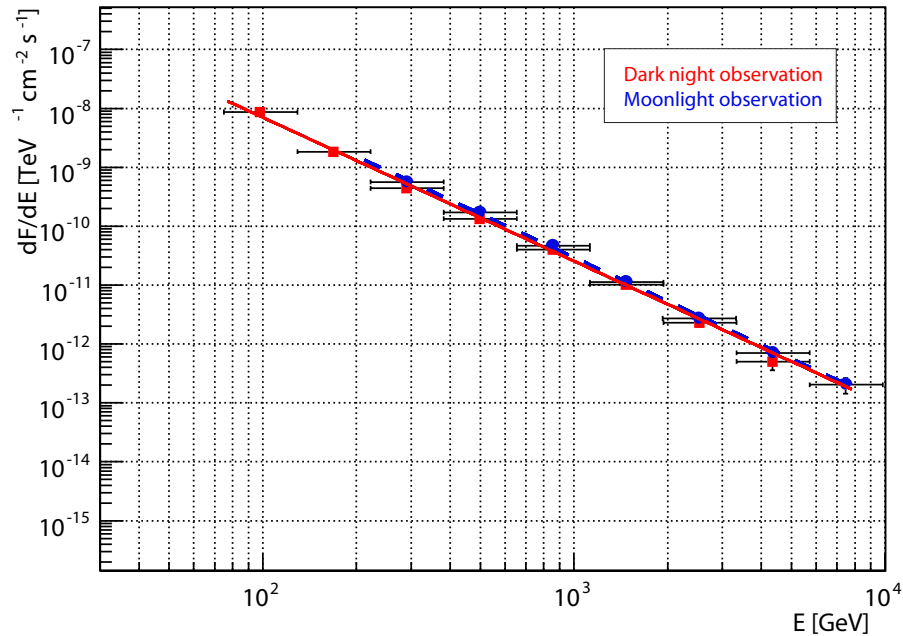


Figure 6.5: The Crab Nebula spectral energy distribution for dark night (red squares and solid line) and moonlight (blue points and dashed line). Apart from the higher threshold for moon observations, both spectral energy distributions agree very well.

the analysis presented in this thesis. The effect of stronger moonlight contamination (visible by higher DT's) might have effects on the high level data, but all data presented in this thesis is only taken partially under moonlight (a few percent of the observation time of individual nights) or in the presence of a crescent moon (low DT values). Since no extensive study with various atmospheric conditions can be performed due to the lack of appropriate Crab Nebula data, an additional systematic uncertainty of 10% is assumed for the integral flux level of observations in the presence of the moon. This systematic uncertainty is, of course, an one-sided correction towards higher fluxes compared to the measured ones. Fortunately, no data analyzed in this thesis which contributed to a spectrum was taken under moonlight and thus the uncertainty introduced by moonlight on the spectral shapes need not be investigated.

6.6 Performance summary of MAGIC I

The telescope shows stable performances in individual OC's. The spectra are affected by a systematic shift in the spectral index after the installation of the new read-out system in March 2007. The systematic uncertainty of the spectral index is estimated to be $\Delta\Gamma_{\text{sys}} = \pm 0.2$. The estimated systematic shift of the integral flux to higher values for the new read-out system is 12%. These systematic uncertainties are rather small when compared to typical

statistical errors in measured fluxes. Thus, the system is very stable within the individual OC's. The performance stability is better for the MUX read out data (after March 2007) but good for the 300 MHz read-out.

The effect of moonlight increases the analysis threshold but has no effect on the integral flux or the spectral shape (at least for Crab Nebula-like spectra) if the moonlight is only moderately strong (maximum averaged DT < 25). Conservatively, an additional 10% systematic uncertainty on the integral flux value is assumed in the presence of moonlight to account for possible stronger influence on the background light intensity due to the dust and humidity content in the atmosphere.

Finally, the observation under higher zenith angle (32° – 44°) shows that only the analysis threshold increases but no systematic difference is observed compared to the small zenith angle results, as was expected.

The performance of the MAGIC telescope is, despite the many hardware upgrades, very stable and within individual OC's, the analysis presented here shows no temporal variation of the systematic effects. This enables meaningful studies of spectral changes within individual OC's. Only by comparing spectra taken with the different read-out systems must an additional small systematic uncertainty be taken into account, which limits the sensitivity to long-term (more than 2 years) variations of the spectral index in VHE gamma-ray sources.

Chapter 7

Observation of LS I +61°303

The main part of this thesis is the detailed study of the binary system LS I +61°303 which was discovered by MAGIC in VHE gamma-rays. Due to this work, LS I +61°303 is one of, if not the best, studied VHE gamma-ray binary system. In this chapter, I shall explain the observational results before the MAGIC discovery and then give a detailed report about the MAGIC observations and the results. After this, I shall discuss the multiwavelength behavior of the system and report on the first strictly simultaneous measurements in VHE and X-rays (to which I contributed a major part). The final section will discuss the considerable impact of these exciting discoveries on the various theories and I shall describe the conclusions drawn from my analysis about the emission mechanism in LS I +61°303.

7.1 The orbital parameters of LS I +61°303

To understand the different processes taking place in a binary system, it is fundamental to know as much as possible about its composition and the orbital parameters. In the case of LS I +61°303 some confusion is found in the publications concerning the orbital solutions derived from optical measurements. This issue seems to be settled now but I will discuss the earlier assumptions since they affect many of the currently published models describing the emission of the system.

The first report of an orbital modulation with a period $P = 26.4 \pm 0.1$ d comes from Hutchings and Crampton (1981). A variation in the flux of the line emission of a factor ~ 4 with small significance is reported. A periodic modulation could be proven by Mendelson and Mazeh (1989) and the derived period $P = 26.62 \pm 0.09$ d is compatible (on the 2σ level) with the best known value obtained from radio measurements ($P = 26.4960 \pm 0.0028$ d, Gregory 2002). The same orbital modulation is reported from infrared measurements (Paredes et al., 1994) and H α line spectroscopy (Zamanov et al., 1999). In addition, a (in my opinion, weak)

hint of a 4 y modulation is reported by Zamanov et al. (1999) from their H α measurements.

The companion star of the compact object is classified as a B0Ve star. This means it is a fast rotating, early type B star on its main sequence surrounded by an equatorial disc which expands radially around the star. The mass is roughly constrained between $10 M_{\odot} - 15 M_{\odot}$ (Swihart 1968, Hutchings and Crampton 1981, Marti and Paredes 1995). The companion is favored to be a compact object and suggested to be of low mass $1.1-4.0 M_{\odot}$ for the usually assumed inclinations of $i \sim 10^{\circ}-60^{\circ}$ (Casares et al., 2005). The nature of the compact object cannot be determined since the inclination of the orbit to the line of sight of the observer is not known. The object could either be a neutron star ($i < 25^{\circ}$) or a black hole ($i > 60^{\circ}$).

Another important component for understanding the emission of the system is the stellar wind. There are two distinct stellar winds: The slow equatorial outflow with a speed of $v_{disk} \approx 3$ km/s and a fast ($v_{polar} \approx 2 \cdot 10^3$ km/s) isotropic polar wind. The equatorial disc wind is rather dense and causes a high mass loss $\dot{M} \sim 2 \cdot 10^{-7} M_{\odot} \text{ yr}^{-1}$ (Waters et al., 1988) while the polar wind component produces a mass loss rate one order of magnitude lower. The total luminosity of the star is $L \approx 10^{38}$ erg s $^{-1}$. The system is measured to be at a distance of 2.0 ± 0.2 kpc as derived by Frail and Hjellming (1991) and this distance is assumed in luminosity values presented in this thesis unless stated otherwise.

The orbital parameters like orbital phases of the periastron; superior conjunction and inferior conjunction as well as the inclination, eccentricity and mass ratio function are vital parameters for any model of the emission from LS I +61°303. Spectroscopic investigations are needed to obtain these parameters from radial velocity measurements. To obtain the radial velocity, the doppler broadening of spectral lines of the optical companion are used. The doppler broadening indicates the relative movement of the optical companion with respect to the observer. By evaluating these line broadenings in relation to the orbital phase, the parameters of the relative orbit of the compact object can be determined.

Precise measurements of these parameters were carried out by Casares et al. (2005), who used the He lines for the measurements. Other studies of Grundstrom et al. (2007) reported different parameters and the inconsistency of the parameter sets indicate additional systematic effects in the measurements. The best parameters up to date are reported from the analysis of a huge set of historical data including all previous measurements in Aragona et al. (2009b). In this publication, the differences in the previous measurements are discussed and resolved. In most publications about LS I +61°303 the values of Casares et al. (2005) are used. In this thesis, new more precise values will be taken for the interpretation. The different values are listed in Table 7.1 and their orbital solutions are shown in Fig. 7.1.

Element	Hutchings and Crampton (1981)	Casares et al. (2005)	Aragona et al. (2009b)
e	0.60 ± 0.13	0.72 ± 0.15	0.537 ± 0.034
ϕ_p	0.25 ± 0.04	0.23 ± 0.02	0.275
$f(M) [M_\odot]$	0.019 ± 0.015	$0.011^{+0.016}_{-0.008}$	0.012 ± 0.002

Table 7.1: The orbital parameters of LS I +61°303: eccentricity (e), periastron passage (ϕ_p) and mass function $f(M)$.

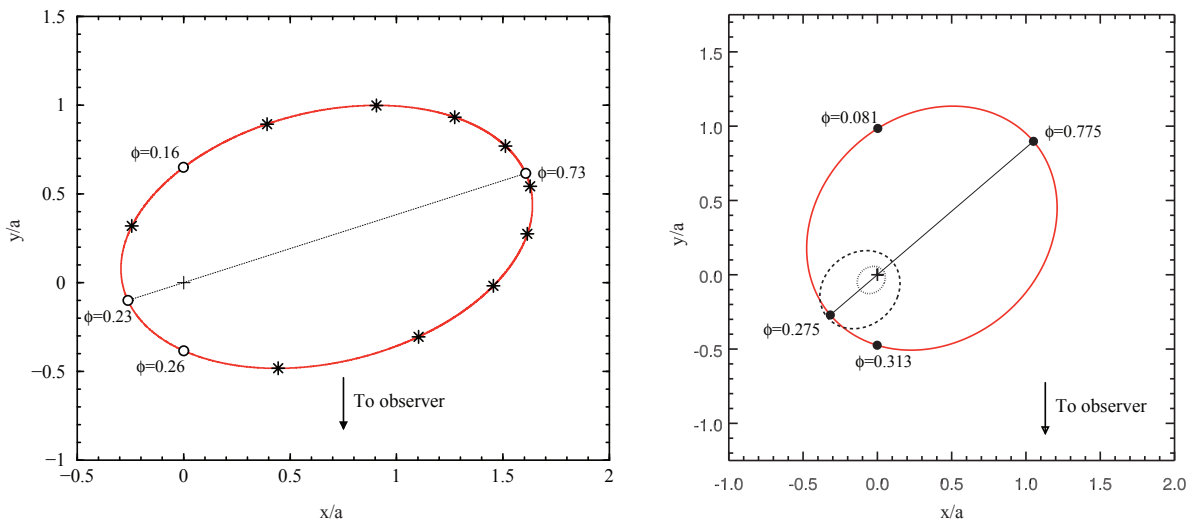


Figure 7.1: The left panel shows the orbital solution of LS I +61°303 obtained by the Casares et al. (2005) measurements and the right panel the preferred solution obtained from a much larger data sample by Aragona et al. (2009b). The relative orbit of the compact object is shown in red and the phases (ϕ) of periastron, apastron, superior conjunction and inferior conjunction marked by circles. The center of gravity is indicated by a cross and the units of the x - and y -axes are fractions of the major semiaxis (a) of the system. In the left figure, the relative orbit of the optical companion is shown for a $4 M_\odot$ (dashed) and $1.1 M_\odot$ (dotted) compact object.

7.2 The multiwavelength behavior of LS I +61°303

In this section, the general multiwavelength behavior of LS I +61°303 is described. The description is divided into radio, X-ray and high energy ($E > 100$ MeV) gamma-ray sections. This description is necessary in order to compare the multiwavelength data obtained in this thesis with the general behavior of LS I +61°303 at these wavelengths.

7.2.1 The radio behavior of LS I +61°303

The discovery of the highly variable radio source GT 0236+610 by Gregory and Taylor (1978) and its possible association with the gamma-ray source CG135+1, made this source very interesting and started a detailed study of it in all wavelengths. While the radio source was immediately associated with the optical star LS I +61°303, the final confirmation of the system as a gamma-ray emitter could not be made before the MAGIC detection, as reported in Albert et al. (2006) and this work.

The system was studied at radio frequencies in more detail and a periodic modulation of the signal with $P = 26.52 \pm 0.04$ d was found (Taylor and Gregory, 1982). Currently, the best known orbital period is derived from long-term radio measurements by the Green Banks Interferometer (GBI) combined with the earlier published radio measurements and reported to be $P = 26.4960 \pm 0.0028$ d (Gregory, 2002). In addition to the orbital periodic emission, there is evidence for a super orbital modulation which has the result that the phases of the radio outbursts in LS I +61°303 are not phase-locked with respect to the orbital period. The super-orbital period is derived to be $P_{sup} = 1667 \pm 8$ d and, for both periods (orbital and super-orbital), the time of $\phi = 0$ is set to $T_0 = 2443366.775$ JD which is an arbitrary choice by Gregory (2002) but commonly used in studies of LS I +61°303 at all wavelengths. So I adapted these values and they will be assumed in all periodicity discussions, if not explicitly mentioned otherwise.

The spectral index of the various radio measurements indicate a hard power law which favors the interpretation of the radio signal as synchrotron emission produced by relativistic electrons. The process by which the relativistic particles are produced is still debated. A possible acceleration of particles in a relativistic collimated outflow (jet) is suggested after European Very Long Baseline Interferometry Network (EVN) and Very Long Baseline Interferometer (VLBI) radio observations which yield evidence for an elongated emission feature in LS I +61°303. This is interpreted as a mildly ($v > 0.4c$) relativistic jet by Massi et al. (2001). Additional radio measurements with the Multi-Element Radio Linked Interferometer Network (MERLIN) on two consecutive days (April 22 and 23, 2001) yielded an elongated

feature of 200 mas scale on the radio map which changed the position between the two measurements. This was interpreted in terms of a possible precessing jet and seemed to confirm the classification of LS I +61°303 as a microquasar (Massi et al., 2004).

A much more detailed VLBI observation of a full orbital cycle of LS I +61°303 conducted by Dhawan et al. (2006) gives serious doubts about the classification of LS I +61°303 as a microquasar. The radio maps obtained yield pictures of a rapidly changing radio morphology in the source which is not compatible with the classical understanding of jet-like features. The authors of the measurement suggest that the radio emission displays the deformation of the pulsar wind by the Be star wind. A slightly corrected¹ schema of the emission along the orbit of LS I +61°303 is shown in Fig. 7.2. A counter-argument to save the microquasar scenario is that the VLBI maps show much smaller scales compared to the MERLIN map which indicates the jet-like feature. So the jet might not be clearly developed at the smaller scale and might be only identified on larger scales. Furthermore, measurements carried out as part of a MW campaign with MAGIC and MERLIN on several different days do not show a jet-like feature (Albert et al. (2008d) and this work). Thus no strong evidence for a persistent radio jet in the binary LS I +61°303 is at hand at any scale. Nevertheless, a final conclusion about the emission from LS I +61°303 cannot be found by studying a single wavelength band.

7.2.2 The X-ray behavior of LS I +61°303

The first discovery of X-rays from LS I +61°303 was achieved by the *EINSTEIN* satellite (Bignami et al., 1981). While the identification of LS I +61°303 as the counterpart of the newly discovered X-ray source was firmly proven by positional coincidence with the radio source, no indication of flux variability nor information about the spectral distribution of the X-rays could be obtained. The first spectral information of the X-ray emission comes from *ROSAT* observations between 0.1–2.4 keV (Goldoni and Mereghetti, 1995). These measurements established LS I +61°303 as a variable X-ray source and reported a hard ($\Gamma = 1.1 \pm 0.3$) power law as the best description of the X-ray spectrum. The first simultaneous radio and X-ray observations of LS I +61°303 were carried out with the *ROSAT* satellite and the VLA observatory (Taylor et al., 1996). An outburst in both energy bands with a duration of ten days is reported with flux variations of a factor of ten at both energies. The observations revealed a possible anticorrelation between the radio and X-ray LC since the radio emission peaks at phase 0.95 while the X-ray peak occurs at phase 0.5.

¹The original plot by Dhawan et al. (2006) is produced using the older orbital solution of Casares et al. (2005).

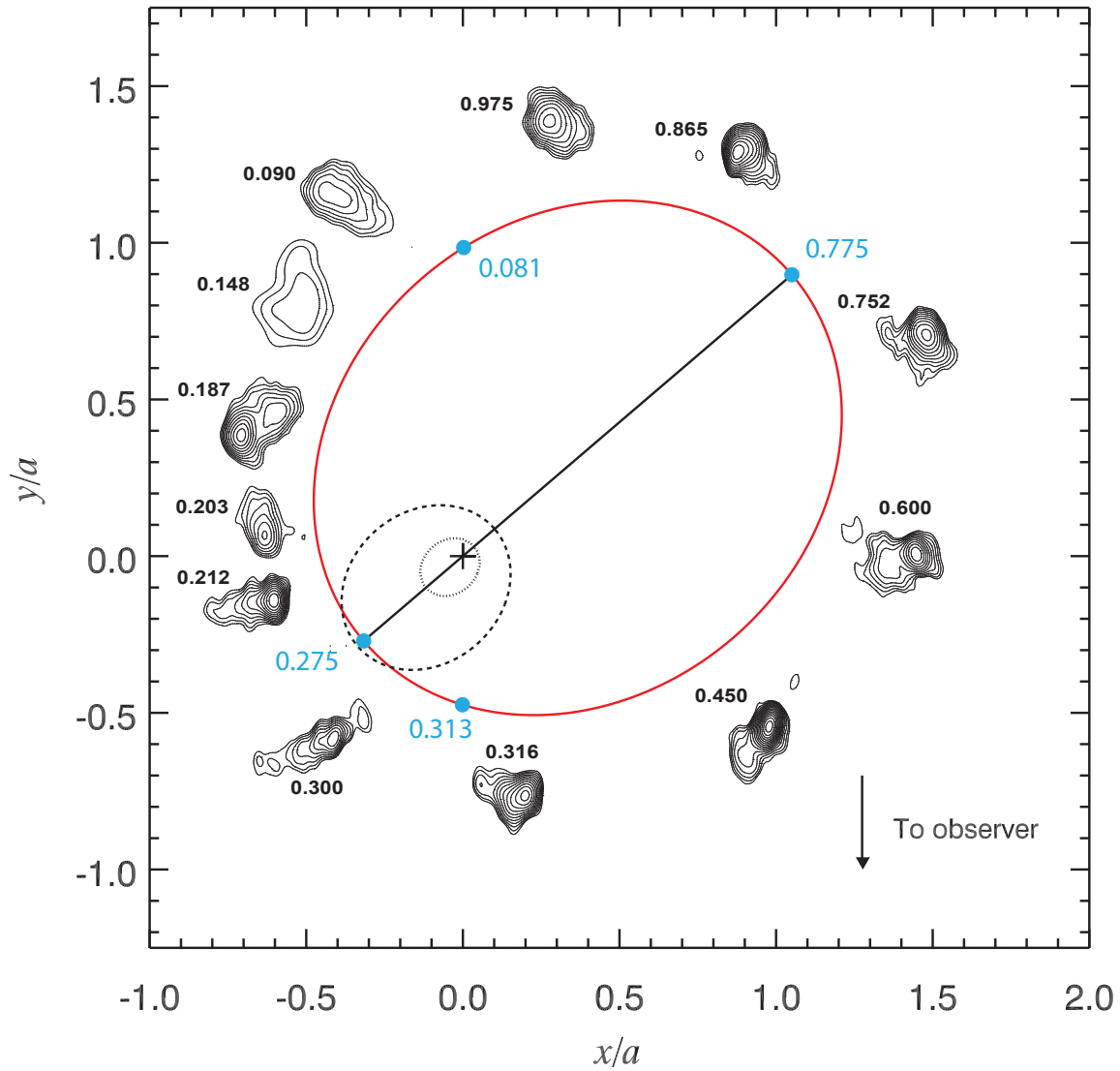


Figure 7.2: Shown is the schematic view of the orbital solution of LS I +61°303 and the (roughly) aligned VLBI radio contour maps obtained by Dhawan et al. (2006). The black labels correspond to the orbital phase where the radio images are obtained and the blue points and labels indicate the periastron passage, inferior and superior conjunction and the apastron passage. The red ellipse denotes the relative orbit of the compact object while the relative orbit of the Be star is indicated by a dashed line for a compact object of $4 M_{\odot}$ and dotted for $1.4 M_{\odot}$.

The *ASCA* X-ray satellite observed LS I +61°303 in 1994 with two pointings of each 18–19 ks in the same orbital cycle (Leahy et al., 1997). The obtained spectra are best fitted by absorbed power laws. The spectral index for the first pointing is $\Gamma = 1.63$ – 1.78 and for the second pointing $\Gamma = 1.75$ – 1.90 indicating a slight variation in the spectral index. An upper limit of 9×10^{-6} photons $\text{cm}^{-2} \text{s}^{-1}$ for a possible iron line at 6.4 keV is derived.

In several publications, evidence for periodic X-ray emission is reported (Leahy, 2001; Paredes et al., 1997; Wen et al., 2006) and the derived periods agree, within errors, with the orbital period. All these observations used the all sky monitor (ASM) instrument on board of the *RXTE* satellite. The data set was always only a small subset of the up-to-now collected data by ASM. A search for periodicity conducted by me in the full data set of ASM (~ 13 y) did not yield any significant periodicity. This probably explains why only the first 2.5 y are used in the most detailed periodicity analysis up to now by Wen et al. (2006) and not the full 8.5 y of data used for the periodicity study of the other X-ray sources in the same publication. It is also an indication that there is no persistent periodicity present in the X-ray LC.

More sensitive X-ray observations were carried out in 2002 with *XMM-Newton* (0.3 – 10 keV) and from 2003 to 2005 with *INTEGRAL* (Chernyakova et al., 2006). The *XMM-Newton* data revealed a variable flux with the highest emission after phase 0.5 to 1.0 and minimum flux at phase 0.23. The derived spectrum is compatible with a pure power law and the spectral index is reported to vary with phase. Closer investigation yields indication that the spectral index softens during the transition between high and low flux states. No indications are found of a thermal (black body) spectral component or line emission as would be expected in the case of the presence of an accretion disk around the compact object.

In January 2005 another deep (~ 50 ks) *XMM-Newton* exposure was taken and the data revealed a fast (order of 1000 s) drop in the X-ray flux accompanied by a softening in the spectral energy distribution (Sidoli et al., 2006). In the same work, archival *BeppoSAX* data is published which hints at two different spectral states in the hard X-rays (15–70 keV) as well. The spectral hardening with increasing flux is most likely present in soft (2–10 keV) and hard X-rays. The high flux state is found in orbital phases $\phi \in [0.4, 1.0]$ and thus deviated from earlier reports of Paredes et al. (1997). Since no correlation between the X-ray spectral parameters and the super-orbital modulation reported in radio observations could be found, it is unclear if LS I +61°303 exhibits periodic X-ray emission or maybe only partly² periodic emission.

²see section 5.4.1 for the definition of partly periodic

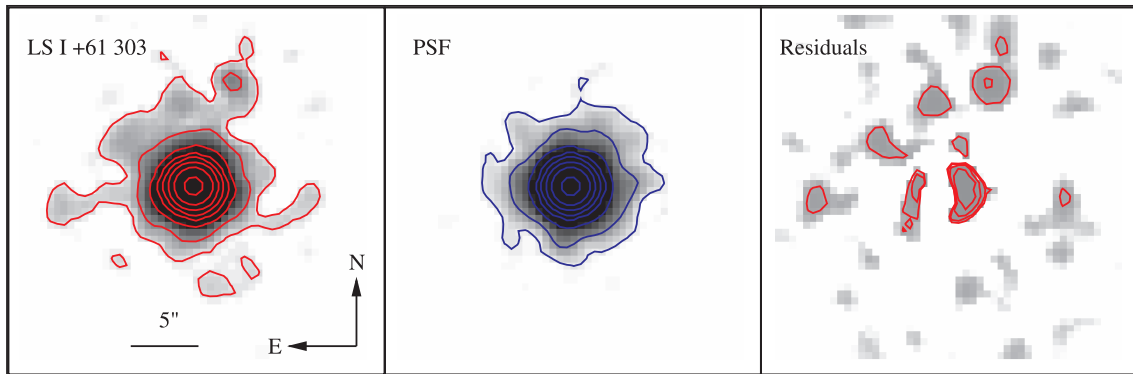


Figure 7.3: The left panel displays the X-ray image of LS I +61°303 obtained from a 50 ks *Chandra* exposure. The middle panel shows the expected PSF of *Chandra* corrected for the source position in the detector and the right panel shows the residuals after subtracting the PSF from the LS I +61°303 image. No clear jet-like structure can be seen; only some small regions to the NE of the source with low significance (3.2σ) are left after the PSF subtraction. LS I +61°303 is not resolvable, even for the best available angular resolution in X-rays. Figure taken from Paredes et al. (2007).

To investigate further the nature of the X-ray emission, the excellent angular resolution of *Chandra* was used by Paredes et al. (2007). This measurement gives the up-to-now most precise dimensional picture of LS I +61°303 in X-rays. The skymap is shown in Fig. 7.3. One of the main motivations of this study is the search for small scale hard X-ray jets which would be likely to be present in the case of the microquasar scenario (see e.g. Punsly (1999)). Even with the excellent angular resolution of *Chandra* no hard small scale X-ray jets or other significant features can be detected. First indications by low significant (3.2σ) X-ray excesses to the north-east of the source hint at an almost high enough angular resolution to resolve LS I +61°303. Unfortunately, no X-ray mission is planned in the near or midterm future which surpasses the angular resolution of *Chandra*, so LS I +61°303 will not be resolved at X-ray energies for a long time.

One interesting fact of the *Chandra* data is that a spectral index of 1.25 ± 0.09 is obtained for the energy range 0.3–10 keV. This is considerably harder than any value measured before or (up-to-now) afterwards³. This is remarkable since the spectral index is much harder than the canonical value of 1.5 which would be produced by an electron population following a power law of index $\Gamma = 2$ which is generally the result of shock acceleration.

More recent studies by the *Swift* XRT camera (Esposito et al., 2007), which are con-

³The earlier measurement by *ROSAT* yielded an even harder spectral index but the energy range is very narrow and thus the result affected by larger uncertainties compared to the later measured spectra.

temporaneous to the MAGIC OC II but are not strictly simultaneous with the MAGIC measurements, monitored the system over several orbital periods. Again, the spectral properties of LS I +61°303 could be well described by an absorbed power law and no indication of thermal components or line emission are observed. This data is the first sensitive study over several orbits of LS I +61°303 in X-rays. Still the statistical errors of the data did not allow the derivation of meaningful energy spectra for individual observations or phase bins ($\Delta\phi = 0.1$). A high X-ray flux is observed in the phaserange $\phi \in [0.5, 0.8]$ and in $\phi \in [0.0, 0.1]$. The authors report short time variability on a sub-hour timescale which is in agreement with the previous *Chandra* and *XMM-Newton* observations (Sidoli et al., 2006; Paredes et al., 2007).

To summarize the X-ray observations of the past 30 years, it is evident that LS I +61°303 is not easy to classify. The system shows clear variable X-ray emission with fluctuations up to factors of ten but, in general, in the order of three to four within several hours, as well on timescales of less than 1000 s. While indications for periodic emission were found in the past, these are not clearly seen in later measurements. The peak emission is not locked to a specific orbital phase range but yield different results for the individual observations. Very good agreement is found in the spectral shape and the hydrogen column density $N_{\text{H}} \sim 0.5 \cdot 10^{-22} \text{ cm}^{-2}$ for the absorption of the X-ray photons. No orbital variation are found in the column density which is expected if the X-rays are produced in the direct vicinity of the compact object orbiting the variable photonfields of the Be star (Leahy et al., 1997; Paredes et al., 2007). This is a pending problem which needs further investigation.

No experiment found X-ray pulsation from a possible neutron star as the compact object nor is a clear feature of an accretion disc such as a black body component or Fe line emission seen in any spectrum obtained so far.

7.2.3 The high energy emission from the vicinity of LS I +61°303

The first report of high energy ($E > 100 \text{ MeV}$) gamma-rays from the direction of LS I +61°303 came from *COS B* (Hermsen et al., 1977). Due to the large positional uncertainty of the *COS B* experiment, the association with the variable radio source was not unambiguous. The quasar 4U0241+62 is contained in the same field of view and would also have been a possible counterpart. The more precise measurements by the EGRET instrument on board the Compton Gamma Ray Observatory (*CGRO*) also detected a high energy gamma-ray source (2EG J0241+6119) in the same direction (Kniffen et al., 1997). The better positional accuracy of EGRET compared to *COS B* favored LS I +61°303 as a counterpart for the high energy emission but could not prove the association. The search for flux periodicity in

the emission is not conclusive from the EGRET measurements, despite many attempts to do so (Kniffen et al., 1997). At least a hint for variability could be found after analyzing all of the data collected by EGRET (Tavani et al., 1998; Torres et al., 2001).

The spectral energy distribution reported by Kniffen et al. (1997) is compatible with a pure power law with spectral photon index $\Gamma = 2.05 \pm 0.06$. The orbital phase averaged integral flux above 100 MeV is reported to be $F = (7.9 \pm 0.5) \times 10^{-7}$ photons $\text{cm}^{-2} \text{s}^{-1}$ which corresponds to a luminosity of $\sim 2 \times 10^{34} d_{\text{kpc}}^2 \text{erg s}^{-1}$ (here d_{kpc} is the distance in kiloparsec). This means that the luminosity of LS I +61°303 is considerably higher in gamma-rays compared to X-rays. There are only two other systems displaying the same behavior and both are detected in VHE gamma-rays.

At slightly lower energies (1–30 MeV), an excess from the direction of LS I +61°303 was found by COMPTEL⁴ (van Dijk et al., 1996). The excess seen in the data cannot be associated with LS I +61°303 alone, since the angular resolution of 1° leads to contamination of emission from the quasar 4U0241+62. In addition, only a low significant excess of about 3σ is reported. Thus definite conclusion about the emission mechanism of LS I +61°303 from the COMPTEL data are difficult to make.

The clear identification of LS I +61°303 as a gamma-ray emitter had to await the high sensitivity measurements by MAGIC presented in this thesis. Despite the results from MAGIC, which considerably improve our understanding of the system, it is very important to have an SED which covers the whole energy range and, if possible, without any gaps. The new high energy gamma-ray satellite *FERMI*⁵ detected LS I +61°303 without any doubt as a high energy gamma-ray emitter. Up to now, a daily LC is available along with some preliminary results shown at conferences. The LAT instrument on board *FERMI* is, in principle, sensitive to gamma-ray energies up to $E = 300$ GeV but the small effective area of the instrument makes very long integration times necessary to obtain enough statistics to provide meaningful measurements above 100 GeV. So far, no phase resolved energy spectrum is published by the *FERMI* collaboration nor simultaneous measurements with MAGIC performed and thus the *FERMI* data cannot be used in this thesis to constrain the emission models of LS I +61°303.

7.3 VHE gamma-ray observations with MAGIC

The binary system LS I +61°303 is the most detailed studied binary system with the MAGIC telescope. The system was observed in three different cycles (spanning from 2005 to 2008) which I will call observation campaigns (OC). The observation in OC I led to the discovery

⁴COMPTEL was a part of *CGRO* as well as EGRET.

⁵*FERMI* was launched after the LS I +61°303 observations of MAGIC presented in this thesis.

of LS I +61°303 as a VHE gamma-ray emitter. The OC II and OC III were conducted to study the emission properties of the system further. The OC II was mainly motivated to test for periodicity in the variable emission of the system and the OC III was performed to obtain the first strictly simultaneous multiwavelength LC and SED.

The observation parameters like the zenith angle (ϑ), observation time, phase coverage, number of orbital periods observed and the fraction of moon observation time are given in Table. 7.2.

OC	Date	T_{obs} [h]	% T_m	ϑ [deg]	Φ -range	#P	FADC	Mode
I	2005-09 - 2006-03	54	22	32-55	0.1 - 0.8	6	300 MHz	ON/OFF
II	2006-09 - 2006-12	112	17	32-44	0.0 - 1.0	4	300 MHz	wobble
III	2007-09 & 2008-01	58.8	32.7	32-44	0.4 - 0.1	3	MUX	wobble

Table 7.2: The OC number, the observation start and end month, the observation time and its percentage under moonlight, the zenith angle and orbital phase range covered, the number of orbital periods observed, the read-out system used and the observation mode.

Most of the data are taken with different hardware setups and observation modes. The improved hardware setup and performance of MAGIC I after 2007 result in a more sensitive analysis in OC III compared with the previous measurements. However, the measured fluxes in OC III are affected by the 12% systematic shift (to higher flux values) compared to the other OC's as described in chapter 6.3.

In OC I, the observations are spread over the largest number of orbital periods but the sampling of each individual orbit is much more sparse compared to the other OC's. The reason for this difference is that most theoretical models predicted significant fluxes around the periastron passage of the compact object and thus the observations are scheduled around this phase. After failing to detect VHE gamma-ray emission in this phase range (best periastron value known during OC I $\phi_{per} = 0.23$) within three orbital periods, the observations were extended to higher phase values. With the knowledge about the emission of OC I the phase coverage of OC II is much better and, for the first time, the system is observed during all phases but the sampling in OC II is still most dense around the emission phases found in OC I.

In OC III, the observation time per night is greatly increased during all observations. This is required in order to be able to derive spectra for individual nights and to reduce the statistical errors for each LC point. This is vital for the correlation studies of the emission in different energy ranges. The more detailed observations in OC III are much more sensitive compared to the previous observations since exploiting the time information improved the sensitivity by 40%.

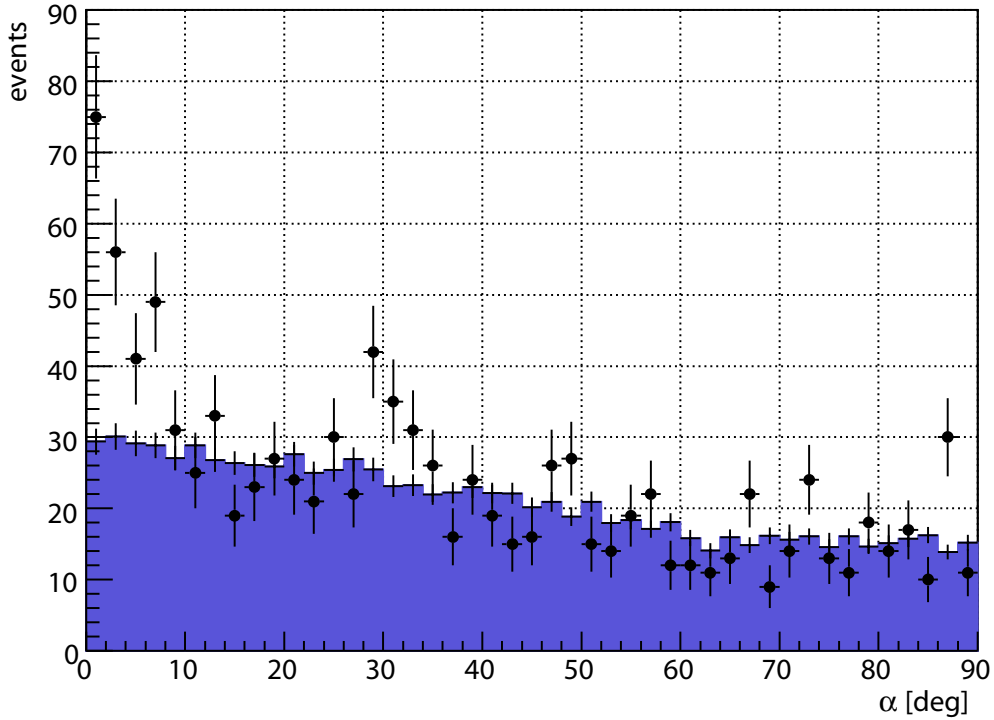


Figure 7.4: The α distribution of the events obtained from LS I +61°303 in the phaserange $\phi \in [0.6, 0.7]$ during OC I is shown as black points. The background sample data with the same selection cuts applied is shown by the blue region. An excess of 103.5 ± 16.1 events was observed above a background of 117.5 ± 6.1 events for $\alpha < 8^\circ$. The significance with seven trials (without) is 6.8σ (7.2σ).

7.4 LS I +61°303 a VHE gamma-ray emitting binary

With the MAGIC observations, VHE gamma-ray emission is reported for the first time from the HMXB LS I +61°303. The system is not detected during all of its orbital phases and the signal is strongest in the orbital phase range 0.6–0.7 (The orbit of a binary is divided in phases ϕ reaching from 0.0 to 1.0). The α -Plot (see chapter 5.1.7) for the phase range 0.6–0.7 given in Fig. 7.4 shows a clear detection with 7.2σ significance in $t_{\text{obs}} = 3.7$ h above an energy of $E > 400$ GeV. Taking into account the seven trials (one for each orbital phase bin $\Delta\phi = 0.1$ observed in OC I) the significance is slightly reduced to $\sim 6.8\sigma$ - which is still a very significant detection.

The position of the VHE gamma-ray excess agrees excellent with the position of the Be star of LS I +61°303 as shown in Fig. 7.5. This establishes undoubtedly LS I +61°303 as the source of gamma-rays seen at lower energies by *COS B* and EGRET.

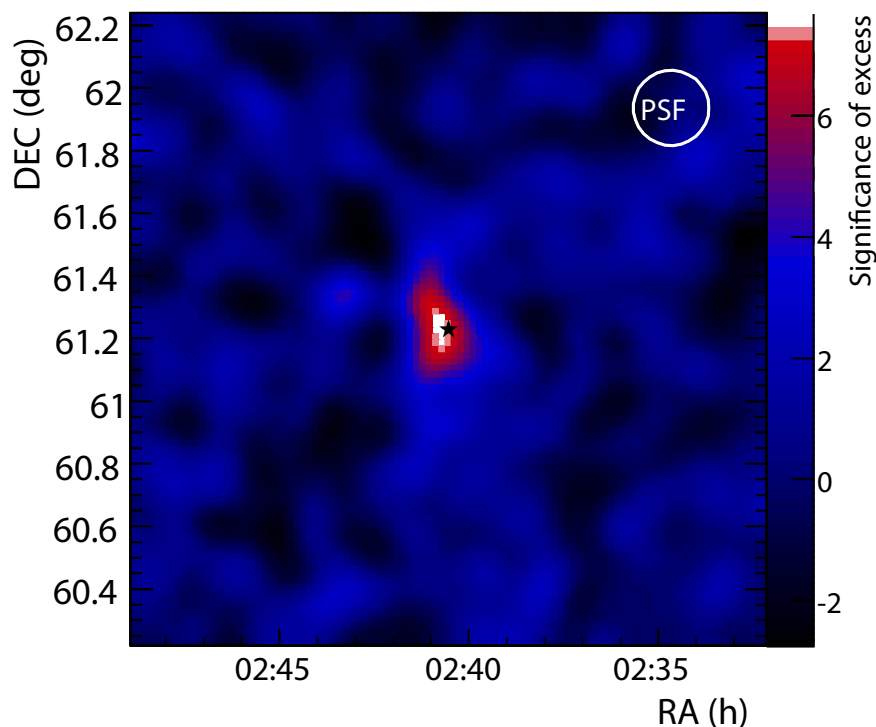


Figure 7.5: The significance of the VHE gamma-ray signal obtained from each sky position. The PSF of MAGIC is shown in the upper right. The emission is point like for the angular resolution of MAGIC. The position of LS I +61°303 is marked by the star and agrees excellent with the VHE gamma-ray source discovered by MAGIC. The plot is obtained from OC III for the phase range 0.6–0.7.

7.5 The temporal behavior of the integral flux measurements

As described in the previous section, one of the main interests in the observation of LS I +61°303 is the temporal variation of the emission. The temporal variations are studied in terms of a diurnally binned LC and an orbital phase binned ($\Delta\phi = 0.1$) averaged LC. It should be noted that the effective observation time for each night is different resulting in a non-uniform sensitivity of the individual LC points. To obtain the LC points, the integral flux above an energy of $E > 400$ GeV is extracted from the data. The analysis energy threshold is chosen a bit higher compared to other mid-zenith angle observations to reduce systematic effects near the trigger threshold and allow the use of the same threshold for all OC's. With smaller systematic effects, the interpretation of the results is more robust and the data from different OC's can be compared without possible bias due to threshold uncertainties. For OC III, with its much higher sensitivity measurements, the LC is derived as well for $E > 300$ GeV and a lower cut in $S > 250$ phe. The higher sensitivity enables a more detailed study of the

system. The obtained measurements are given in Table 7.3 for the phase-averaged LC and in Table 7.4 for the diurnal LC for all OC's. The data partially taken under moonlight conditions is marked by an asterisk and an additional systematic uncertainty of 10% is assumed for these measurements (see chapter 6.5). This assumption is a very conservative one since it is based on the investigations of data taken only under moonlight while the affected nights of the LS I +61°303 observations were only partially performed in the presence of the moon.

In addition to the data presented in Table 7.4, the values for the analysis above $E > 300$ GeV are given in appendix A.1. These values are used for the interpretation if no direct comparison to the previous OC's is made.

The LC's for the different OC's are folded with the orbital phase as derived from the most precise radio measurements ($T_0 = 43366.275$ MJD, $P = 26.4960$ d (Gregory, 2002)) are shown in Fig. 7.6, Fig. 7.7 and Fig. 7.8. The LC's are derived for the integral flux $F(E > 400$ GeV) and in addition for OC III above $E > 300$ GeV (see Fig. A.1 in appendix A.1). The phasefolding is justified since the TeV emission is periodic (with the orbital period) as shown in this chapter.

From the LC's of the different OC's, it is immediately evident that the highest emission in the averaged phasefolded LC occurs almost always in the phase range 0.6–0.7. This emission is seen as an emission peak (outburst) in almost all (five out of six) orbits of the system as observed in this phase range. The position of the highest emission seems not to be constant in orbital phase but might shift slightly in the phase range 0.6–0.7, if compared between different orbits. In addition, the emission flux level is slightly variable between different observed orbits as well. The sampling of the emission peak might cause some shift in the emission level but this seems not to be the sole reason for the different flux levels of the peak emission. If only the sampling would be responsible for the slightly variable flux levels, then the peak should be exactly at the same phase in all orbits; however this is not the case, as can be seen from the LC's if, for example, the last orbit observed in OC I is compared to the first orbit of OC III.

The emission in the phase range 0.6–0.7 has the shape of an outburst which has a duration of about 2–4 nights. A detailed determination of the shape of this outburst is not possible since the sampling is too coarse (consecutive measurements one day apart) and even larger gaps are present in some orbits due to bad weather conditions. From the individual diurnal LC's, it is evident that the maximum flux level is restricted to one night (see e.g. first orbit of OC II and OC III) and then falling off within one to two days. The determination of the outburst shape requires the definition of a start- and end-orbital phase of the outburst. To do so, the deviation between the last baseline flux point of the system and the first flux

Orbital phase	OC I		OC II		OC III	
	Flux	Flux UL	Flux	Flux UL	Flux	Flux UL
	10^{-12} ($\text{cm}^{-2} \text{s}^{-1}$)					
0.0–0.1	3.7 ± 2.3	8.5	1.5 ± 0.9	3.3
0.1–0.2	0.4 ± 0.9	2.3	0.2 ± 1.2	2.7
0.2–0.3	0.9 ± 0.8	2.5	0.3 ± 0.9	2.2
0.3–0.4	1.3 ± 0.9	3.0	-1.2 ± 2.8	4.3
0.4–0.5	3.4 ± 0.9	...	0.7 ± 0.8	2.4	-0.3 ± 1.0	1.8
0.5–0.6	4.1 ± 1.2	...	3.1 ± 1.0	...	-0.1 ± 0.8	1.4
0.6–0.7	10.4 ± 1.6	...	7.9 ± 0.9	...	5.7 ± 0.9	...
0.7–0.8	3.1 ± 2.7	8.8	4.3 ± 1.2	...	0.1 ± 0.9	1.9
0.8–0.9	2.8 ± 1.1	...	5.1 ± 1.2	...
0.9–1.0	0.7 ± 2.0	4.8	3.1 ± 0.7	...

Table 7.3: The averaged flux and 95% flux upper limits (UL) for fluxes less than 2σ significance for the individual OC's.

point in the outburst must be significant. No baseline flux is detected in VHE gamma-rays and besides the highest emission, during the outburst in the phase range 0.6–0.7, no significant (more than 3σ) detections occur in directly adjacent phase bins. While individual nights outside of the outburst emission do not show significant fluxes the investigation of the phase bin- averaged LC might reveal a baseline flux. From Table 7.3, it can be seen that the adjacent phase bins of the main emission bin show a signal in some OC's while, in other OC's, no significant signal is detected. The detected signal significance depends on the observation time spent for each phase bin in individual OC's. Still, if one compares the measurements in the same orbital phases between individual OC's, some variability is visible but no base line flux, which should be constant, is detected. Without more sensitive measurements, it is not possible to determine a baseline flux level. The upper limits in the phases outside of the main emission (e.g. $\phi \in [0.2, 0.3]$ or $\phi \in [0.7, 0.8]$ in OC III) suggest a much lower baseline flux level when compared to the outburst emission, if it exists at all. Furthermore, a determination of the FWHM of the outburst requires an even more detailed sampling compared to OC III and shall be studied in the future with stereo observation by MAGIC I and II.

According to the orbital solution of the optical measurements on LS I +61°303 the peak emission in VHE gamma-rays occurs close to the apastron passage of the compact object. The other significant detections of the system occur in phases close to the main emission. A feature only visible in OC III is the high significant ($\sim 7\sigma$) emission in the phase range 0.8–1.0 which is not seen in earlier OC's apart from a sharp peak at phase 0.84 in the last

orbit of OC II. This might be an indication of some super-orbital modulation of the emission or that there are additional non-periodic emission components in LS I +61°303. The higher sensitivity is an advantage of OC III but the phase-averaged flux for the phase range 0.8–1.0 is high enough to be detected in OC II as well. The phase bin averaged flux measured in OC II is still compatible with the OC III measurements (see Table 7.3). When comparing the diurnal LC's of these phases in OC II and OC III, it is clear that only the night of $\phi = 0.84$ (MJD 54092.92) contributes to the averaged flux in OC II, while in OC III not a single but several nights contribute to the flux (compare Fig. 7.7 and Fig. 7.8). This provides evidence that the flux level in the phase range 0.8–1.0 is a time-dependent effect and not linked to the orbital phase alone. This raises the very interesting question of what mechanism causes the variability of the emission and whether both components are produced by the same particle population. This question cannot be solved by the MAGIC measurements alone but needs additional multiwavelength data, as presented in later sections.

Finally, it is interesting that the system is not detected in the phase range 0.2–0.3 in which the periastron passage of the compact object occurs. The derived flux upper limits are below the lowest significant measured flux in the whole orbit and thus any possible VHE gamma-ray emission around periastron must be below the sensitivity of MAGIC I.

Middle Time (MJD)	Obs. Time (min)	Phase	Flux 10^{-12} ($\text{cm}^{-2} \text{s}^{-1}$)	Flux upper limit 10^{-12} ($\text{cm}^{-2} \text{s}^{-1}$)
53650.12	99	0.13	0.1 ± 1.1	2.4
53654.12	79	0.28	1.1 ± 2.6	6.4
53655.11	151	0.32	0.4 ± 1.7	4.0
53677.07	151	0.15	-0.4 ± 1.9	3.5
53678.03	106	0.18	1.1 ± 2.0	5.2
53679.03	87	0.22	-1.3 ± 2.4	3.9
53680.06	145	0.26	-0.3 ± 1.8	3.4
53681.04	143	0.29	-1.0 ± 1.9	3.0
53682.04	174	0.33	-0.9 ± 1.5	2.3
53706.01	88	0.24	2.6 ± 2.1	6.9
53706.97	146	0.27	0.0 ± 1.6	3.2
53707.94	72	0.31	2.8 ± 2.1	7.2
53708.97	148	0.35	4.1 ± 1.8	...
53710.98	68	0.43	1.4 ± 2.4	6.5
53736.83	16	0.40	5.1 ± 5.8	17.9
53737.86	81	0.44	1.5 ± 2.2	6.1
53738.84	13	0.48	-1.8 ± 4.6	9.3
53740.96	77	0.56	3.9 ± 2.3	8.6
53763.88	116	0.42	3.7 ± 1.9	7.6
53764.88	116	0.46	4.2 ± 1.9	...

Middle Time (MJD)	Obs. Time (min)	Phase	Flux 10^{-12} ($\text{cm}^{-2} \text{s}^{-1}$)	Flux upper limit 10^{-12} ($\text{cm}^{-2} \text{s}^{-1}$)
53765.88	106	0.50	4.6 ± 2.1	...
53766.86	40	0.53	1.0 ± 1.5	4.4
53767.88	97	0.57	5.4 ± 2.2	...
53768.88	104	0.61	11.2 ± 2.3	...
53769.88	66	0.65	4.3 ± 2.3	9.1
53782.90	104	0.14	0.1 ± 1.8	3.9
53783.90	116	0.18	0.4 ± 1.9	4.4
53784.90	96	0.21	2.7 ± 1.9	6.8
53785.89	114	0.25	5.1 ± 2.0	...
53788.89	103	0.37	0.8 ± 2.1	5.2
53789.89	96	0.40	0.8 ± 2.1	5.2
53790.89	95	0.44	5.3 ± 2.4	...
53792.88	83	0.52	3.5 ± 2.3	8.4
53796.88	51	0.67	16.1 ± 3.8	...
53797.88	52	0.70	3.4 ± 2.8	9.4
53798.91	5	0.74	-0.1 ± 8.7	23.8
53993.18*	137	0.08	3.7 ± 2.3	8.5
53994.17*	112	0.11	0.6 ± 2.7	6.2
53995.17*	157	0.15	-2.0 ± 2.2	3.0
53997.15	229	0.23	0.3 ± 1.8	4.0
53998.15	211	0.26	2.0 ± 2.0	6.0
53999.10	133	0.30	5.3 ± 2.4	...
54001.12	82	0.38	-3.6 ± 3.8	5.1
54002.09	188	0.41	2.4 ± 2.3	7.1
54003.08	144	0.45	1.8 ± 2.7	7.2
54004.08	158	0.49	-4.0 ± 2.5	2.5
54005.07	155	0.52	3.0 ± 2.5	8.1
54006.07	162	0.56	1.8 ± 2.7	7.2
54007.08	139	0.60	4.4 ± 2.8	10.2
54008.07	152	0.64	8.8 ± 3.1	...
54009.08	147	0.68	4.4 ± 2.6	9.7
54013.24	7	0.83	0.8 ± 10.7	26.7
54022.10*	186	0.17	1.7 ± 2.0	5.8
54023.10*	269	0.20	-2.9 ± 1.5	1.4
54024.08*	20	0.24	-0.4 ± 7.0	15.2
54029.02	134	0.43	-1.1 ± 2.5	4.1
54030.01	161	0.47	-0.4 ± 2.3	4.2
54031.01	163	0.50	5.9 ± 2.6	...
54032.01	139	0.54	3.4 ± 2.9	9.2
54035.11	150	0.66	12.7 ± 2.9	...
54039.09	93	0.81	-1.4 ± 1.2	1.7
54055.97	181	0.45	4.0 ± 2.2	8.5

Middle Time (MJD)	Obs. Time (min)	Phase	Flux 10^{-12} ($\text{cm}^{-2} \text{s}^{-1}$)	Flux upper limit 10^{-12} ($\text{cm}^{-2} \text{s}^{-1}$)
54056.96	223	0.48	-0.2 ± 2.1	4.2
54057.90	66	0.52	3.3 ± 3.8	11.2
54058.90	57	0.56	2.3 ± 3.3	9.2
54060.00	17	0.60	16.5 ± 6.8	...
54061.96	221	0.67	5.9 ± 2.2	...
54062.96	228	0.71	5.5 ± 2.1	...
54063.95	56	0.75	3.6 ± 4.0	12.1
54065.00*	71	0.79	4.5 ± 3.8	12.4
54066.02*	185	0.82	1.1 ± 2.4	5.9
54067.04*	188	0.86	0.3 ± 2.3	5.0
54068.08*	77	0.90	-1.5 ± 3.6	6.1
54081.89	17	0.42	-0.3 ± 5.4	12.6
54082.85	77	0.46	2.9 ± 3.7	10.6
54083.88	31	0.50	4.4 ± 5.3	15.9
54084.85	63	0.54	1.5 ± 4.5	10.8
54085.95	111	0.58	2.4 ± 1.4	5.5
54086.95	282	0.61	8.6 ± 1.8	...
54088.01	82	0.65	9.7 ± 3.6	...
54088.95	83	0.69	3.4 ± 2.9	9.4
54089.89	29	0.73	0.4 ± 3.7	9.0
54090.88	176	0.76	3.6 ± 2.2	8.1
54091.90	140	0.80	1.9 ± 2.8	7.6
54092.92	92	0.84	15.6 ± 3.8	...
54093.97	92	0.88	7.0 ± 3.5	...
54095.01*	57	0.92	1.1 ± 1.1	4.1
54096.02*	49	0.96	3.6 ± 4.4	12.8
54348.15*	203	0.47	-0.3 ± 1.0	1.8
54349.16*	210	0.51	-0.2 ± 1.2	2.4
54350.14*	215	0.55	-1.2 ± 1.3	1.8
54351.16*	220	0.59	1.1 ± 1.4	3.9
54352.16*	221	0.62	8.4 ± 1.5	...
54353.16	224	0.66	5.3 ± 1.4	...
54354.17	213	0.70	0.6 ± 1.3	3.1
54355.15	172	0.74	-0.4 ± 1.4	2.4
54356.14	149	0.77	0.8 ± 1.7	4.2
54357.15	178	0.81	3.2 ± 1.5	...
54358.15	179	0.85	4.5 ± 1.5	...
54359.15	184	0.89	0.8 ± 1.5	3.9
54360.15	177	0.93	4.0 ± 1.6	...
54361.15	183	0.96	0.8 ± 1.6	4.0
54362.15	189	0.00	-1.1 ± 1.5	2.2
54363.16	139	0.04	1.5 ± 1.7	5.0

Middle Time (MJD)	Obs. Time (min)	Phase	Flux 10^{-12} ($\text{cm}^{-2} \text{s}^{-1}$)	Flux upper limit 10^{-12} ($\text{cm}^{-2} \text{s}^{-1}$)
54364.15	196	0.08	2.7 ± 1.2	...
54464.86	131	0.88	2.3 ± 1.7	5.8
54465.86	131	0.92	4.1 ± 1.9	...
54466.87	100	0.95	5.7 ± 2.3	...
54467.86	121	0.99	5.7 ± 1.9	...

Table 7.4: Observation time, orbital phase, integral flux (above 400 GeV), flux upper limit at the 95% confidence level (given in case flux significance is $\lesssim 2\sigma$ (see (Rolke et al., 2005))). Nights partly taken under moonlight conditions are labelled with an asterisk. Horizontal double lines indicate the start of a new OC and horizontal single lines the start of a new orbital period.

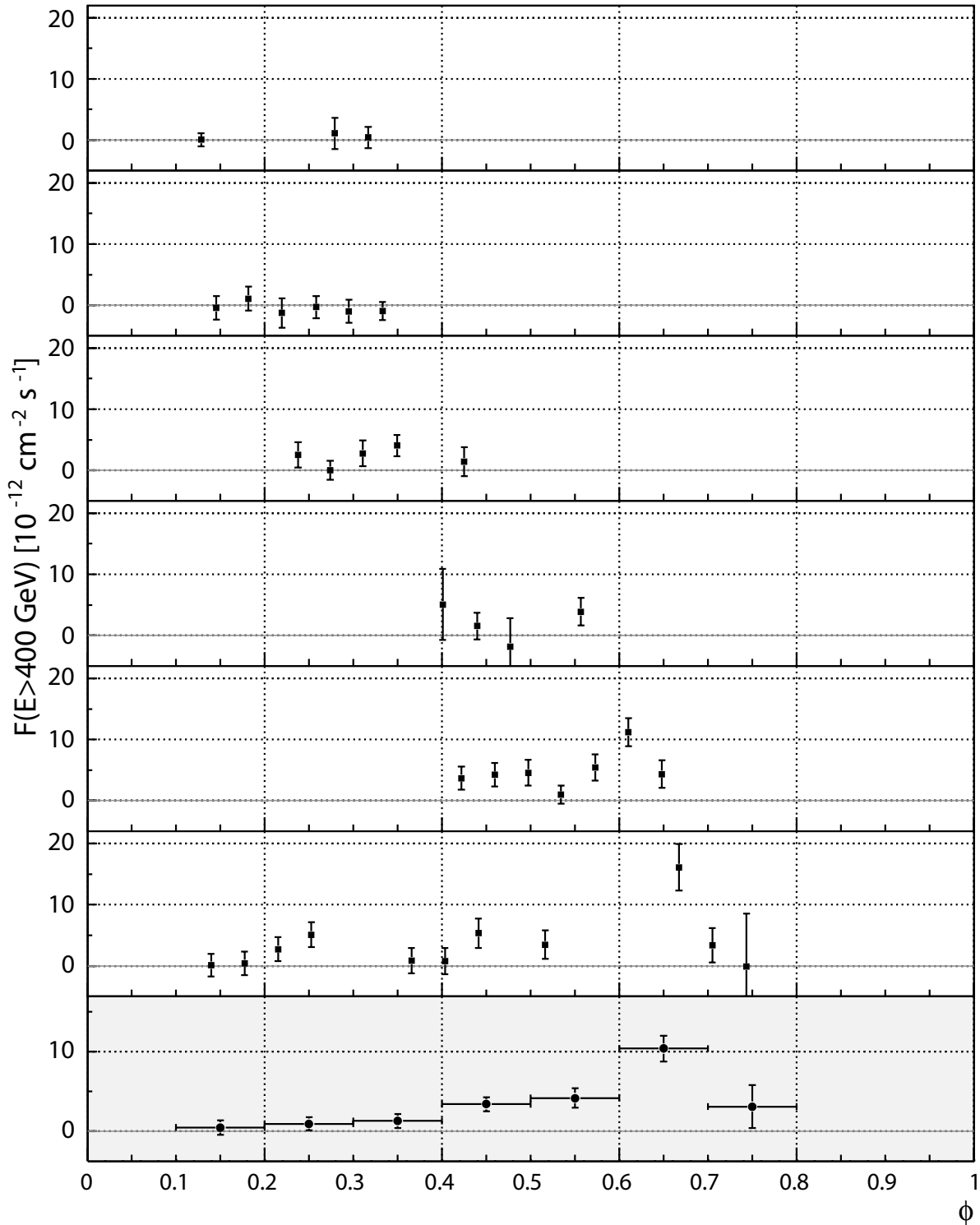


Figure 7.6: The integral flux above $E > 400$ GeV of LS I +61°303 versus the orbital phase for OC I is shown for each orbit. The lowermost panel shows the averaged integral flux in phase range intervals of $\Delta\phi = 0.1$.

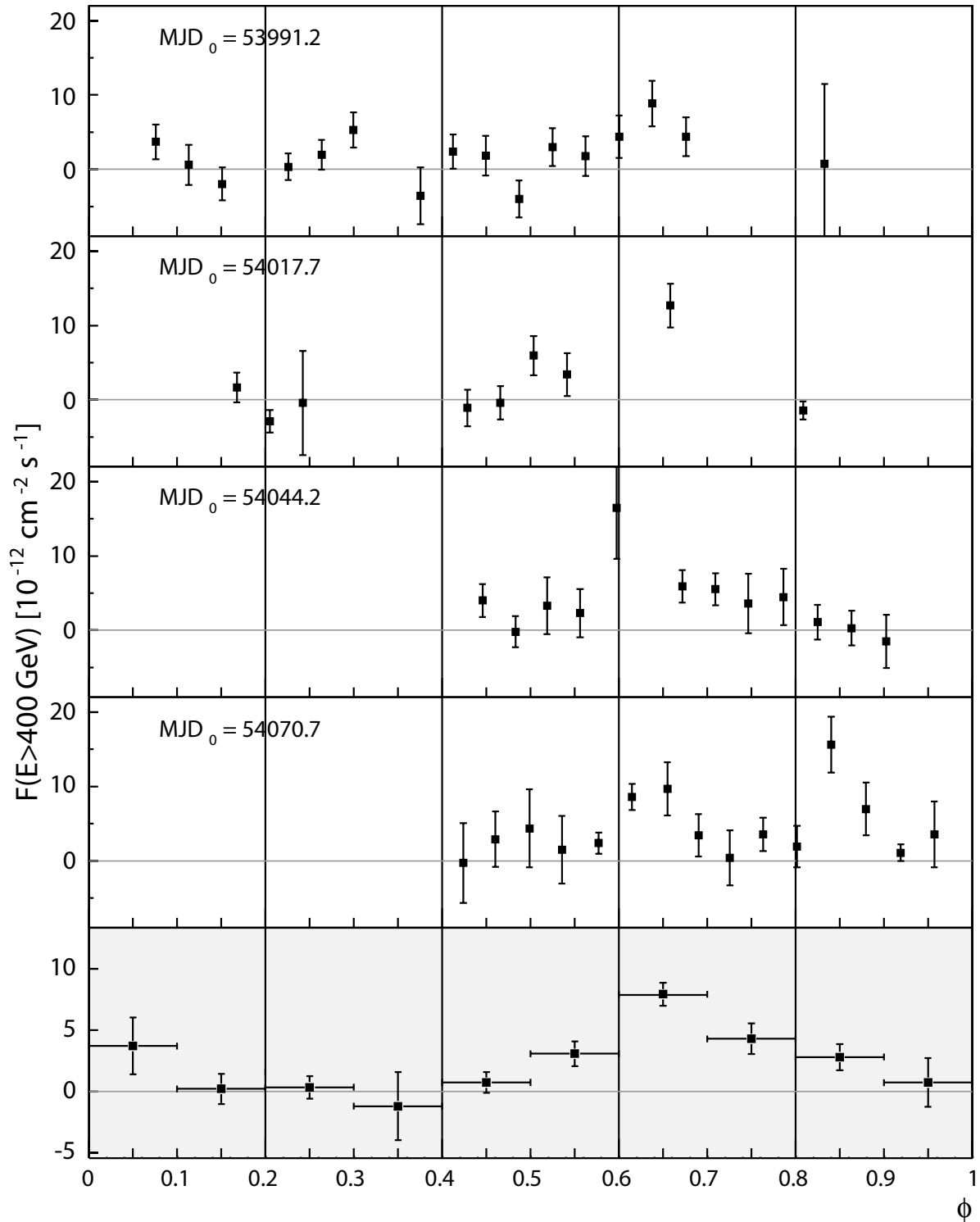


Figure 7.7: The integral flux above $E > 400 \text{ GeV}$ of LS I +61°303 versus the orbital phase for OC II is shown for each orbit. The lowermost panel shows the averaged integral flux in phase range intervals of $\Delta\phi = 0.1$.

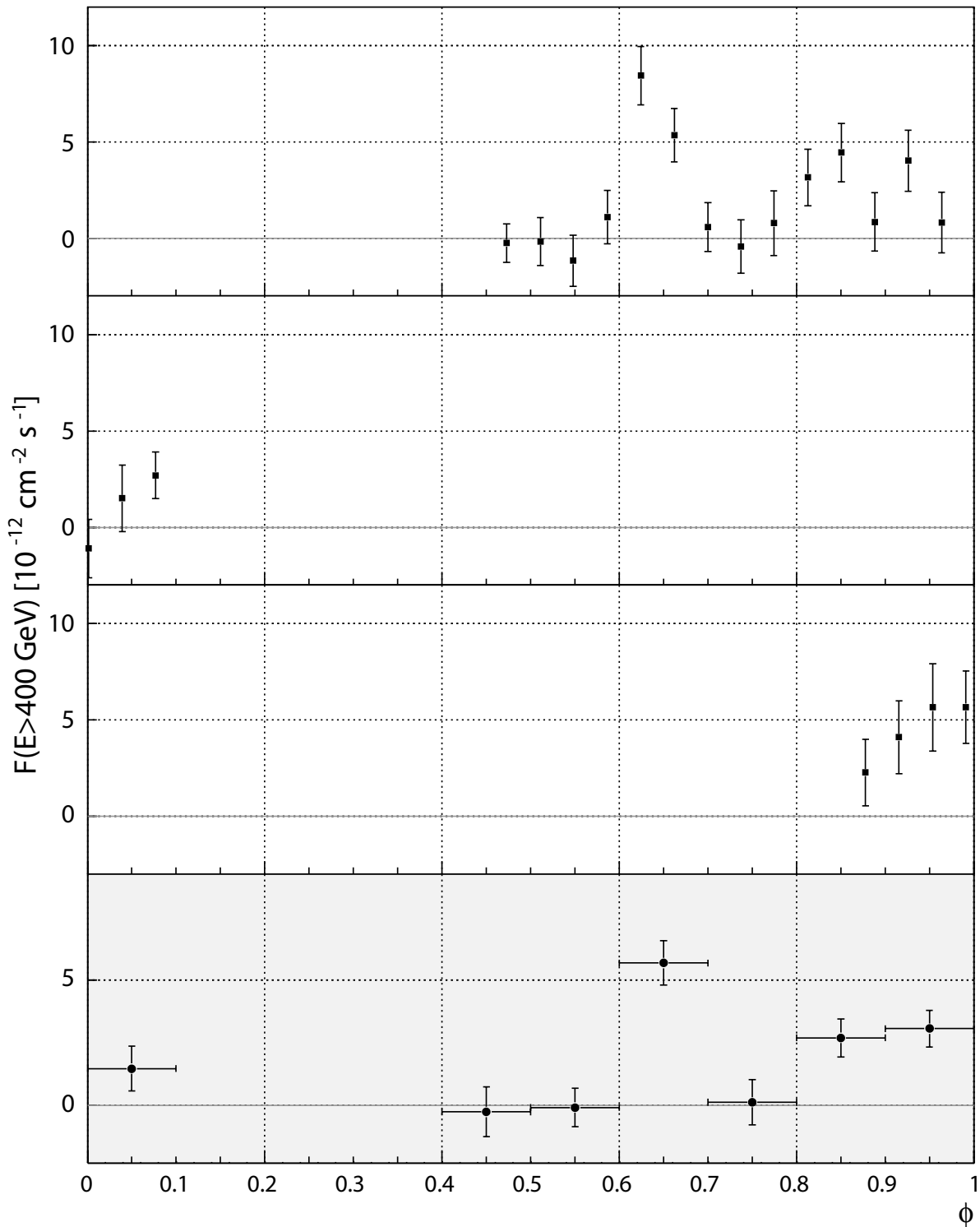


Figure 7.8: The integral flux above $E > 400 \text{ GeV}$ of LS I +61°303 versus the orbital phase for OC III is shown for each orbit. The lowermost panel shows the averaged integral flux in phase range intervals of $\Delta\phi = 0.1$.

Flux variability timescales

From the LC's, it is evident that significant flux variations take place on timescales of about one day. These fast changes happen mainly around the main emission peak but also in the case of the second emission peak in OC II's last orbit. To test the timescales of the flux variability, LC's for each observation night are produced with different time binnings and each LC is fitted by a constant flux and the probability of the derived χ^2 computed. The longer observations in OC III are the best candidates to test variability on timescales of one to two hours. In the other OC's, only the longest observations have enough bins to give reasonable testing conditions. Nevertheless, the higher sensitivity of OC III gives the best chances of detecting significant variability on short timescales. The LC's for each OC are given in appendix A.2, together with their fit values to a constant flux, for 30 min time binning. Evidence for short time variability are found in the LC's of MJD 54005, 54035, 54352 and 54357. The criteria for the selection of these days is the total observation time (at least four points required in the LC) and an overall positive flux level during the night. LC's in which only one point shows a larger discrepancy compared to a baseline flux are not considered since there are example LC's which show the same behavior only with negative fluctuations. No short time variability can be proven on simple statistical tests but the LC of MJD 54352, which is the highest emission measurement of OC III, indicates a clear flux increase in less than 30 min by a factor of three. The LC is shown in Fig. 7.9. The probability to obtain a χ^2 , if all points are fitted with a single constant value, is 10% and thus not very low. Nevertheless, the LC shows a distinct characteristic between the first five and last three flux measurements which shows that these indications for short time variability are likely not to have been produced by chance. No hardware problem or environmental influences could have caused this rapid increase in flux. The rate is constant within 10%, which is an excellent value for MAGIC, and the number of stars identified by the star guider tracking monitor are constant and the number of stars indicate a transparent night. The time distribution of the two quantities are shown in Fig. 7.10 and they prove that the observed flux differences are not caused by systematic effects. Nevertheless, to get a final test, without any doubt, on the short time variability, more sensitivity is needed which will be provided by MAGIC II operated in stereo mode together with MAGIC I.

7.6 Periodicity searches

In the periodicity search, the full data sample (2005–2008) of LS I +61°303 is used and the Lomb-Scargle method applied (as described in section 5.4.2). The STI is chosen to be

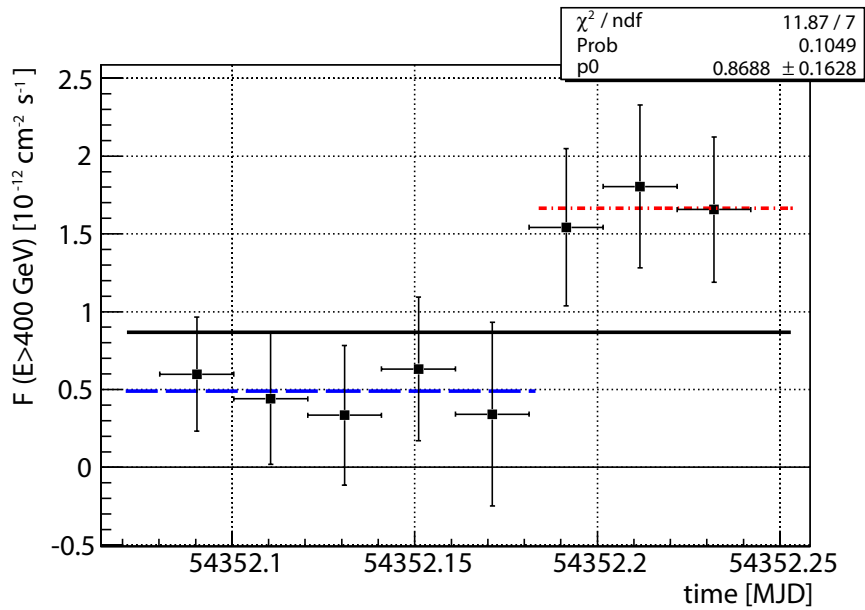


Figure 7.9: The LC of MJD 54352 with 30 minutes time binning. The given fit parameters correspond to a fit of the complete LC with a constant (black line). The step-like structure of the LC is clearly evident. The first five measurements are well described by a constant flux (blue dashed line) and the last three as well - but with a factor of 3 higher flux (red dot dashed line). The shown vertical errors are statistical only and the horizontal error bars indicate the bin width of the observation time.

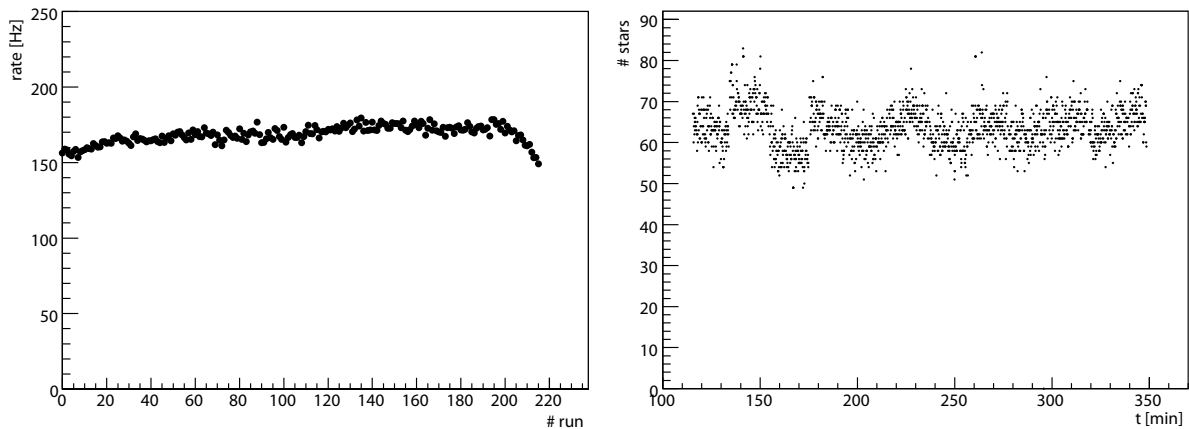


Figure 7.10: The rate versus the observation run number is shown on the left. The rate is constant during the whole night within 10% of the average rate. The left panel shows the number of identified stars by the tracking monitor camera versus the time. The number of stars is a measurement of the transparency of the atmosphere and the number indicates a very transparent sky. The saw-tooth shape in the number of identified stars is caused by the wobble position changes since a unique star field belongs to each wobble position, so the number of stars can be different for the wobble positions. No other trend beside the wobble position changes is seen.

15 minutes to assure equally sized error bars on the flux values. Since the system is known to be periodic in other wavebands with periods equal or very close to the orbital period, the search for periodicity in the VHE gamma-ray domain is carried out in two steps.

1. Search in a narrow frequency band around the orbital period, where the test frequency range is taken as the cumulative 2σ confidence interval of the already established periodicity frequencies in the other wavebands.
2. A blind search for periodic emission in a larger frequency range $[0.00128 \text{ d}^{-1}, 0.25 \text{ d}^{-1}]$ to look for other periodic components in the LS I +61°303 data set.

In the search around the orbital period, an oversampling factor of ten is chosen to make a dense sampling of the frequency space to get an accurate frequency position of the highest power. In the case of the frequency range scan, an oversampling factor of ~ 5 is chosen. This guarantees that each peak in the periodogram is still sampled by several test frequencies but reduces the needed computation time dramatically. The probability of each power in the periodogram is computed from the cCPF which is given in Fig. 7.11 for the frequency range scan. The fit parameters of the theoretical predicted function of the post trial cCPF ($F = P(z > z_0) \equiv 1 - (1 - e^{-z})^M$) to the simulated cCPF yield $M = 686$ independent frequencies for the frequency scan. In the search around the orbital frequency, $M = 28$ is used which corresponds to the number of frequencies tested.

The errors for the period are calculated conservatively as the independent Fourier spacing; here, it should be noted that this leads to (slightly) asymmetric error intervals. This approach to the uncertainty treatment is chosen since the maximal amount of information is present in the independent frequencies and all oversampling does not add new information. This can be readily seen as each power peak has the same FWHM regardless of the oversampling factor⁶.

7.6.1 The search at the orbital period

In any scenario which might describe the VHE emission of LS I +61°303 a periodic modulation of the emission with the orbital period is predicted. This is either due to the increased accretion rate close to the periastron passage or due to absorption effects in the changing absorbing photon densities along the orbit of the compact object. Thus, due to simple geometric effects alone, a modulation of the emission is possible and indeed a periodic emission is evident at radio-, infrared-, optical- wavelengths and at least temporarily in the X-ray

⁶It is assumed that the oversampling is high enough to resolve the peak power, as is the case in this study.

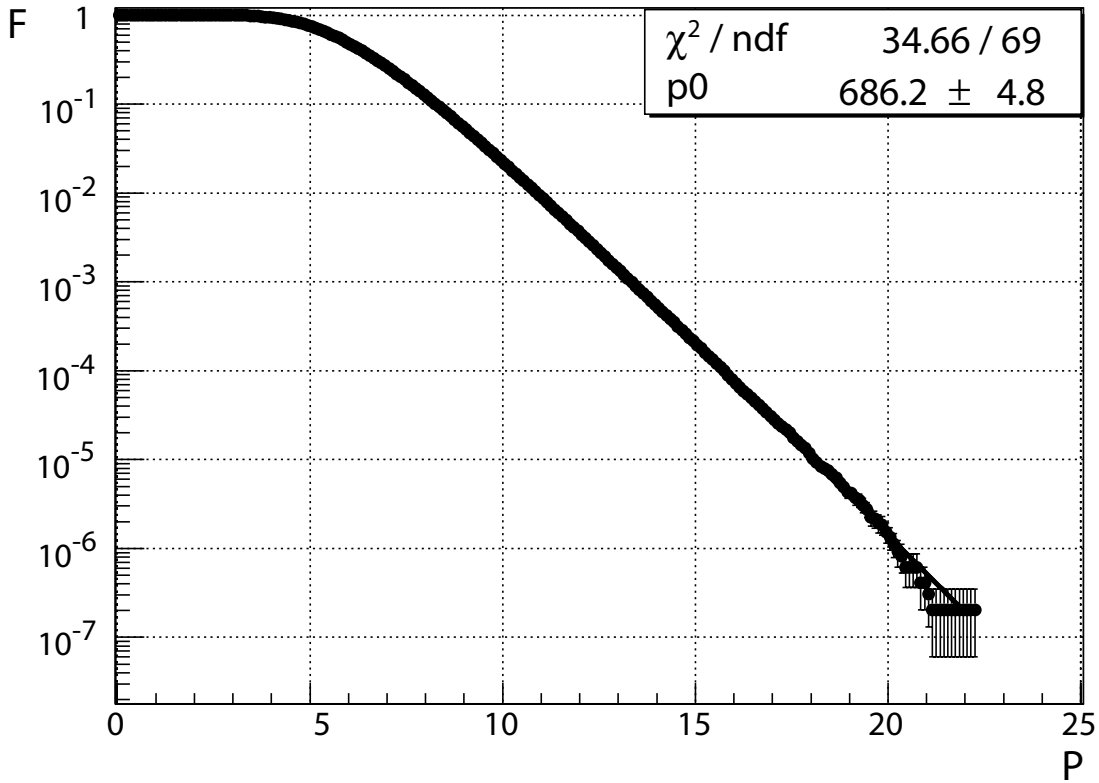


Figure 7.11: The post trial false alarm probability (cCPF) for the STI of LS I +61°303 and a 15 min time binning is shown. The number of tested frequencies in the frequency range $0.00128 - 0.25 \text{ d}^{-1}$ is 968. The fit by $F = P(z > z_0) \equiv 1 - (1 - e^{-z})^M$ yields 686 independent frequencies and the cCPF is well described for $P > 15$ by the theoretical expected function F . Details about the method are given in chapter 5.4.2

energy band, as described in the previous sections. Thus, it is natural to look for a periodic emission at the orbital period of the system. The corresponding periodogram obtained by the Lomb-Scargle method is shown together with the false alarm probability for each peak in the periodogram in Fig. 7.12. It is evident that a periodic modulation with $P = 26.60_{-0.45}^{+0.46} \text{ d}$ is present in the LS I +61°303 VHE data. This modulation is significant since its false alarm probability is $P(z > z_0) = 8.5 \times 10^{-9}$. This test does not provide any information about the shape of the emission or at which phase it occurs. Since almost no theory predicts a pure sine wave, the emission can follow any periodic shape. The phase-folded light curve indeed reveals a relatively confined orbital phase region (0.6–0.7) where the highest emission is regularly detected as an outburst. The quantitative test shows that this is really a periodic component in the flux of LS I +61°303.

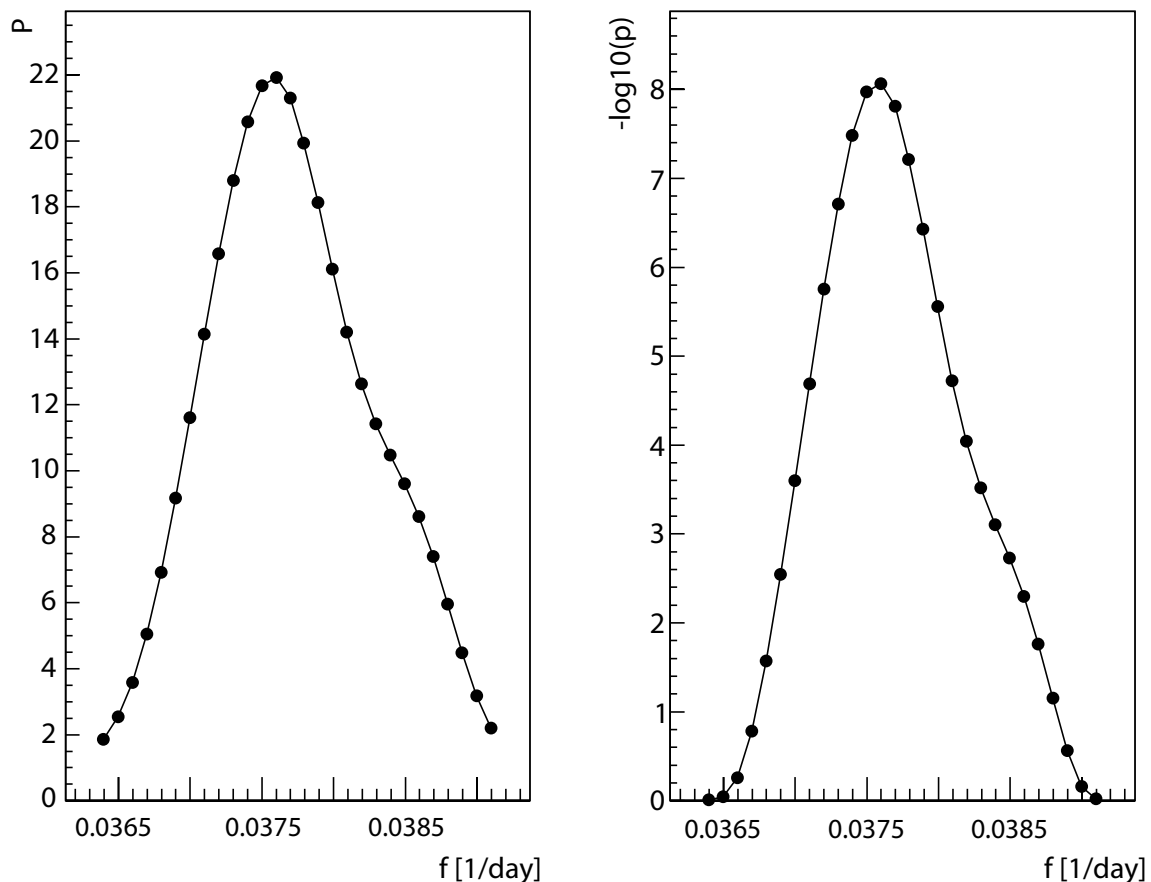


Figure 7.12: The left panel shows the power distribution of the 28 test frequency (oversampling factor 10) and the right panel the corresponding false alarm probability to generate a peak of at least this height only in the presence of gaussian white noise. The period is found to be 26.596 days with a false alarm probability of $P(z > z_0) = 8.5 \times 10^{-9}$.

7.6.2 Scan of a larger frequency domain

In addition to the test for the orbital periodicity, a wider frequency range is scanned to find possible additional periodic components and verify that the orbital periodicity is the most significant present.

In this scan, 968 frequencies are scanned in the frequency range 0.00128 – 0.25 d^{-1} . The corresponding periodogram and its false alarm probability are given in Fig. 7.13. Besides the significant peak at the orbital frequency, only very few additional peaks are present and their false alarm probability is much lower but may still be significant. To test if these peaks are caused by aliasing of the main component (at the orbital frequency), a sinus function with the orbital period is fitted to the phase-folded LC of LS I +61°303 and subtracted from it. The thus obtained signal subtracted LC is again tested for periodicity. The result of this

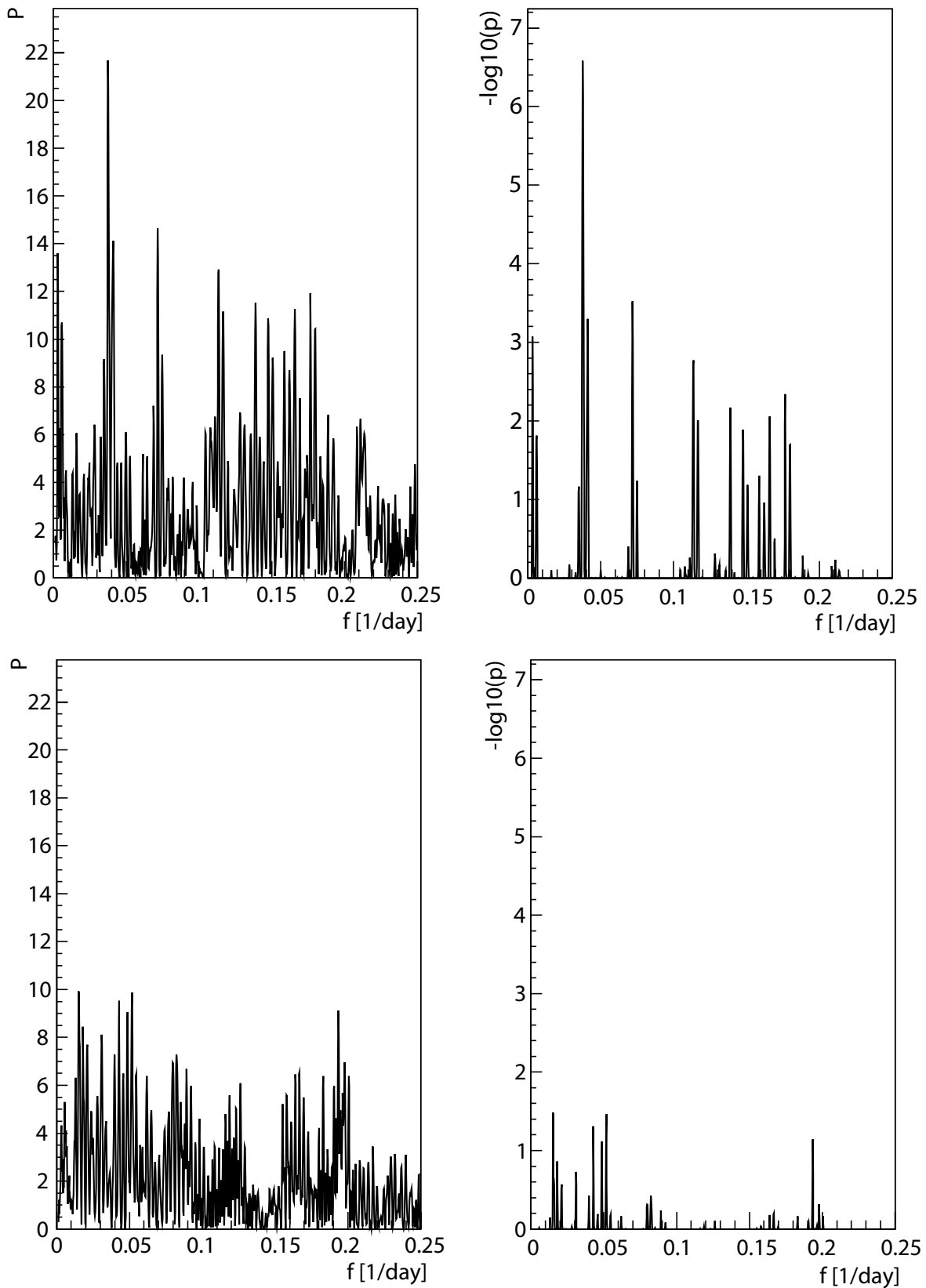


Figure 7.13: The upper panel shows the periodogram for the LS I +61°303 data on the left side and, on the right side, the corresponding post-trial false alarm probability (p for each peak (as $\log_{10}(p)$). The lower panel shows the same for the simultaneously taken background data. For further details see section 7.6.2.

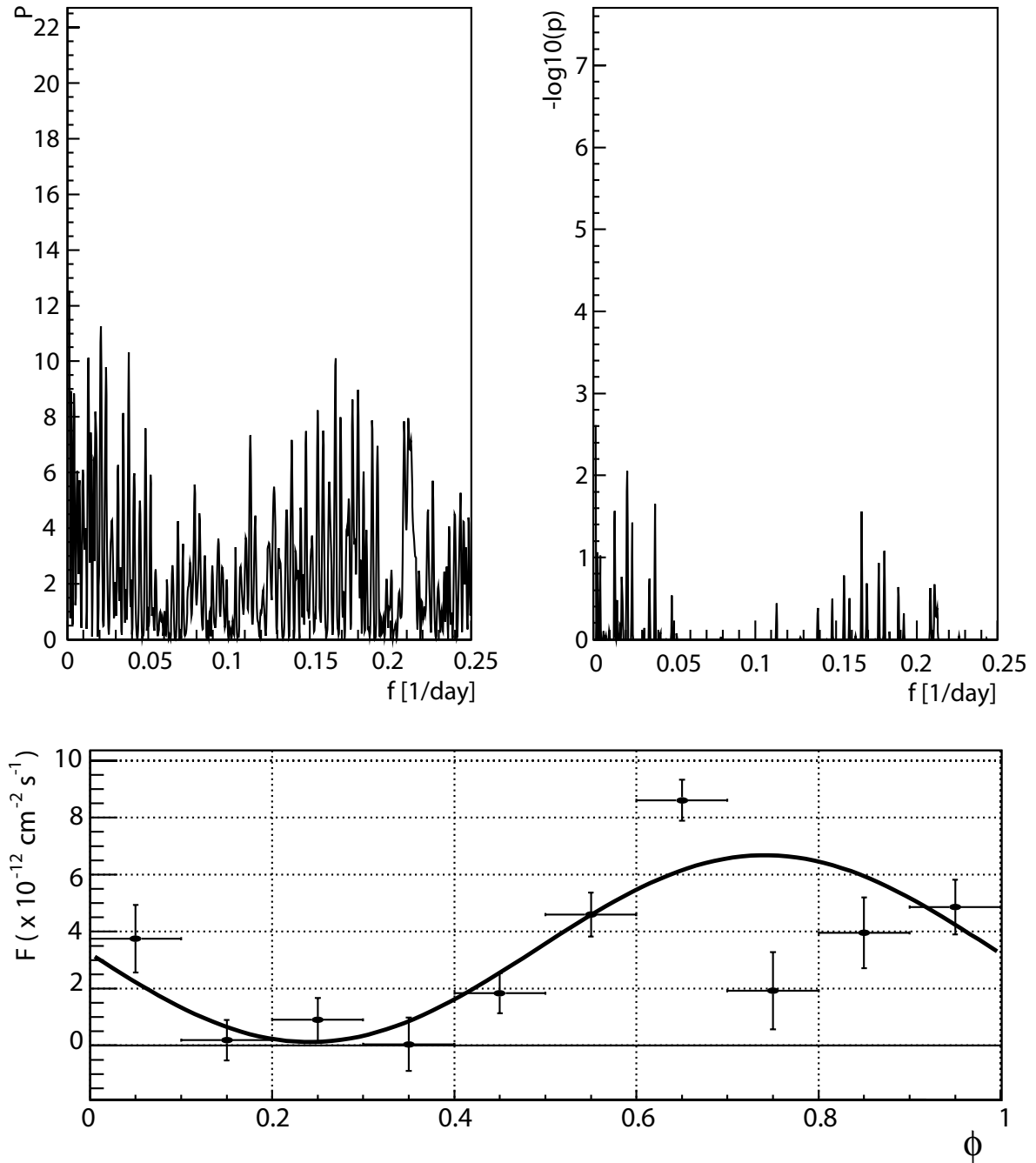


Figure 7.14: The periodogram does not show any significant peak after subtracting a sine wave with the orbital frequency from the LC of LS I +61°303. Nevertheless, the LC itself is not well described by a sinus function as the lower panel shows ($\chi^2/\text{NDF} = 24.85/7$).

search is shown in Fig. 7.14 and no significant peak is found in this periodogram.

Thus, no additional periodic component is present besides the orbital one. Of course, the data has very large gaps between the different observational campaigns and the total time coverage is too short to test for the super-orbital periodicity found in radio. Taking these circumstances into account, it might be possible that additional periodic modulations with periods considerably larger compared to the orbital period are present but can not be detected in the periodogram due to sparse sampling of the total time interval. The periodogram of the simultaneously taken background sample is also shown in Fig. 7.13 and does not show any significant peak in the power distribution. This demonstrates that no periodic effect during the data-taking such as zenith angle distribution or observation gaps due to strong moon light can cause the significant peak found in the power distribution of the LS I +61°303 source data sample.

7.6.3 Conclusions from the periodicity search

The main conclusion from the periodicity search is that a significant periodic modulation of the signal from LS I +61°303 is found at its orbital period. The obtained period agrees well with the measurements of other wavebands, as can be seen in Fig. 7.15. The VHE gamma-ray emission of LS I +61°303 does not follow a sine shape, as can be seen from the orbital phase-folded LC's presented in section 7.5.

The shape of the emission is a rather narrow peak concentrated at later orbital phases near or around the apastron. This emission is not the only one found in the LS I +61°303 LC. Additional significant fluxes are measured at phases later than the main emission phase. These fluxes were first seen in December 2006 on MJD 54092.92 at phase 0.84. In the next observation campaign, no such clear feature (like a second peak) is observed but rather a broader phase range with an averaged signal of about 7σ significance. These additional significant fluxes indicate that there is not only a periodic emission in the system but either a non-periodic emission or a periodic one with a different period. Since the additional fluxes are only found in some orbits and, up to now, only in some orbital phases, they should not belong to a shorter periodicity compared to the orbital one. A super-orbital modulation is known to be present in the radio waveband and possibly in the $H\alpha$ line, with a much larger period ($P_{\text{radio}} = 1667 \pm 8$ d). In the radio data, additional emission peaks during one orbit of LS I +61°303 are found in certain super-orbital phases. It would be interesting to test if this behavior is present in the VHE regime as well. The current data does not allow tests for this and, for solid conclusions, several more years of intense monitoring with MAGIC will be needed. One indication should be mentioned here: The additional fluxes seem not to be

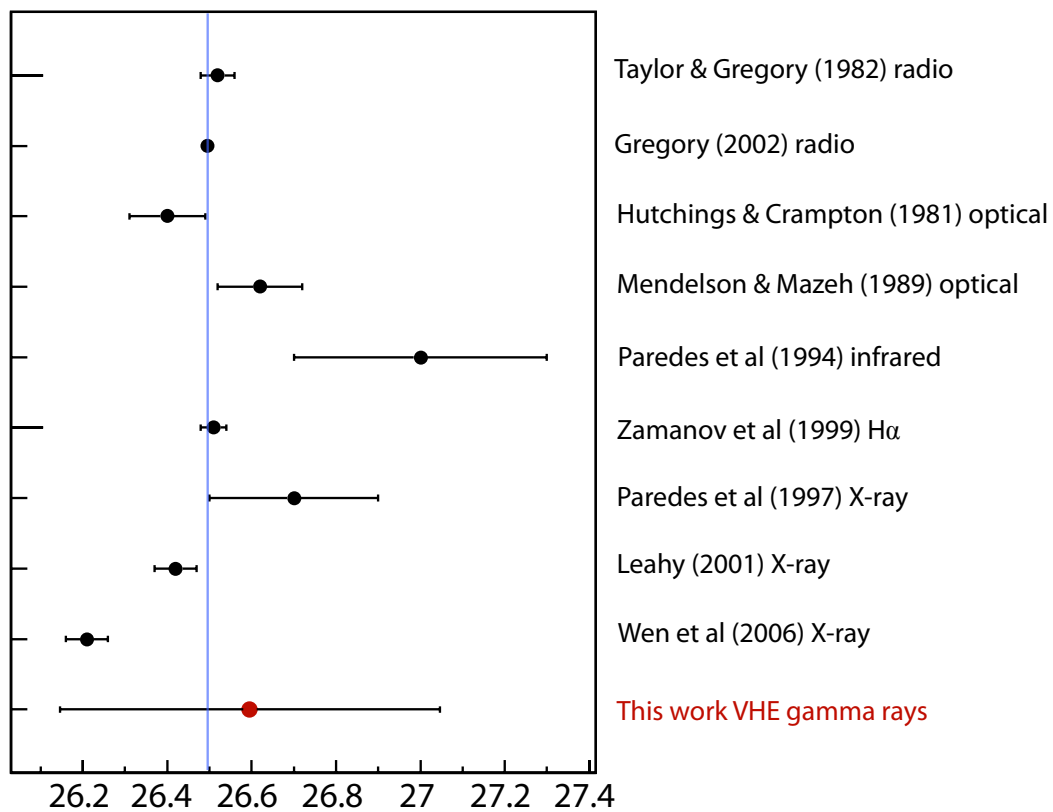


Figure 7.15: The periods obtained from different measurements in the various energy bands. The up to now most precise measurement by Gregory (2002) is marked by the blue line and only three other measurements agree with it on the one sigma level (two more are almost compatible on the one sigma level). This emphasizes the fact that most measurements seem to underestimate their errors. In the work presented here, the IFS is used as the error and gives a realistic uncertainty.

very regular in their appearance in the LC's and, especially in the 2007 to 2008 observations, the additional fluxes appear more often. This might be due to the sensitivity improvement of MAGIC I (due to the MUX read out) and the longer observation times. An even better view would have been possible if a target of opportunity observation had not appeared during these phases and took away one precious hour per night of the observation time from the LS I +61°303 campaign. At this time, no definite conclusion can be drawn about the additional emission in the system but in my opinion it indicates an additional component which is not regular but might appear only in some phases. The emission of LS I +61°303 is thus partly periodic according to the definition in chapter 5.4.1.

OC	orbital phase	f_0 [10^{-12} cm $^{-2}$ s $^{-1}$]	Γ	a_0 [TeV]	χ^2/ndf
I	[0.6,0.7]	$26.7 \pm 3.5_{\text{stat}} \pm 8.0_{\text{syst}}$	$2.6 \pm 0.2_{\text{stat}} \pm 0.2_{\text{syst}}$	0.5	4.56/4
II	[0.5,0.6]	$1.2 \pm 0.4_{\text{stat}} \pm 0.3_{\text{syst}}$	$2.7 \pm 0.4_{\text{stat}} \pm 0.2_{\text{syst}}$	1.0	1.42/3
II	[0.6,0.7]	$2.6 \pm 0.3_{\text{stat}} \pm 0.8_{\text{syst}}$	$2.6 \pm 0.2_{\text{stat}} \pm 0.2_{\text{syst}}$	1.0	5.22/5
III	[0.6,0.7]	$5.8 \pm 0.8_{\text{stat}} \pm 1.7_{\text{syst}}$	$2.75 \pm 0.21_{\text{stat}} \pm 0.2_{\text{syst}}$	0.7	0.71/5
III	[0.8,1.0]	$41.6 \pm 7.3_{\text{stat}} \pm 12.5_{\text{syst}}$	$3.37 \pm 0.38_{\text{stat}} \pm 0.2_{\text{syst}}$	0.3	6.58/3

Table 7.5: Spectral fit parameters of the spectra extracted from the data of the different OC's. The fit function is a power law and the parameters are defined by equation (7.1)

7.7 Spectral properties

The spectral properties of LS I +61°303 are of great interest since they are related to the particle acceleration mechanism and particle interactions in the system and give an indication whether the gamma-ray emission is due to a hadronic or leptonic mechanism.

Since the flux level of the emission from LS I +61°303 is rather low for most of the phases, only during the main emission phase is it possible to derive spectra for individual nights. Thus, it is more convenient to calculate spectra for phase intervals and compare them. The unfolded spectra from each OC are compared in Table 7.5 and all of them can be well described by pure power laws of the form:

$$\frac{dF}{dE} = f_0 \left(\frac{E}{a_0} \right)^{-\Gamma} \quad (7.1)$$

The normalization constant f_0 is different for individual OC's since it is chosen to be at the energy bin which has the highest significance and which is not the lowest or highest energy bin. For flux comparisons, it is more convenient to look at the flux tables presented in section 7.5. The spectrum in OC I differs from the one reported in Albert et al. (2006) but they are compatible within the errors. The difference is most likely caused by the improved analysis methods, i.e. the Albert et al. (2006) spectrum is not unfolded since the software for this task was still under development during the time of the publication. Another difference is that, in my analysis, a systematic search in the natural binning of orbital phase bins (with $\Delta\phi = 0.1$) is carried out while in Albert et al. (2006) more data than contained in this phase range is summed up and used for the spectrum. This leads of course to different flux values in the first MAGIC analysis since the flux is not constant in the individual phase ranges.

The spectral indexes in all OC's in the phase range $\phi \in [0.6, 0.7]$ are compatible within errors with each other. The averaged flux value is slightly different in the OC's but this can be attributed to the number of sampled outbursts (one per orbit) because either the emission level can differ between orbits or the maximum of the emission does not coincide

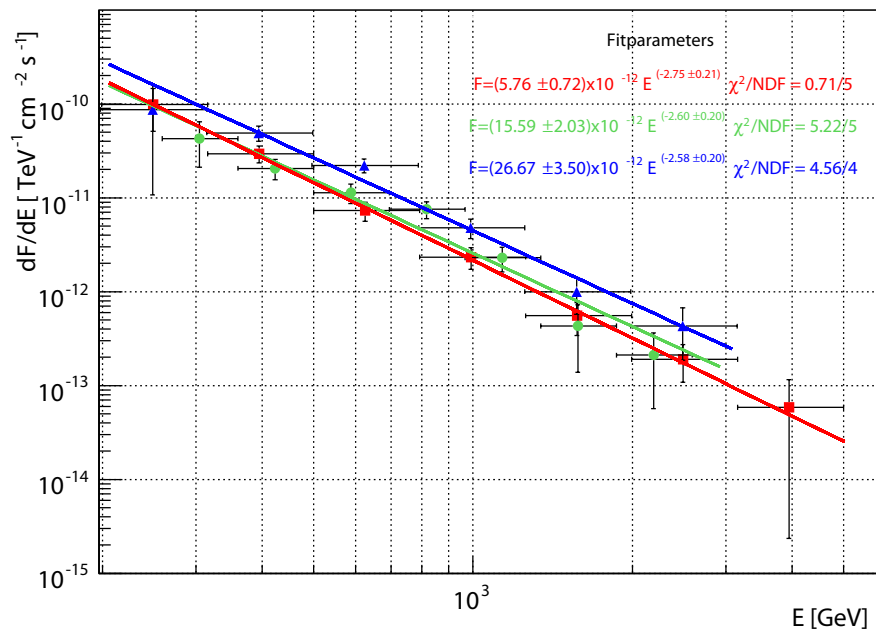


Figure 7.16: The spectra in the phase range 0.6–0.7 for OC I (blue), OC II (green) and OC III (red) are shown. The flux in OC I is higher compared to the other OC’s because the peak emission of the outburst is almost the sole contributor to the average in this OC, while in the other OC’s many smaller fluxes beside the peak flux of the outburst contribute to the average (compare Figs. 7.6, 7.7 and 7.8). The spectral index agrees within the statistical errors for all OC’s.

with a measurement. The spectra are shown in Fig. 7.16. Another interesting question is if the spectral index depends on the flux level and, consequently, the spectra of individual nights obtained in individual OC’s are compared with each other. The obtained spectra for the three most significant nights together with the fit parameters of a power law are shown in Fig. 7.17. It is clear that the fluxes of the highest emission of the outburst are very similar and this emphasizes that the difference observed in the phase bin averaged spectra originates from the sampling of the outburst. The spectral index agrees very well for the highest emission spectra and does not deviate within the errors from the phase bin averaged spectra. Thus, no hardness/flux level correlation can be detected with the current sensitivity.

The conclusion from the spectral study is that no significant spectral variation is found in the phase range $\phi \in [0.6, 0.7]$ during the three years of observation of LS I +61°303 with MAGIC. The remaining question is what about the other phase ranges?. It is not possible to obtain any meaningful spectrum⁷ in other phase ranges with $\Delta\phi = 0.1$ except in the phases $\phi \in [0.5, 0.6]$ in OC II. The fit parameters of this spectrum are given in Table 7.5. No

⁷At least four significant points should be contained in any meaningful spectrum to be able to fit a power law to it.

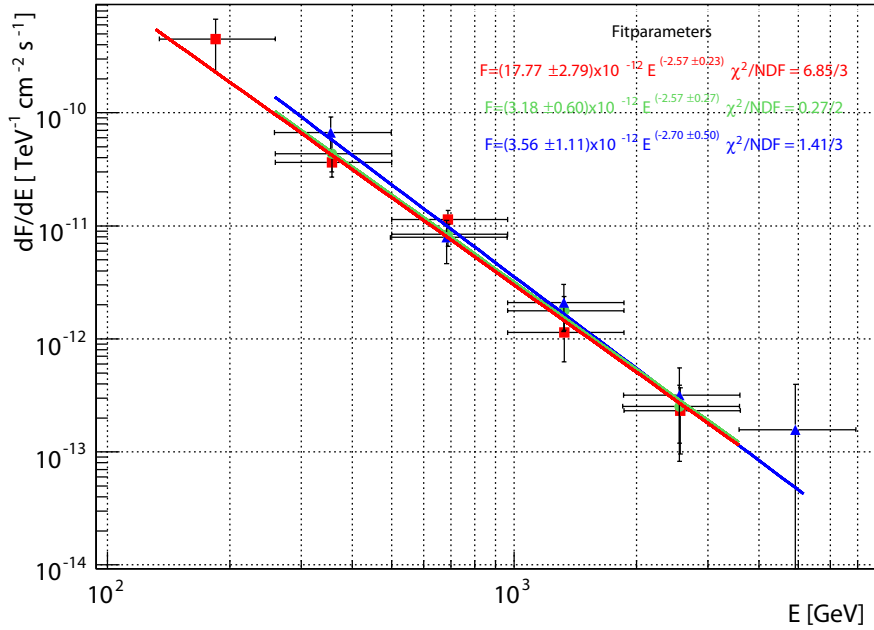


Figure 7.17: The spectra of three individual nights MJD 54035 (blue), MJD 54086.95 (green) and MJD 54352.12 (red) of the highest emission in the phase range 0.6–0.7. Flux level and spectral indices are compatible within the statistical errors. The higher sensitive measurements of OC III (red curve) allow for a lower energy threshold. Note that the normalization of the flux is different for the red spectrum compared to the other two.

difference is found between this spectrum and the one derived for $\phi \in [0.6, 0.7]$.

The significant flux in the phase range 0.8–1.0 in OC III is strong enough to derive a spectrum. This phase range is chosen since the flux in both sub bins $\phi \in [0.8, 0.9]$ and $\phi \in [0.9, 1.0]$ is significant but not enough to produce a spectrum within the smaller phase binning. The spectrum derived for $\phi \in [0.8, 1.0]$ yields a very steep spectrum which can be moderately well described by a power law ($\chi^2/\text{ndf} = 6.58/3$). The spectrum is shown in Fig. 7.18 together with the spectrum obtained from the $\phi \in [0.6, 0.7]$ data of the same OC. It is evident that the later phase spectrum extends to lower energies compared to the main emission peak spectrum. Since the same cuts are applied for both spectra, no systematic differences should be present. The spectral index is not compatible with the one derived for the $\phi \in [0.6, 0.7]$ data. The effect of the unfolding suggests an even softer spectrum for the later phase data (compare Fig. A.10 in Appendix A.3). The relatively large χ^2 value of the power law fit indicates that additional features could be present in the spectrum. Through investigation of the spectrum, it is evident that the spectral point at $E = 500$ GeV displays a lower flux in all unfolding methods (see Fig. A.10) as well as for a shape expected from a power law. In consequence, another spectral shape given in eq. (7.2) was fitted to the

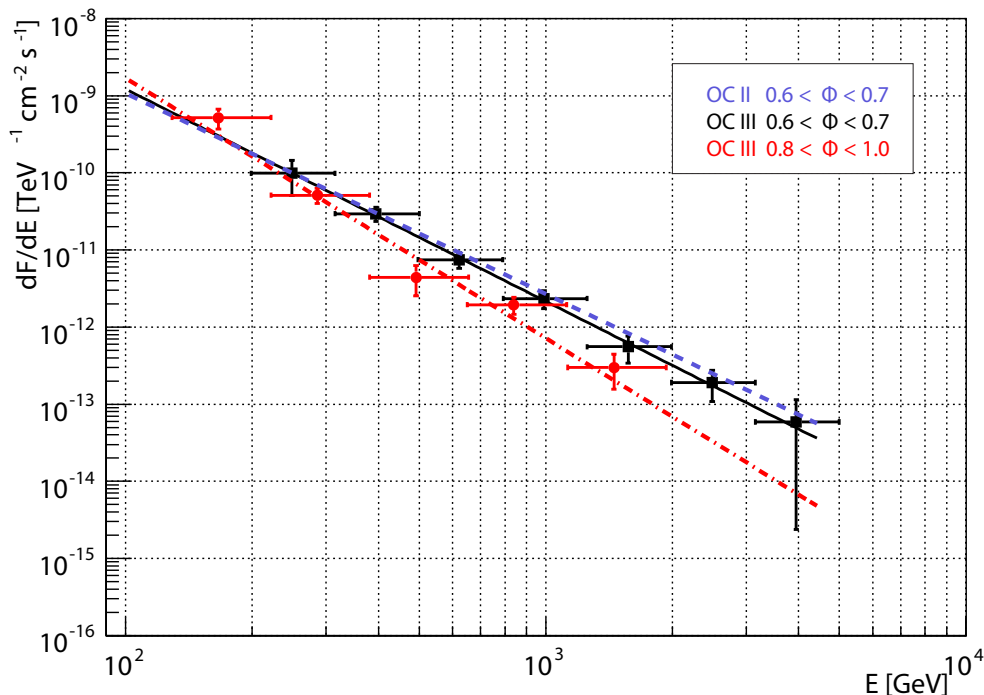


Figure 7.18: The spectra derived for OC III $\phi \in [0.6, 0.7]$ (black solid), OC III $\phi \in [0.8, 1.0]$ (red dot dashed) are shown together with the fit function of OC II $\phi \in [0.6, 0.7]$ (blue dashed). The spectral shape of OC III $\phi \in [0.8, 1.0]$ does not have compatible fit parameters with the OC III and OC II spectra in the phase range $\phi \in [0.6, 0.7]$. This indicates a possible phase dependent spectrum. For further details see section 7.7.

unfolded spectrum (see Fig. A.9).

$$\frac{dF}{dE} = f_0 \cdot \left(\frac{E}{a_0} \right)^{\Gamma_1 + \Gamma_2 \log(E)} \quad (7.2)$$

The resulting $\chi^2/\text{ndf} = 3.77/2$ gives a better description of the data compared to the simple power law fit ($\chi^2/\text{ndf} = 6.58/3$). In general, this could indicate a spectral hardening above ~ 500 GeV. Such a spectral hardening could be caused by an absorption process affecting the VHE gamma-rays or a different physical mechanism causing the VHE gamma-ray emission above the break energy. Unfortunately the statistical significance of absorption features or spectral changes cannot be tested with the small data sample at hand. Taking into account that the systematic effects are strongest at the threshold energy, caution is needed and thus only a hint of spectral differences between the main emission peak and the later (possibly non-periodic) emission can be concluded. Here it should be mentioned that the spectral shape obtained between the same individual OC does not suffer from any spectral systematic uncertainty.

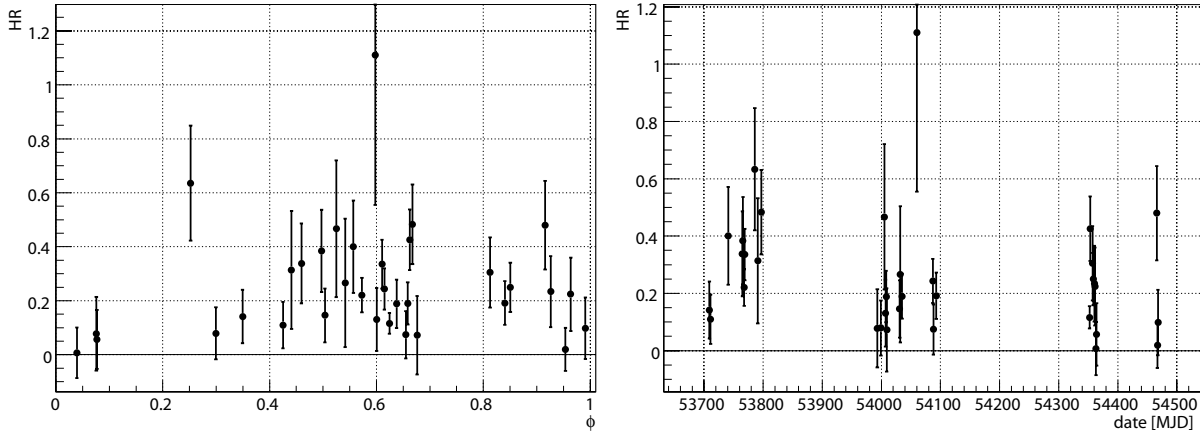


Figure 7.19: The HR as defined in the text vs the orbital phase of LS I +61°303 is displayed in the left plot and the HR vs time in MJD on the right. No statistically significant trend is visible. There is some indication of lower HR 's at $\phi \in [0.0, 0.1]$ but the total number of measurements is too small for statistical investigation.

Another investigation with less significant measurements can be conducted in terms of the hardness ratio (HR). The HR is defined as the ratio of integral fluxes as follows.

$$HR = \frac{F(E > 900 \text{ GeV})}{F(300 < E < 900 \text{ GeV})} \quad (7.3)$$

The HR is computed for all flux measurements in all OC's and evaluated if the total flux ($F(E > 300 \text{ GeV})$) is measured with at least 2σ significance. The lower energy threshold of 300 GeV is selected for several reasons: Firstly, to get more excess events, second, to take advantage of the higher sensitivity of OC III and, finally, to be more sensitive to soft spectral distributions such as those obtained for the phase range 0.8–1.0. The threshold of 2σ guarantees that the most likely signal-containing measurements are investigated and very few measurements displaying only statistical fluctuations are included.

The HR for all OC's is shown in Fig 7.19 and no statistically significant trend is seen, neither if investigated in the different phase ranges nor if compared between the different OC's. The HR vs the $F(E > 300 \text{ GeV})$ is also derived and shown in Fig. 7.20. The linear correlation coefficient is $r = 0.25^{+0.16}_{-0.17}$ indicating no correlation between the HR and the integral flux of LS I +61°303. Further investigations of the HR vs. the integral flux for individual OC's or individual phase ranges did not reveal any linear correlation either. The large error bars and the sparse detections in most phasebins challenge the linear correlation investigation. More refined methods would most likely not help, since significant measurements are required to produce meaningful HR 's if the spectral difference is not very large. This can be seen by the large uncertainties in the HR in Fig 7.19 and Fig.7.20.

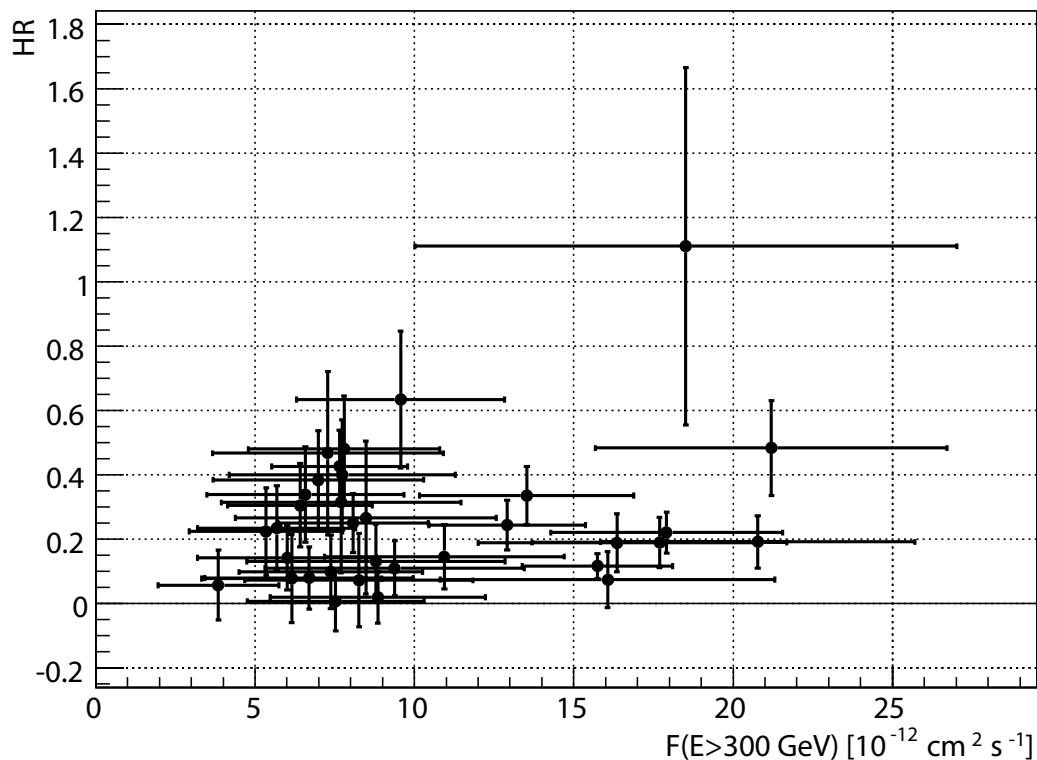


Figure 7.20: Shown is the HR vs the integral flux above $E > 300$ GeV for all OC's. The linear correlation coefficient is $r = 0.25^{+0.16}_{-0.17}$ indicating no correlation between the two quantities.

7.8 Summary of the LS I +61°303 measurements by MAGIC

The detailed study for more than three years of LS I +61°303 with the MAGIC I telescope leads not only to the discovery of the VHE emission of the source but gives a much more detailed picture of the emission than in most other VHE gamma-ray sources. For the first time a periodic VHE signal could be proven with MAGIC with high significance (post trial false alarm probability $p \sim 8.5 \times 10^{-9}$). The derived period 26.6 ± 0.5 d is in very good agreement with the best orbital period derived for LS I +61°303. This periodic signal is evident as an emission peak at the orbital phase range $\phi \in [0.6, 0.7]$ and cannot be well described by a sine wave. The VHE emission is best described as a sharp peak with a total duration of about $\Delta\phi = 0.1$. Further study of LS I +61°303 reveals that the system displays additional significant emission in the phase range $\phi \in [0.8, 1.0]$ which might not be modulated with the orbital period. This emission might be either due to a super-orbital modulation or be non-periodic. If the emission is super-orbital, the frequency should be much smaller compared to the orbital frequency since no significant peak is observed in a wide frequency

scan of the LS I +61°303 data.

Hints for short timescale variability are found in several nights which cannot be attributed to systematic effects like weather changes or hardware instabilities. The most compelling hint is found in the observations on MJD 54352, where the flux rises in less than 30 min by a factor of more than three. While the errors of the individual flux measurements of 30 min time bins are too large to give an overall significant deviation from a constant flux ($p_{\text{fab}} \sim 10\%$), the distribution in two clearly separated flux levels (one formed by the first five and the other by the last three flux values), gives confidence in a real short-time variability of the emission.

The spectral energy distribution of the emission of the system can be described as a pure power law for the periodic emission peak with a spectral index of $\Gamma = 2.6 \pm 0.2_{\text{stat}} \pm 0.2_{\text{syst}}$. The spectral energy distribution derived for $\phi \in [0.8, 1.0]$ in OC III is not well described by a power law and gives a considerably different spectral photon index of $\Gamma = 3.37 \pm 0.38_{\text{stat}} \pm 0.2_{\text{syst}}$, which is not compatible with the spectral index obtained for $\phi \in [0.6, 0.7]$. This is an indication of a spectral difference between the main emissions and the one found in later phases. Further constraints on the shape of the spectral distribution in the phase range $\phi \in [0.8, 1.0]$ need more measurements.

No correlation between the HR and the integral flux level can be found, nor any significant change of the HR versus time nor in different phase bins. Further studies of the spectral changes between different phase ranges need higher sensitivity measurements, as will be provided by MAGIC II operated in stereo mode with MAGIC I.

7.9 Observations of LS I +61°303 by VERITAS

The VERITAS collaboration observed LS I +61°303 in 2006 and 2007. The measurements cover much less orbital phases compared to the MAGIC measurements provided in this work. For example, VERITAS spent only 45.9 h observation time between September 2006 and February 2007 (Acciari et al., 2008), while MAGIC observed LS I +61°303 in the much shorter time span between September 2006 and December 2006 for 112 h. The VERITAS data show similarity in the detection of the maximum emission around the orbital phases 0.6–0.7. The spectrum derived by the VERITAS collaboration is obtained from all data between phases 0.5–0.8 and thus spans a much wider phase range compared to the MAGIC spectra which average data in the phase ranges 0.5–0.6, 0.6–0.7 and 0.8–1.0. The spectrum obtained by VERITAS is compatible with a simple power law and the spectral index of $2.40 \pm 0.16_{\text{stat}}$ agrees very well within the errors with the spectral index obtained in this work. The most

recently published results of VERITAS on LS I +61°303 are from observations between 2007 and 2008 yielding additional 20.7 h observation time. The spectrum obtained from this period has a spectral index of $\Gamma = 2.6 \pm 0.6_{\text{stat}} \pm 0.2_{\text{sys}}$ and this is also compatible with the MAGIC OC III spectral index ($2.75 \pm 0.21_{\text{stat}} \pm 0.2_{\text{syst}}$) presented in chapter 7.7 of this thesis.

7.10 The multiwavelength data

For a detailed understanding of the emission processes in LS I +61°303 the VHE gamma-ray data alone is not enough. Only due to the study of the full MW SED can the particle population(s) be identified and the acceleration and absorption effects at work be revealed.

The importance that the MW data is taken strictly simultaneously implies several problems. The coordination of several instruments to the same observation schedule is more than difficult, especially since very sensitive instruments are needed to detect the weak emission of LS I +61°303 in order to study it with high enough sensitivity in radio and X-rays. This makes the competition for observation time difficult, despite its considerable scientific importance, as shown by the body of related literature. For example the *Swift* satellite (Gehrels et al., 2004) surveys the sky in hard X-rays (15–150 keV) with its wide field instrument, the Burst Alert Telescope (BAT) but BAT’s sensitivity is not high enough to detect LS I +61°303 in almost any orbital phase. In addition, the PSF of BAT is 17 arcmin and thus generally contamination by background sources is possible. The same problem applies to the ASM on board the *RXTE* which is sensitive to soft X-rays (1.5–12 keV). The PSF of *RXTE* is smaller (3×15 arcmin) but the sensitivity is 30 mCrab per revolution. This makes it necessary to sum up the measurements of several revolutions to obtain a significant signal from LS I +61°303.

This renders the wide FoV X-ray instruments almost useless for detailed studies of LS I +61°303 on short timescales. Nevertheless, they can be used to investigate possible flaring activity which might yield considerably higher (up to factor of 10–100) fluxes compared to the average highest emission in an orbital cycle of LS I +61°303. Due to their large FoV, they have a very large duty cycle and a very good chance to detect rapid but high flux outbursts as reported from other HMXB’s.

The highly sensitive instrument XRT on board *Swift* is much more sensitive compared to ASM or BAT. With a PSF of 47 arcsec diameter,⁸ it is sensitive in the energy range 0.2–10 keV (for more information see Godet et al. (2009) and references therein). The detector of the instrument is the same as the *XMM-Newton* EPIC CCD’s (Holland et al., 1996). The

⁸The PSF value here quoted is the one from the XRT analysis guide and applied for the LS I +61°303 analysis presented in this thesis.

FoV of XRT is only 23.6×23.6 arcmin which makes pointing observations for LS I +61°303 necessary. These pointings cannot be obtained too often since the major task of *Swift* is the study of GRB's and thus its natural observation mode is survey and not pointing.

The other very sensitive X-ray detectors are on board of *Chandra* and *XMM-Newton*. Both satellites were used to study LS I +61°303 simultaneously to the MAGIC observations. Especially in the case of *XMM-Newton* a huge amount of observation time ($t_{\text{obs}} > 150$ ks) was granted but it is still not possible to cover a complete orbital cycle with MAGIC and any sensitive X-ray instrument simultaneously.

Another very interesting energy range is the radio band in which LS I +61°303 was studied in great detail (Gregory, 2002). The system was studied by the RATAN telescope, MERLIN, VLBA and VLBI during the same time intervals as the MAGIC OC's. The data was partially taken strictly simultaneously or at least with small time differences (about six hours) compared to the MAGIC measurements. In addition, long-term monitoring was carried out during OC I in radio and the general behavior of LS I +61°303 in this time span was analyzed.

7.10.1 X-ray and TeV data

LS I +61°303 is monitored by the BAT instrument on board the *Swift* satellite but, due to the weak flux level of LS I +61°303 the system is not detected by BAT most of the time. Phasefolding of the BAT LC with the orbital period of LS I +61°303 does not show any significant flux in any phase interval with $\Delta\phi = 0.1$.

The XRT LC of LS I +61°303 is also available at (<http://www.swift.psu.edu/monitoring/>) and, phasefolded with the orbital period of LS I +61°303 is presented in Fig. 7.21. Significant flux differences between the phase bins are clearly visible. The data sample includes the already published data but new unpublished data as well. From the description of the general X-ray behavior of LS I +61°303 in section 7.2.2, it is apparent that only data which is at least taken around the same time as MAGIC data can be used for interpretation of the signals from the two energy bands. The data published by Esposito et al. (2007) is taken in the same time span as the MAGIC OC II but the individual measurements of *Swift* are not strictly simultaneous but a few hours to days apart from the MAGIC observations.

For the correlation study of the averaged phase bin ($\Delta\phi = 0.1$ binning), I used the data from <http://www.swift.psu.edu/monitoring> and not from the paper of Esposito et al. (2007) since the averaging in orbital phase bins is not convincing for some orbital phases. The averaged phasefolded LC's and correlation plot of the X-ray and TeV measurements are shown in Fig. 7.22. A linear correlation coefficient of $r = 0.71_{-0.30}^{+0.16}$ is obtained which yields

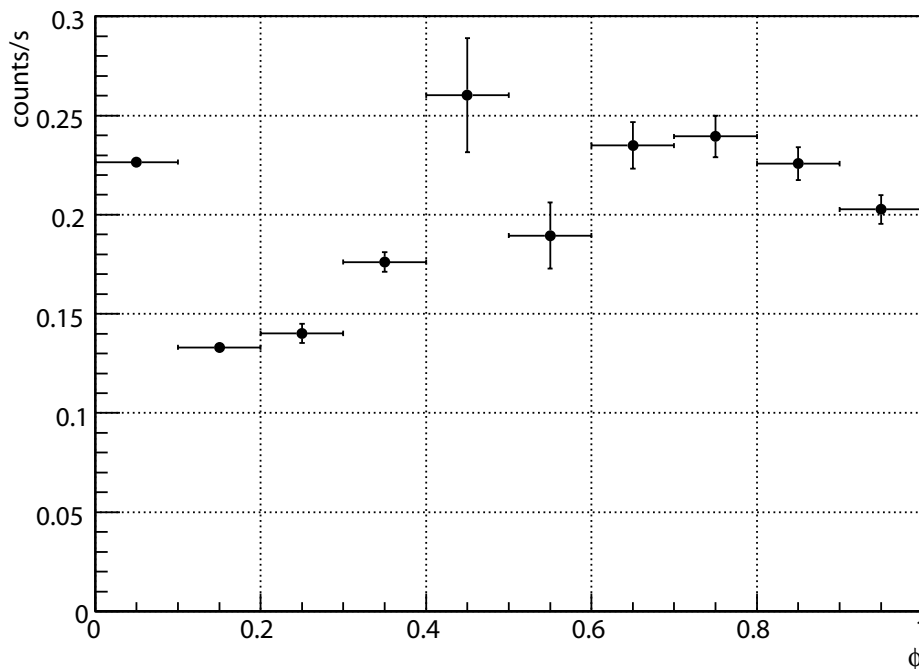


Figure 7.21: All LS I +61°303 XRT data available at <http://www.swift.psu.edu/monitoring> averaged in phase ranges $\Delta\phi = 0.1$. Vertical errors indicate the variance of the measured rates and horizontal error bars indicate the bin width. A broad emission peak for the phase range $\phi \in [0.4, 0.1]$ is visible, which is in agreement with other measurements in the same time interval (from 2005 to 2008).

a $\sim 2\sigma$ significance for correlation between the emission bands. Nevertheless, it is evident from the phasefolded X-ray LC that the high emission phases in the X-ray band correspond to the phases of LS I +61°303 detected by MAGIC.

A dedicated multiwavelength campaign was performed to test for X-ray/TeV correlation during OC II of the MAGIC measurements including the *Chandra* satellite. Bad weather at the MAGIC observation site prevented simultaneous data-taking in VHE gamma-rays. The *Chandra* measurements are in agreement with previous X-ray observations and LS I +61°303 is observed in a hard and high flux X-ray state. Further information about the *Chandra* X-ray measurements can be found in Albert et al. (2008d).

7.10.2 Simultaneous X-ray and TeV observations

Since a lot of X-ray observations reported short-time variability on timescales of a few ks, it is necessary to obtain strictly simultaneous data between the different energy bands for serious correlation studies.

A dedicated multiwavelength campaign was performed in September 2007 comprising

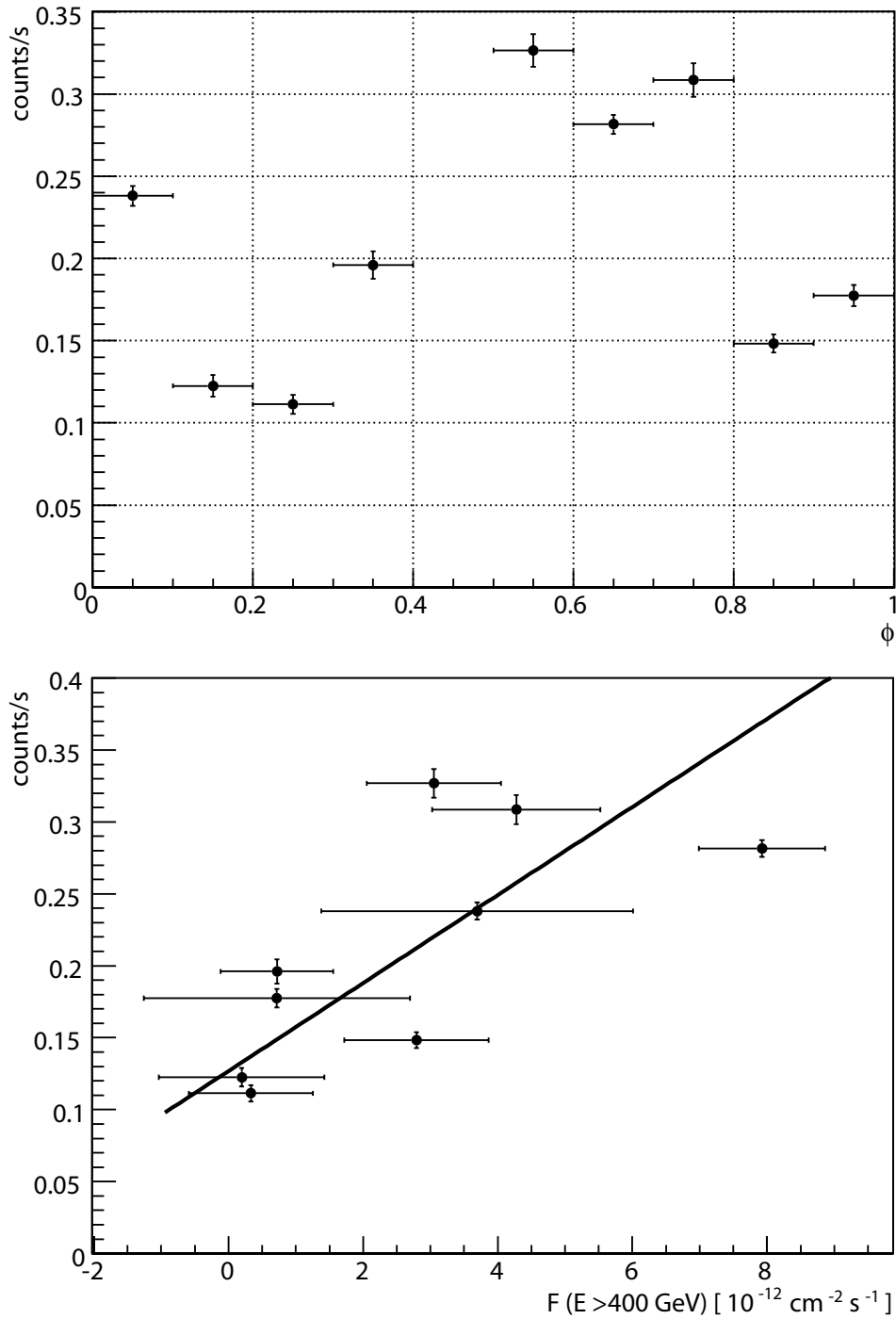


Figure 7.22: The upper panel shows the phase folded X-ray LC taken during the same time as the MAGIC OC II by the XRT instrument on board *Swift*. The lower panel shows the correlation between the upper panel LC and the phase-folded LC of the OC II taken by MAGIC. The obtained linear correlation coefficient is $r = 0.71_{-0.30}^{+0.16}$.

MJD	t_{obs} [ks]	orbital phase	$F(0.3 - 10 \text{ keV})$ [$10^{-12} \text{ erg cm}^{-2} \text{ s}^{-1}$]	Γ	N_{H} [10^{22} cm^{-2}]	χ^2/ndf
54347.202 ± 0.072	12.4	0.434–0.440	13.8 ± 0.2	1.87 ± 0.03	0.517 ± 0.014	446.2/ 382
54349.140 ± 0.076	13.1	0.507–0.513	12.4 ± 0.2	1.66 ± 0.03	0.504 ± 0.019	379.8/ 352
54350.199 ± 0.106	18.3	0.546–0.554	13.3 ± 0.2	1.66 ± 0.02	0.514 ± 0.013	536.5/422
54351.160 ± 0.099	17.1	0.583–0.590	13.4 ± 0.2	1.68 ± 0.03	0.525 ± 0.015	431.6/ 400
54352.146 ± 0.085	14.7	0.621–0.627	22.9 ± 0.2	1.54 ± 0.02	0.538 ± 0.012	496.7/ 447
54353.167 ± 0.084	14.5	0.659–0.665	18.6 ± 0.2	1.58 ± 0.02	0.529 ± 0.013	467.5/ 429
54354.144 ± 0.082	14.2	0.696–0.702	12.6 ± 0.2	1.65 ± 0.03	0.520 ± 0.015	439.5/ 407
54354.663 ± 0.073	3.3	0.716–0.722	10.5 ± 0.8	1.66 ± 0.16	0.5 (fixed)	5.69/ 14
54355.670 ± 0.070	2.7	0.754–0.759	13.4 ± 1.1	1.34 ± 0.16	0.5 (fixed)	11.59/ 14
54356.671 ± 0.073	3.3	0.792–0.797	18.6 ± 1.1	1.34 ± 0.10	0.5 (fixed)	18.4/ 26
54357.674 ± 0.073	3.3	0.830–0.835	18.8 ± 1.2	1.48 ± 0.13	0.5 (fixed)	12.83/ 20
54358.178 ± 0.103	3.8	0.848–0.855	19.0 ± 1.0	1.45 ± 0.09	0.5 (fixed)	19.06/ 31
54359.951 ± 0.205	4.7	0.911–0.926	18.1 ± 0.7	1.55 ± 0.08	0.5 (fixed)	36.50/ 46
54362.247 ± 0.237	2.1	0.996–0.014	12.3 ± 1.0	1.77 ± 0.18	0.5 (fixed)	5.78/ 11
54363.121 ± 0.102	2.5	0.034–0.042	13.4 ± 1.1	1.50 ± 0.16	0.5 (fixed)	7.33/ 13
54365.530 ± 0.040	2.2	0.127–0.130	13.2 ± 1.0	1.45 ± 0.15	0.5 (fixed)	10.59/ 12

Table 7.6: The log of the X-ray observations: First seven observations are *XMM-Newton* and the others *Swift*.

MAGIC, *XMM-Newton* and *Swift* to study possible X-ray/TeV correlation. In addition, LS I +61°303 was observed with the VLBI and RATAN radio observatories and monitored in the optical waveband at the H α emission line with the Skinakas (1.8 m) telescope.

The MAGIC data taken in OC III during September 2007 has already been described in section 7.3. The X-ray data taken by *XMM-Newton* was scheduled prior to this date and, during the main emission peak ($\phi \in [0.43, 0.70]$) in the VHE gamma-rays, sought to obtain a simultaneous spectral energy density to compose a meaningful SED for the first time.

The *Swift* data were taken at later orbital phases ($\phi \in [0.72, 0.13]$) and are not always strictly simultaneous to the MAGIC measurements. The data obtained by both X-ray satellites can be found in Table 7.6. The X-ray data analysis is described in chapter 5.3. The event selection of the *XMM-Newton* data was performed by Víctor Zabalza while the *Swift* data is completely analyzed by me. Due to the low number of events in the spectra obtained by *Swift* the column density of hydrogen (N_{H}), which is responsible for the absorption, is fixed to $0.5 \times 10^{22} \text{ cm}^{-2}$ which is a common measured value in X-ray data of LS I +61°303 as can be seen from the fit to the *XMM-Newton* data (see Table 7.6).

The LC of both energy bands is shown in Fig. 7.23. It is evident that the high flux peak in $\phi \in [0.6, 0.7]$ is prominent and with the same shape visible at both energies. For orbital phases higher than $\phi > 0.7$ the similarity is not so clear. To get a quantitative measure on the correlation between X-rays and VHE gamma-rays only strictly simultaneous data are used. This requirement yields ten points in the correlation graph shown in Fig. 7.24. The linear correlation coefficient is $r = 0.89_{-0.13}^{+0.06}$ with a false alarm probability to obtain it by

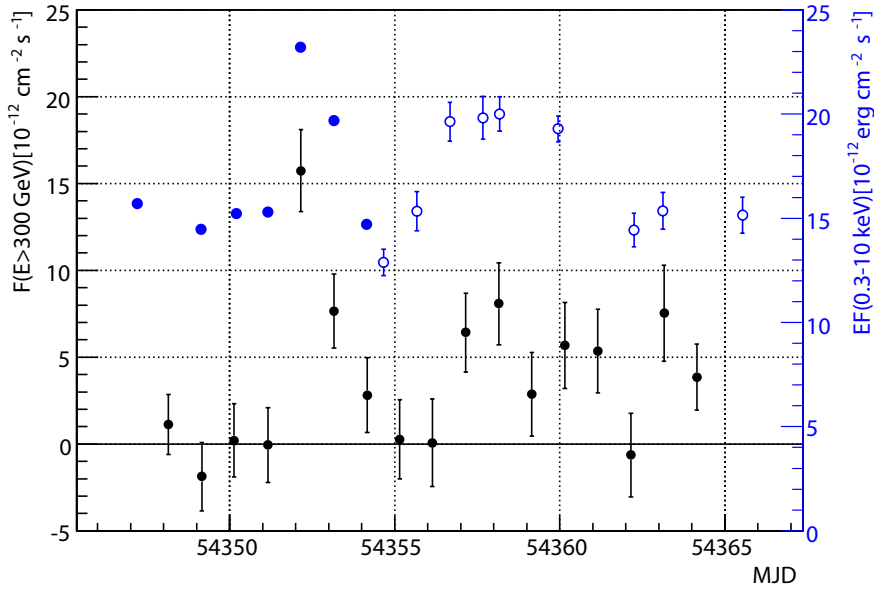


Figure 7.23: The measured integral fluxes by MAGIC (black) and the LC obtained in the X-ray band (blue) in full points for *XMM-Newton* and hollow points for *Swift* measurements. Especially the emission peak at MJD 54351–54354 is remarkably similar in both wavebands. The *XMM-Newton* flux errors are too small to be visible.

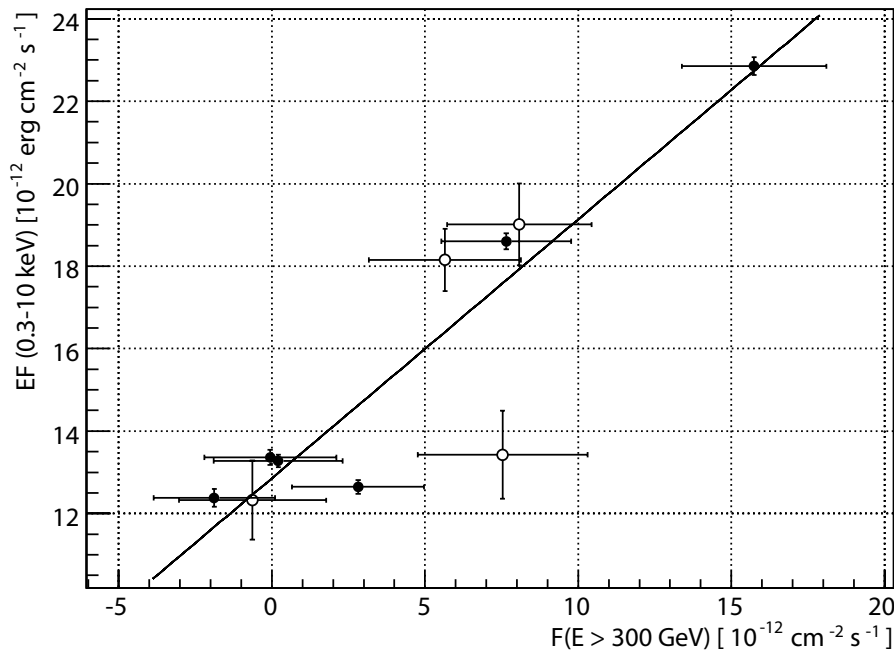


Figure 7.24: The unabsorbed X-ray fluxes vs. the VHE gamma-ray fluxes for LS I +61°303 obtained strictly simultaneously during September 2007 are shown. The *XMM-Newton* measurements are shown by black points and the *Swift* ones by hollow points. A linear trend is visible which is shown by the fitted straight line. A linear correlation coefficient of $r = 0.89^{+0.06}_{-0.13}$ is obtained which provides evidence for a X-ray/VHE gamma-ray flux correlation.

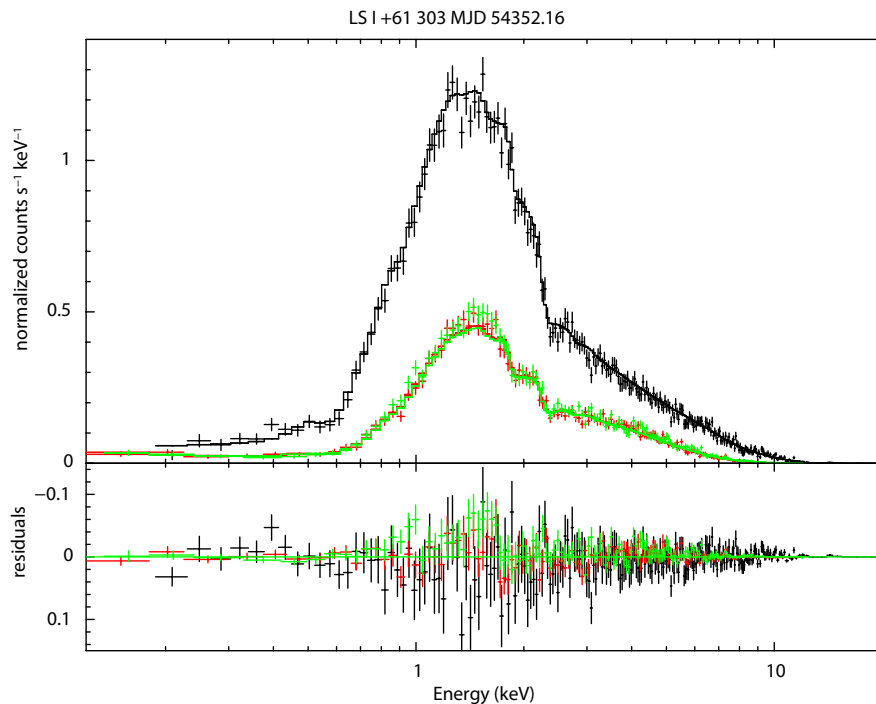


Figure 7.25: In the upper panel the three spectra of the *XMM-Newton* EPIC cameras are shown. The green and red spectra are taken by the MOS-1 and MOS-2 camera and the black one by the more sensitive pn camera. All spectra are cumulatively fitted by the same absorbed power law shape. The lower panel shows the residual of all measured spectra from the fitted absorbed power law.

chance from two independent flat distributed variables of $p_{\text{fap}} = 6 \times 10^{-4}$ corresponding to 3.4σ significance. For details on the false alarm probability estimation see appendix A.4. Thus, for the first time an evidence for correlation between X-ray and VHE gamma-ray flux can be revealed in LS I +61°303.

To further study the simultaneous emission of LS I +61°303 an SED has been constructed from the X-ray measurements of *XMM-Newton* and the VHE measurements of MAGIC in $\phi \in [0.6, 0.7]$. The restriction on these phase range is needed since the MAGIC measurements show hints of a spectral difference between the different phase intervals. A spectrum for only simultaneous data in later phases cannot be constructed from the MAGIC data. Furthermore, a non-negligible difference in the spectral slope of the *XMM-Newton* data is evident for the individual measurements in the phase $\phi \in [0.6, 0.7]$. Due to this spectral variation, only data from MJD 54352 is used in the SED. The derived *XMM-Newton* spectrum for this day obtained by all three EPIC cameras (MOS-1, MOS-2 and pn) is shown in Fig. 7.25, the MAGIC VHE gamma-ray spectrum is shown in Fig. 7.17 in chapter 7.7.

The SED is shown in section 7.11 together with simultaneous radio data. A very in-

interesting question is which acceleration mechanism is at work? Is the relativistic emission caused by leptons or hadrons? The flux correlation alone (with zero time shift) indicates that both emission processes happen at the same time. This can be concluded because no strong absorption in the system is visible in X-rays or in the VHE gamma-ray emission. It is interesting to note that the flux during the phase $\phi \in [0.6, 0.7]$ is $\sim 11 \times 10^{-12} \text{ erg cm}^{-2} \text{ s}^{-1}$ for VHE gamma-rays and thus is a factor of ~ 2 lower than the X-ray flux. For the highest emission (shown in the SED) during the MW campaign, the fluxes in both energy regimes are about the same level. The difference between the flux level of the two energy bands leads to further constraints on the emission process. In times prior to the MAGIC discovery of VHE gamma-ray emission from LS I +61°303 the X-ray emission was described by inverse Compton up-scattering of synchrotron photons at radio energies by the same relativistic electrons which produced the synchrotron emission or by inverse Compton scattering of stellar UV photons. It is difficult to explain the two times lower (or same) flux at TeV energies compared to the X-ray flux if both emissions are produced due to inverse Compton up-scattering by the same particle population. The reason for this is that the IC cooling is much less efficient in producing X-rays compared to TeV photons and thus the X-ray flux should be lower compared to the VHE gamma-ray flux if IC upscattering is responsible for both emissions. Since a correlation between the fluxes is seen in both energy domains, it is more likely that the X-rays originate from synchrotron emission of relativistic electrons and the same electrons produce by IC upscattering of lower energy photons the VHE gamma-ray emission. Nevertheless, it is not possible to prove that the VHE gamma-rays are produced by the same particle population as the X-rays and only in this case the former argument holds true.

7.10.3 Simultaneous radio and TeV observations

The multiwavelength campaign during OC II includes data taken by the VLBA, EVN and MERLIN radio telescopes. The VLBA and MERLIN data coverage was restricted to 25th/26th and 26th/27th October 2006. Additional MERLIN data was taken in November 2006 (16th to 20th) and high resolution EVN data is available for 26th October. Thus, not all data were taken simultaneously with the MAGIC telescope data but on 27th October and 16th - 19th November 2006 the data is simultaneously obtained. The MAGIC observations were performed in the main emission phase of the VHE emission in LS I +61°303 in October and a peak flux of $F(E > 300 \text{ GeV}) = (17 \pm 4) \times 10^{-12} \text{ cm}^{-2} \text{ s}^{-1}$ was measured. The MAGIC data from November were taken in an earlier phase range ($\phi \in [0.44, 0.56]$). The radio flux level is rather low in the October data and in November, when the flux measured by MER-

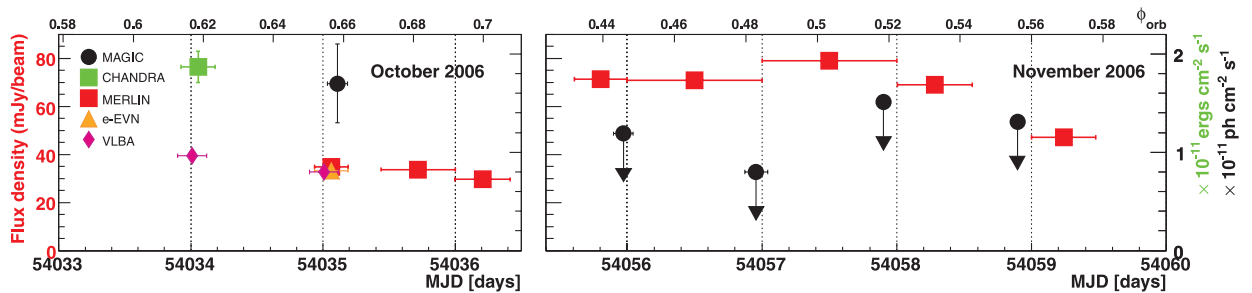


Figure 7.26: The measurements in the radio energy band and at X-ray and VHE gamma-rays from the MW campaign in 2006 (OC II). The vertical error bars show the timespan of the observations. The color-coded identification of the different experiments is given in the inset. The figure is adapted from Albert et al. (2008d).

LIN reaches a higher radio flux level, LS I +61°303 is not detected in VHE gamma-rays by MAGIC. Thus, no correlation is seen between the two energy bands. The sensitivity of the MAGIC measurements is not high enough to test for possible anti-correlation as found between the radio/X-ray emission of LS I +61°303. The radio LC together with the MAGIC and *Chandra* measurements taken in 2006 are shown in Fig. 7.26. A detailed investigation of the MERLIN radio images revealed no jet-like feature in any observation. This excludes the presence of a persistent radio jet on the ~ 100 mas scale.

In the strictly simultaneous MW campaign in 2007 (MAGIC OC III), additional radio data was taken by the VLBA and the images shown in Fig. 7.27 indicate no jet-like feature either. A spatial change of the peak emission position with the orbital phase is evident. This changing peak position is already observed in Dhawan et al. (2006) and in the 2006 multiwavelength campaign. This presents a strong evidence that no persistent radio jet exists in the system and no temporal jet when LS I +61°303 emits VHE radiation. The MAGIC and VLBA light curves are shown in Fig. 7.28 and indicate no correlation between the two energy bands, in agreement with the results of the previous campaign. It is interesting that the time evolution of the flux is different for the 8.4 GHz and the 4.9 GHz frequency band.

7.11 The spectral energy density of LS I +61°303

With the multiwavelength campaign presented here, a simultaneous SED can be computed. The strictly simultaneous data from MJD 54352.16 is used for the X-ray and TeV energy domains. In the radio waveband there is no strictly simultaneous data taken but the VLBA

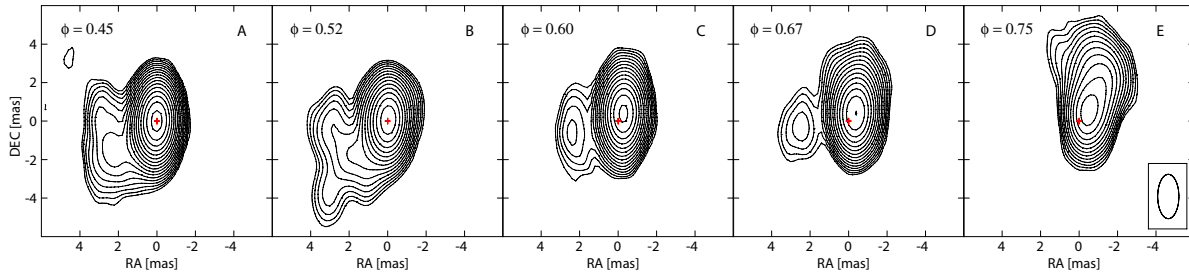


Figure 7.27: Shown are the self calibrated VLBA images taken of LS I +61°303 at 8.4 GHz. The red cross marks the peak emission position of the frame A taken as reference and its size corresponds to the astrometric uncertainty of the calibration source. The first contour is 3 times the RMS radio flux and all consecutive ones scale with 2.5 times the RMS. In the last frame the synthesized beam is shown, its dimensions are 2.3×1.1 mas. Data courtesy of Javier Moldón.

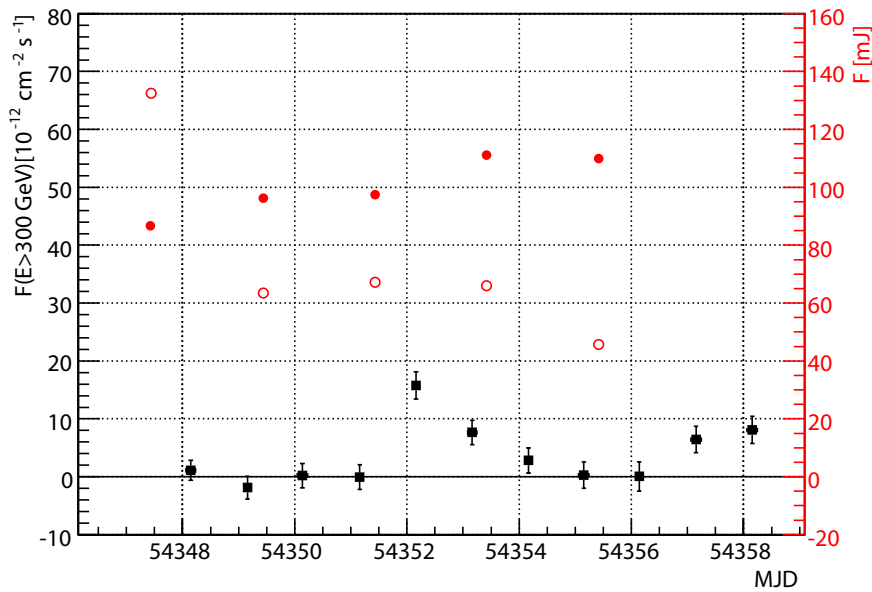


Figure 7.28: The red solid points indicate the 8.4 GHz VLBA measurements, while the red open circle shows those for the 4.9 GHz energy band. The black triangles are the MAGIC VHE gamma-ray measurements. No correlation between the radio and the VHE domain could be observed. The VLBA data reduction was carried out by Javier Moldón.

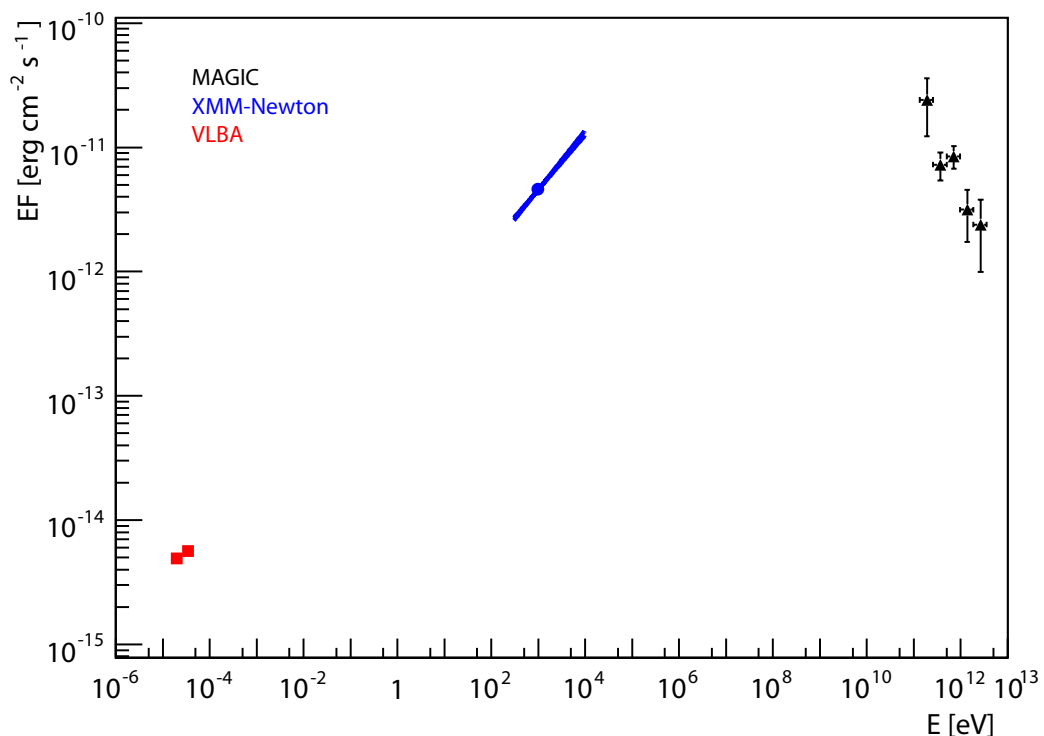


Figure 7.29: The radio data is shown by the red squares and the error bars are too small to be visible. The blue lines show the X-ray spectrum and uncertainties obtained from *XMM-Newton* measurements, the black points the MAGIC data. The X-ray and VHE gamma-ray data were taken at the same time (MJD 54352.16) and the radio data about half a day earlier (MJD 54351.44).

observations were performed only half a day earlier (MJD 54351.44). As can be seen from Fig. 7.28, no strong variability is indicated around this time at radio energies.

The SED is shown in Fig. 7.29. Compared to previous measurements, the X-ray and the TeV flux are not extremely high during the peak emission (here at phase $\phi = 0.62$) of the TeV outburst but well within the previous measurements in this phase range. This simultaneous SED is the new benchmark to test all models describing the multiwavelength spectrum of LS I +61°303.

7.12 Interpretation of the LS I +61°303 observations

Two types of possible scenario exist which might explain the non-thermal emission of LS I +61°303: One is the accretion-powered microquasar scenario, the other the rotationally powered pulsar wind scenario. Both models have quite a number of sub-models to describe the various features of the emission from the system.

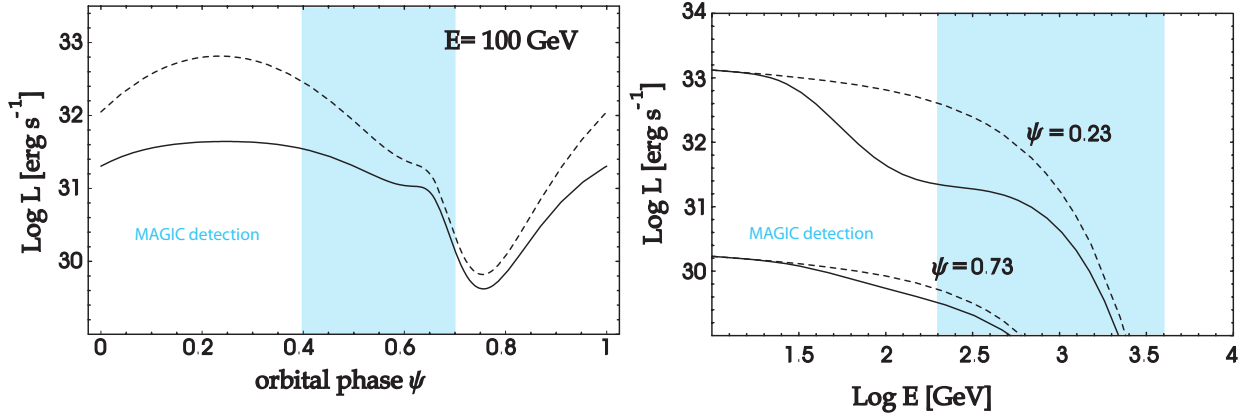


Figure 7.30: The predicted luminosity (L) versus the orbital phase (left) and versus the photon energy (right) for the hadronic microquasar scenario of Romero et al. (2005). The solid line shows the luminosity with absorption and the dashed gives the unabsorbed value. In addition the detection of MAGIC in OC I is shown in cyan. It is clear that the predicted emission level differs significantly from the detected. The figure is adapted from Romero et al. (2005).

With the detection of LS I +61°303 as a VHE gamma-ray emitter, some models could be readily excluded since they predicted the emission in completely different orbital phases. After the publication of the OC I data (Albert et al., 2006), the models are adapted (or new models created) to describe the emission at the correct phases⁹. Here, I will discuss the impact of the VHE gamma-ray data on the various model types. Several models need revision to explain the correct emission profile of the multiwavelength data of LS I +61°303. This shows how the data presented in this thesis contributes to the understanding of the emission and absorption processes in the system.

7.12.1 The microquasar scenario

Prior to the detection of LS I +61°303 as a VHE gamma-ray emitter, the system was predicted in the frame of a hadronic microquasar model to produce TeV particles by Romero et al. (2005). The model assumes that relativistic protons present in a jet would interact with cold protons from the stellar wind. The jet is powered by accretion from the dense circum-stellar disc of the Be star. The predicted luminosity vs. the orbital phase and vs. the gamma-ray energy is shown in Fig. 7.30. According to the model, the predicted flux level (solid line in Fig. 7.30) should be highest around periastron and considerably lower at the phases where the maximum emission is detected by MAGIC. In addition, a rather sharp cutoff is predicted

⁹The original published data by Albert et al. (2006) detects the highest flux at $\phi \in [0.5, 0.6]$, see section 7.5 for the discussion of this measurement

for the energy spectrum which is also not observed in the data taken with MAGIC. This leads to the exclusion of this model.

After the MAGIC measurements became public, the model was modified by applying a more realistic absorption scenario, taking into account the various features of the Be star wind (see Dubus (2006a)). In addition, the compact object changed to a $2.5 M_{\odot}$ black hole (before a $1.4 M_{\odot}$ accreting neutron star) and the power law energy spectrum of the relativistic jet protons was softened to $\Gamma = 2.5$ to match the VHE gamma-ray spectrum. For further details on the modified model see. (Orellana and Romero, 2007). In this model the spectral energy distribution can be matched to the MAGIC measurement but again a two-peaked emission is predicted where a broad peak is around phase $\phi = 0.5$ and a lower one at periastron. The MAGIC OC II provided additional data with high sampling of the periastron passage and the other phases and did not detect the predicted flux level. Furthermore, the highest emission is undoubtedly detected for $\phi \in [0.6, 0.7]$. These facts reject the modified model by Orellana and Romero (2007) as well. One effect possibly contributing into wrong predictions of the model might be that the orbital solution from Casares et al. (2005) is used because the significantly different and more accurate parameters measured by Aragona et al. (2009b) were not yet available.

Another type of microquasar model describes the non-thermal emission from LS I +61°303 in terms of a leptonic emission. The variability is - the same scenario as in the hadronic case - caused by the variable accretion rate and the opacity of the surrounding medium. The VHE gamma-rays are produced by IC upscattering of stellar disk and polar wind photons by the relativistic jet electrons. The accretion model of Marti and Paredes (1995) is used to calculate the accretion rate and the polar wind dominates the accretion for most of the orbital phases apart from the periastron passage where disc accretion is highest. The injected jet luminosity is $\sim 1/1000$ of the total accreting luminosity and thus not high but reasonable. The predicted model fluxes in the different energy ranges are shown in Fig. 7.31. For details on the model parameters and calculations, see Bosch-Ramon et al. (2006). The predicted LC differs significantly from the measurements in all three MAGIC OC's. Especially the significant detection for phases 0.8–1.0 in OC III and the fact that the maximum flux level takes place in the phase range 0.6–0.7 render the model incompatible with the measurements.

Another effect which should be taken into account is the production of secondary gamma-rays by either secondary pair creation (from electrons) or due to IC e^{\pm} cascading of the VHE gamma-rays propagating through the binary system. In terms of a microquasar scenario, these secondary gamma-ray production mechanisms have been considered to explain the lower energy (radio to MeV gamma-rays) emission in hadronic interaction mechanism (Romero

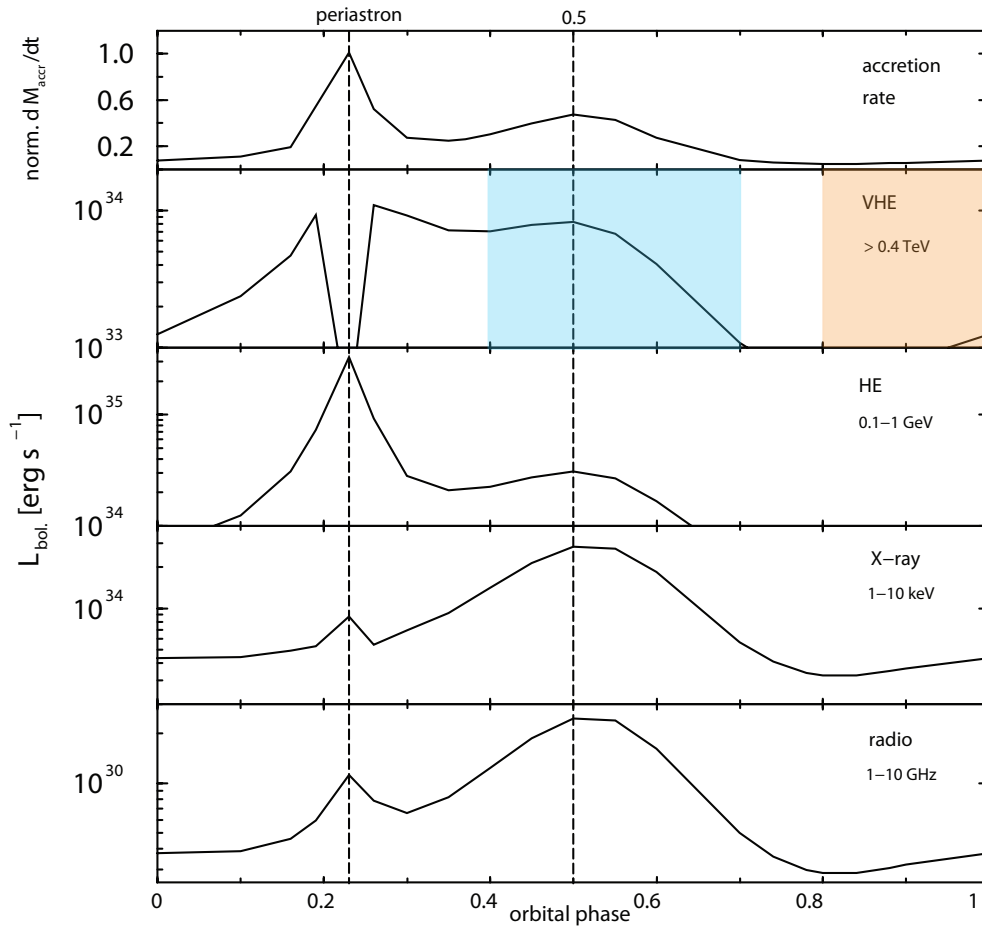


Figure 7.31: The upper panel shows the normalized accretion rate prediction in LS I +61°303 and the other panels from top to bottom show the predicted LC’s for VHE, HE gamma-rays, X-rays and radio emission. In the VHE LC, the phases of LS I +61°303 detected by MAGIC in OC I (blue) and in addition in OC III (orange) are indicated. The prediction does not agree with the measurements (see Fig. 7.6 to 7.8). Figure adapted from Bosch-Ramon et al. (2006).

et al., 2005). Further work on this topic takes the IC cascading into account as well (Orellana et al., 2007). The IC cascading due to the propagation of the VHE gamma-rays was first applied by Bednarek (2006b) to predict the VHE and HE gamma-ray emission of LS I +61°303 prior to the MAGIC detection. Remarkably, the highest flux in VHE gamma-rays is predicted at a phase 0.2–0.4 later than the periastron passage. This is at least close to the phases where the highest flux is measured. A more detailed modelling of LS I +61°303 is presented just after the MAGIC detection (Bednarek, 2006a). This microquasar model can at least describe the dominant emission at the right phase range of OC I but it remains an open question if the emission in the other phases detected in OC II and OC III with MAGIC can be described as well, especially the possible spectral shape difference. In the descrip-

tion of Bednarek (2006a), the multiwavelength behavior is also discussed but the data is not taken simultaneously and, thus, it is not conclusive if it really does describe the correct multiwavelength emission. This model is a good candidate for describing the emission of LS I +61°303.

Another candidate for a reasonable description of the broadband emission of LS I +61°303 is the SSC microquasar description of Gupta et al. (2006) which was adapted to the geometry of LS I +61°303 and included full Klein-Nishina cross-section calculation to describe the emission (Gupta and Böttcher, 2006). In this model, electrons are injected with a power law energy distribution and produce synchrotron emission, which is then upscattered by the same electrons to VHE gamma-rays. The additional Compton scattering of the isotropic wind from the Be star is taken into account as well. The authors describe the highest flux orbital phase of LS I +61°303 well and predict a global flux minimum at the superior conjunction ($\phi = 0.16$) of $F(E > 400 \text{ GeV}) \sim 2.2 \times 10^{-12} \text{ photons cm}^{-2} \text{ s}^{-1}$. This flux is compatible with the upper limit of the MAGIC OC I data. The MAGIC OC II has the lowest upper limit around periastron and it is exactly at the predicted level. This restricts the model already and makes it necessary to calculate the precise model prediction for periastron to check if the model is still valid. The fit to the MAGIC data yields several model parameter values, of which the most interesting is the electron spectral index of $\Gamma_e = 1.7$. Such a spectral index cannot be produced by first order Fermi acceleration (Gallant et al., 1999; Achterberg et al., 2001) and this would imply that shear acceleration (Rieger and Duffy, 2004) or second order Fermi acceleration (Virtanen and Vainio, 2005) plays a vital role in LS I +61°303. Several important effects are not taken into account in the model such as the variable accretion rate and the emission of the circum stellar disc. The authors of this model say that this is an advantage but calculations by the other microquasar models clearly show the importance of these effects (see the previous descriptions and figures). To get more realistic fit parameters the variable accretion rate and circum stellar disc emission should be taken into account and the simultaneous SED as presented in Fig. 7.29 be fitted.

It should be noted that all models described until now use the orbital solution of Casares et al. (2005) which is not the most precise one presently available. The exact orbital parameters are especially important for the cascading process and the propagation of the VHE gamma-rays (with respect to the angle of the observer) to predict correctly the LC and spectrum of LS I +61°303 (see e.g. Bednarek (2006b) and references therein). In addition, most models tried to describe the system with the maximum emission at $\phi \in [0.5, 0.6]$ because the MAGIC publication showed the highest flux in this phase bin. According to the data presented in this thesis which is analyzed using the latest improved software and further

developed analysis tools - such as the unfolding and signal extraction - the highest emission phase range is given by $\phi \in [0.6, 0.7]$ for all observations. Nevertheless, apart from the models of Bednarek (2006a) and Gupta and Böttcher (2006), fundamental differences are found between the measurements and the predictions. In consequence, all other microquasar scenarios described here can be excluded in their current versions.

To check if the model by Bednarek (2006a) can describe the emission of LS I +61°303 along the complete orbit of the compact object, a detailed calculation with the new orbital solutions should be done taking into account the spectral difference as well, since possible short time variability should be explained in VHE gamma-rays. Following their work in 2006, Gupta and Böttcher might like to take the important effects of accretion rate variability and circum stellar disc emission into account to produce a more realistic and complete picture of LS I +61°303. Finally, any model which is able to explain successfully the presented SED would be an important achievement in the process of understanding the emission of LS I +61°303. Of course, it might also be necessary to develop models with more than one particle population to account for the multiwavelength spectrum of LS I +61°303.

7.12.2 The pulsar wind scenario

The pulsar wind scenario explains the emission of LS I +61°303 by the interaction of the pulsar wind with the stellar photons of the Be star. There are several different types of models which try to explain the various emission features observed at different wavelengths in LS I +61°303. Most of the predictions are negated following the detection of VHE gamma-rays from the system by MAGIC. More elaborate theories are now available which strongly endeavor to match not only the lower energy emission but the MAGIC measurements as well. The absence of clear microquasar signatures in LS I +61°303 makes the pulsar wind scenario more likely but there are still problems to explain the details of the MAGIC measurements and the radio and X-ray behavior in one consistent model. In this section, I will describe the interpretation of the VHE emission under the assumption of the pulsar wind models and show where the MAGIC measurements can place severe constraints on the model parameters - or even exclude some scenarios.

The basic description of variable emission in the high energy gamma-rays could be due to photon-photon absorption. The optical depth for VHE gamma-rays depends on the stellar photon field as a function of orbital phase. Here, all the orbital parameters play a vital role and, since they are at least partially exposed to uncertainties, it is a challenging task to describe the VHE gamma-ray propagation. A simple absorption scenario which predicted the VHE gamma-ray emission along the orbit of the compact object is given by Dubus

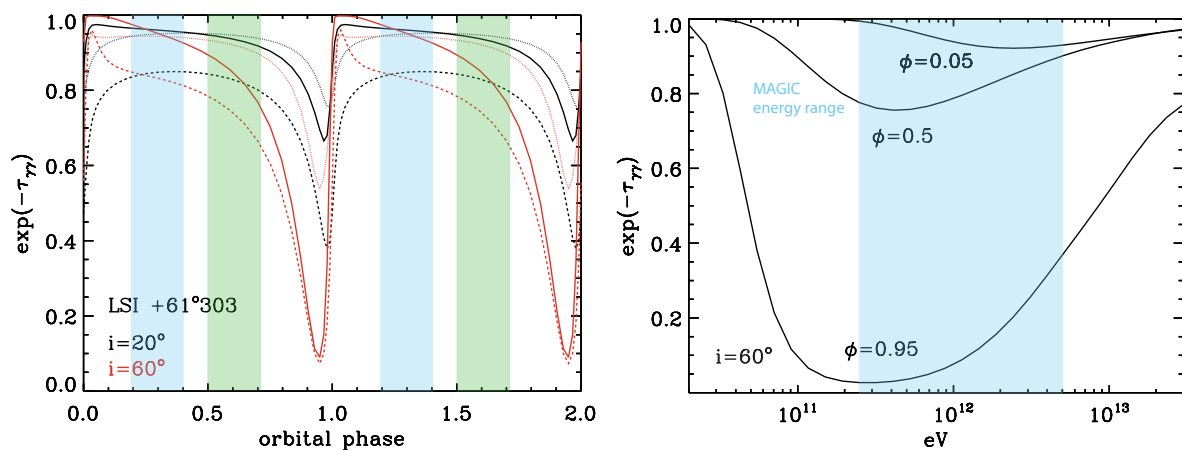


Figure 7.32: The left plot shows the optical depth against the orbital phase in LS I +61°303 adapting the orbital solution of Grundstrom et al. (2007) and setting the period of the periastron to $\phi = 0$. The red lines are for inclination 60° (pulsar) and the black one for 20° (black hole). Solid lines are for 100 GeV, dashed for 1 TeV and dotted for 10 TeV gamma-rays. The MAGIC detection is shown by the blue shaded region for OC I and by the green shaded region for OC III. The right plot shows the optical depth versus energy in case of $i = 60^\circ$ and for three different orbital phases. The energy range of the MAGIC measurements is indicated by the blue shaded region. For the interpretation see section 7.12.2.

(2006a). The prediction shows only significant absorption around the periastron passage of the system (see Fig. 7.32). If the source of the VHE gamma-rays is a constant emitter and only absorption would cause the variation in the flux level, then the system should show a broad constant emission interval and would only be undetectable in a narrow phase range around periastron. This scenario is clearly incompatible with the MAGIC measurements presented here.

The emission from the termination shock

When the stellar wind hits the pulsar wind, a termination shock is produced between both winds. Where this termination shock takes place depends on the orbital solution of the system and the strength of the stellar and pulsar winds. The stellar wind has two components in LS I +61°303, the disc wind and the polar wind. Besides a small phase range around the periastron passage, the isotropic polar wind dominates the total stellar emission. The place of the termination shock is calculated e.g. by Sierpowska-Bartosik and Torres (2009).

The geometrical location of the termination shock for the orbital solutions of LS I +61°303 derived by Grundstrom et al. (2007) is shown in Fig. 7.33.

The first model of the emission from LS I +61°303 assuming a pulsar wind scenario was published by Maraschi and Treves (1981). They assumed a young relativistic pulsar

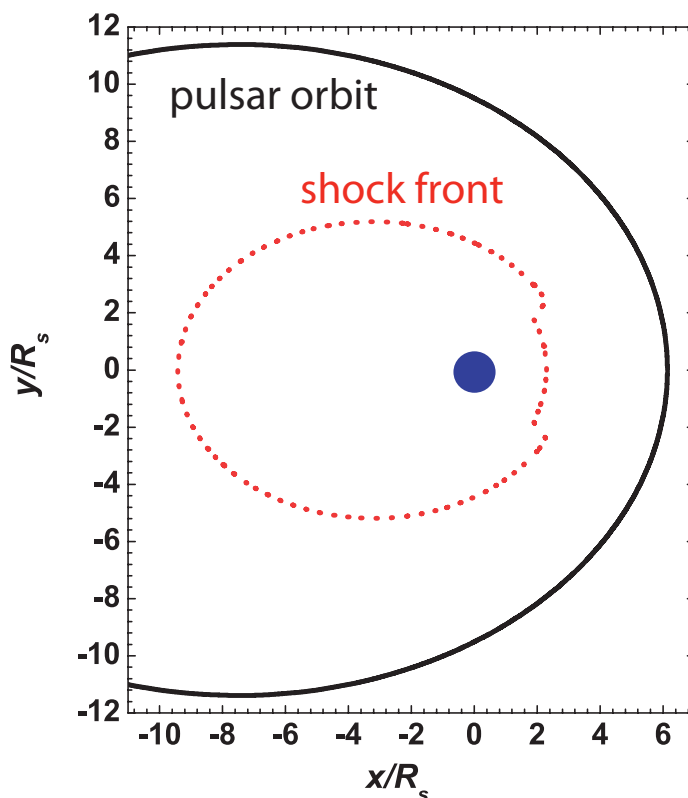


Figure 7.33: The location of the termination shock (red-dotted line) for the Be star rest frame in LS I +61°303 calculated by Sierpowska-Bartosik and Torres (2009). The x- and y-axis scale is given in units of R_* . The Be star is indicated by the blue circle. The shape of the termination shock is not shown.

and calculated that the loss of rotational energy could power the emission from radio to gamma-rays. No HE gamma-rays were detected during this time.

More recently, a pulsar wind model is suggested to describe the whole broad band spectrum, including the MAGIC OC I data by Chernyakova et al. (2006). The model assumes that the radio signature is produced from synchrotron radiation of electrons and the X-ray emission by the same electrons due to IC upscattering of UV stellar photons. The electrons are suggested to possess energies larger than 100 MeV to explain the broad band shape of the spectrum. The authors suggest that these electrons are produced in interactions of energetic protons, accelerated at the termination shock, with cold protons from the stellar wind. The resulting pions from the hadronic interaction ($p + p \rightarrow \pi^0 + \pi^+ + \pi^-$) would decay to electrons and gamma-rays. The lower energy threshold for the electrons is needed to account for emission on a long enough timescale. If the energy is smaller, then the cooling time would be too short. In this model, the hadronic interaction would produce a significant if not the dominant part of the VHE gamma-rays. No detailed LC or spectra for the individual orbital

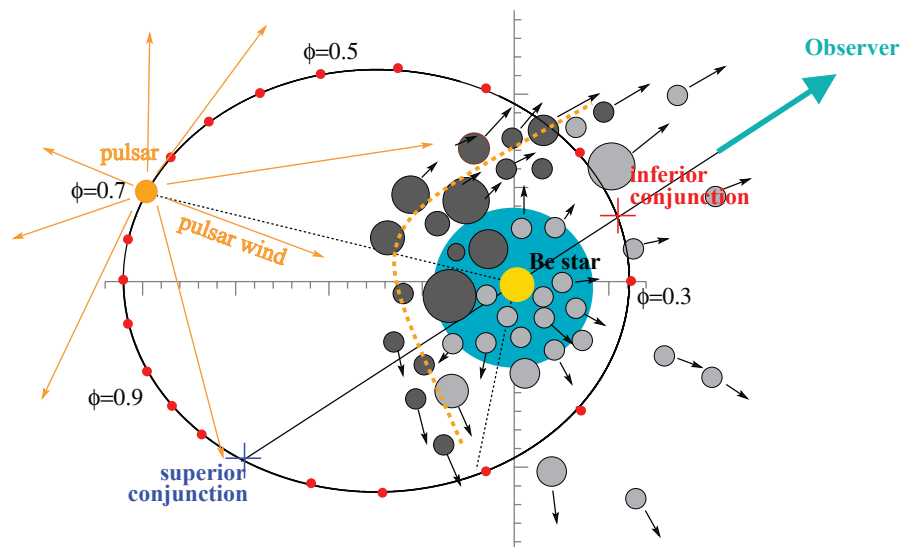


Figure 7.34: The orbital solution of LS I +61°303 with the parameters derived by Grundstrom et al. (2007). The polar wind clumps are shown in grey and the darker grey circles represent the clumps shocked by the pulsar wind. In addition, the Be star is indicated by a yellow circle and the circum stellar disc around it by a cyan circle. The pulsar, its wind as well as the termination shock formation expected from a isotropic stellar wind (dotted line) are shown in orange. The escape directions and speed of the wind clumps is illustrated by the arrows attached to them. The figure is a modified version taken from Zdziarski et al. (2008).

phases are predicted in this model and the data used is not simultaneously taken, thus giving no evidence if the combined spectral distributions in their SED can occur in reality.

Another pulsar wind model, which might be able to describe the short time variation in both X-rays as well as in the VHE gamma-rays, is the clumped wind model. This type of scenario was first suggested by Zdziarski et al. (2008). In this type of model, the orbital geometry is not the sole reason for variability: The polar wind of the Be star is clumped and thus mixes with the pulsar wind; the electrons of the pulsar wind can be trapped in the magnetic inhomogeneities of the polar wind clumps, causing fast X-ray variability. Notice that, in this model, the TeV emission is produced by a compactified pulsar wind nebula which is formed after the termination shock and extends on scales of one AU (roughly the system dimensions) (Neronov and Chernyakova, 2007). The clumpy wind will result in an irregular termination shock instead of a smooth bow shock shape. An illustration of the system and the clumpy wind interaction is shown in Fig. 7.34. No detailed TeV emission LC along the orbit of the compact object is provided by the authors nor any spectral energy distribution. The problem is that the detailed shape of the bow shock geometry is not known which prevents detailed calculations in the case of the clumped wind. Nevertheless, it is shown

that the gamma-ray emitting plasma can flow along the contact surface of the bow shock and thus can be considerably boosted in the direction of the absorber. Furthermore, two maxima are expected in the TeV emission as one of them is almost completely absorbed by $\gamma\gamma$ -absorption. So at least as qualitative an LC as detected by MAGIC (one highest emission peak) can be explained by the model and it has promising capabilities to describe short-time variation in the flux level.

The emission from the free pulsar wind

VHE and HE gamma-rays cannot only be produced in the termination shock of the pulsar wind but in the free (unshocked) pulsar wind as well. In the free pulsar wind, the production of the VHE gamma-ray is caused by inverse Compton scattering of soft photons by the mono-energetic electrons injected by the pulsar: This would result in an emission line-like feature (Cerutti et al., 2008). For LS I +61°303 such a feature cannot be detected in the spectrum and the strongest constraint on a contribution of the free pulsar wind to the total VHE and HE emission comes from the MAGIC measurements. Furthermore, the emission should be strong around the periastron. The non-detection of LS I +61°303 at the periastron in VHE gamma-rays suggests that, in the case of the pulsar wind scenario, the emission probably comes from the shocked wind. In the case of the shocked wind, the shock occurs much closer to the neutron star at the periastron passage and, thus, the much higher B field leads to higher synchrotron losses and explains a possible cutoff at VHE's. The missing signature of a free pulsar wind in the VHE measurements of LS I +61°303 places the pulsar wind scenario in some trouble but it does not exclude it. The stripped wind model in which the free pulsar wind remains highly magnetized up to the termination shock would give different signatures. For a description of the striped wind model see Kirk et al. (2007) and references therein.

It should be mentioned that the free pulsar wind might consist of non-mono-energetic particles, as suggested by Sierpowska-Bartosik and Torres (2008). In their scenario, the free wind cannot be distinguished from the shocked one and no line-like feature would occur. A drawback is that the model cannot explain the lower energy X-ray and radio emission, since most of the pulsar energy is carried by hadrons to match the pulsar wind requirements to explain the TeV emission. Maybe cascading into secondary pairs within the stellar wind can explain the lower energy emission such as the radio outflow seen in the VLBA measurements as suggested by Bosch-Ramon et al. (2008). Nevertheless, if the complete emission is produced by the free pulsar wind with a power law energy distribution of the electrons, then the high emission would be expected around the periastron.

More detailed investigations of the free pulsar wind VHE gamma-ray production and the absorption effects present in LS I +61°303 with respect to the geometry of the system are performed by Sierpowska-Bartosik and Torres (2009). The pulsar wind model is based on their earlier work (Sierpowska-Bartosik and Torres, 2008) and a power law electron spectrum with spectral index $\alpha = 2.6$ is assumed to be present in the free wind. The free pulsar wind is seen by the observer for most of the orbital cycle as an unshocked wind and so only the free wind is investigated in this model. The new geometrical parameters of LS I +61°303 obtained by Aragona et al. (2009a) are not yet considered in this model but they are closer to the Grundstrom et al. (2007) values than the Casares et al. (2005) parameters. The calculations of the model are performed for both orbital solutions published up to 2008. A two-component wind model of the Be star is assumed, which takes into account the slow massive (dense) wind of the circum-stellar disc and the isotropic, fast and less massive polar wind. The calculated optical depth along the orbit of the compact object predicts no significant absorption beside the periastron passage. The quantitative behavior depends on the details of the orbital solution. It is possible with this model to describe the spectrum and light curve obtained in OC II by MAGIC if the normalization is increased by 5%. According to Sierpowska-Bartosik and Torres (2009), it is not a problem to obtain higher flux values in phases where MAGIC detected LS I +61°303 only with marginal significance. To show the different behavior in VHE gamma-rays in the phases around the outburst, the more sensitive measurements of OC III are added to the model LC and shown in Fig. 7.35. From this figure, it is evident that the emission just before or around the periastron is already above the upper limits derived from the MAGIC measurements presented in this thesis. The more sensitive OC III measurement in the other phases should be described by the model as well; a description of the somewhat different spectral shape in the phases 0.8–1.0 would provide further confidence in the model. It will be very interesting to see if the model can describe these features as well. One possibility to improve the model would be to include the termination shock emission in the scenario.

The indication for a spectral change of the VHE gamma-ray spectrum in the later orbital phases ($\phi \in [0.8, 1.0]$) found in the MAGIC data might possibly indicate a contribution by the shocked pulsar wind. Since the free pulsar wind model does not give any prediction about spectral changes in the VHE photon spectrum along the orbit, a second spectral shape produced by the shocked pulsar wind overlaid with the free pulsar wind might explain the observed spectrum presented in section 7.3. More detailed measurements by MAGIC II could give vital input for the testing of the model. Up to now, the rather coarsely defined shape

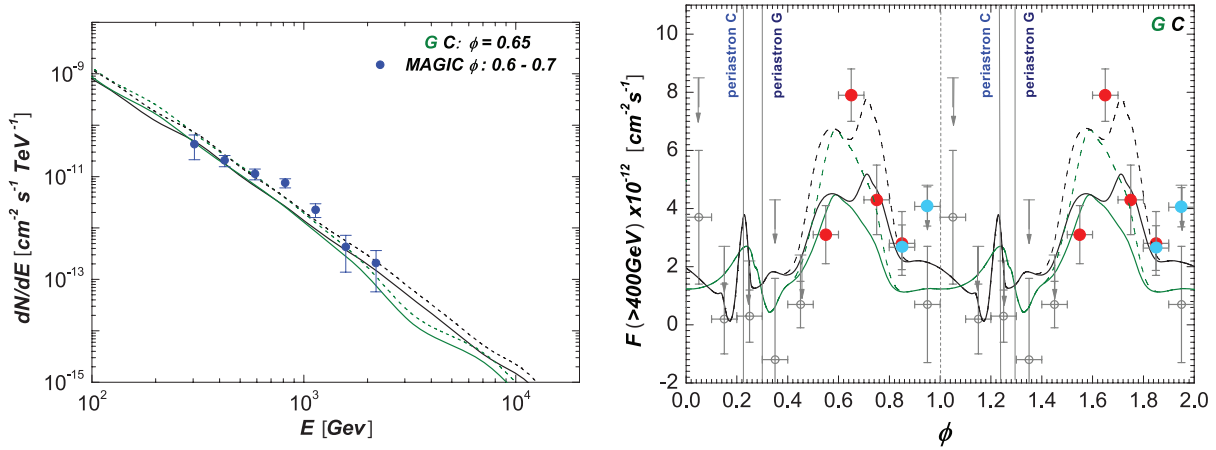


Figure 7.35: The left plot shows the spectral energy shape predicted by the free pulsar wind model with power law energy distribution for the Grundstrom et al. (2007) (green) and Casares et al. (2005) (black) orbital solutions. The dashed lines represent the model prescription with a 5% increased normalization. The data points are the unfolded energy spectrum of the MAGIC OC II measurements in the main emission phase. The right side shows the light curve but, in addition to the OC II measurements of MAGIC (red points more than 2σ , grey ones less than 2σ), the measurements of OC III are added in blue points which lead to further constraints to the LC compared to the data available when the model was published.

of the VHE gamma-ray spectrum in the phases $\phi \in [0.8, 1.0]$ could not be used as a detailed constraint to the model but it should encourage the investigation of the contribution of the shocked wind for the later orbital phases.

Another possible flaw of the model by Sierpowska-Bartosik and Torres (2009) might arise from the indications of short-time variability found not only in the X-rays (no X-ray emission description included in the model) but possibly in the VHE gamma-rays as well. Even if the current significance of the short-time variability found in the LS I +61°303 data of MAGIC is not strong enough to establish this feature firmly, the evidence for it presented in this thesis is compelling enough to consider models to be more realistic which are able to explain such fast changes in the flux level in both X-rays and VHE gamma-rays. This is even further backed up by the evidence for X-ray/TeV correlation presented in this thesis. While the VHE spectrum can at least be partly described by the free pulsar wind model (with a power law energy spectrum for the electrons), the new challenge is to describe the simultaneous SED presented here.

7.13 Conclusions resulting from the LS I +61°303 observations

The detailed investigation of the emission processes in LS I +61°303 disproved almost all models available at the time of its discovery in VHE gamma-rays. The VHE data presented here should increase the interest in this new class of TeV sources. Several new or modified models were developed to explain the emission profile of LS I +61°303. Both microquasar and pulsar wind models can describe certain features such as the position of the maximum flux level in the VHE gamma-ray domain. The models of Bednarek (2006a) and Gupta and Böttcher (2006) are currently the best description in the framework of the microquasar scenario. Nonetheless, they have yet to describe the simultaneously derived SED (see Fig. 7.29) and to give a more detailed description of the light curve obtained in the VHE gamma-ray band.

Of all the pulsar wind models, the one developed by Sierpowska-Bartosik and Torres (2009) describes the light curve and the spectral shape in VHE gamma-rays best. The model still lacks an explanation of the broad band spectrum and possible short-time variability, but it is still one of the most promising candidates to explain the observed VHE emission of LS I +61°303.

To summarize, it is clear that the geometry of the system imposes several crucial parameters for a successful understanding of the processes taking place in LS I +61°303. The emission cannot be explained only by absorption or accretion rate variability - additional, more complex, processes like cascading lead to a better description of the system. Finally, none of the models supposing a hadronic origin of the VHE gamma-rays can give a good description of the radiation emitted by LS I +61°303.

7.14 Future observations with MAGIC I and MAGIC II

The sensitivity of MAGIC I and MAGIC II in stereo mode¹⁰ will be about two times better compare to MAGIC I. In 2009 and 2010 an observation campaign of 70 hours duration is planned on LS I +61°303 with both telescopes. These observations are expected to yield a 5σ detection within an observation time of 4 hours if the flux of LS I +61°303 exceeds 2.8% of the Crab Nebula flux which corresponds to $F(E > 300\text{GeV}) = 3.2 \times 10^{-12} \text{ cm}^2 \text{ s}^{-1}$. This implies a huge advantage compared to the present measurements. With this sensitivity a spectrum of LS I +61°303 could be derived for almost each night in the orbital phases 0.8–1.0 if the

¹⁰The term "stereo mode means to observe the same shower simultaneous with both telescopes

emission level is the same as in OC III¹¹. With this large number of spectra, details about spectral variability (which are already hinted in the analysis presented in chapter 7.7) can be verified with high significance. In addition, a correlation study between the VHE gamma-ray spectral index and the X-ray spectral index will be possible. For this correlation study, the number of obtained spectra must be as large as possible and the errors on the spectral index must be small enough to achieve a high significance for the correlation coefficient. These requirements are fulfilled due to the improved sensitivity in the planned observations. A spectral index correlation between the X-ray and the VHE gamma-ray emission is important to identify the particle population (hadrons or leptons) causing both emissions.

Furthermore, the higher sensitivity will allow to detect LS I +61°303 in phases where the current sensitivity of MAGIC I was too low to yield a confident detection. Even in the case of improved upper limits in orbital phases where currently no gamma-ray emission is detected the restrictions placed on the model description of the phasefolded LC will be at least two times stronger compared to the current restrictions. With these even stronger constraints a further discrimination between the emission models might be possible.

Another advantage of the higher sensitivity will be the improved chances in search for short timescale variability. In the study presented in this thesis, hints for variability on the time scale of about 30 minutes were already found. The measurements of MAGIC I and MAGIC II will provide a solid evidence (more than 4σ significance) for short timescale variability if the same increase of flux is measured as shown in Fig. 7.9.

Altogether, the observation of LS I +61°303 with both MAGIC telescopes will further increase the understanding of the processes taking place in the system.

¹¹No individual night yielded a detection with 5σ in OC III

Chapter 8

Conclusion and Outlook

This work demonstrates that the detailed study of a single object with a large amount of observation time can yield very valuable scientific information and leads to definite exclusion of certain emission scenarios in the newly established gamma-ray binary LS I +61°303, based only on the VHE gamma-rays emitted by it. The fascinating but very complicated multi-wavelength emission of gamma-ray binary systems is just beginning to be understood, and this thesis points out the strong impact of the VHE gamma-ray data on our understanding of the emission processes in this system.

A vital requirement to perform long-term studies over time spans of several years is the study of performance stability of the instrument used in the investigation. For this reason, I have checked the long-term stability of the MAGIC telescope using data from the Crab Nebula taken in the years 2005–2008 and studied properties such as the spectrum and light curve. In this performance study, in total 32.5 hours of data were taken in smaller subsamples, covering all different observation modes, telescope hardware setups, different zenith angle ranges and background light conditions (dark and moon nights). The study demonstrates that the system is very stable and the spectrum and light curve are not influenced by the zenith angle distribution or moonlight, except (as expected) for an increase in the energy threshold of the analysis. This enables the use of data taken under various observation conditions and thus increases tremendously the duty cycle of the observations. In binary systems, a high-duty cycle is the key factor to study variability timescales in order to search for periodicity and to observe potentially irregular behavior from the averaged emission.

The performance study reveals a systematic increase of the flux level by 12% and a hardening of the spectral index of $\Delta\Gamma = 0.2$, after upgrading the read-out system of MAGIC I to the 2 GHz MUX FADC read-out. On the other hand, the change of the read-out improved the sensitivity by 40% and the system became more stable.

The very high stability of MAGIC I enabled the detailed long-term study of the LS I +61°303

binary system between 2005 and 2008. A total observation time of 225 hours places LS I +61°303 among the best-studied objects by MAGIC. The huge amount of observation time has led to the discovery of the variable VHE gamma-ray emission of LS I +61°303. Thus, for the first time (after almost 30 years of observations), LS I +61°303 is clearly identified as the source of gamma-rays from this region, as first reported by *COS B*. In addition to the variability, the periodic nature of the emission was proven with high significance. The period of $P = 26.60 \pm 0.45$ d is compatible with the most precisely measured orbital period. This is the first time that a periodicity could be proven by MAGIC and the second time in the field of VHE gamma-ray astronomy.

The detailed investigation of the light curve exhibits that the emission takes place in outbursts between the orbital phases 0.6–0.7, with a peak gamma-ray flux of $F(E > 400\text{GeV}) \sim 15 \times 10^{-12} \text{ cm}^{-2}\text{s}^{-1}$ and varies slightly between individual orbital phases. In addition to this periodically observed emission, additional sporadic significant fluxes are detected in other orbital phases. These fluxes are irregularly observed in orbital phases after the outburst. Whether this component is periodic could not be verified with the presently available data. Nevertheless, the emissions cannot belong to a period of shorter timescale than the orbital one, since there are no other prominent peaks at higher frequencies in the periodogram (after subtracting the orbital periodic signal). To investigate if the additional signals are connected to a longer super-orbital modulation, as observed in the radio emission of LS I +61°303, the observation must span an even longer time compared to the three years of data available for my work.

The spectra derived from the periodic outburst do not differ in their spectral index and are all compatible with the spectral index derived from the most significant spectrum of observational campaign (OC) II ($\Gamma = 2.6 \pm 0.2_{\text{stat}} \pm 0.2_{\text{sys}}$). The spectra observed in phases 0.5–0.6 are compatible with the spectrum obtained from the phase range 0.6–0.7. Contrary to this, a hint of spectral variability is found in the comparison of the spectra obtained in the phase ranges 0.6–0.7 and 0.8–1.0 in OC III. It is shown that the latter spectrum can be better described by a power law with variable spectral index compared to a simple power law. The spectral variability could indicate that different production processes are responsible for the VHE gamma-ray emission in the periodic outburst and the irregular detected fluxes in OC III.

In addition to the VHE gamma-ray measurements, several multiwavelength campaigns in the radio and X-ray bands were conducted. While no correlation between the radio and the VHE gamma-ray emission from LS I +61°303 was found, evidence for correlation between data taken strictly simultaneously in X-rays (by *XMM-Newton* and *Swift*) and VHE gamma-

rays in OC III could be revealed. The linear correlation has a coefficient $r = 0.89_{-0.13}^{+0.06}$ and yields a 3.4σ significance. In addition, another correlation ($r = 0.71_{-0.30}^{+0.16}$) with about 2σ significance is found for the phase-binned light curve in X-rays obtained by *Swift* and in VHE gamma-rays obtained by MAGIC, taken in the same OC II. Thus, both correlations - even though moderately significant - together provide compelling evidence for a connection between both emissions. The correlated emission is probably produced by the same particle population. This possibility could be verified if a correlation of the spectral index in the X-ray and VHE gamma-ray emission was found. Such a spectral index correlation requires much higher sensitivity in the VHE gamma-ray measurements to obtain smaller errors on the spectral index of low flux level measurements and might be provided by future observations of MAGIC I and II.

For the first time, a strictly simultaneous SED is composed from the simultaneous X-ray and VHE gamma-ray measurements. The ratio between the energy density in X-rays and VHE gamma-rays ($EF_{\text{X-rays}}/EF_{\text{VHE}} > 1$) favors synchrotron emission as the origin of the X-rays while the VHE gamma-rays are most likely produced by inverse Compton emission of relativistic electrons if the emission originates from the same particle population.

Finally, most of the models suggested to describe the emission of LS I +61°303 prior to its discovery in VHE gamma-rays need to be modified due to their incompatibility with the measurements presented in this work. Several modified models appeared after the first MAGIC data was published but most of them do not describe the light curve and spectrum correctly of the most recent measurements by MAGIC. The best description of the VHE gamma-ray data is provided by the pulsar wind model assuming that a power law distribution of relativistic electrons in the free pulsar wind produces the VHE gamma-ray emission, due to inverse Compton upscattering of UV stellar photons (Sierpowska-Bartosik and Torres, 2009). While a leptonic microquasar model, assuming cascading as the dominating emission mechanism (Bednarek, 2006a) and another leptonic SSC microquasar model (Gupta and Böttcher, 2006) well describe the flux level at VHE gamma-rays - at least in the main emission phase - a detailed prediction for the full orbit has not yet been published. Furthermore, all models can be tested on the first ever taken simultaneous SED presented here. All fits to SED's performed so far are composed from data taken up to decades apart in time (because of the lack of simultaneous data) and are in consequence not useful to test models. Since no compelling evidence at other wavelengths such as a radio jet or an X-ray emitting accretion disc has been found, the microquasar scenario is disfavored by the results of the observations presented in this thesis but this scenario cannot be fully excluded yet.

More sensitive measurements are needed to confirm the hints provided in this thesis for

spectral and short timescale variability. Another observation campaign of 70 hours duration is planned for 2009/2010 with MAGIC I and II. These two times more sensitive measurements (compared to MAGIC I) will allow to detect spectral variability between the emissions in individual orbital phases significantly, as well as to test for a potentially lower flux level present at orbital phases where LS I +61°303 is not yet detected. Within the planned observation time of four hours per night, fluxes down to 2.8% of the Crab Nebula flux will be detected with 5σ significance. This sensitivity will allow the extraction of a spectrum in almost each night in the phase range 0.8–1.0 if the flux level is the same as in 2007 and 2008. These spectra will allow to verify the hint for spectral differences between the phase ranges 0.8–1.0 and 0.6–0.7 with high confidence. Furthermore, the flux errors of the 30 minutes binning used in the search for short timescale variability will yield already $\sim 4\sigma$ significance in the simple and robust χ^2 -test procedure described in chapter 7.5. The short timescale variability will provide an upper limit to the emitter extension and thus constrain all emission models of LS I +61°303. In addition, vital information about the emitter can be gained by the investigation of spectral index correlation between the X-ray and the VHE gamma-ray emission and will reveal the particle population causing the emissions. This correlation study will only be possible if the error of the spectral index of the MAGIC spectrum is at least as small as the one obtained from the outburst fluxes in phase 0.6–0.7. This will be achieved in phase ranges where the flux of LS I +61°303 is at least about 5% of the Crab Nebula flux. On the other hand, a sensitive X-ray instrument providing excellent time coverage of the source is needed for the correlation study as well. Since long-term studies will most probably not be granted with the most sensitive X-ray instruments on board *XMM-Newton* and *Chandra* the only tools for this kind of study are the future sensitive all-sky monitoring missions such as the Japanese X-ray observatory, MAXI which is scheduled to be launched this summer (2009). In addition, the simultaneous measurements by *FERMI* and MAGIC (in 2009/2010) will close the gap in the SED between the X-ray and VHE gamma-ray spectra and will help in judging which emission process is at work in all energy ranges.

The longer-term future of VHE gamma-ray binary studies lies in the planned Cherenkov Telescope Array (CTA) which might host up to 100 Cherenkov telescopes and will cover an energy range between several ten's of GeV to about 100 TeV, with a peak sensitivity ten times better than the current experiments. With this extremely sensitive instrument, it is likely that many more binary systems shall be discovered and the currently established systems like LS I +61°303 might be the base model for the whole population of gamma-ray binaries to be discovered.

Appendix A

LS I +61°303 observational details

In this Appendix, the details on the observations of LS I +61°303 are reported which are not presented in the main text. These details mainly serve the purpose to provide the reader with the full information of data, so that he will be able to form his own opinion about the conclusions of the author.

A.1 LS I +61°303 light curve for MAGIC OC III

The full information about the data with lower analysis energy threshold of $E < 300$ GeV.

Middle Time (MJD)	Obs. Time (min)	Phase	Flux 10^{-12} ($\text{cm}^{-2} \text{s}^{-1}$)	Upper limit 10^{-12} ($\text{cm}^{-2} \text{s}^{-1}$)
54348.15*	203	0.47	1.1±1.7	4.6
54349.16*	210	0.51	-1.9±2.0	2.5
54350.14*	215	0.55	0.2±2.1	4.4
54351.16*	220	0.59	-0.1±2.2	4.2
54352.16*	221	0.62	15.7±2.4	...
54353.16	224	0.66	7.7±2.1	...
54354.17	213	0.70	2.8±2.2	7.1
54355.15	172	0.74	0.3±2.3	4.8
54356.14	149	0.77	0.1±2.5	5.1
54357.15	178	0.81	6.4±2.3	...
54358.15	179	0.85	8.1±2.4	...
54359.15	184	0.89	2.9±2.4	7.7
54360.15	177	0.93	5.7±2.5	...
54361.15	183	0.96	5.3±2.4	...
54362.15	189	0.00	-0.6±2.4	4.2
54363.16	139	0.04	7.5±2.8	...
54364.15	196	0.08	3.8±1.9	...
54464.86	131	0.88	2.0±2.9	7.9
54465.86	131	0.92	7.8±3.0	...
54466.87	100	0.95	8.9±3.4	...
54467.86	121	0.99	7.4±2.9	...

Table A.1: Observation time, orbital phase, integral flux (above 300 GeV), flux upper limit at the 95% confidence level (given in case flux significance is $\lesssim 2\sigma$, (Rolke et al., 2005, following)). Nights partly taken under moonlight conditions are labeled with an asterisk.

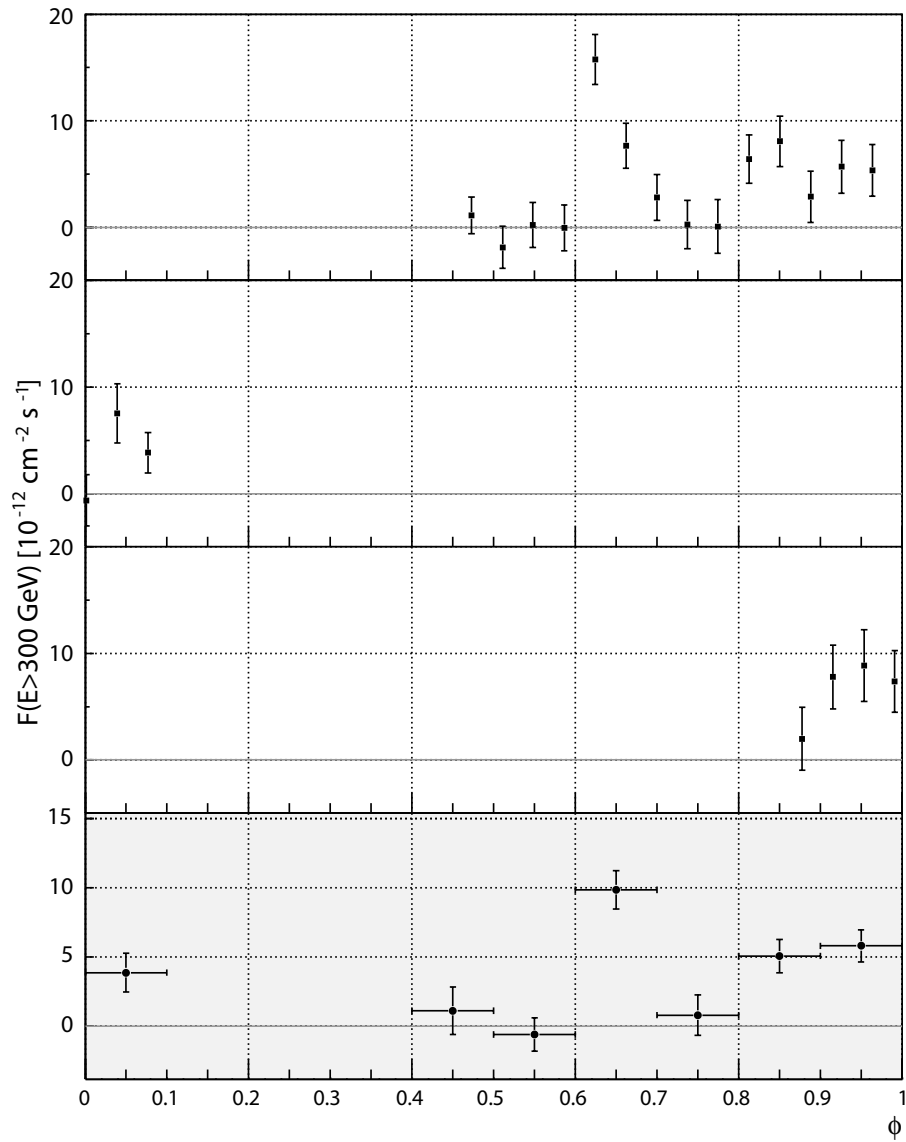


Figure A.1: The integral flux above $E > 300 \text{ GeV}$ of LS I +61°303 versus the orbital phase for OC III is shown for each orbit. The lowermost panel shows the averaged integral flux in phase range intervals of $\Delta\phi = 0.1$.

A.2 LS I +61°303 intranight light curves

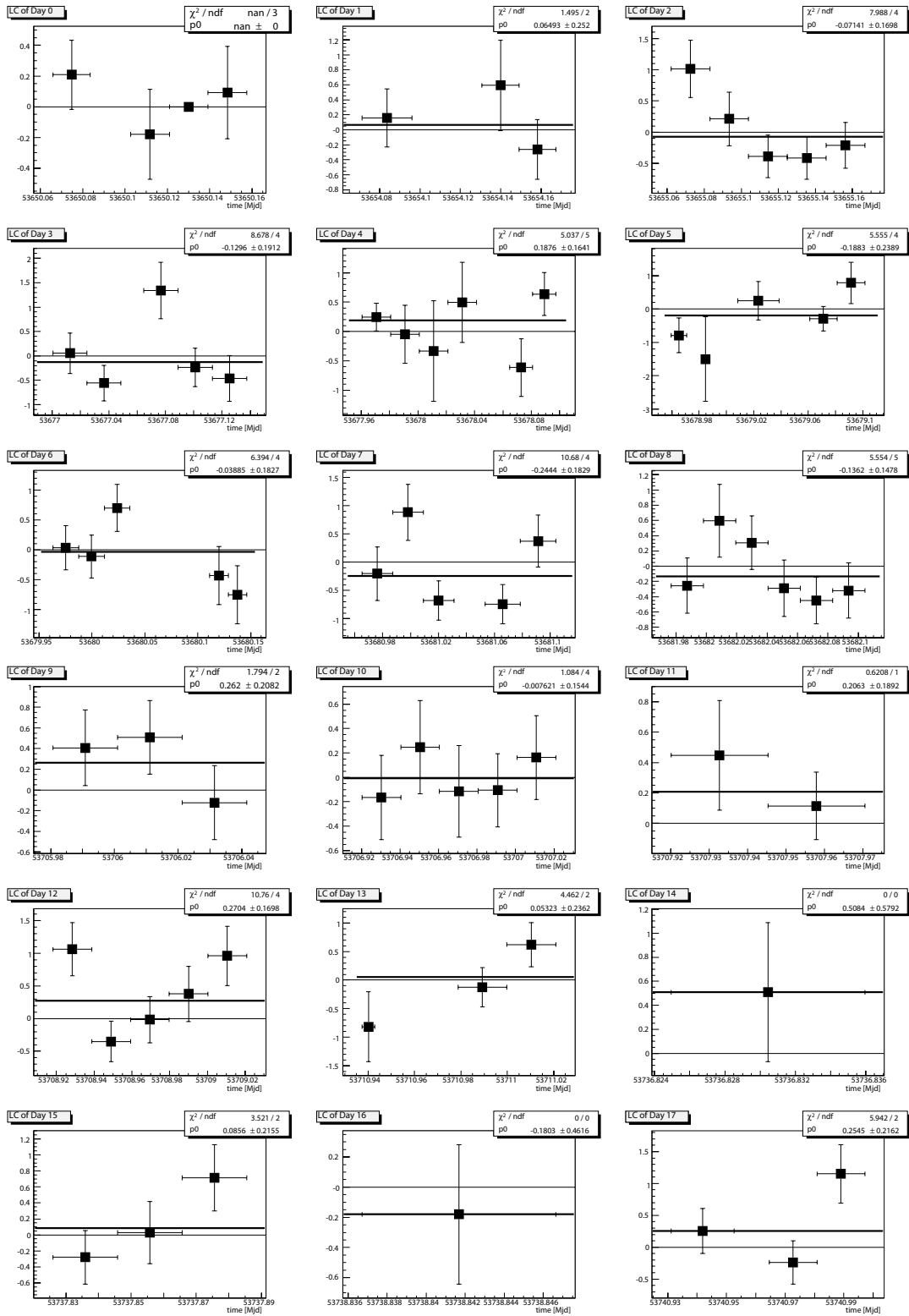
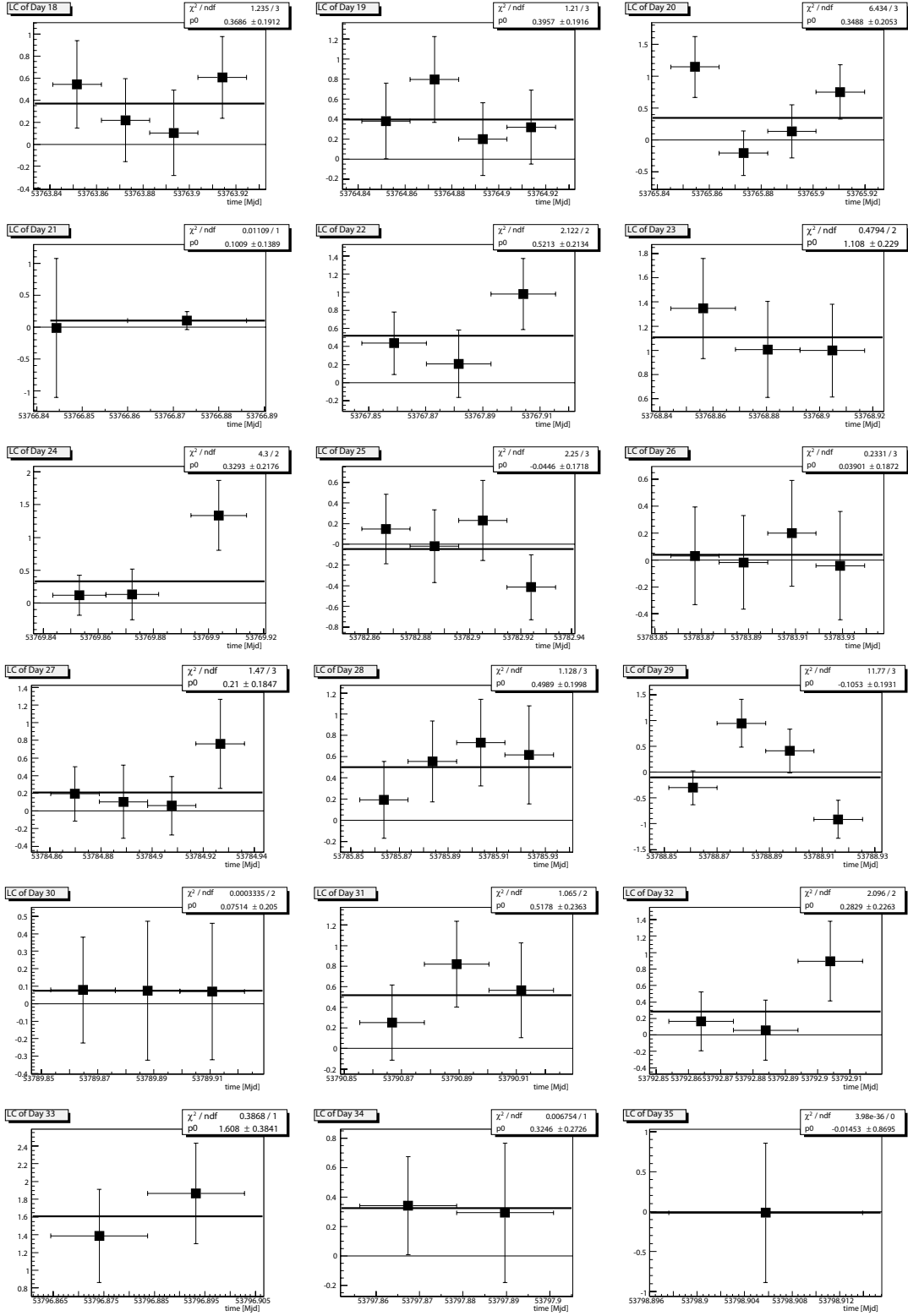


Figure A.2: Intranight light curves of *LS I +61°303* in OC I with $\Delta t = 30$ min binning

Figure A.3: Intranight light curves of LS I +61°303 in OC I with $\Delta t = 30$ min binning

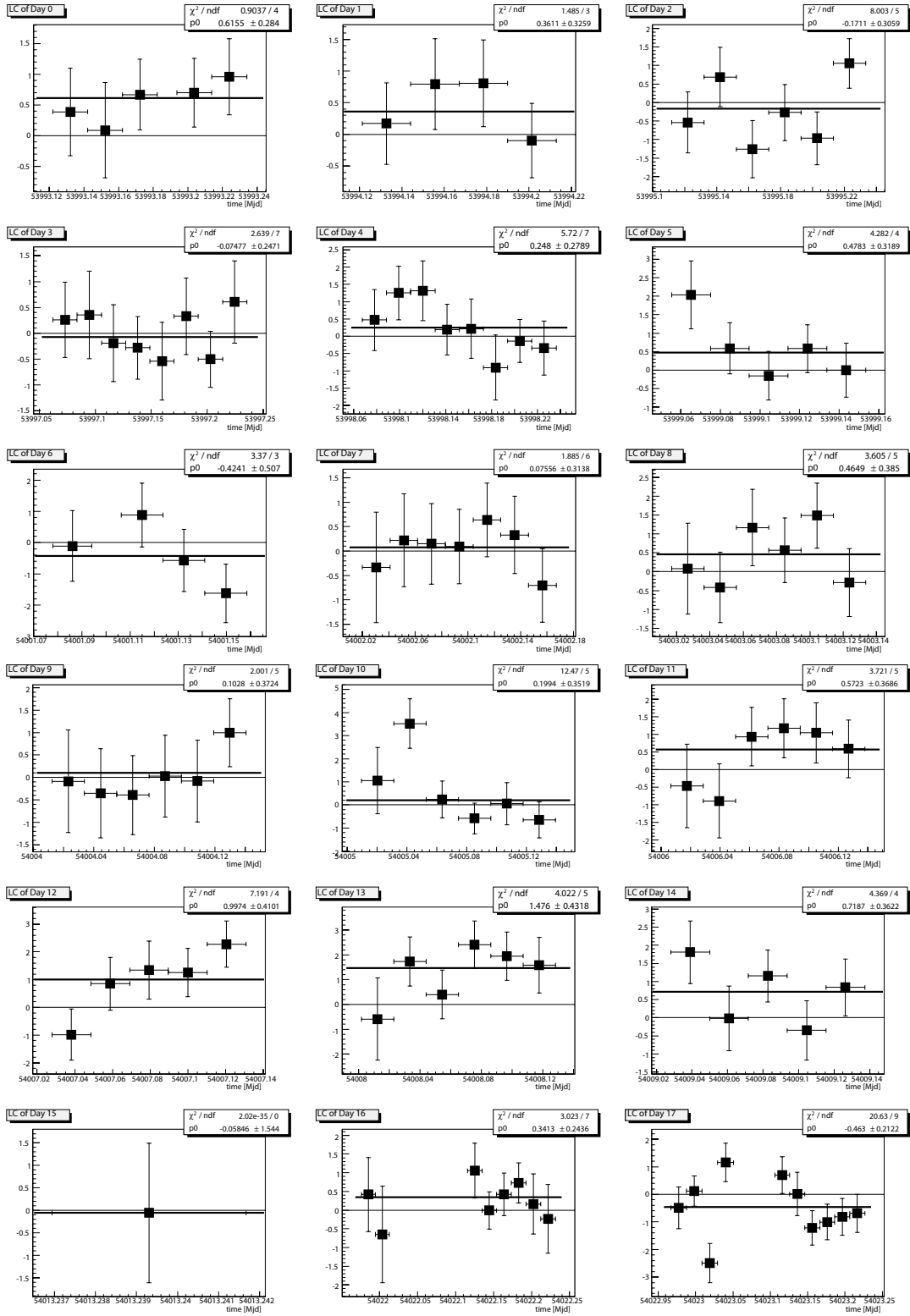
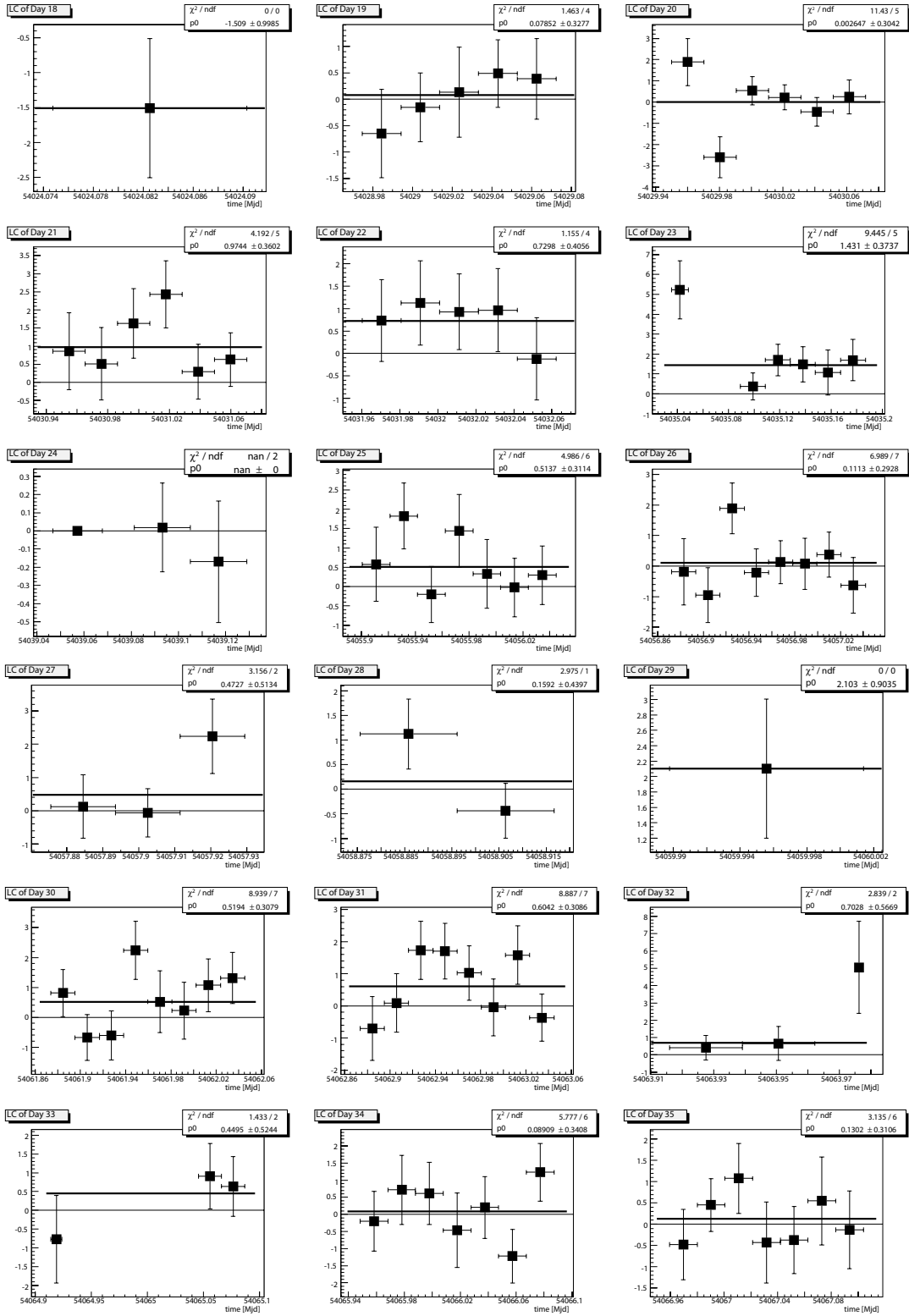


Figure A.4: Intranight light curves of *LS I +61°303* in OC II with $\Delta t = 30$ min binning

Figure A.5: Intranight light curves of LS I +61°303 in OC II with $\Delta t = 30$ min binning

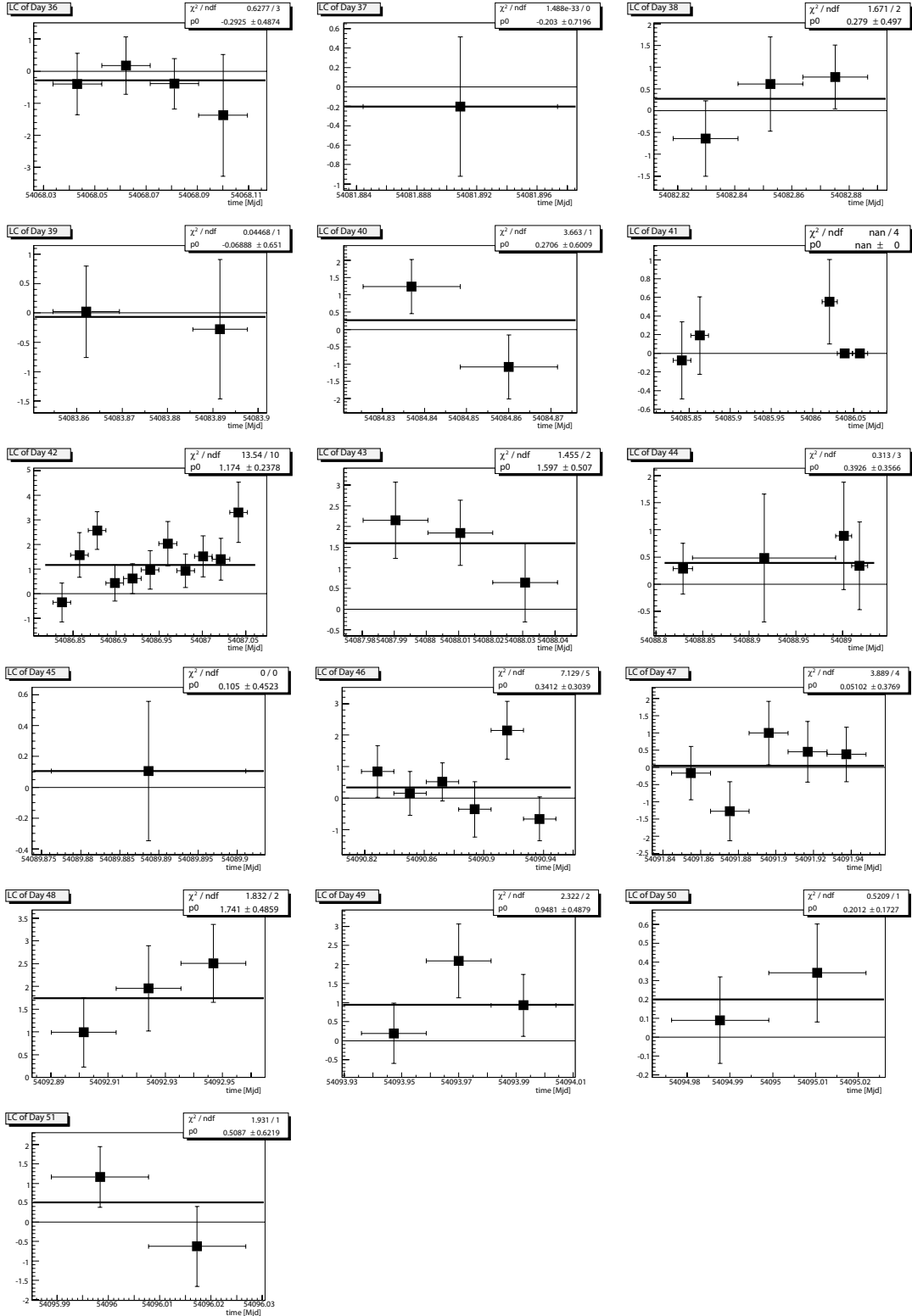
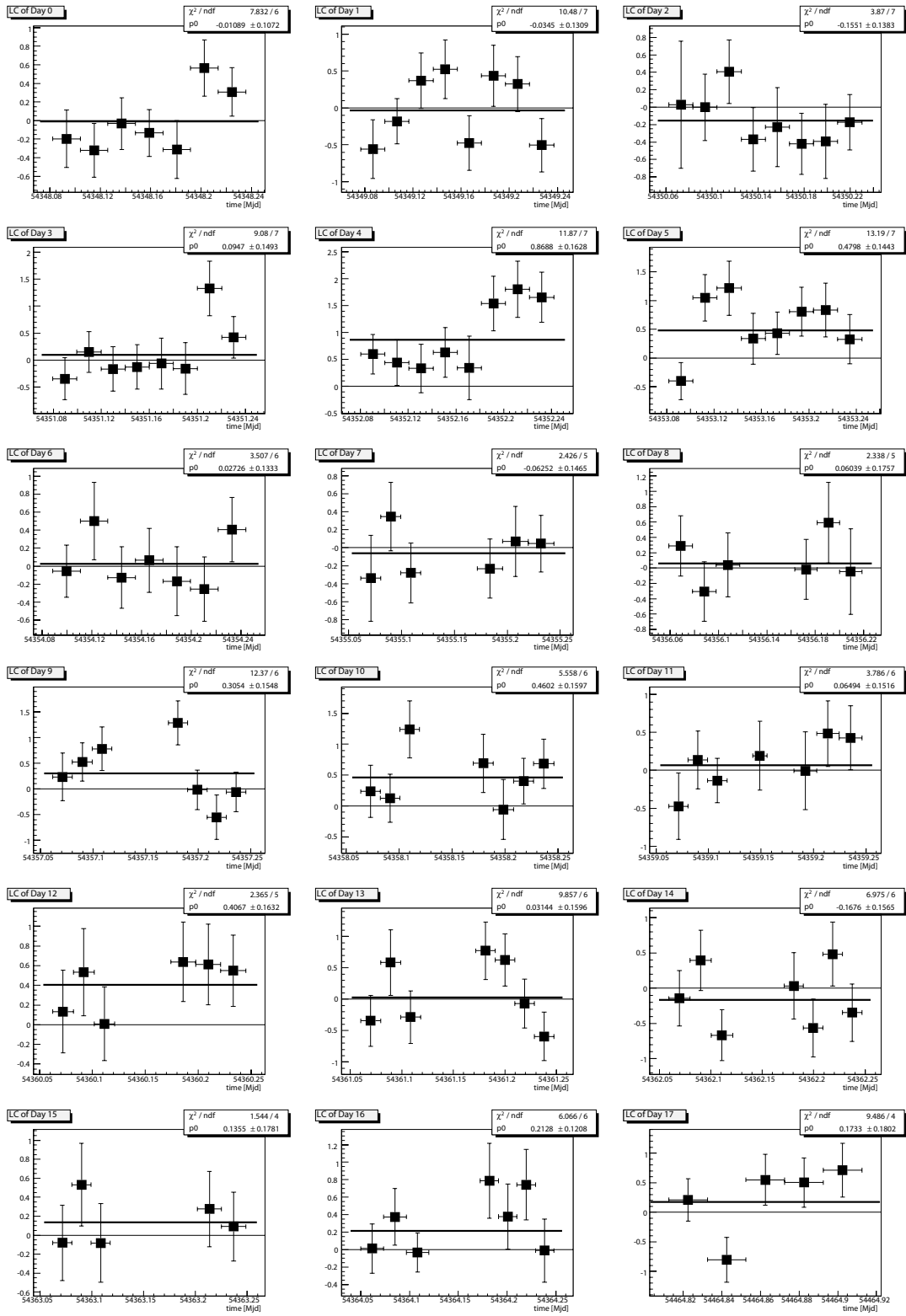


Figure A.6: Intranight light curves of *LS I +61°303* in OC II with $\Delta t = 30$ min binning

Figure A.7: Intranight light curves of LS I +61°303 in OC III with $\Delta t = 30$ min binning

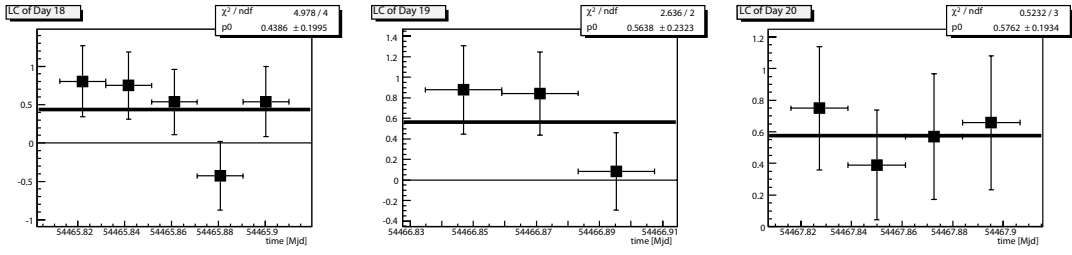


Figure A.8: Intranight light curves of LS I +61°303 in OC III with $\Delta t = 30$ min binning

A.3 LS I +61°303 spectra

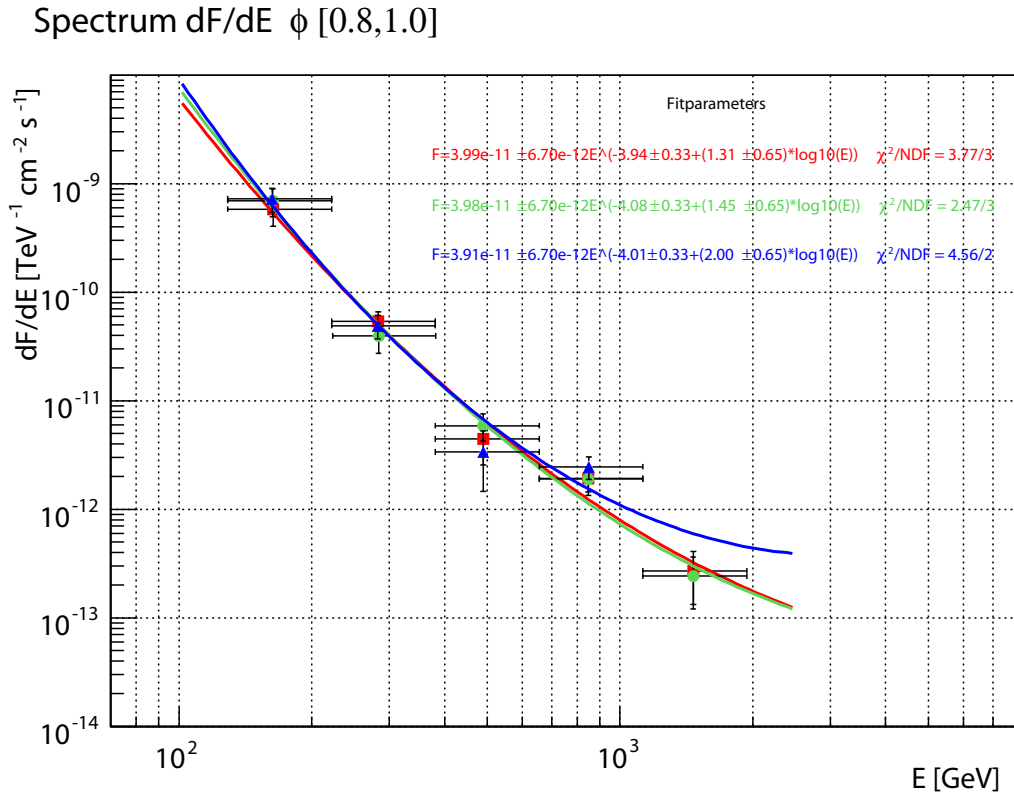


Figure A.9: The spectral energy distribution obtained from LS I +61°303 of OC III, fitted with a power law with variable spectral index. The Bertero method (red), Tikonove (green) and the Schmelling method (blue) agree very well within the errors. The spectral energy distribution is much better described by this shape compared to a simple power law (see A.10).

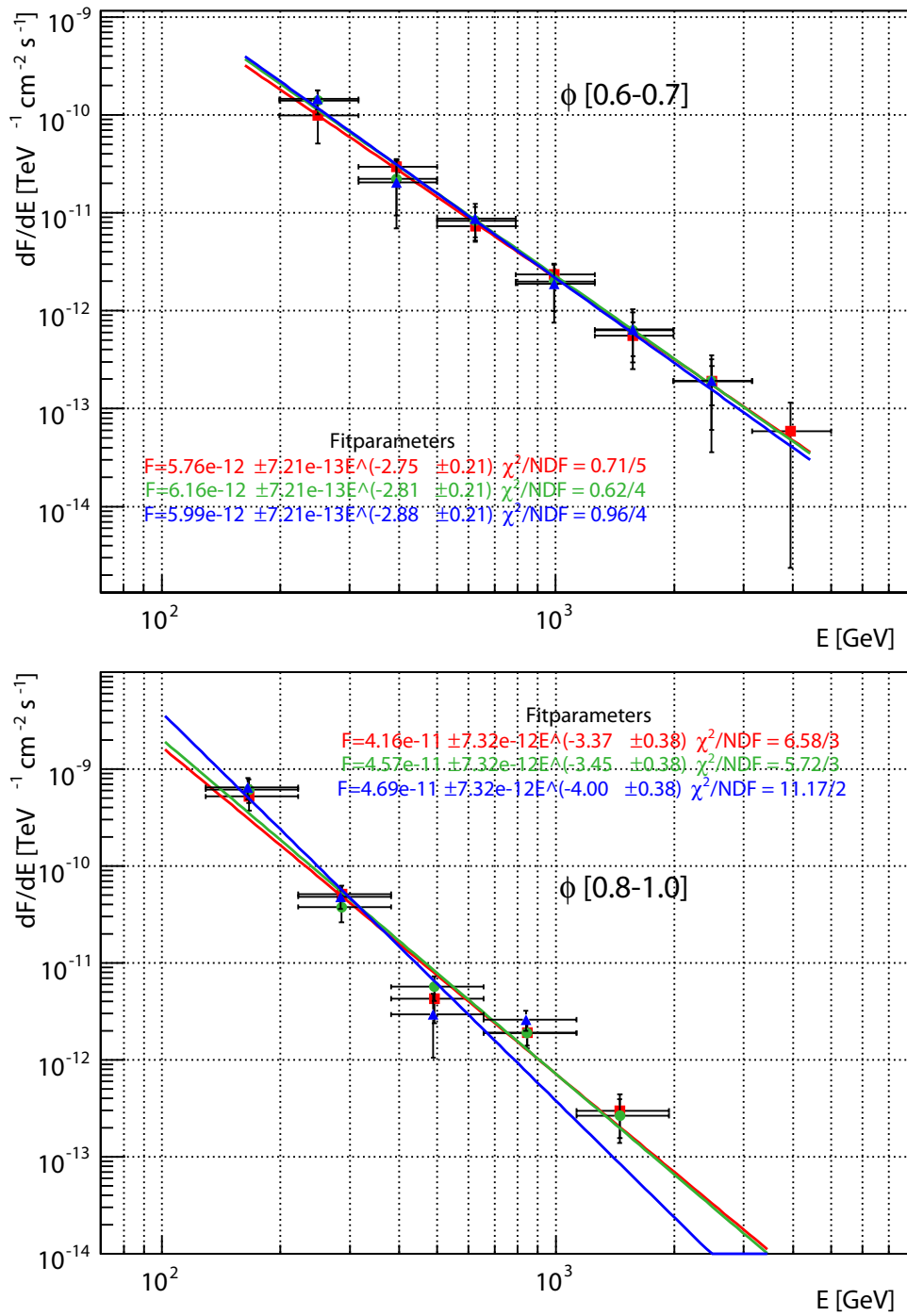


Figure A.10: The upper panel shows the three different unfolding procedures for the spectral energy distribution of OC III in the phase range $\phi \in [0.6, 0.7]$. The Betero method (red), Tikonove (green) and the Schmelling method (blue) agree very well within the errors. The lower panel displays the same for the phase range $\phi \in [0.8, 1.0]$. While in the upper panel the power law describes the spectral energy distribution well, the spectra in the lower panel are poorly described by this shape.

A.4 Estimation of the significance of the X-ray/TeV correlation in LS I +61°303

To estimate the significance of the linear correlation coefficient of $r = 0.89_{-0.13}^{+0.06}$ as obtained in chapter 7.10.2, two simulations are performed. In the first simulation two independent variables are randomly drawn from flat distributions. Ten such uncorrelated pairs are drawn (the same number as the correlated points in case of the LS I +61°303 measurements) and the correlation coefficient is calculated. This is repeated 10^7 times and the obtained correlation coefficient distribution is used to calculate the probability that $r > 0.89$ is obtained. The obtained probability is $\sim 6 \times 10^{-4}$ and the corresponding histogram of r shown in Fig. A.11.

The second type of simulation shuffles the measured distribution of X-ray and TeV flux measurements. Each value is used only once and in total (10!) different combinations are possible. I computed 10^6 random shuffles and calculated in the same way as for the flat distribution simulation the probability of obtaining an $r > 0.89$. The probability is $\sim 6.5 \times 10^{-4}$. The corresponding r-distribution is shown in Fig. A.12. Notice, that the r-distribution obtained due to shuffling is not symmetric, indicating that the flux points are not symmetrically distributed around the mean value. In principle, a bias due to our measurements is possible and thus, the shuffling method might be in some cases not a good approximation of the real distribution of the flux values. The main problem is that only very few measurements (10) are taken and that there is no guarantee that these form a representative sample of the real distribution of flux values. For this reason the flat distribution simulation is performed, which leads to a similar false alarm probability. Consequently the linear correlation coefficient gives a 3.4σ evidence for a correlation between both flux distributions.

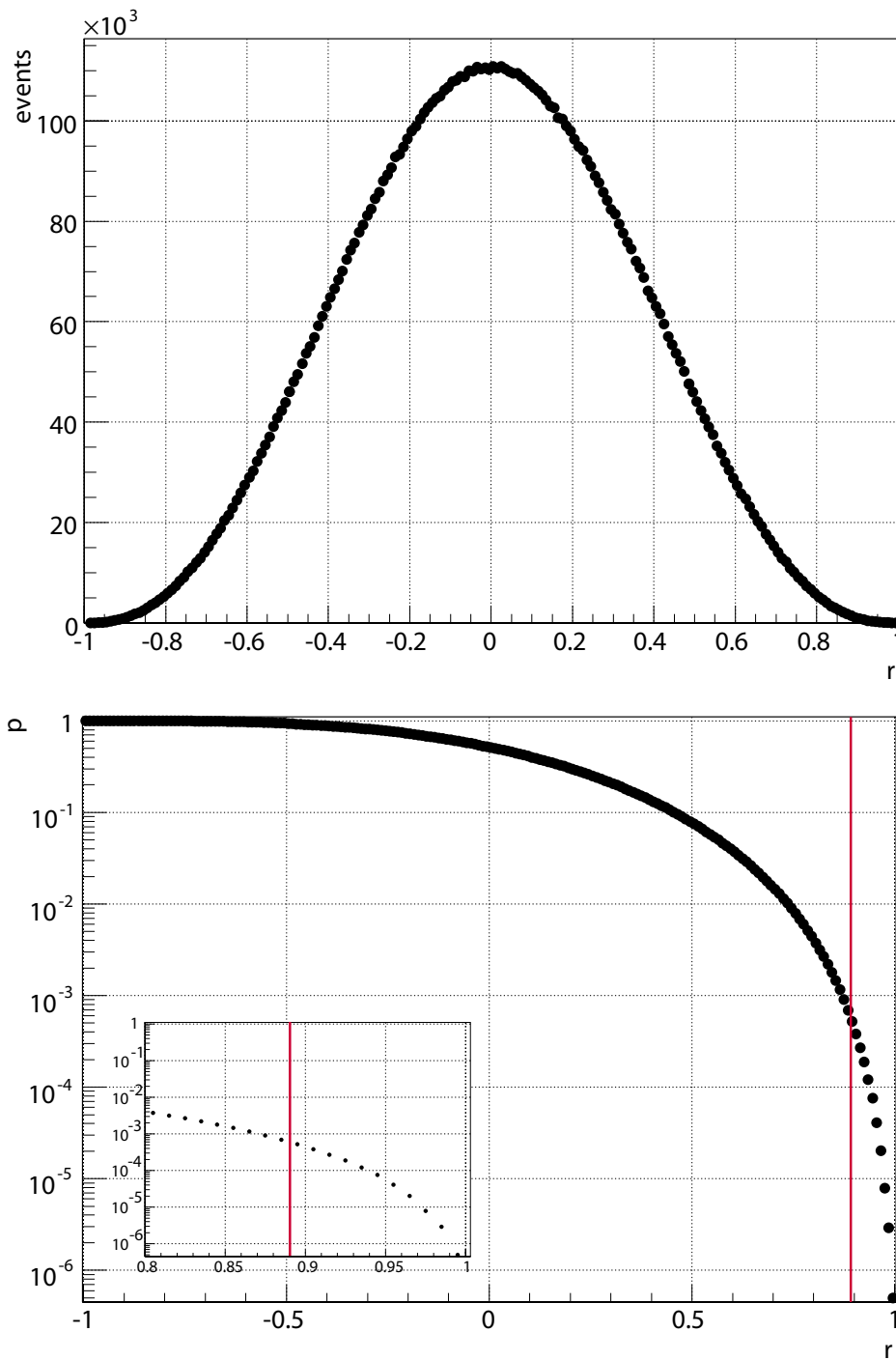


Figure A.11: The obtained linear correlation coefficient distribution after 10^7 simulations of ten pairs of two independent flat distributed variables is shown in the upper panel. The lower panel shows the probability to obtain a higher linear correlation coefficient than r . The red line displays the correlation coefficient obtained from the X-ra/TeV correlation in *LS I +61°303*.

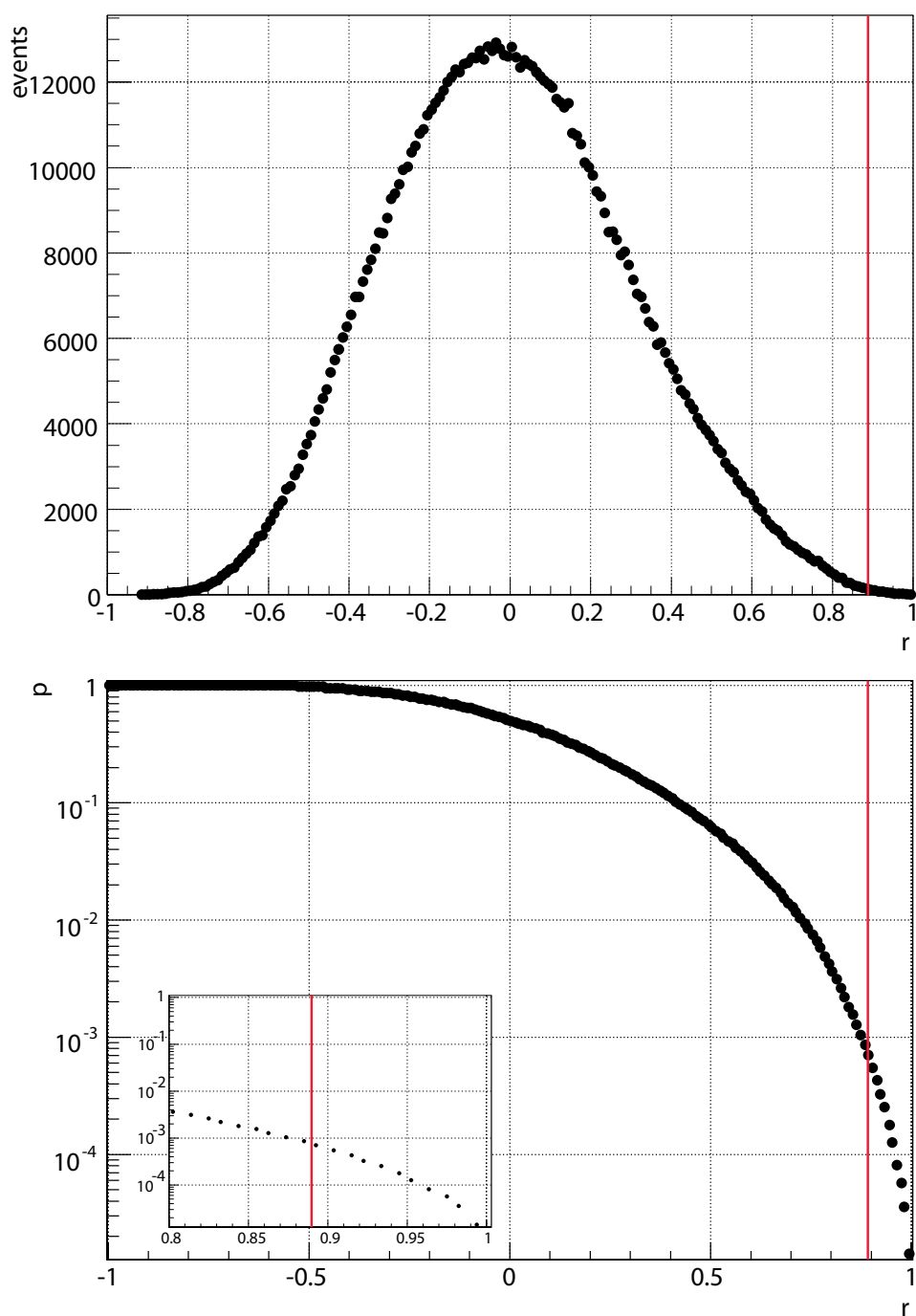


Figure A.12: The obtained linear correlation coefficient distribution after 10^6 random shuffling of the ten measured flux pairs is shown in the upper panel. The lower panel shows the probability to obtain a higher linear correlation coefficient than r . The red line displays the correlation coefficient obtained from the X-ra/TeV correlation in LS I +61°303.

List of Figures

1.1	Cosmic ray spectrum	8
1.2	Potential ultra high energy cosmic ray accelerators	9
1.3	VHE gamma-ray sources discovered up to February 2009	17
1.4	Scheme of the pulsar magnetosphere	18
1.5	Pulsar wind nebula composition	20
2.1	Quasar microquasar comparison	27
2.2	Individual jet regions and their scales	30
2.3	Jet ejecta evolution observed in GRS 1915+105 in 1994	32
2.4	X-ray emission states of microquasars	33
2.5	X-ray emission features in microquasars and their dependency on the emission state	35
2.6	Example of a hadronic SED of a microquasar	37
2.7	SED produced by secondary pairs in a binary system	38
3.1	MC simulated gamma-ray- and proton- induced air showers	47
3.2	Longitudinal electron and positron number in a Cherenkov air shower versus the height above the observation level	49
3.3	Energy threshold for Cherenkov light production of various particles	50
3.4	Cherenkov light pool comparison of gamma-ray- and proton- induced showers	51
3.5	Cherenkov light emission and absorption in the atmosphere	52
3.6	Shower image in the MAGIC camera	54
4.1	The MAGIC telescopes just after sunset in December 2008	57
4.2	Trigger configuration of MAGIC I	61
4.3	The schematic view of the MAGIC I calibration system setup.	62
4.4	Picture of MAGIC II	63
4.5	MAGIC II camera layout	64
4.6	Pixel design used in MAGIC II	65

4.7	Cluster support and mounted cluster in the MAGIC II camera	66
4.8	MAGIC II camera communication scheme	67
4.9	MAGIC II camera control program layout	69
5.1	Steps from raw data to primary particle parameters	75
5.2	Data processing pipeline	76
5.3	Comparison of the different image cleaning types	78
5.4	Geometrical interpretation of the Hillas parameters	80
5.5	Dependency of W and L on the parameter S	82
5.6	Dependency of W and L on the parameter D	83
5.7	Working principle of the random forest	85
5.8	Dependency of the hadroness on S for simulated gamma-ray and real back- ground data events	86
5.9	Hillas parameter distribution for simulated gamma-ray events and real back- ground data events	87
5.10	Energy resolution and energy bias as obtained from MC simulated gamma-ray events	89
5.11	Shower pointing direction reconstruction	91
5.12	Illustration of the wobble observation mode	93
5.13	Signal event selection	95
5.14	Source extension determination of the Crab Nebula	98
5.15	Effective Area versus estimated energy	100
5.16	Selection of source- and background region in X-ray analysis	106
5.17	Test of independency of PDF on the test frequency	111
5.18	Example periodogram of a simulated sinus signal overlaid by gaussian white noise	112
6.1	Flux LC of the Crab Nebula from 2005 to 2008	117
6.2	Derived spectra from the Crab Nebula data from 2005 to 2008	120
6.3	Comparison of the Crab Nebula spectra for different zenith angle ranges . .	121
6.4	Average DT value for dark nights and moon nights	122
6.5	Comparison of spectra obtained during moonlight and dark nights from the Crab Nebula	123
7.1	Different orbital solutions of LS I +61°303 as obtained from optical measure- ments	127
7.2	VLBI radio contours aligned along the orbit of LS I +61°303	130

7.3	Highest resolution X-ray image of LS I +61°303 obtained by <i>Chandra</i>	132
7.4	Discovery α -plot of LS I +61°303	136
7.5	Skymap of the vicinity of LS I +61°303, obtained with MAGIC in OC III	137
7.6	Phase folded LS I +61°303 LC for OC I	144
7.7	Phase folded LS I +61°303 LC for OC II	145
7.8	Phase folded LS I +61°303 LC for OC III	146
7.9	Intranight LC of LS I +61°303, showing a hint for short timescale variability	148
7.10	Temporal evolution of the rate and the number of visible stars for the night showing possible short timescale variability	148
7.11	Post trial false alarm probability for the periodogram power of LS I +61°303	150
7.12	Periodogram for LS I +61°303 around the orbital period	151
7.13	Scan for periodicity present in LS I +61°303 in a wider frequency range	152
7.14	Signal subtracted periodogram of LS I +61°303	153
7.15	Comparison of the LS I +61°303 emission period measurements in the various energy bands	155
7.16	Comparison of the spectra for the phase range 0.6–0.7 for all OC's	157
7.17	Spectra of three high flux nights of LS I +61°303	158
7.18	Possible spectral variability in LS I +61°303	159
7.19	Hardness ratio of the individual LC measurements of LS I +61°303	160
7.20	Hardness ratio versus integral flux of LS I +61°303	161
7.21	The <i>Swift</i> XRT LC of LS I +61°303	165
7.22	Phasefolded LC correlation of LS I +61°303 between X-rays and VHE gamma-rays during OC II	166
7.23	Simultaneously obtained X-ray and VHE gamma-ray LC's of LS I +61°303	168
7.24	X-ray versus VHE gamma-ray fluxes of LS I +61°303	168
7.25	X-ray spectrum of LS I +61°303 obtained on MJD 54352 with <i>XMM-Newton</i>	169
7.26	The multiwavelength measurements in OC II of LS I +61°303	171
7.27	VLBA radio maps of LS I +61°303 obtained in OC III	172
7.28	Simultaneous LC's in radio and VHE gamma-rays of LS I +61°303 obtained in OC III	172
7.29	Simultaneous spectral energy distribution from radio to VHE gamma-rays of LS I +61°303	173
7.30	Luminosity prediction of hadronic microquasar scenario for LS I +61°303	174
7.31	Luminosity prediction of leptonic microquasar scenario for LS I +61°303	176
7.32	Expected absorption modulation of the VHE gamma-ray fluxes in LS I +61°303	179

7.33	Termination shock location along the orbit of the compact object in LS I +61°303	180
7.34	Pulsar wind and clumpy stellar wind model of LS I +61°303	181
7.35	Prediction for spectrum and LC of the VHE gamma-ray emission in LS I +61°303 assuming a free pulsar wind with a power law distribution of electron energies	184
A.1	LC $E > 300$ GeV above LS I +61°303 OC III	193
A.2	Intranight light curves of LS I +61°303 in OC I with $\Delta t = 30$ min binning .	195
A.3	Intranight light curves of LS I +61°303 in OC I with $\Delta t = 30$ min binning .	196
A.4	Intranight light curves of LS I +61°303 in OC II with $\Delta t = 30$ min binning .	197
A.5	Intranight light curves of LS I +61°303 in OC II with $\Delta t = 30$ min binning .	198
A.6	Intranight light curves of LS I +61°303 in OC II with $\Delta t = 30$ min binning .	199
A.7	Intranight light curves of LS I +61°303 in OC III with $\Delta t = 30$ min binning	200
A.8	Intranight light curves of LS I +61°303 in OC III with $\Delta t = 30$ min binning	201
A.9	Comparison of different unfolding methods for a power law with variable index for LS I +61°303 in $0.8 < \phi < 0.9$	201
A.10	Comparison of different unfolding methods of the spectra of LS I +61°303 in different phase ranges	202
A.11	Probability estimation of the linear correlation coefficient from flat distributed random numbers	204
A.12	Probability estimation of the linear correlation coefficient from random shuf- fling of the obtained measurement pairs	205

List of Tables

5.1	Used S - cut values	102
5.2	The dependency of the false alarm probability and the derived frequency on the STI, as shown for a simulated sinus signal.	114
6.1	Observation log of the Crab Nebula data used for the performance study of MAGIC I.	116
6.2	The Crab Nebula data and the fit parameters of a constant flux to the different observation cycles. The χ^2 and its corresponding probability to obtain an even higher χ^2 value are given as well.	117
6.3	The spectral fit parameters of the individual OC Crab Nebula spectra.	119
7.1	The orbital parameters of LS I +61°303: eccentricity (e), periastron passage (ϕ_p) and mass function $f(M)$	127
7.2	MAGIC observation log of LS I +61°303	135
7.3	Orbital phase bin averaged LC table for all OC's	139
7.4	LS I +61°303 light curve OC III table	143
7.5	Spectral fit parameters in all OC's for LS I +61°303	156
7.6	The log of the X-ray observations: First seven observations are <i>XMM-Newton</i> and the others <i>Swift</i>	167
A.1	LS I +61°303 LC values for OC III with above $E = 300$ GeV	192

Bibliography

- Abdo, A. A. (2009). Fermi Large Area Telescope Bright Gamma-ray Source List. *ArXiv e-prints*, 0902.1340.
- Acciari, V. A. et al. (2008). VERITAS Observations of the γ -Ray Binary LS I +61 303. *The Astrophysical Journal*, 679:1427–1432, 0802.2363.
- Acciari, V. A. et al. (2009). Evidence for Long-Term Gamma-Ray and X-Ray Variability from the Unidentified TeV Source HESS J0632+057. *The Astrophysical Journal, Letters*, 698:L94–L97, 0905.3139.
- Achterberg, A., Gallant, Y. A., Kirk, J. G., and Guthmann, A. W. (2001). Particle acceleration by ultrarelativistic shocks: theory and simulations. *MNRAS*, 328:393–408, arXiv:astro-ph/0107530.
- Aharonian, F., Anchordoqui, L., Khangulyan, D., and Montaruli, T. (2006a). Microquasar LS 5039: a TeV gamma-ray emitter and a potential TeV neutrino source. *Journal of Physics Conference Series*, 39:408–415, arXiv:astro-ph/0508658.
- Aharonian, F. et al. (2001). Evidence for TeV gamma ray emission from Cassiopeia A. *Astronomy & Astrophysics*, 370:112–120.
- Aharonian, F. et al. (2002). An unidentified TeV source in the vicinity of Cygnus OB2. *Astronomy & Astrophysics*, 393:L37–L40, arXiv:astro-ph/0207528.
- Aharonian, F. et al. (2004a). The Crab Nebula and Pulsar between 500 GeV and 80 TeV: Observations with the HEGRA Stereoscopic Air Cerenkov Telescopes. *The Astrophysical Journal*, 614:897–913, arXiv:astro-ph/0407118.
- Aharonian, F. et al. (2005a). Discovery of the binary pulsar PSR B1259-63 in very-high-energy gamma rays around periastron with HESS. *Astronomy & Astrophysics*, 442:1–10, arXiv:astro-ph/0506280.

- Aharonian, F. et al. (2005b). Discovery of Very High Energy Gamma Rays Associated with an X-ray Binary. *Science*, 309:746–749, arXiv:astro-ph/0508298.
- Aharonian, F. et al. (2006b). Fast variability of tera-electron volt rays from the radio galaxy M87. *Science*, 314:1424–1427, arXiv:astro-ph/0612016.
- Aharonian, F. et al. (2006c). Observations of the Crab nebula with HESS. *Astronomy & Astrophysics*, 457:899–915, arXiv:astro-ph/0607333.
- Aharonian, F. et al. (2007a). An Exceptional Very High Energy Gamma-Ray Flare of PKS 2155-304. *The Astrophysical Journal, Letters*, 664:L71–L74, 0706.0797.
- Aharonian, F. et al. (2007b). Detection of extended very-high-energy γ -ray emission towards the young stellar cluster Westerlund 2. *Astronomy & Astrophysics*, 467:1075–1080, arXiv:astro-ph/0703427.
- Aharonian, F. et al. (2008). HESS very-high-energy gamma-ray sources without identified counterparts. *Astronomy & Astrophysics*, 477:353–363, 0712.1173.
- Aharonian, F. et al. (2009a). Discovery of Very High Energy γ -Ray Emission from Centaurus a with H.E.S.S. *The Astrophysical Journal, Letters*, 695:L40–L44, 0903.1582.
- Aharonian, F. et al. (2009b). HESS upper limit on the very high energy γ -ray emission from the globular cluster 47 Tucanae. *Astronomy & Astrophysics*, 499:273–277.
- Aharonian, F. A. and Bogovalov, S. V. (2003). Exploring physics of rotation powered pulsars with sub-10 GeV imaging atmospheric Cherenkov telescopes. *New Astronomy*, 8:85–103, arXiv:astro-ph/0208036.
- Aharonian, F. A., Drury, L. O., and Voelk, H. J. (1994). GeV/TeV gamma-ray emission from dense molecular clouds overtaken by supernova shells. *Astronomy & Astrophysics*, 285:645–647.
- Aharonian, F. A. et al. (1999). The temporal characteristics of the TeV gamma-radiation from MKN 501 in 1997. I. Data from the stereoscopic imaging atmospheric Cherenkov telescope system of HEGRA. *Astronomy & Astrophysics*, 342:69–86, arXiv:astro-ph/9808296.
- Aharonian, F. A. et al. (2004b). High-energy particle acceleration in the shell of a supernova remnant. *Nature*, 432:75–77, arXiv:astro-ph/0411533.
- Aharonian, F. A. et al. (2007c). Discovery of a point-like very-high-energy γ -ray source in Monoceros. *Astronomy & Astrophysics*, 469:L1–L4, 0704.0171.

- Albert, J. et al. (2006). Variable very high energy gamma-ray emission from the microquasar ls i +61 303. *Science*, 312:1771–1773, astro-ph/0605549.
- Albert, J. et al. (2007a). Discovery of Very High Energy Gamma Radiation from IC 443 with the MAGIC Telescope. *The Astrophysical Journal, Letters*, 664:L87–L90, 0705.3119.
- Albert, J. et al. (2007b). MAGIC Upper Limits on the Very High Energy Emission from Gamma-Ray Bursts. *The Astrophysical Journal*, 667:358–366, arXiv:astro-ph/0612548.
- Albert, J. et al. (2007c). Observation of VHE γ -rays from Cassiopeia A with the MAGIC telescope. *Astronomy & Astrophysics*, 474:937–940, 0706.4065.
- Albert, J. et al. (2007d). Unfolding of differential energy spectra in the MAGIC experiment. *Nuclear Instruments and Methods in Physics Research A*, 583:494–506, 0707.2453.
- Albert, J. et al. (2007e). Variable Very High Energy γ -Ray Emission from Markarian 501. *The Astrophysical Journal*, 669:862–883, arXiv:astro-ph/0702008.
- Albert, J. et al. (2007f). Very High Energy Gamma-Ray Radiation from the Stellar Mass Black Hole Binary Cygnus X-1. *The Astrophysical Journal, Letters*, 665:L51–L54, 0706.1505.
- Albert, J. et al. (2008a). FADC signal reconstruction for the MAGIC telescope. *Nuclear Instruments and Methods in Physics Research A*, 594:407–419, arXiv:astro-ph/0612385.
- Albert, J. et al. (2008b). Implementation of the Random Forest method for the Imaging Atmospheric Cherenkov Telescope MAGIC. *Nuclear Instruments and Methods in Physics Research A*, 588:424–432, 0709.3719.
- Albert, J. et al. (2008c). MAGIC Observations of the Unidentified γ -Ray Source TeV J2032+4130. *The Astrophysical Journal, Letters*, 675:L25–L28, 0801.2391.
- Albert, J. et al. (2008d). Multiwavelength (Radio, X-Ray, and γ -Ray) Observations of the γ -Ray Binary LS I +61 303. *The Astrophysical Journal*, 684:1351–1358, 0801.3150.
- Albert, J. et al. (2008). Probing quantum gravity using photons from a flare of the active galactic nucleus markarian 501 observed by the magic telescope. *Physics Letters B*, 668(4):253 – 257.
- Albert, J. et al. (2008a). Upper Limit for γ -Ray Emission above 140 GeV from the Dwarf Spheroidal Galaxy Draco. *The Astrophysical Journal*, 679:428–431, 0711.2574.

- Albert, J. et al. (2008b). Very High Energy Gamma-Ray Observations of Strong Flaring Activity in M87 in 2008 February. *The Astrophysical Journal, Letters*, 685:L23–L26, 0806.0988.
- Albert, J. et al. (2008c). Very-High-Energy gamma rays from a Distant Quasar: How Transparent Is the Universe? *Science*, 320:1752–, 0807.2822.
- Aliu, E. et al. (2008a). First Bounds on the High-Energy Emission from Isolated Wolf-Rayet Binary Systems. *The Astrophysical Journal, Letters*, 685:L71–L74, 0808.1832.
- Aliu, E. et al. (2008b). Observation of Pulsed γ -Rays Above 25 GeV from the Crab Pulsar with MAGIC. *Science*, 322:1221–, 0809.2998.
- Aliu, E. et al. (2009a). Improving the performance of the single-dish Cherenkov telescope MAGIC through the use of signal timing. *Astroparticle Physics*, 30:293–305, 0810.3568.
- Aliu, E. et al. (2009b). Upper Limits on the VHE Gamma-Ray Emission from the Willman 1 Satellite Galaxy with the Magic Telescope. *The Astrophysical Journal*, 697:1299–1304, 0810.3561.
- Aragona, C., McSwain, M. V., Grundstrom, E. D., Bolton, C. T., Ray, P. S., Ransom, S. M., Roberts, M. S. E., Dougherty, S., Hartman, J. M., and Pooley, G. (2009a). Optical Spectroscopy of Gamma-ray Binaries. In *American Astronomical Society Meeting Abstracts*, volume 213 of *American Astronomical Society Meeting Abstracts*, pages 410.08–+.
- Aragona, C., McSwain, M. V., Grundstrom, E. D., Marsh, A. N., Roettenbacher, R. M., Hessler, K. M., Boyajian, T. S., and Ray, P. S. (2009b). The Orbits of the Gamma-ray Binaries LS I +61 303 and LS 5039. *The Astrophysical Journal* *accepted*, 0902.4015.
- Arnaud, K. A. (1996). XSPEC: The First Ten Years. In Jacoby, G. H. and Barnes, J., editors, *Astronomical Data Analysis Software and Systems V*, volume 101 of *Astronomical Society of the Pacific Conference Series*, pages 17–+.
- Atoyan, A. M. and Aharonian, F. A. (1999). Modelling of the non-thermal flares in the Galactic microquasar GRS 1915+105. *MNRAS*, 302:253–276.
- Bastieri, D. et al. (2007). The reflecting surface of the MAGIC-II Telescope. *ArXiv e-prints*, 0709.1372.
- Bednarek, W. (1997). Cascade initiated by VHE γ -rays in the radiation field of a close massive companion. *Astronomy & Astrophysics*, 322:523–532.

- Bednarek, W. (2005). TeV Neutrinos from Microquasars in Compact Massive Binaries. *The Astrophysical Journal*, 631:466–470, arXiv:astro-ph/0505547.
- Bednarek, W. (2006a). Inverse Compton $e^{+/-}$ pair cascade model for the γ -ray production in massive binary LSI +61° 303. *MNRAS*, 371:1737–1743, arXiv:astro-ph/0606421.
- Bednarek, W. (2006b). Propagation of very high energy γ -rays inside massive binaries LS 5039 and LSI +61° 303. *MNRAS*, 368:579–591, arXiv:astro-ph/0601657.
- Bednarek, W. and Sitarek, J. (2007). High-energy γ -rays from globular clusters. *MNRAS*, 377:920–930, arXiv:astro-ph/0701522.
- Berezhko, E. G. (1996). Maximum energy of cosmic rays accelerated by supernova shocks. *Astroparticle Physics*, 5:367–378.
- Berezhko, E. G. and Völk, H. J. (1997). Kinetic theory of cosmic rays and gamma rays in supernova remnants. I. Uniform interstellar medium. *Astroparticle Physics*, 7:183–202.
- Bernlöhr, K. (2000). Impact of atmospheric parameters on the atmospheric Cherenkov technique*. *Astroparticle Physics*, 12:255–268, arXiv:astro-ph/9908093.
- Bertero, M. (1989). Linear inverse and ill-posed problems. *Advances in Electronics and Electron Physics*, 75:1–120.
- Bethe, H. and Heitler, W. (1934). On the stopping of fast particles and on the creation of positive electrons. *Proc. Roy. Soc. Lond.*, A146:83–112.
- Bignami, G. F., Caraveo, P. A., Lamb, R. C., Markert, T. H., and Paul, J. A. (1981). Einstein X-ray identification of the variable radio star LSI plus 61 deg 303. *The Astrophysical Journal, Letters*, 247:L85–L88.
- Biland, A. et al. (2008). The Active Mirror Control of the MAGIC Telescopes. In *International Cosmic Ray Conference*, volume 3 of *International Cosmic Ray Conference*, pages 1353–1356.
- Blandford, R. D. and Payne, D. G. (1982). Hydromagnetic flows from accretion discs and the production of radio jets. *MNRAS*, 199:883–903.
- Blandford, R. D. and Znajek, R. L. (1977). Electromagnetic extraction of energy from Kerr black holes. *MNRAS*, 179:433–456.

- Bluemer, J., Engel, R., and Hoerandel, J. R. (2009). Cosmic Rays from the Knee to the Highest Energies. *ArXiv e-prints*, 0904.0725.
- Blümer, H. and Kampert, K.-H. (2000). Die Suche nach den Quellen der kosmischen Strahlung. *Physics Bulletin*, 56:39–45.
- Bosch-Ramon, V., Khangulyan, D., and Aharonian, F. A. (2008). Non-thermal emission from secondary pairs in close TeV binary systems. *Astronomy & Astrophysics*, 482:397–402, 0801.4547.
- Bosch-Ramon, V., Paredes, J. M., Romero, G. E., and Ribó, M. (2006). The radio to TeV orbital variability of the microquasar LS I +61 303. *Astronomy & Astrophysics*, 459:L25–L28.
- Böttcher, M. and Dermer, C. D. (2005). Photon-Photon Absorption of Very High Energy Gamma Rays from Microquasars: Application to LS 5039. *The Astrophysical Journal, Letters*, 634:L81–L84, arXiv:astro-ph/0508359.
- Britzger, D. et al. (2009). Studies of the influence of moonlight on observations with magic. In *31th ICRC, Łódź*.
- Casares, J., Ribas, I., Paredes, J. M., Marti, J., and Allende Prieto, C. (2005). Orbital parameters of the microquasar lsi +61 303. *Mon. Not. Roy. Astron. Soc.*, 360:1091–1104, astro-ph/0504332.
- Cerutti, B., Dubus, G., and Henri, G. (2008). Spectral signature of a free pulsar wind in the gamma-ray binaries LS 5039 and LSI +61°303. *Astronomy & Astrophysics*, 488:37–46, 0807.1226.
- Cheng, K. S., Ho, C., and Ruderman, M. (1986a). Energetic radiation from rapidly spinning pulsars. I - Outer magnetosphere gaps. II - VELA and Crab. *The Astrophysical Journal*, 300:500–539.
- Cheng, K. S., Ho, C., and Ruderman, M. (1986b). Energetic Radiation from Rapidly Spinning Pulsars. II. VELA and Crab. *The Astrophysical Journal*, 300:522–+.
- Chernyakova, M., Neronov, A., and Walter, R. (2006). INTEGRAL and XMM-Newton observations of LSI +61° 303. *MNRAS*, 372:1585–1592, arXiv:astro-ph/0606070.
- Crowther, P. A. (2007). Physical Properties of Wolf-Rayet Stars. *ARA&A*, 45:177–219, arXiv:astro-ph/0610356.

- Daugherty, J. K. and Harding, A. K. (1982). Electromagnetic cascades in pulsars. *The Astrophysical Journal*, 252:337–347.
- Dessart, L. and Owocki, S. P. (2003). Two-dimensional simulations of the line-driven instability in hot-star winds. *Astronomy & Astrophysics*, 406:L1–L4.
- Dessart, L. and Owocki, S. P. (2005). 2D simulations of the line-driven instability in hot-star winds. II. Approximations for the 2D radiation force. *Astronomy & Astrophysics*, 437:657–666, arXiv:astro-ph/0503514.
- Dhawan, V., Mioduszewski, A., and Rupen, M. (2006). LS I +61 303 is a Be-Pulsar binary, not a Microquasar. In *Proceedings of the VI Microquasar Workshop: Microquasars and Beyond. September 18-22, 2006, Como, Italy.*, p.52.1.
- Domingo Santamaria, E. (2006). *Gamma-ray emission from regions of star formation: Theory and observations with the MAGIC telescope*. PhD thesis, Universitat Autònoma de Barcelona.
- Done, C., Gierliński, M., and Kubota, A. (2007). Modelling the behaviour of accretion flows in X-ray binaries. Everything you always wanted to know about accretion but were afraid to ask. *Astronomy & Astrophysics Review*, 15:1–66, 0708.0148.
- Dubus, G. (2006a). Gamma-ray absorption in massive X-ray binaries. *Astronomy & Astrophysics*, 451:9–18, arXiv:astro-ph/0509633.
- Dubus, G. (2006b). Gamma-ray binaries: pulsars in disguise? *Astronomy & Astrophysics*, 456:801–817, arXiv:astro-ph/0605287.
- Elterman, L. (1964). Parameters for attenuation in the atmospheric windows for fifteen wavelengths. *Appl. Opt.*, 3:745–+.
- Esposito, P., Caraveo, P. A., Pellizzoni, A., de Luca, A., Gehrels, N., and Marelli, M. A. (2007). Swift/XRT monitoring of five orbital cycles of LS I +61° 303. *Astronomy & Astrophysics*, 474:575–578, 0708.3330.
- Fender, R. P., Belloni, T. M., and Gallo, E. (2004). Towards a unified model for black hole X-ray binary jets. *MNRAS*, 355:1105–1118, arXiv:astro-ph/0409360.
- Fermi, E. (1949). On the Origin of the Cosmic Radiation. *Physical Review*, 75:1169–1174.
- Ferreira, J. (1997). Magnetically-driven jets from Keplerian accretion discs. *Astronomy & Astrophysics*, 319:340–359, arXiv:astro-ph/9607057.

- Fomin, V. P., Stepanian, A. A., Lamb, R. C., Lewis, D. A., Punch, M., and Weekes, T. C. (1994). New methods of atmospheric Cherenkov imaging for gamma-ray astronomy. I. The false source method. *Astroparticle Physics*, 2:137–150.
- Frail, D. A. and Hjellming, R. M. (1991). Distance and total column density to the periodic radio star LSI + 61 deg 303. *AJ*, 101:2126–2130.
- Gabici, S., Aharonian, F. A., and Blasi, P. (2007). Gamma rays from molecular clouds. *Ap&SS*, 309:365–371, arXiv:astro-ph/0610032.
- Gaisser, T. K. (1990). *Cosmic Ray and Particle Physics*. Cambridge University Press, first edition.
- Galante, N. (2006). *Very High Energy observation of GRBs with the MAGIC Telescope*. Ph.d, Universita degli studi siena.
- Gallant, Y. A., Achterberg, A., and Kirk, J. G. (1999). Particle acceleration at ultra-relativistic shocks. Gamma-ray burst afterglow spectra and UHECRs. *Astronomy & Astrophysics, Supplement*, 138:549–550.
- Gaug, M. (2006). *Calibration of the MAGIC Telescope and Observation of Gamma Ray Bursts*. Phd thesis, Universitat Autònoma de Barcelona Departament de Física.
- Gehrels, N. (1986). Confidence limits for small numbers of events in astrophysical data. *The Astrophysical Journal*, 303:336–346.
- Gehrels, N. et al. (2004). *The Astrophysical Journal*, 611:1005–1020.
- Georganopoulos, M., Aharonian, F. A., and Kirk, J. G. (2002). External Compton emission from relativistic jets in Galactic black hole candidates and ultraluminous X-ray sources. *Astronomy & Astrophysics*, 388:L25–L28, arXiv:astro-ph/0110379.
- Ghisellini, G., Celotti, A., Fossati, G., Maraschi, L., and Comastri, A. (1998). A theoretical unifying scheme for gamma-ray bright blazars. *MNRAS*, 301:451–468, arXiv:astro-ph/9807317.
- Gierliński, M., Zdziarski, A. A., Poutanen, J., Coppi, P. S., Ebisawa, K., and Johnson, W. N. (1999). Radiation mechanisms and geometry of Cygnus X-1 in the soft state. *MNRAS*, 309:496–512, arXiv:astro-ph/9905146.
- Gini, C. (1921). Measurement of inequality of income. *Economic Journal*, 31:22–43.

- Godet, O. et al. (2009). Modelling the spectral response of the Swift-XRT CCD camera: experience learnt from in-flight calibration. *Astronomy & Astrophysics*, 494:775–797, 0811.4246.
- Goebel, F., Bartko, H., Carmona, E., Galante, N., Jogler, T., Mirzoyan, R., Coarasa, J. A., and Teshima, M. (2007). Upgrade of the MAGIC Telescope with a Multiplexed Fiber-Optic 2 GSamples/s FADC Data Acquisition system. *ArXiv e-prints*, 0709.2363.
- Goldoni, P. and Mereghetti, S. (1995). X-ray observations of the peculiar Be star LSI +61 303. *Astronomy & Astrophysics*, 299:751–+, arXiv:astro-ph/9502044.
- Goldreich, P. and Julian, W. H. (1969). Pulsar Electrodynamics. *The Astrophysical Journal*, 157:869–+.
- Gregory, P. C. (2002). *Astrophys. J.*, 575:427–434.
- Gregory, P. C. (2002). Bayesian Analysis of Radio Observations of the Be X-Ray Binary LS I +61°303. *The Astrophysical Journal*, 575:427–434.
- Gregory, P. C. and Taylor, A. R. (1978). New highly variable radio source, possible counterpart of gamma-ray source CG135+1. *Nature*, 272:704–706.
- Greisen, K. (1956). *Prog. Cosmic Ray Physics*, (3):1.
- Greisen, K. (1966). End to the Cosmic-Ray Spectrum? *Physical Review Letters*, 16:748–750.
- Grundstrom, E. D., Caballero-Nieves, S. M., Gies, D. R., Huang, W., McSwain, M. V., Rafter, S. E., Riddle, R. L., Williams, S. J., and Wingert, D. W. (2007). Joint H α and X-Ray Observations of Massive X-Ray Binaries. II. The Be X-Ray Binary and Microquasar LS I +61 303. *The Astrophysical Journal*, 656:437–443, arXiv:astro-ph/0610608.
- Gupta, S. and Böttcher, M. (2006). A Time-dependent Leptonic Model for Microquasar Jets: Application to LS I +61 303. *The Astrophysical Journal, Letters*, 650:L123–L126, arXiv:astro-ph/0606590.
- Gupta, S., Böttcher, M., and Dermer, C. D. (2006). Time-dependent Synchrotron and Compton Spectra from Jets of Microquasars. *The Astrophysical Journal*, 644:409–423, arXiv:astro-ph/0602439.
- Harding, A. K., Muslimov, A. G., and Zhang, B. (2002). Regimes of Pulsar Pair Formation and Particle Energetics. *The Astrophysical Journal*, 576:366–375, arXiv:astro-ph/0205077.

- Harris, D. E. (2001). Current Problems for X-ray Emission from Radio Jets. In Laing, R. A. and Blundell, K. M., editors, *Particles and Fields in Radio Galaxies Conference*, volume 250 of *Astronomical Society of the Pacific Conference Series*, pages 204–+.
- Heavens, A. F. and Meisenheimer, K. (1987). Particle acceleration in extragalactic sources - The role of synchrotron losses in determining the spectrum. *MNRAS*, 225:335–353.
- Heck, D. et al. (1998). Corsika: A monte carlo code to simulate extensive air showers. Technical Report FZKA 6019, Forschungszentrum Karlsruhe.
- Heinz, S. and Sunyaev, R. (2002). Cosmic rays from microquasars: A narrow component to the CR spectrum? *Astronomy & Astrophysics*, 390:751–766, arXiv:astro-ph/0204183.
- Hermesen, W., Swanenburg, B. N., Bignami, G. F., Boella, G., Buccheri, R., Scarsi, L., Kanbach, G., Mayer-Hasselwander, H. A., Masnou, J. L., and Paul, J. A. (1977). New high energy gamma-ray sources observed by COS B. *Nature*, 269:494–+.
- Hess, V. (1912). Über beobachtungen der durchdringenden strahlung bei sieben freiballon-fahrten. *Physikalische Zeitschrift*, (13):1084.
- Hillas, A. M. (1984). The Origin of Ultra-High-Energy Cosmic Rays. *ARA&A*, 22:425–444.
- Hillas, A. M. (1985). *Proc. 19th ICRC*, 3:445.
- Hillas, A. M. et al. (1998). The Spectrum of TeV Gamma Rays from the Crab Nebula. *The Astrophysical Journal*, 503:744–+.
- Hinton, J. A. et al. (2009). HESS J0632+057: A New Gamma-Ray Binary? *The Astrophysical Journal, Letters*, 690:L101–L104, 0809.0584.
- Hirovani, K. (2007). High-Energy Emission from Pulsar Outer Magnetospheres. *The Astrophysical Journal*, 662:1173–1176, arXiv:astro-ph/0307236.
- Holland, A. D., Turner, M. J., Abbey, A. F., and Pool, P. J. (1996). MOS CCDs for the EPIC on XMM. In Siegmund, O. H. and Gummin, M. A., editors, *Society of Photo-Optical Instrumentation Engineers (SPIE) Conference Series*, volume 2808 of *Presented at the Society of Photo-Optical Instrumentation Engineers (SPIE) Conference*, pages 414–420.
- Hutchings, J. B. and Crampton, D. (1981). Spectroscopy of the unique degenerate binary star LSI + 61°303. *PASP*, 93:486–489.

- Jogler, T. et al. (2009). Magic observation of globular cluster m13 and its millisecond pulsars. In *31th ICRC, Łódź*.
- Johnston, S., Ball, L., Wang, N., and Manchester, R. N. (2005). Radio observations of PSR B1259-63 through the 2004 periastron passage. *MNRAS*, 358:1069–1075, arXiv:astro-ph/0501660.
- Kelner, S. R. and Aharonian, F. A. (2008). Energy spectra of gamma rays, electrons, and neutrinos produced at interactions of relativistic protons with low energy radiation. *Phys. Rev. D*, 78(3):034013–+, 0803.0688.
- Kelner, S. R., Aharonian, F. A., and Bugayov, V. V. (2006). Energy spectra of gamma rays, electrons, and neutrinos produced at proton-proton interactions in the very high energy regime. *Phys. Rev. D*, 74(3):034018–+, arXiv:astro-ph/0606058.
- Khangulyan, D., Aharonian, F., and Bosch-Ramon, V. (2008). On the formation of TeV radiation in LS 5039. *MNRAS*, 383:467–478, 0707.1689.
- Kirk, J. G., Lyubarsky, Y., and Petri, J. (2007). The theory of pulsar winds and nebulae. astro-ph/0703116.
- Kniffen, D. A., Alberts, W. C. K., Bertsch, D. L., Dingus, B. L., Esposito, J. A., Fichtel, C. E., Foster, R. S., Hartman, R. C., Hunter, S. D., Kanbach, G., Lin, Y. C., Mattox, J. R., Mayer-Hasselwander, H. A., Michelson, P. F., von Montigny, C., Mukherjee, R., Nolan, P. L., Paredes, J. M., Ray, P. S., Schneid, E. J., Sreekumar, P., Tavani, M., and Thompson, D. J. (1997). EGRET Observations of the Gamma-Ray Source 2CG 135+01. *The Astrophysical Journal*, 486:126–+.
- Leahy, D. A. (2001). The gamma-ray source LSI +61deg303. I. RXTE/ASM observations. *Astronomy & Astrophysics*, 380:516–519.
- Leahy, D. A., Harrison, F. A., and Yoshida, A. (1997). The ASCA X-Ray Spectrum of the Unusual Binary LSI +61 degrees 303. *The Astrophysical Journal*, 475:823–+.
- Lewin, W. H. G. and van der Klis, M. (2006). *Compact stellar X-ray sources*.
- Li, T. P. and Ma, Y. Q. (1983). Analysis methods for results in gamma-ray astronomy. *Astrophys. J.*, 272:317–324.
- Liu, Q. Z., van Paradijs, J., and van den Heuvel, E. P. J. (2005). High-mass X-ray binaries in the Magellanic Clouds. *Astronomy & Astrophysics*, 442:1135–1138.

- Liu, Q. Z., van Paradijs, J., and van den Heuvel, E. P. J. (2006). Catalogue of high-mass X-ray binaries in the Galaxy (4th edition). *Astronomy & Astrophysics*, 455:1165–1168, 0707.0549.
- Liu, Q. Z., van Paradijs, J., and van den Heuvel, E. P. J. (2007). A catalogue of low-mass X-ray binaries in the Galaxy, LMC, and SMC (Fourth edition). *Astronomy & Astrophysics*, 469:807–810, 0707.0544.
- Lomb, N. R. (1976). Least-squares frequency analysis of unequally spaced data. *Ap&SS*, 39:447–462.
- Longair, M. S. (1994). *High Energy Astrophysics*, volume 2. 2nd edition.
- Majumdar, P. et al. (2005). Monte Carlo simulation for the MAGIC telescope. In *International Cosmic Ray Conference*, volume 5 of *International Cosmic Ray Conference*, pages 203–+.
- Maraschi, L. and Treves, A. (1981). A model for LSI61 deg 303. *MNRAS*, 194:1P–5P.
- Marti, J. and Paredes, J. M. (1995). Modelling of LSI+61 303 from near infrared data. *Astronomy & Astrophysics*, 298:151–+.
- Massi, M., Ribó, M., Paredes, J. M., Garrington, S. T., Peracaula, M., and Martí, J. (2004). Hints for a fast precessing relativistic radio jet in LS I +61°303. *Astronomy & Astrophysics*, 414:L1–L4, arXiv:astro-ph/0312091.
- Massi, M., Ribó, M., Paredes, J. M., Peracaula, M., and Estalella, R. (2001). One-sided jet at milliarcsecond scales in LS I +61°303. *Astronomy & Astrophysics*, 376:217–223, arXiv:astro-ph/0107093.
- Mendelson, H. and Mazeh, T. (1989). Discovery of a 26.5-day optical periodicity of LSI+61°303. *MNRAS*, 239:733–740.
- Mészáros, P. (2002). Theories of Gamma-Ray Bursts. *ARA&A*, 40:137–169, arXiv:astro-ph/0111170.
- Mioduszewski, A. J., Rupen, M. P., Hjellming, R. M., Pooley, G. G., and Waltman, E. B. (2001). A One-sided Highly Relativistic Jet from Cygnus X-3. *The Astrophysical Journal*, 553:766–775, arXiv:astro-ph/0102018.
- Mirabel, I. F. and Rodriguez, L. F. (1994). A Superluminal Source in the Galaxy. *Nature*, 371:46–+.

- Mirabel, I. F. and Rodríguez, L. F. (1998). Microquasars in our Galaxy. *Nature*, 392:673–676.
- Mirabel, I. F. and Rodríguez, L. F. (1999). Sources of Relativistic Jets in the Galaxy. *ARA&A*, 37:409–443, arXiv:astro-ph/9902062.
- Mirabel, I. F., Rodríguez, L. F., Cordier, B., Paul, J., and Lebrun, F. (1992). A double-sided radio jet from the compact Galactic Centre annihilator 1E140.7 - 2942. *Nature*, 358:215–217.
- Moskalenko, I. V. and Karakula, S. (1994). Light curves of close binaries in TeV energy region. *ApJS*, 92:567–573.
- Muslimov, A. G. and Harding, A. K. (2003). Extended Acceleration in Slot Gaps and Pulsar High-Energy Emission. *The Astrophysical Journal*, 588:430–440, arXiv:astro-ph/0301023.
- National, G. D. C. (1992). U.S. standard atmosphere (1976). *Planet. Space Sci.*, 40:553–554.
- Neronov, A. and Aharonian, F. A. (2007). Production of TeV Gamma Radiation in the Vicinity of the Supermassive Black Hole in the Giant Radio Galaxy M87. *The Astrophysical Journal*, 671:85–96, 0704.3282.
- Neronov, A. and Chernyakova, M. (2007). Radio-to-TeV γ -ray emission from PSR B1259 63. *Ap&SS*, 309:253–259, arXiv:astro-ph/0610139.
- Orellana, M., Bordas, P., Bosch-Ramon, V., Romero, G. E., and Paredes, J. M. (2007). Leptonic secondary emission in a hadronic microquasar model. *Astronomy & Astrophysics*, 476:9–15, 0710.0751.
- Orellana, M. and Romero, G. E. (2007). High-energy gamma-ray emission from the inner jet of LS I +61 303: the hadronic contribution revisited. *Ap&SS*, 309:333–338, arXiv:astro-ph/0608707.
- Ostrowski, M. (2000). On possible ‘cosmic ray cocoons’ of relativistic jets. *MNRAS*, 312:579–584, arXiv:astro-ph/9910491.
- Owocki, S. P., Romero, G. E., Townsend, R. H. D., and Araudo, A. T. (2009). Gamma-Ray Variability from Wind Clumping in High-Mass X-Ray Binaries with Jets. *The Astrophysical Journal*, 696:690–693, 0902.2278.
- Paneque, D. (2004). *The MAGIC Telescope: development of new technologies and first observations*. Ph.d., Technische Universität München.

- Paneque, D., Gebauer, H. J., Lorenz, E., Martinez, M., Mase, K., Mirzoyan, R., Ostankov, A., and Schweizer, T. (2003). A method to enhance the sensitivity of photomultipliers for air Cherenkov telescopes. *Nuclear Instruments and Methods in Physics Research A*, 504:109–115.
- Paredes, J. M., Marti, J., Peracaula, M., and Ribo, M. (1997). Evidence of X-ray periodicity in LSI+61 303. *Astronomy & Astrophysics*, 320:L25–L28.
- Paredes, J. M., Marziani, P., Marti, J., Fabregat, J., Coe, M. J., Everall, C., Figueras, F., Jordi, C., Norton, A. J., Prince, T., Reglero, V., Roche, P., Torra, J., Unger, S. J., and Zamanov, R. (1994). Photometric and H α observations of LSI+61 303: detection of a \sim 26 day V and JHK band modulation. *Astronomy & Astrophysics*, 288:519–528, arXiv:astro-ph/9402016.
- Paredes, J. M., Ribó, M., Bosch-Ramon, V., West, J. R., Butt, Y. M., Torres, D. F., and Martí, J. (2007). Chandra Observations of the Gamma-Ray Binary LS I +61 303: Extended X-Ray Structure? *The Astrophysical Journal, Letters*, 664:L39–L42, 0706.0877.
- Perucho, M. and Bosch-Ramon, V. (2008). On the interaction of microquasar jets with stellar winds. *Astronomy & Astrophysics*, 482:917–927, 0802.1134.
- Protheroe, R. J. and Stanev, T. (1987). Constraints on models of Cygnus X-3 from high-energy gamma-ray absorption at source. *The Astrophysical Journal*, 322:838–841.
- Puls, J., Markova, N., Scuderi, S., Stanghellini, C., Taranova, O. G., Burnley, A. W., and Howarth, I. D. (2006). Bright OB stars in the Galaxy. III. Constraints on the radial stratification of the clumping factor in hot star winds from a combined H α , IR and radio analysis. *Astronomy & Astrophysics*, 454:625–651, arXiv:astro-ph/0604372.
- Punsly, B. (1999). A Magnetized Black Hole Model of LS I +61°303. *The Astrophysical Journal*, 519:336–344.
- Reynoso, M. M., Christiansen, H. R., and Romero, G. E. (2008). Gamma-ray absorption in the microquasar SS433. *Astroparticle Physics*, 28:565–572, 0707.1844.
- Rieger, F. M. and Aharonian, F. A. (2008). Variable VHE gamma-ray emission from non-blazar AGNs. *Astronomy & Astrophysics*, 479:L5–L8, 0712.2902.
- Rieger, F. M. and Duffy, P. (2004). Shear Acceleration in Relativistic Astrophysical Jets. *The Astrophysical Journal*, 617:155–161, arXiv:astro-ph/0410269.

- Roach, F. E. and Gordon, J. L. (1973). *The light of the night sky*. Dordrecht, Boston, Reidel [1973].
- Rolke, W., Lopez, A., and Conrad, J. (2005). Confidence intervals with frequentist treatment of statistical and systematic uncertainties. *Nucl. Instrum. Meth.*, A551:493–503, physics/0403059.
- Romero, G. E. (2008). High-energy emission from microquasars. *ArXiv e-prints*, 0810.0202.
- Romero, G. E., Christiansen, H. R., and Orellana, M. (2005). Hadronic High-Energy Gamma-Ray Emission from the Microquasar LS I +61 303. *The Astrophysical Journal*, 632:1093–1098, arXiv:astro-ph/0506735.
- Romero, G. E., Torres, D. F., Kaufman Bernadó, M. M., and Mirabel, I. F. (2003). Hadronic gamma-ray emission from windy microquasars. *Astronomy & Astrophysics*, 410:L1–L4, arXiv:astro-ph/0309123.
- Ruderman, M. A. and Sutherland, P. G. (1975). Theory of pulsars - Polar caps, sparks, and coherent microwave radiation. *The Astrophysical Journal*, 196:51–72.
- Saito, T., Zanin, R., Bordas, P., Bosh-Ramon, V., Jogler, T., Paredes, J., Ribo, M., Rissi, M., Rico, J., and Torres, D. (2009). Microquasars observed with the magic telescope. In *31th ICRC, Łódź*.
- Scargle, J. D. (1982). Studies in astronomical time series analysis. II - Statistical aspects of spectral analysis of unevenly spaced data. *The Astrophysical Journal*, 263:835–853.
- Schmelling, M. (1994). The method of reduced cross-entropy A general approach to unfold probability distributions. *Nuclear Instruments and Methods in Physics Research A*, 340:400–412.
- Shapiro, S. L. and Teukolsky, S. A. (1986). *Black Holes, White Dwarfs and Neutron Stars: The Physics of Compact Objects*.
- Sidoli, L., Pellizzoni, A., Vercellone, S., Moroni, M., Mereghetti, S., and Tavani, M. (2006). XMM-Newton observation of a spectral state transition in the peculiar radio/X-ray/ γ -ray source LS I +61 303. *Astronomy & Astrophysics*, 459:901–907, arXiv:astro-ph/0606722.
- Sierpowska-Bartosik, A. and Torres, D. F. (2008). Pulsar wind zone processes in LS 5039. *Astroparticle Physics*, 30:239–263, 0801.3427.

- Sierpowska-Bartosik, A. and Torres, D. F. (2009). γ -Ray Emission from LS I +61 303: The Impact of Basic System Uncertainties. *The Astrophysical Journal*, 693:1462–1473, 0811.2466.
- Sturrock, P. A. (1971). A Model of Pulsars. *The Astrophysical Journal*, 164:529–+.
- Swihart, T. L. (1968). *Astrophysics and stellar astronomy*. Space Science Text Series. New York: Wiley.
- Swordy, S. (1997). http://astroparticle.uchicago.edu/cosmic_ray_spectrum_picture.htm.
- Tavani, M. (1993). Gamma rays from globular clusters. *The Astrophysical Journal*, 407:135–141.
- Tavani, M., Kniffen, D., Mattox, J. R., Paredes, J. M., and Foster, R. (1998). The Variable Gamma-Ray Source 2CG 135+01. *The Astrophysical Journal, Letters*, 497:L89+.
- Taylor, A. R. and Gregory, P. C. (1982). Periodic radio emission from LS I +61 deg 303. *The Astrophysical Journal*, 255:210–216.
- Taylor, A. R., Young, G., Peracaula, M., Kenny, H. T., and Gregory, P. C. (1996). An X-ray outburst. from the radio emitting X-ray binary LSI+61 303. *Astronomy & Astrophysics*, 305:817–+.
- Tescaro, D., Aleksic, J., Barcelo, M., Bitossi, M., Cortina, J., Illa, J. M., Martinez, M., Mazin, D., Paoletti, R., Pegna, R., and on behalf of the MAGIC collaboration (2009). The readout system of the magic-ii cherenkov telescope. In *31th ICRC, Łódź*.
- The Pierre Auger Collaboration, Abraham, J., et al. (2007). Correlation of the Highest-Energy Cosmic Rays with Nearby Extragalactic Objects. *Science*, 318:938–, 0711.2256.
- Tikhonov, A. N. and Arsenin, V. J. (1979). *Methods of Solution of Ill-posed Problems*. Navka, M.
- Torres, D. F., Romero, G. E., Combi, J. A., Benaglia, P., Andernach, H., and Punsly, B. (2001). A variability analysis of low-latitude unidentified gamma-ray sources. *Astronomy & Astrophysics*, 370:468–478, arXiv:astro-ph/0007464.
- van Dijk, R., Bennett, K., Bloemen, H., Collmar, W., Connors, A., Diehl, R., Hermsen, W., Lichti, G. G., McConnell, M., Much, R., Schoenfelder, V., Steinle, H., Strong, A., and Tavani, M. (1996). COMPTEL detection of the high-energy γ -ray source 2CG 135+01. *Astronomy & Astrophysics*, 315:485–492, arXiv:astro-ph/9604136.

- van Paradijs, J., Kouveliotou, C., and Wijers, R. A. M. J. (2000). Gamma-Ray Burst Afterglows. *ARA&A*, 38:379–425.
- Venter, C., DeJager, O. C., and Clapson, A.-C. (2009). Predictions of Gamma-Ray Emission from Globular Cluster Millisecond Pulsars Above 100 MeV. *The Astrophysical Journal Letters*, 696:L52–L55, 0903.3031.
- Virtanen, J. J. P. and Vainio, R. (2005). Stochastic Acceleration in Relativistic Parallel Shocks. *The Astrophysical Journal*, 621:313–323, arXiv:astro-ph/0411184.
- Wagner, R. M. (2006). *Measurement of very high energy gamma-ray emission from four blazars using the MAGIC telescope and a comparative blazar study*. PhD thesis, Max-Planck-Institut für Physik, Föhringer Ring 6, 80805 München, Germany.
- Waters, L. B. F. M., van den Heuvel, E. P. J., Taylor, A. R., Habets, G. M. H. J., and Persi, P. (1988). Evidence for low-velocity winds in Be/X-ray binaries. *Astronomy & Astrophysics*, 198:200–210.
- Wen, L., Levine, A. M., Corbet, R. H. D., and Bradt, H. V. (2006). A Systematic Search for Periodicities in RXTE ASM Data. *ApJS*, 163:372–392, arXiv:astro-ph/0512529.
- Winter, L. M., Mushotzky, R. F., and Reynolds, C. S. (2006). XMM-Newton Archival Study of the Ultraluminous X-Ray Population in Nearby Galaxies. *The Astrophysical Journal*, 649:730–752, arXiv:astro-ph/0512480.
- Zamanov, R. K., Martí, J., Paredes, J. M., Fabregat, J., Ribó, M., and Tarasov, A. E. (1999). Evidence of H α periodicities in LS I+61°303. *Astronomy & Astrophysics*, 351:543–550, arXiv:astro-ph/9909233.
- Zanin, R., Cortina, J., and on behalf of the MAGIC collaboration (2009). The central control of the magic telescopes. In *31th ICRC, Łódź*.
- Zatsepin, G. T. and Kuz'min, V. A. (1966). Upper Limit of the Spectrum of Cosmic Rays. *Soviet Journal of Experimental and Theoretical Physics Letters*, 4:78–+.
- Zdziarski, A. A. and Gierliński, M. (2004). Radiative Processes, Spectral States and Variability of Black-Hole Binaries. *Progress of Theoretical Physics Supplement*, 155:99–119, arXiv:astro-ph/0403683.
- Zdziarski, A. A., Neronov, A., and Chernyakova, M. (2008). A compact pulsar wind nebula model of the gamma-ray loud binary LS I +61 303. *ArXiv e-prints*, 0802.1174.

Zenitani, S. and Hoshino, M. (2001). The Generation of Nonthermal Particles in the Relativistic Magnetic Reconnection of Pair Plasmas. *The Astrophysical Journal, Letters*, 562:L63–L66.

Acknowledgements

I am very thankful to Siegfried Bethke, Masahiro Teshima and Razmick Mirzoyan for granting me the possibility to do a PhD thesis in the MAGIC group of the MPI for Physics. My work on the MAGIC telescopes and the study of VHE gamma-ray binaries profited a lot from the excellent facilities and working environment provided by the MPI and particularly by the MAGIC group. Especially, I am in debt to Masahiro Teshima for supporting my attendance at several international conferences.

I specially thank Emiliano Carmona for plenty of discussions of physics and for his attentive review of my thesis. In addition, I want to thank all the other group members for fruitful and enlightening discussions: Eckart Lorenz, Nepomuk Otte, Daniel Mazin, Robert Wagner, Thomas Schweizer, Maxim Shayduk, Takayuki Saito, Daniela Borla Tridon, Julian Sitarek, Masaaki Hayashida, Nicola Galante, Wolfgang Wittek, Pratik Majumdar, Ching Cheng Hsu, Rudi Bock, Hendrik Bartko, Pierre Collin, Hiroko Miyamoto, Sybille Rodriguez, Ina Wacker and Burkhard Steinke.

I am in debt to Corey Ray and Natasha Wilcke for revising my English.

I am very thankful for the discussions with members of the MAGIC collaboration outside of the Munich group. Special thanks to: Daniel Kranich for the discussion about periodicity tests and to Víctor Zabalza for the help and cross check of the X-ray analysis. Many thanks for the discussion about LS I +61°303 to: Nuria Sidro, Neus Puchades, Valenti Bosch-Ramon, Marc Ribó, Josep Maria Paredes, Miguel Ángel Pérez Torres, Diego F. Torres, Javier Rico, Juan Cortina and Javier Moldón.

I enjoyed the excellent team work with Werner Haberer on the MAGIC II camera control as well as the help of David Fink and Jens Schlammer in the commissioning of the camera in La Palma. I am in debt to Burkhard Steinke for taking care of the camera control program in the last months when I focused on writing this thesis.

The tragic death of Florian Goebel, with whom I worked closely together on the MAGIC II camera and from whom I learned a lot, grieves me very much.

Finally, I want to thank my parents for all their support and love for me during all my life. The greatest thank of all goes to Saskia, my love, which supported me more than anyone else.